UNIVERSITY OF CALIFORNIA

Santa Barbara

Quantum Dot Lasers for Silicon Photonics

A dissertation submitted in partial satisfaction of the
requirements for the degree

Doctor of Philosophy
in
Materials

by

Justin Colby Norman

Committee in charge:

Professor John Bowers, Co-Chair
Professor Arthur Gossard, Co-Chair
Professor Chris Palmstrøm
Professor Dirk Bouwmeester

December 2018

The dissertation of Justin Colby Norman is approved.

_____

Professor Dirk Bouwmeester

_____

Professor Chris Palmstrøm

_____

Professor Arthur Gossard, Committee Co-Chair

_____

Professor John Bowers, Committee Co-Chair

December 2018

Quantum Dot Lasers for Silicon Photonics

by

Justin Colby Norman

Dedicated to April Norman

ACKNOWLEDGEMENTS

If a thesis were like a journal article and all contributors given credit in the author list, then my title page would exceed entire length of this body of work. Pursuing a Ph.D. is not a simple endeavor, and its pursuit begins long before a student begins their journey in graduate school. To do proper justice to everyone in my life who contributed to my efforts would not be possible in the limited scope of this document, but I will attempt to acknowledge the key individuals who got me here, helped along the way in my scientific endeavors, and who helped me maintain the tenuous grip on sanity inherent to graduate studies.

First, I must acknowledge my committee. Each member has helped in their own way with useful feedback and new ideas throughout my studies. Prof. John Bowers as my primary advisor must receive special recognition for offering continuous feedback throughout the project to keep my "eye on the ball" regarding real world relevance and specific goals in terms of device performance. His knack for acquiring funding ensured that money was never a concern during my studies and made it feel as if I was operating on a semi-infinite budget. He also granted me the freedom to pursue my own ideas--even when they were not necessarily good ones. My co-advisor, Prof. Arthur Gossard, was also instrumental in my success by offering useful advice, and his seemingly ubiquitous contact with anyone who has ever done molecular beam epitaxy or utilized devices produced by the technique led to several opportunities for fruitful collaborations that expanded my knowledge of other materials systems, different types of devices and physics, and helped me to build my professional network. He also provided considerable amounts of enjoyable lunch time conversation. Prof. Chris Palmstrom's most notable contributions to my success were in shooting down my poor,

ill-formed ideas and teaching me to be critical of published literature. If not for his advice I may have wasted considerable time attempting to reproduce shoddy science. Prof. Bouwmeester was the last addition to my committee but also had significant impact through allowing me to grow material for studies within his group that enriched my understanding of QD physics and exposed me to a new application space in quantum communications, something I could easily return to in the future.

My original mentor, Alan Liu, deserves his own paragraph. Alan selected me for the internship during my undergraduate that first made me aware of the University of California, Santa Barbara and provided my first exposure to molecular beam epitaxy, semiconductor lasers in general, and to quantum dots in particular. In retrospect, his decision to involve me in the entire process from thin film characterization to device processing to laser testing was likely foolhardy and almost surely took several years from his life as he watched my precarious attempts at using tweezers on what would eventually become his first successful laser devices. Alan was my primary mentor and taught me most of what I know regarding semiconductor processing, lasers, and molecular beam epitaxy. His development of this project also provided a springboard for my work allowing for progress to be made at a much faster rate.

While Alan is responsible for the bulk of my training, Hong Lu and Peter Burke also deserve credit for teaching me the basics of molecular beam epitaxy and answering questions. Chong Zhang also deserves credit for teaching me a lot regarding device processing and supplementing Alan's explanations of laser physics. Michael Davenport was particularly insightful regarding the finer details of processing in the UCSB cleanroom and laser characterization and led to the adoption of Andrekson's method for laser characterization

which has revealed several unique properties of quantum dot lasers. All members of the Bowers group and the MBE lab, past and present, deserve their own credit for contributions large and small. Kunal Mukherjee also deserves his own shoutout for providing stimulating discussion and significantly increasing my understanding of dislocations.

Daehwan Jung deserves special recognition for making critical contributions to the project leading to orders of magnitude improvement in device results in a few short months by demonstrating low defect density buffers on GaP/Si. His ideas, in a few short months, managed to outpace several years of our previous work and provided templates for my optimized quantum dot growths to demonstrate not only the unique performance advantages of dots over wells but to also do so on silicon substrates. Prior to his advancements in the III-V/Si buffer, no laser on Si had ever been reported with performance remotely similar to native substrate devices. Daehwan has also proved invaluable for bouncing around my half-baked ideas about buffer and laser designs and provided a check against my tendency to too rapidly jump from idea to idea.

The younger students who have worked on the project including Chen Shang, Robert Zhang, Jenny Selvidge, Brian Cabinian, and Mario Dumont also deserve credit for asking difficult questions and forcing me to attempt to teach my knowledge, which has enhanced my own understanding. They have also each contributed in major ways to the project in terms of device characterization and material development which have guided many recent results and future plans.

The cleanroom team, including MJ Kennedy, Yating Wan, Alfredo Torres, and Jon Peters, are the unsung heroes of this project. When I started, the growers did their own processing, and perhaps it is coincidence, but after two of my own ill-fated processing runs, John decided

to expand the team, adding MJ, Alfredo, and Yating such that I never again had to touch a wafer once it entered the cleanroom until the fabrication was completed. The expertise provided by dedicated staff and their efficiency dramatically increased the throughput on results for my work. I should also thank the dedicated university staff that keep the cleanroom and various material characterization facilities running.

John English. Few living remember his origin, but the legends speak of a being formed in the cold vacuum of the first molecular beam epitaxy system emerging on its first opening muttering vulgar comments and chastising a graduate student for gross incompetence. They say he can speak to MBE chambers and diagnose any fault with merely a glance. Many believe this silver-haired demigod to be truly immortal having endured decades of As exposure, the raging infernos of elemental P in atmosphere, and the endless onslaught against one's sanity that is working with graduate students. While the true nature of his being may never be understood by mere mortals, what cannot be denied is his innate ability to transfer wisdom and keep an MBE lab running smoothly.

Kurt Olsson is John's successor and has proved himself worthy of the title. His dedication to the logistics of running a multi-user MBE facility while keeping up with maintenance on nine separate systems yields productivity that is not matched in any MBE lab anywhere else in the world. Without Kurt (and John previously) the achievements of various groups in the MBE labs at UCSB would be a mere fraction of what they are now.

I offer sincere gratitude to everyone who has worked behind the scenes in supporting my work. Particularly I want to thank Ceanna Bowman, Tina Hang, Jon Winterbottom, and Jane Kittle who have all worked to make sure my paychecks and reimbursements arrived in a timely fashion and to correct the seemingly infinite number of ways I have found to incorrectly enter

purchase orders and travel reimbursement forms. Their work controlling the money flow has kept the project moving smoothly allowing me to focus on research and has also kept me from ending up as a starving beach bum years ago.

I also offer a special thanks to the many collaborators who have helped to demonstrate the full capabilities of the material I worked to develop, and the others that prompted me to explore entirely new areas of research. In particular, thanks again to Prof. Dirk Bouwmeester and his team including Wolfgang Loffler, John Frey, and the full team at Leiden. Also special thanks to Dr. Robert Herrick, Prof. Frederic Grillot and Dr. Weng Chow whose collaborations were instrumental to the most ground-breaking results of this thesis. Thank you to Prof. Sascha Preu for exposing me to the field of THz devices and ErAs nanostructures and Prof. Leonid Butov for allowing me to contribute to some very interesting research in excitonic devices.

As I mentioned previously, a Ph.D. does not begin in graduate school; it is the culmination of a lifetime of promoted interest in continued learning and the value of knowledge. My parents, sister, grandparents, and great grandparents all encouraged my curiosity and interest in science long before my formal education started in kindergarten, and several instrumental teachers along the way including Sandy Mathews, Bobby Burch, Brian Leonard, and Roberta Watts led to my specific interests in engineering and physics. I should also acknowledge my undergraduate thesis advisor, Prof. Keith Roper, who provided my first significant exposure to scientific research.

I must also acknowledge those outside of my academic life who kept me sane throughout this process including my first-year roommates in 1217 (including honorary members), the pint night drinking crew of the middle years, the UCSB club fencing team, my various Dungeons and Dragons groups, the Bowers basketball group, and, most importantly, my wife.

April has provided unyielding support and encouragement throughout my graduate studies. She has been there through the fun parts and the stressful parts always offering encouragement and helping to ease my burdens by helping with the often-neglected aspects of life that exist outside of research. She is a constant reminder that there is more to life than science and has provided a valuable check against my ego in the recent years of seemingly endless positive results. She has made many sacrifices to allow me to pursue my goals, and for that, I am forever grateful.

Curriculum Vitae of Justin Norman

December 2018

EDUCATION

Ph.D.	**University of California, Santa Barbara** Electronic & Photonic Materials, 2018 Dissertation: *Quantum Dot Lasers for Silicon Photonics* Advisor: Prof. John Bowers & Prof. Arthur Gossard
B.S.	**University of Arkansas, Fayetteville** Chemical Engineering, 2013
B.S.	**University of Arkansas, Fayetteville** Physics, 2013

AWARDS & HONORS

North American MBE Conference Best Student Paper	2018
Frenkel Foundation Fellow	2018
1st Place IEEE Photonics Conference Best Student Paper	2017
National Science Foundation Graduate Research Fellowship	2014
1st Place International Environmental Design Competition	2013
Statewide Undergraduate Research Fellowship	2012
EPSCoR Statewide Undergraduate Research Fellowship	2011
University of Arkansas Honors College Fellowship	2009

PUBLICATIONS

1. H. Huang, J. Duan, D. Jung, A. Y. Liu, Z. Zhang, J. Norman, J. E. Bowers, F. Grillot, *Analysis of the optical feedback dynamics in InAs/GaAs quantum dot lasers directly grown on silicon*, J. Opt. Soc. Am. B, 35, 2780-2787 (2018).
2. D. Inoue, Y. Wan, D. Jung, J. Norman, C. Shang, N. Nishiyama, S. Arai, A. C. Gossard, J. E. Bowers, *Low-dark current 10 Gb/s operation of InAs/InGaAs quantum dot pin photodiode grown on on-axis (001) GaP/Si*, Appl. Phys. Lett. 113, 093506 (2018).
3. Z. Zhang, D. Jung, J. C. Norman, P. Patel, W. W. Chow, J. E. Bowers, *Effects of modulation p doping in InAs quantum dot lasers on silicon*, Appl. Phys. Lett. 113, 061105 (2018).
4. S. Liu, J. C. Norman, D. Jung, M. Kennedy, A. C. Gossard, J. E. Bowers, *Monolithic 9 GHz passively mode locked quantum dot lasers directly grown on on-axis (001) Si*, Appl. Phys. Lett., 113, 041108 (2018).
5. Y. Wan, D. Inoue, D. Jung, J. C. Norman, C. Shang, A. C. Gossard, J. E. Bowers, *Directly modulated quantum dot lasers on silicon with a milliampere threshold and high temperature stability*, Photon. Reas. 6, 776-781 (2018).
6. P. Bhasker, J. Norman, J. Bowers, N. Dagli, *Intensity and phase modulators at 1.55 μm in GaAs/AlGaAs layers directly grown on silicon*, J. Light. Technol. In Press (2018).
7. J. Duan, H. Huang, D. Jung, Z. Zhang, J. Norman, J. E. Bowers, F. Grillot, *Semiconductor quantum dot lasers epitaxially grown on silicon with low linewidth enhancement factor*, Appl. Phys. Lett. 112, 251111 (2018).

8. J. A. Frey, H. J. Snijders, J. Norman, A. C. Gossard, J. E. Bowers, W. Loffler, D. Bouwmeester, *Electro-optic polarization tuning of microcavities with a single quantum dot*, arXiv preprint arXiv:1805.03387 (2018).
9. D. Inoue, D. Jung, J. Norman, Y. Wan, N. Nishiyama, S. Arai, A. C. Gossard, J. E. Bowers, *Directly modulated 1.3 μm quantum dot lasers epitaxially grown on silicon*, Opt. Exp., 26, 7022-7033 (2018).
10. H. J. Snijders, J. A. Frey, J. Norman, H. Flayac, V. Savona, A. C. Gossard, J. E. Bowers, M. P. van Exter, D. Bouwmeester, W. Loffler, *Single photons and unconventional photon blockade in quantum dot cavity-QED*, arXiv preprint arXiv:1803.10992 (2018).
11. U. Nandi, J. C. Norman, A. C. Gossard, H. Lu, S. Preu, *1550-nm driven ErAs:In(Al)GaAs photoconductor-based terhartz time domain system with 6.5 THz bandwidth*, J. Infrared Millim. Terahertz Waves, 39, 340-348 (2018).
12. D. Jung, R. Herrick, J. Norman, K. Turnlund, C. Jan, K. Feng, A. C. Gossard, J. E. Bowers, *Impact of threading dislocation density on the lifetime of InAs quantum dot lasers on Si*, Appl. Phys. Lett., 112, 153507 (2018).
13. [Invited] J. C. Norman, D. Jung, Y. Wan, J. E. Bowers, *Perspective: The future of quantum dot photonic integrated circtuits*, Appl. Phys. Lett. Photon., 3, 030901 (2018).
14. S. Liu, D. Jung, J. C. Norman, M. Kennedy, A. C. Gossard, J. E. Bowers, *490 fs pulse generation from a passively mode-locked single section quantum dot laser directly grown on on-axis silicon*, Electron. Lett., 54, 404 (2018).
15. H. J. Snijders, J. A. Frey, J. Norman, V. P. Post, A. C. Gossard, J. E. Bowers, M. P. van Exter, W. Loffler, D. Bouwmeester, *A fiber coupled cavity QED source of identical single photons*, Phys. Rev. Appl., 9, 031002 (2018).
16. D. Jung, Z. Zhang, J. Norman, R. Herrick, M. Kennedy, P. Patel, K. Turnlund, C. Jan, Y. Wan, A. C. Gossard, J. E. Bowers, *Highly reliable low threshold InAs quantum dot lasers on on-axis (001) Si with 87% injection efficiency*, ACS Photon. (2017).
17. D. Jung, J. Norman, MJ Kennedy, C. Shang, B. Shin, Y. Wan, A. C. Gossard, J. E. Bowers, *High efficiency low threshold current 1.3 μm InAs quantum dot lasers on on-axis (001) GaP/Si*, Appl. Phys. Lett., 111, 122107 (2017)
18. Y. Wan, Z. Zhang, R. Chao, J. Norman, D. Jung, C. Shang, Q. Li, MJ Kennedy, J-W. Shi, A. C. Gossard, K. M. Lau, J. E. Bowers, *Monolithically integrated InAs/InGaAs Quantum Dot Photodetectors on Silicon Substrates*, Opt. Exp., 25, 27715-27723 (2017).
19. Y. Wan, D. Jung, J. Norman, C. Shang, I. McFarlane, Q. Li, MJ Kennedy, A. C. Gossard, K. M. Lau, J. E. Bowers, *O-band electrically injected quantum dot micro-ring lasers on exact (001) GaP/Si and V-groove Si*, Opt. Exp., 25, 26853-26860 (2017).
20. Y. Wan, J. Norman, Q. Li, MJ Kennedy, D. Liang, C. Zhang, D. Huang, Z. Zhang, A. Y. Liu, A. Torres, D. Jung, A. C. Gossard, E. L. Hu, K. M. Lau, J. E. Bowers, *1.3 μm submilliamp threshold quantum dot mico-lasers on Si*, Optica 4, 940-944 (2017).
21. J. Norman, MJ Kennedy, J. Selvidge, Q. Li, Y. Wan, A. Y. Liu, P. G. Callahan, M. P. Echlin, T. M. Pollock, K. M. Lau, A. C. Gossard, J. E. Bowers, *Electrically pumped continuous wave quantum dot lasers epitaxially grown on patterned, on-axis Si*, Opt. Exp. 25, 3927-3934 (2017).
22. A. Y. Liu, J. Peters, X. Huang, D. Jung, J. Norman, M. L. Lee, A. C. Gossard, J. E. Bowers, *Electrically pumped continuous-wave 1.3 μm quantum-dot lasers epitaxially grown on on-axis (001) GaP/Si*. Opt. Lett. 42, 338-341 (2017).
23. H. Snijders, J. A. Frey, J. Norman, M. P. Bakker, E. C. Langman, A. C. Gossard, J. E. Bowers, M. P. Van Exter, D. Bouwmeester, W. Loeffler, *Purification of a single-photon nonlinearity*. Nat. Commun. 7, 12578 (2016).
24. [Invited] A. Y. Liu, S. Srinivasan, J. Norman, A. C. Gossard, J. E. Bowers, *Quantum dot lasers for silicon photonics*. Phot. Reas. 3, B1-B9 (2015).

25. A. Y. Liu, C. Zhang, J. Norman, A. Snyder, D. Lubyshev, J. M. Fastenau, A. W. K. Liu, A. C. Gossard, J. E. Bowers, *High performance continuous wave 1.3 μm quantum dot lasers on silicon*. Appl. Phys. Lett. 104, 041104 (2014).
26. M. Lisunova, J. Norman, P. Blake, G. T. Forcherio, D. F. DeJarnette, D. K. Roper. *Modulation plasmonic Fano resonance by the shape of the nanoparticles in ordered arrays*. J. Phys. D 46, 485103 (2013).
27. D. DeJarnette, J. Norman, and D. K. Roper. *Attribution of Fano resonant features to plasmonic particle size, lattice constant, and dielectric wavenumber in square nanoparticle lattices*. Photon. Reas. 2, 15-23 (2013).
28. J. Norman, D. DeJarnette, D. K. Roper. *Polylogarithm-based computation on Fano resonance in arrayed dipole scatterers.* J. Phys. Chem. C 118, 627-634 (2013).
29. M. Lisunova*, J. Norman*, W. Xingfei, S. Jenkins, J. Chen, D. K. Roper. *Aqueous dispersion of plasmonic hollow metal nanoparticles.* Mat. Lett. 117, 241-243 (2013).
30. D. DeJarnette, J. Norman, and D. K. Roper. *Spectral patterns underlying polarization-enhanced diffractive interference are distinguishable by complex trigonometry*. Appl. Phys. Lett. 101, 183104 (2012).

*Authors contributed equally

CONFERENCE PRESENTATIONS (as presenter)

1. **[Best Student Paper]** J. C. Norman, S. Liu, D. Jung, M. Kennedy, A. C. Gossard, J. E. Bowers, *96 GHz colliding pulse mode-locked quantum dot lasers grown on silicon*, 34th North American Conference on Molecular Beam Epitaxy, Banff, Canada, 2018.
2. J. C. Norman, D. Jung, P. Pintus, Y. Wan, Q. Li, P. Bhasker, Z. Zhang, C. Shang, M. Kennedy, N. Dagli, K. M. Lau, A. C. Gossard, J. E. Bowers, *InAs quantum dot devices for epitaxial photonic integrated circuits on silicon*, 20th International Conference on Molecular Beam Epitaxy, Shanghai, China, 2018.
3. J. C. Norman, Z. Zhang, D. Jung, Y. Wan, A. Torres, A. C. Gossard, J. E. Bowers, *High performance quantum dot lasers epitaxially integrated on silicon*, Quantum Communications and Quantum Imaging XVI, San Diego, California, 2018.
4. **[Invited]** J. Norman, D. Jung, A. C. Gossard, J. E. Bowers, *Low threshold, high gain 1300 nm quantum dot lasers epitaxially grown on Si*, Winter Colloquium on the Physics of Quantum Electronics, Snowbird, Utah, 2018.
5. **[Best Student Paper]** J. Norman, D. Jung, MJ Kennedy, C. Shang, A. C. Gossard, J. E. Bowers, *Low Threshold Epitaxial InAs Quantum Dot Lasers on On-Axis GaP/Si (001)*, IEEE Photonics Conference, Orlando, Florida, 2017.
6. J. Norman, D. Jung, Z. Zhang, MJ Kennedy, K. Turnlund, C. Shang, Y. Wan, A. C. Gossard, *The impact of threading dislocation density in InAs/GaAs quantum dot lasers grown on (001) silicon*, North American Conference on Molecular Beam Epitaxy, Galveston, Texas, 2017.
7. Y. Wan, J. Norman, Q. Li, MJ Kennedy, D. Liang, C. Zhang, D. Huang, A. Liu, A. Torres, D. Jung, A. C. Gossard, E. Hu, K. M. Lau, J. Bowers, *Sub-mA threshold 1.3 μm CW lasing from electrically pumped micro-rings grown on (001) Si*, CLEO: Applications and Technology, San Jose, California, 2017.
8. J. Norman, A. Y. Liu, Y. Wan, Q. Li, E. L. Hu, K. M. Lau, A. C. Gossard, J. E. Bowers. *1.3 μm quantum-dot micro-disk lasers directly grown on (001) silicon.* International Conference on Molecular Beam Epitaxy, Montpellier, France, September, 2016.
9. D. Jung, A. Y. Liu, J. Peters, J. Norman, X. Huang, M. L. Lee, A. C. Gossard, J. E. Bowers. *Electrically pumped continuous wave III-V quantum dot lasers epitaxially grown on exact GaP/Si (001).* International Conference on Molecular Beam Epitaxy, Montpellier, France, September, 2016. (Postdeadline)

CONFERENCE PRESENTATIONS (co-authored)

1. J. Duan, H. Huang, D. Jung, J. Norman, J. E. Bowers, F. Grillot, *Low linewidth enhancement factor and high optical feedback resistance of p-doped silicon based quantum dot lasers*, IEEE Photonics Conference, Rreston, VA, 2018.
2. I. P. Marko, A. Baltusis, A. R. Adams, D. Jung, J. C. Norman, J. E. Bowers, S. J. Sweeney, *Physical properties of 1.3 µm InAs-based quantum dot laser on silicon,* IEEE International Semiconductor Laser Conference, Santa Fe, NM, 2018.
3. Z. Zhang, D. Jung, J. C. Norman, P. Patel, W. W. Chow, J. E. Bowers, *Gain characterization of p-doped 1.3 µm InAs quantum dot lasers on silicon: theory and experiment*, IEEE International Semiconductor Laser Conference, Santa Fe, NM, 2018.
4. Z. Zhang, D. Jung, J. C. Norman, P. Patel, W. W. Chow, J. E. Bowers, *Continuous tuning of gain peak linewidth enhancement factor from negative to positive with p doping in InAs QD laser on Si*, IEEE International Semiconductor Laser Conference, Santa Fe, NM, 2018. (Postdeadline)
5. P. Bhasker, J. Norman, J. Bowers, N. Dagli, *Low voltage, high optical power handling, bulk GaAs/AlGaAs electro-optic modulators*, Integrated Photonics Research, Silicon and Nanophotonics, Zurich, Switzerland, July, 2018.
6. C. Shang, Y. Wan, D. Jung, J. Norman, M. Kennedy, D. Liang, C. Zhang, A. C. Gossard, J. E. Bowers, *Quantum dot mico-lasers integrated with photodetectors and optical amplifiers on (001) Si via waveguide coupling*, CLEO: Science and Innovations, San Jose, CA, May 13, 2018.
7. J. E. Bowers, A. Gossard, D. Jung, J. Norman, Y. Wan, *Quantum dot photonic integrated circuits on silicon*, CLEO: Science and Innovations, San Jose, CA, May 13, 2018.
8. Zeyu Zhang, D. Jung, J. Norman, P. Patel, A. C. Gossard, J. E. Bowers, *Gain characterization and parameter extraction of 1.3 µm InAs quantum dot lasers on silicon*, CLEO: Science and Innovations, San Jose, CA, May 13, 2018.
9. D. Jung, R. Herrick, J. Norman, C. Jan, N. Caranto, A. Torres, Y. Wan, A. C. Gossard, J. E. Bowers, *Highly improved reliability of low threshold 1.3 µm III/V quantum dot laser epitaxially grown on on-axis Si*, CLEO: Science and Innovations, San Jose, CA, May 13, 2018.
10. Y. Wan, D. Jung, J. Norman, K. Feng, A. Dagli, A. C. Gossard, J. E. Bowers, *Quadruple reduction of threshold current density for micro-ring quantum dot lasers epitaxially grown on (001) Si*, CLEO: Science and Innovations, San Jose, CA, May 13, 2018.
11. D. Jung, J. Norman, M. Kennedy, R. Herrick, C. Shang, C. Jan, A. C. Gossard, J. E. Bowers, *Low threshold current 1.3 µm Fabry-Perot III-V quantum dot lasers on (001) Si with superior reliability*, Optical Fiber Communications Conference, San Diego CA, March 11, 2018.
12. A. D. J. Fernandez Olvera, U. Nandi, J. Norman, A. C. Gossard, H. Roskos, S. Preu, *Dispersive properties of self-complementary log-periodic antennas in pulsed THz systems*, IEEE 42nd International Conferences on IRMMW-THz, Cancun, Mexico, 2017.
13. P. Bhasker, J. Norman, J. Bowers, N. Dagli, *Intensity and Phase Modulators in Epitaxial III-V Layers Directly Grown on Silicon Operating at 1.55 µm*, Frontiers in Optics, Washington D.C., 2017.
14. U. Nandi, A. D. J. Fernandez Olvera, J. Norman, A. C. Gossard, H. Lu, S. Preu, *1550 nm driven terahertz time domain spectroscopy system with more than 4 THz bandwidth using ErAs:In(Al)GaAs Photoconductors*, Progress in Electromagnetics Research Symposium, Singapore, Singapore, 2017.

15. R. Herrick, D. Jung, A. Y. Liu, J. Norman, C. Jan, J. E. Bowers, *Reliability of quantum well and quantum dot lasers for silicon photonics*, IEEE Photonics Conference, Orlando, Florida, 2017.
16. J. Norman, A. Y. Liu, J. Peters, D. Jung, X. Huang, J. Norman, M. L. Lee, A. C. Gossard, J. E. Bowers. *InAs/GaAs quantum dot lasers on exact GaP/Si (001).* North American Conference on Molecular Beam Epitaxy, Saratoga Springs, New York, September, 2016. (Postdeadline).
17. Y. Wan, Q. Li, A. Y. Liu, J. Norman, W. Chow, A. C. Gossard, J. E. Bowers, E. Hu, K. M. Lau, *Quantum dot lasers grown on (001) Si substrate for integration with amorphous Si waveguides*. Optical Fiber Communication Conference, Anaheim, CA, Mar 19 2017.
18. J. A. Frey, H. Snijders, J. Norman, E. C. Langman, M. P. Bakker, A. C. Gossard, J. E. Bowers, M. P. van Exter, W. Loeffler, D. Bouwmeester. *Strongly correlated photons from single quantum dots in polarization degenerate micropillar cavities*. American Physical Society March Meeting, New Orleans, LA, Mar 15, 2017
19. A. Y. Liu, J. Peters, X. Huang, T. Komljenovic, J. Norman, D. Jung, M. Davenport, M. L. Lee, A. C. Gossard, J. E. Bowers. *Electrically pumped continuous wave 1.3 μm quantum dot lasers epitaxially grown on on-axis (001) Si*. International Semiconductor Laser Conference, Tokyo, Japan, Sep 12, 2016.
20. A. Y. Liu, C. Zhang, J. Norman, A. Snyder, D. Lubyshev, J. M. Fastenau, A. W. K. Liu, A. C. Gossard, J. E. Bowers. *Quantum Dot versus Quantum Wells on Silicon*. International Conference on Molecular Beam Epitaxy, Flagstaff, AZ, Sep 7, 2014
21. A. Y. Liu, C. Zhang, J. Norman, A. C. Gossard, and J. E. Bowers. *Record lifetimes of GaAs based lasers epitaxially grown on silicon*. Electronic Materials Conference, Santa Barbara, CA, June 26th, 2014. (Postdeadline)
22. D. DeJarnette, J. Norman, D. K. Roper. *Fano resonance from constructive interference of scattered light in square plasmonic nanoparticle arrays tunable for wavelength specific applications*. 6th International Conference on Surface Plasmon Photonics, Ottawa, Canada, May 26-31 2013.
23. D. DeJarnette, J. Norman, and D.K. Roper. *Nanooptics for refractive index sensors in fuel cycle application.* Fuel Cycle Technologies Annual Review Meeting, Argonne, IL 5-7 November 2013. [Invited].

Abstract

Quantum Dot Lasers for Silicon Photonics

by

Justin Colby Norman

Direct epitaxial integration of III-V optoelectronic devices on Si offers a substantial manufacturing cost and scalability advantage over heterogeneous integration via wafer bonding. The challenge in utilizing direct epitaxy of III-Vs on Si is that epitaxial growth introduces high densities of crystalline defects that limit device performance and lifetime. As an optical gain medium, quantum dots exhibit a unique tolerance to crystalline defects due to their three-dimensional quantum confined structure.

Quantum dot lasers epitaxially grown on Si are showing promise for achieving low-cost, scalable integration with silicon photonics. Their atom-like, inhomogeneously broadened, discrete density of states yields unique gain properties that show promise for improved performance and new functionalities relative to their quantum well counterparts (even on native substrates). By reducing the dislocation density in III-V/Si material and improving quantum dot size homogeneity, several world record results have been achieved for epitaxial laser performance on silicon.

A subset of the results achieved include continuous-wave threshold currents below 1 mA in micro-scale ring laser cavities, single-facet output powers of 175 mW at 20 °C, continuous wave lasing up to 105°C, near zero linewidth enhancement factor, isolator-free

stability at optical feedback levels of up to 90%, and record long device lifetimes on silicon of more than 100 years at 35°C based on extrapolated 8,000-hour aging studies, and >100,000 h lifetimes at 60°C from extrapolated 4,000-hour aging studies. These results show potential to revolutionize integrated photonics through economic advantages and performance capabilities not achievable in quantum well lasers.

Table of Contents

Chapter 1

Introduction

For decades, the silicon microelectronics industry has developed at an exponential pace improving performance, functionality, and integration density of electronic integrated circuits. Over the last fifty years the integration density of transistors has gone from a few hundred per square millimeter to over 100,000,000 mm^{-2} in Intel's latest 10 nm technology node[1]. In parallel to this downscaling of components, a massive manufacturing infrastructure ecosystem has developed capable of churning out tens of millions of wafers per year at the 300-mm wafer scale with near perfect yield in all fabricated components. Furthermore, the silicon wafer manufacturing processes have improved to the point where defect-free wafers up to 450 mm in diameter can be produced at a price point less than $\$1/cm^2$. This unprecedented level of commercial development has yielded low cost, high performance electronic devices that have revolutionized human society.

Meanwhile, the invention of the laser in 1960 at Hughes Research Laboratories and the eventual demonstration of room temperature, continuous wave lasing in a semiconductor by Alferov[2], following simultaneous key proposals by Kroemer[3] and himself [4] regarding the use of double heterostructures, ushered in a similarly impactful technological paradigm

shift. The invention of the semiconductor laser diode has spawned the fields of integrated photonics, optical communications, and the Internet. Photonic technologies have enabled new methods of materials processing and characterization, sensing and analysis of gasses and liquids, high bandwidth data transmission interconnecting the entire planet, and numerous other applications that have transformed our daily lives. Yet despite these rapid advances, photonic devices have remained bulky, expensive, and modular in nature, in stark contrast to the advancements in high-density integration in Si-based electronics. To address this discrepancy, silicon photonics was proposed whereby established complementary metal-oxide-semiconductor (CMOS) manufacturing processes and materials would be utilized to create photonic components with high integration densities. Such a platform leverages the already developed and highly optimized processing techniques and economy of scale uniquely afforded by decades of silicon microelectronics development to achieve economical manufacturing and, ideally, rapid transition of new technologies from the laboratory to commercial products.

Beyond commercial advantages, silicon also possesses numerous performance capabilities not achievable using other platforms such as III-V materials. The CMOS platform provides a nearly ideal design space for photonic integrated circuits (PICs) due to the high-quality interfaces and refractive index contrasts that can be achieved between Si, Ge, SiO_2, Si_3N_4, and other dielectrics. Using various combinations of these materials with silicon-on-insulator (SOI) substrates, waveguides can be designed to cover optical wavelengths from the ultraviolet to infrared[5-8]. The challenge then becomes how to integrate the other components necessary to form useful PICs with complex functionality. Specifically, how does one obtain lasers, modulators, photodetectors, and non-reciprocal components such as

isolators and circulators? Engineered devices made from Si and Ge can cover modulation and detection for wavelengths around the near-infrared[9, 10] but are not suitable outside that range. Additionally, the indirect band gaps of Si and Ge make them unsuitable for high performance lasers or amplifiers with the only demonstrated laser in this material system having orders of magnitude higher threshold current density[11] at 300 kA/cm^2 than what is achieved in direct-gap III-V materials integrated with Si, as will be detailed below.

Overcoming the inherent limitations of indirect bandgap Group IV materials for gain, efficient modulation, and detection at wavelengths outside the near-infrared requires incorporating III-V materials with the silicon photonics platform. Until recently the entirety of successfully commercialized work done on III-V integration with Si has fallen into two categories that have evolved in terminology to be designated either “hybrid” or “heterogeneous”. Going back in the literature, the terminology is interchanged, but now it is commonly accepted that hybrid integration refers to co-packaged III-V and Si devices on native substrates (more specifically SOI for Si) while heterogeneous integration refers to III-V materials bonded to an SOI substrate. In the case of hybrid integration[12] the light is butt-coupled between III-V and Si chips requiring extremely precise alignment that complicates packaging and arguably limits scalability. Meanwhile in heterogeneous integration, light is evanescently coupled vertically into a Si waveguide from the III-V active material (see Figure 1).

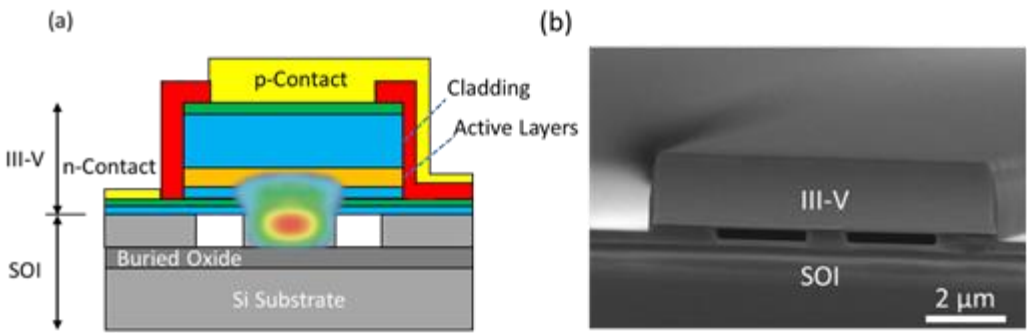

Figure 1. (a) A schematic diagram of heterogeneously integrated III-V laser on Si including the evanescent optical mode. (b) Micrograph of an etched III-V laser ridge bonded to a patterned SOI substrate after [13].

This approach, first demonstrated at UCSB[14] in 2006, simplifies packaging by monolithically integrating all components and transfers the alignment complexity to the lithographic steps in semiconductor device processing where established techniques trivialize the issue. A detailed review of the current state-of-the-art in heterogeneous integration is presented in[15]. Demonstrated performance shows a synergistic relationship between the unique capabilities of III-Vs and Si resulting in performance that can exceed native substrate III-V devices and far exceed what is achievable purely with Si and Ge. Additionally, the PIC complexity of heterogeneous devices has rapidly grown to rival that of PICs on native substrates with over 400 components on a single waveguide in recent results[16]. Historical integration densities of PICs that include lasers are shown in Figure 2. The heterogeneous approach has been widely adopted in industry by Juniper Networks[17], Hewlett Packard Enterprise[18], and Intel[19]. Intel is currently in volume production of optical transceivers using heterogeneous integration[20].

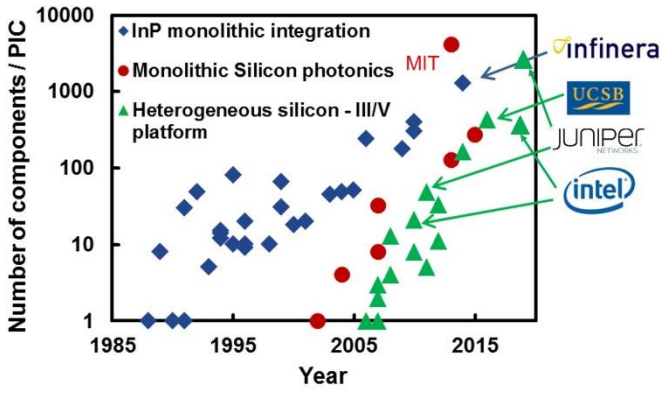

Figure 2. Component counts in a single photonic integrated circuit are shown for PICs on native InP (blue diamonds), monolithic silicon photonics (red), and for heterogeneously integrated PICs with lasers on Si (green triangles) after [21].

Currently the biggest drivers in further developing silicon photonics are datacenter and high-performance computing applications. Optical data transfer can be performed at much higher data rates with much lower energy consumption than can be done with electronics and is needed to overcome the performance bottleneck presented by electronic interconnects within datacenters and supercomputers. Optical transmission has already been adopted for decades in long-haul communications and much more recently for shorter links down to the individual boards within a server rack, mostly through native substrate vertical-cavity surface-emitting laser (VCSEL) solutions, but further downscaling to within the board and eventually to on-chip interconnects has proved challenging. Integrating photonics at these length scales requires small-footprint and low energy devices that are tolerant of the high temperatures sustained near the electronic processors. Designing photonic devices that meet all of these criteria is challenging as sidewall scattering and recombination hinder performance in small devices in addition to the high temperature requirements. Additionally, an in-plane laser cavity is desired for integration with additional on-chip photonic components for increased

functionality. While datacenters are the principle driver for these changes, smaller footprints and higher integration densities are beneficial for any PIC application.

In order to achieve broader commercial viability of PICs, the cost of heterogeneous integration must be further reduced. For heterogeneous integration, all III-V devices are grown first on a native substrate. Then the device is bonded to Si, and the III-V substrate is removed and discarded (or reused). Relative to Si substrates, III-V substrates are orders of magnitude more expensive and only available at much smaller wafer sizes that limit scalability. See Table 1 for a comparison of III-V wafer costs and sizes with Si. If the III-V substrate cost could be avoided, the cost per PIC would go down significantly (by as much as 50%). The only way to do this is by moving to an epitaxial III-V/Si process for photonic integration. Such an approach offers several possible embodiments: 1) growth on Si followed by wafer bonding and Si substrate removal, 2) integrating as-grown III-V components with the Si device layer of an SOI substrate, and 3) using as-grown III-V layers for the entirety of the PIC with Si serving only as a low-cost substrate to facilitate scalable manufacturing. Each approach has its own benefits and drawbacks and will be detailed below. A detailed techno-economic analysis of the benefits of epitaxial integration is the subject of Ref. [22].

Table 1. Comparison of price and wafer diameter for various III-V substrates and Si and SOI substrates.

	InAs	**InP**	**GaAs**	**SOI**	**Si**
Substrate Cost ($/cm^2)	18.25	4.55	1.65	1.30	0.20
Maximum Size (mm)	76	150	200	450	450

In order to realize the benefits of an all-epitaxial process, the challenges associated with mismatched epitaxy must be overcome. Relative to Si, non-nitride III-V materials have larger lattice constants and higher coefficients of thermal expansion (see Table 2) which, for unoptimized growth conditions, result in high densities (~10^9 cm^{-2}) of crystalline defects including primarily threading dislocations and antiphase domains. Fortunately, through careful optimization of growth conditions and utilization of dislocation filtering layers and techniques[23-25], the defect density can be reduced by a few orders of magnitude enabling near native substrate level performance. Such techniques are discussed in detail in later chapters.

Table 2. Comparison of the lattice constants and coefficient of thermal expansion (CTE) mismatch for common III-V semiconductors with Si[26].

	Si	GaAs	InP	GaSb	AlSb
Lattice Constant (Å)	5.431	5.653	5.869	6.096	6.136
% Mismatch w/Si	0	4.09%	8.06%	12.2%	13.0%
CTE Mismatch	0	119%	76.9%	198%	62.3%

While dislocation densities as low as 10^6 cm^{-2} have been reported[24, 27, 28], defect free material or even material comparable to state-of-the-art III-V wafers at 10^3-10^4 cm^{-2} has never been achieved and likely will not be for many years if at all for bulk III-V deposition. The reasoning behind this dire portent is that dislocations can only terminate at a free surface or by meeting a complementary dislocation and forming a closed loop. In bulk films, dislocation interactions are the only mechanism of filtering, and once dislocation densities get sufficiently low, the likelihood of two dislocations meeting each other becomes extremely

low. Dislocations act as nonradiative recombination sites as well as sources of optical scattering and absorption. Fortunately, through the careful choice of an appropriate active region, defect-tolerant photonic devices can be obtained.

To truly achieve native substrate performance and reliability, quantum dot (QD) active regions must be adopted over quantum wells (QW). Quantum dots represent zero-dimensional, particle-in-a-box-like quantum confined structures that can be formed through a self-assembly process using InAs on (In,Ga,Al)(As,P) layers. Their artificial-atom-like properties make them ideal for low threshold, high temperature lasers, high performance semiconductor optical amplifiers (SOA), low dark current photodetectors, and potentially high efficiency quantum confined Stark effect modulators. They also have unique dynamic properties that enable low feedback sensitivity and narrow linewidth lasing, but most importantly, their in-plane carrier confinement dramatically reduces in-plane carrier migration to and recombination at heteroepitaxial defects. All of these attributes as well as the growth of quantum dots are described in following chapters.

The thesis is organized as follows. Chapter 2 introduces quantum dots and their unique properties as relevant to optoelectronic devices. Their useful attributes are highlighted through demonstrated results in the course of this project. A primary focus of this work is the demonstration of high performance quantum dot lasers epitaxially grown on Si, so Chapter 3 provides an overview of the challenges of III-V/Si epitaxy and how they are overcome. Chapter 4 covers quantum dot growth and details the optimization steps that were taken to produce narrow, bright photoluminescence to enable high laser performance. Chapter 5 briefly covers methods of gain characterization for semiconductor lasers and demonstrates the superiority of Andrekson's method [29] over the more prevalent cutback method [30]

commonly seen in literature. Chapter 6 covers device results through multiple generations of improved quantum dot growth conditions and reduced dislocation density. Chapter 7 summarizes the state of the field at the culmination of this thesis and outlines remaining challenges and opportunities for improved lasers, other quantum dot devices, and photonic integration.

Chapter 2

Quantum Dot Fundamentals & Highlights

Introduction

Monolithic photonic integration allows optical systems previously relegated to bulky, bench-scale apparatuses to be developed in compact form factors enabling reduced cost and new applications. In particular, deployable gas and biomolecular sensing systems, lightweight and compact LIDAR components for automobiles, and small footprint, energy efficient interconnects for datacom and telecom applications are all currently driving development of on-chip photonic integration. In all commercial photonic integrated circuits (PIC) quantum wells (QW) have been utilized as the gain medium of choice. However, there are numerous advantages in terms of performance and economic viability to instead utilizing quantum dots (QD) for many applications.

First proposed in 1982 by Arakawa and Sakaki [31] and demonstrated in 1994 by Kirstaedter et al. [32] with Mirin et al. showing the first clear evidence of the theorized atom-like density of states [33], quantum dot lasers have shown numerous performance advantages over QW devices including lower threshold currents [34], higher temperature operation [35],

reduced sensitivity to crystalline defects [36], improved stability against optical feedback [37], and ultrafast gain dynamics applicable to semiconductor optical amplifiers (SOA) [38] and mode-locked lasers (MLL) [39]. Each of these advantages comes about from the discrete density of states and inhomogeneously broadened gain spectra unique to the three-dimensional carrier confinement of QDs. Perhaps most notable among these attributes is that their insensitivity to defects allows for epitaxial integration of QD lasers on silicon, and their insensitivity to feedback offers the prospect of eliminating optical isolators in PICs. The former could allow for future laser growth and processing up to the 450 mm scale, or, in the nearer term, for full wafer bonding to be used in 300 mm heterogeneous silicon photonics processes [13].

In the following sections, the basic physical principles of semiconductor QDs will be introduced, and their implications for performance as a gain medium will be explored in the context of recent results. Where possible, results for QD devices grown on silicon will be emphasized to show the robustness of the material system to defects, and potential for more economical production [22]. In later chapters the advantages provided by QDs in optoelectronic devices will be linked to their molecular beam epitaxy growth conditions, and the dependence of device performance on material quality and design will be demonstrated.

Fundamentals of Semiconductor Quantum Dots

Electronic Density of States

Semiconductor quantum dots can be thought of qualitatively as the textbook case of a particle-in-a-box. The three dimensional quantum confinement provided by band offsets between the narrow gap dot material and surrounding matrix leads to full discretization of the

energy levels into delta-function-like states possessing atom-like degeneracy, in contrast to the step-function-like QW density of states (DoS), ρ(E) (see Figure 3). Analogous to the particle-in-a-box, the energy levels of a QD are determined by the size of the dot and height of the potential barrier.

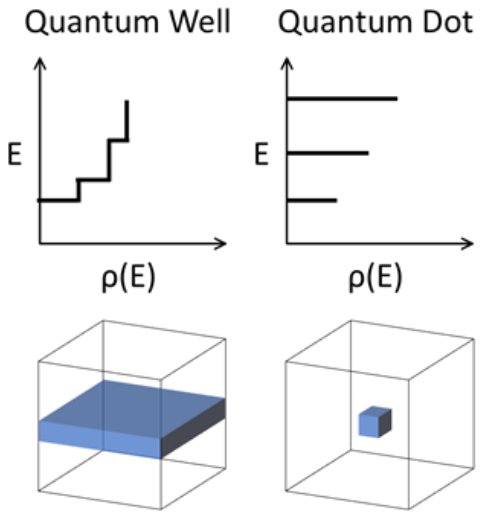

Figure 3. Schematic illustration of quantum confinement and density of states in quantum wells and dots after [40].

In real semiconductor systems the idealities of the particle-in-a-box picture begin to disappear. The random, self-assembled process of QD formation in crystal growth leads to nonuniformity in the size distribution, strain profile, and compositional fluctuations if non-binary alloys are used for the dots or surrounding matrix. These fluctuations lead to inhomogeneous broadening, ΔE_{inh}, of the optical properties of a dot ensemble. The broadening effectively leads to the formation of a quasi-band of states representing the weighted superposition of the discrete states of individual dots, as illustrated in Figure 4(a). Fortunately, the energy level spacing between principal quantum states can be a few times larger than the inhomogeneous broadening such that the quantized separation can be maintained. An important result of this statistical broadening is that it yields a highly symmetric, Gaussian

gain spectrum for the QD states.

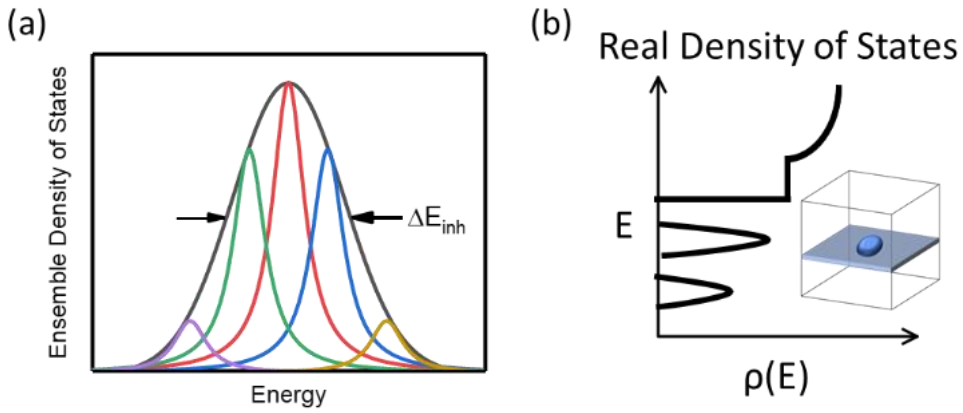

Figure 4. (a)Schematic illustration of inhomogeneous broadening for a quantum dot state. (b) A realistic schematic of the density of states, ρ(E), of a quantum dot structure including inhomogeneous broadening and the wetting layer after [40].

The extent of inhomogeneous broadening is dependent on crystal growth conditions and provides additional tunability to the gain spectrum in QD devices, which can be advantageous for broad bandwidth applications such as for optical amplifiers, tunable lasers, and mode-locked lasers. For single-mode lasing with low threshold and high efficiency, a smaller inhomogeneous broadening is desirable, since off-resonance dots will still capture charge carriers and result in unclamped spontaneous emission. In state-of-the-art QD material, inhomogeneous broadenings, as measured from the photoluminescence spectrum, as low as 24 meV have been realized at room temperature [35].

In further departure from the depiction of Figure 3, the most well-developed QD material systems form via the Stranski-Krastanov growth mode [41], which yields a thin wetting layer of dot material that acts as a QW connecting all the dots in a layer. A more realistic representation of the DoS of QD material is shown in Figure 4(b). Atomic force microscopy micrographs of such material are shown in Figure 5 along with a cross-section transmission

electron microscopy image and representative photoluminescence spectrum.

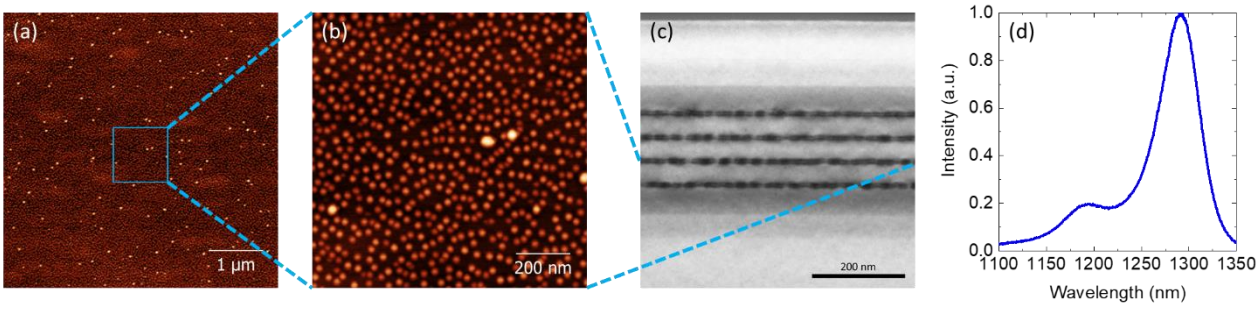

Figure 5. (a) 5 µm × 5 µm atomic force microscopy image of an uncapped quantum dot layer with luminescence around 1300 nm. Larger white spots represent coalesced quantum dots. (b) Zoomed in image from (a). (c) Cross-sectional transmission electron microscope image of four stacked quantum dot layers. (d) Representative photoluminescence spectrum from a single layer of quantum dots after [40].

Material and Structure

The most well-developed quantum dot materials system is that of In(Ga)As grown on (001) GaAs or InP lattice constant materials. This material system provides the flexibility to obtain emission at wavelengths from around 1 µm to nearly 2 µm but has been most utilized at the datacom and telecom wavelengths of 1.3 µm and 1.55 µm, respectively. In the less strained InAs/InP system, asymmetric adatom diffusion lengths on the growth surface can lead to lengthening of the QDs in the [011] direction into structures commonly termed “quantum dashes” (QDash). These structures appear to perform as quasi-one dimensional materials with performance characteristics between dots and wells [42]. Representations of the variation achievable in dot morphology and luminescence are shown in Figure 6.

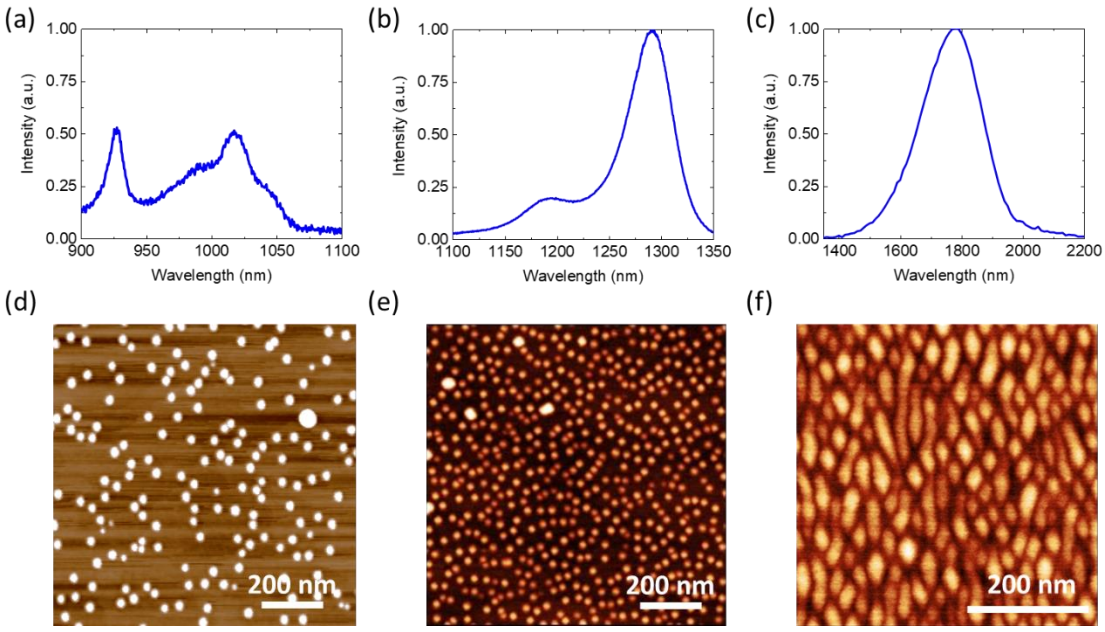

Figure 6. (Top) Photoluminescence spectra and (Bottom) atomic force microscopy images of InAs quantum dots grown at different conditions are shown to emphasize the range of material tunability that is achievable after [40].

Depending on the growth conditions and surrounding material chosen, the size, shape, and strain profile of a QD can be changed [43]. These structural changes can have a dramatic effect on the energy level structure of the QDs [44] changing the transition energies, spacing between energy levels, number of confined states, and the ratio of transverse electric (TE) to transverse magnetic (TM) emission [45]. At the ensemble level, the growth conditions will affect the inhomogeneous broadening as discussed previously and the dot density [46], which is typically maximized for laser and amplifier applications to give the maximum gain.

Quantum Dot Device Structure

The QD material presented in the following results has been grown using solid source molecular beam epitaxy (MBE). The high degree of tunability in the surface adatom mobility makes MBE an ideal technique for growing optimal QD layers. Additionally, the lower

growth temperatures of MBE for Al-containing compounds relative to metalorganic chemical vapor deposition (MOCVD) is beneficial for avoiding harmful intermixing of the QD layers during growth of the top half of the device structure [47], typically a graded-index separate-confinement heterostructure (GRINSCH) composed of 20-50% AlGaAs at a thickness of ~1.5 µm for O-band devices and InP or ternary/quaternary arsenide alloys for C-band devices.

The QD devices presented in the following sections are designed for emission around 1300 nm and have the structure depicted in Figure 7. The cladding consists of a 1.4 µm $Al_{0.4}Ga_{0.6}As$ GRINSCH with p-cladding material on top and n-cladding on the bottom. The results shown utilize five periods of InAs quantum dots in 7 nm $In_{0.15}Ga_{0.85}As$ QWs. The nominal InAs thickness is 2.55 ML, deposited at 500°C and .113 ML/s with a V/III ratio of 35. The bottom cladding is grown at 580°C while the top cladding is grown at 550°C to minimize interdiffusion in the active region. At these QD growth conditions, dot densities of up to 6.5×10^{10} cm^{-2} and photoluminescence (PL) full-width at half maximum (FWHM) as low as 28 meV can be obtained as shown in Figure 5.

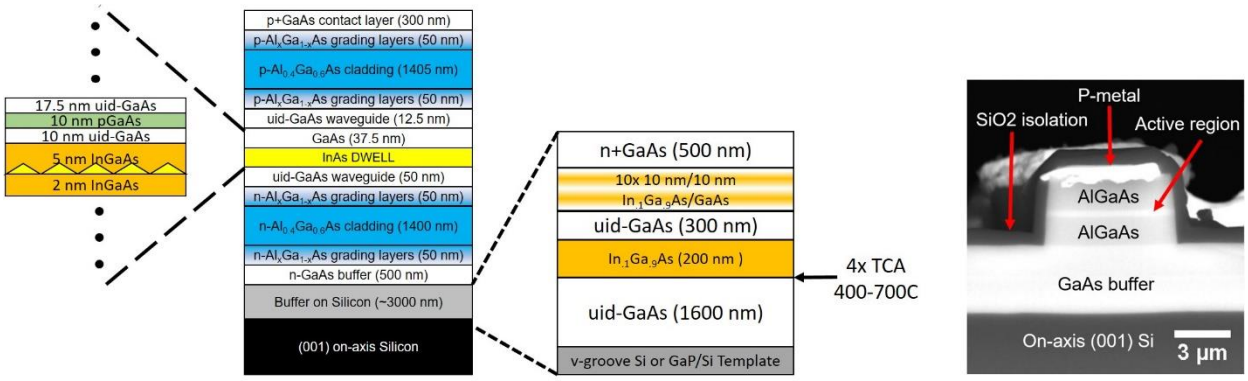

Figure 7. (Left) Schematic illustration of the epitaxial structure used for lasers and amplifiers including one period of the p-modulation doped active region and the III-V/Si buffer including defect filter layers and thermal cycle annealing (TCA) to reduce dislocation densities. (Right) Cross-sectional scanning electron microscope image of a cleaved laser facet after [40].

Devices grown on Si contain the buffer structure shown in Figure 7. For the initial III-V/Si

template we have interchangeably used GaP/Si, which is commercially available from NAsP-$_{III/V}$, GmbH, and MOCVD grown GaAs on v-groove patterned Si [25]. Any other template design could be utilized assuming antiphase domains (APD) are eliminated. Demonstrated APD free techniques in addition to those already mentioned include all-MBE growth using AlGaAs nucleation layers on Si [48], MOCVD growth of GaAs on planar silicon [49], and MBE growth of GaAs on homoepitaxial Si or Ge hollow v-groove structures [50]. More on the III-V/Si buffer details and heteroepitaxy in general are presented in the next chapter.

Devices are processed into laser cavities using inductively coupled plasma dry etching. Sidewall passivation is provided by 30 nm of Al_2O_3 deposited by atomic layer deposition while electrical isolation is provided by subsequent sputtered deposition of 300 nm SiO_2. Metal contacts are deposited using electron beam deposition with AuGe/Ni/Au n-contacts and Ti/Pt/Au p-contacts, both top-side contacts.

Gain in Semiconductor Quantum Dots

Independent Emitters

Each individual QD represents an independent emission source only coupled to neighboring dots through the wetting layer QW, which is separated in energy space by a few hundred meV from the dot ground state. The high separation between energy levels means carrier thermalization is highly suppressed at normal operating temperatures as evidenced by the demonstration of 220°C continuous wave (CW) lasing in a QD laser on GaAs [35], the highest temperature operation of any semiconductor laser, and the demonstration of an athermal optical interposer with error-free data links at 20 Gb/s at 125°C [51]. The net result is that

each dot acts independently at its homogeneously broadened energy with the inhomogeneous broadening resulting in a broad energy distribution of independent emitters.

Since each dot can only exhibit stimulated recombination at its energy, the gain it produces is not tied to other dots in the device with different transition energies. This has positive implications for amplifiers and mode-locked lasers in optical communications. In QW devices, when multiple signals are being amplified simultaneously, cross-gain modulation (XGM) and cross-phase modulation (XPM) can lead to cross-talk between the signals and deteriorate their quality. In a QD amplifier, each wavelength will interact with a different subset of the dot distribution and will not see the spatial and spectral hole burning in the dots at a different wavelength since the charge carriers cannot freely move between dots in the manner that electrons and holes can travel with long diffusion lengths in QWs. The same principles apply for mode-locked lasers where neighboring locked modes will not compete for charge carriers leading to low mode partition noise.

In the high signal regime, QD devices can exhibit enhanced four-wave mixing (FWM) over QWs due to their symmetric gain spectrum, independent emission, and low linewidth enhancement factor [38]. FWM can be useful for applications such as wavelength conversion for signal processing in optical networks. Enhanced FWM in QDs also allows for single-section mode-locked lasers that operate CW with no absorber section [52].

In addition to being independent from each other, the energy ground states of the QD ensemble are also isolated in energy from the wetting layer QW, by 150 meV-200 meV in our 1300 nm material, according to PL. Given that the QD energy levels possess atom-like degeneracy, the carrier density within the dots themselves must be orders of magnitude lower than that of the wetting layer and surrounding material at current injection levels relevant to

lasing or amplification. This means that the overall refractive index of the material will be set by a carrier density that is separate from and can be acted on independently from the carrier density responsible for optical gain. Exploiting this property has led to demonstration of 25 Gb/s differential phase shift keying in a QD SOA [53].

p-Modulation Doping

To realize most of the previously described theoretical benefits of QD gain media, extra p-type doping must be added to the active layers. For most combinations of III-V materials, the valence band offsets are substantially smaller than those in the conduction band, particularly for the technologically relevant InAs/GaAs and InAs/InP. This leads to energy level spacings in the valence band of ~10 meV which is well below kT for room temperature and above applications. As a result, confined holes in QDs can easily thermalize and escape the dots. By adding extra holes through p-type modulation doping (pMD), the effects of thermalization can be compensated thus enhancing population inversion and improving gain in the material [54-56]. First principles theory and experimental results have clearly illustrated this property [57] as shown in Figure 8 which includes a first-principles[58] fit of experimental data obtained via Cassidy's method [59].

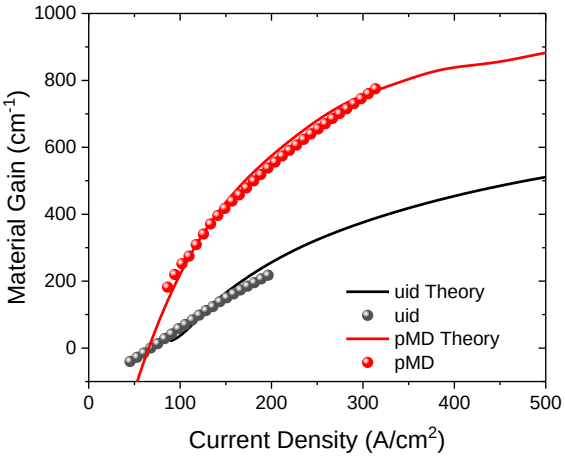

Figure 8. Theoretical and experimental gain curves for quantum dot lasers on silicon with uid and p-modulation doped (pMD) active regions containing five dot layers, adapted from [29].

Increased pMD does come at a cost, however. The extra holes result in increased Auger recombination [60] and optical absorption resulting in higher threshold currents and lower slope efficiencies. These trends are clearly visible in Figure 9 where threshold and slope efficiency are plotted for 1.5 mm Fabry-Perot cavities with five QD layers with varied doping levels including uid, 5×10^{17} cm^{-3}, and 1×10^{18} cm^{-3}. These doping levels correspond to a ratio of 0, 10, or 20 extra holes per dot, respectively.

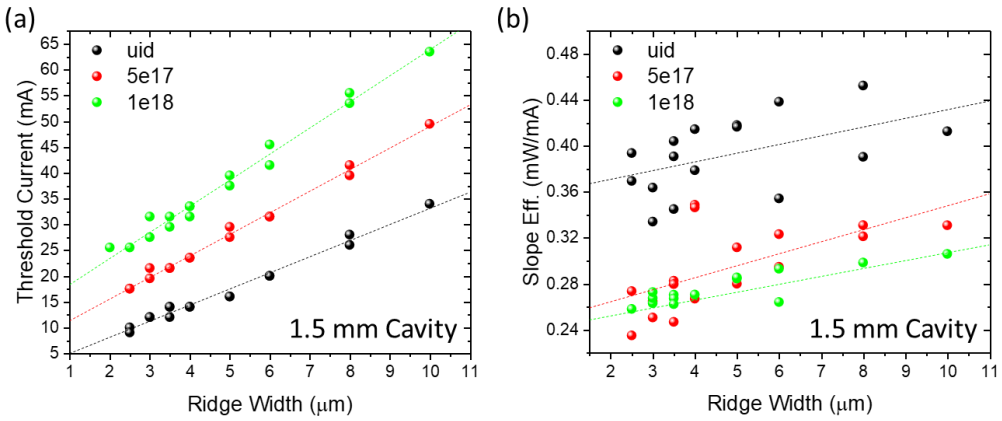

Figure 9. (a) Threshold current and (b) slope efficiency versus ridge width for a 1.5 mm Fabry-Perot cavity with as-cleaved facets and five dot layers grown on GaP/Si at various p-modulation doping levels in the active region, after [40].

Ultrafast Gain Recovery

The energy level spacings and decoupling of the gain in QDs from the surrounding carrier reservoir has significant implications for carrier capture processes and gain recovery. Early works regarding QDs had hypothesized that a "phonon bottleneck" would inhibit efficient carrier capture due to the large energy level separation relative to phonon energies [61]. Fortunately, such effects were found to be limited due to efficient Auger processes within QDs allowing for carriers to rapidly relax to the dot ground state on femtosecond time scales [62, 63]. This rapid relaxation leads to sub-picosecond gain recovery times for QD devices—well below the nanosecond recovery times of the well-like wetting layer carrier reservoir [38]. For QWs, the gain and carrier reservoir represent the same carrier population leading to gain recovery times of a few picoseconds to a nanosecond.

Ultrafast gain recovery allows for amplification of high data rate signals and mode-locking with ultrashort pulse widths. Pulse widths less than 400 fs [52] have been demonstrated in QD MLLs, significantly lower than what is achievable in QW-based semiconductor MLLs.

Tunnel injection structures, where an injector QW is placed near the dot active region, have been shown to further improve carrier injection. The QW is designed such that its ground state energy level is one LO phonon above that of a QD state. Then by optimizing the barrier thickness between the dot and well, an efficient tunnel injection process [64] can be achieved which improves gain, high temperature performance [60, 65], and modulation characteristics[66].

Linewidth Enhancement Factor

For many photonic applications having a narrow linewidth laser is desirable, and for all integrated applications, stability against undesired reflections from other components, waveguide bends, and imperfections is critical to maintaining laser performance. In both cases, the linewidth enhancement factor, α, is a critical parameter. The linewidth enhancement factor describes the ratio of the change in the real part of the refractive index, n, of the laser medium with carrier density to that of the imaginary part, n_i, with respect to carrier density, N, which can be rewritten in terms of the wavelength, λ, and differential gain, dg/dN as follows.

$$\alpha = -\frac{dn/dN}{dn_i/dN} = -\frac{4\pi}{\lambda}\frac{dn/dN}{dg/dN} \tag{1}$$

The laser linewidth scales as[30]

$$\Delta\nu \propto (1+\alpha^2) \tag{2}$$

while the critical feedback level, f_{crit}, to induce optical instability scales as[30]

$$f_{crit} \propto \frac{1+\alpha^2}{\alpha^4}. \tag{3}$$

The functional dependence of α means that lower values can be obtained for materials with high differential gain and a symmetric gain spectrum. Quantum dots are unique in their highly symmetric gain spectrum due to their discrete, inhomogeneously broadened states which result in a Gaussian profile when superimposed. Furthermore, the decoupling of the gain and carrier reservoir means that changes in the real and imaginary parts of the refractive index are decoupled at higher injection levels leading to a low ratio of $\Delta n/\Delta g$.

Typical values of α for quantum well materials are in the range of 3-5 while we have shown values much less than unity over a broad spectral range in subthreshold measurements (as shown in Figure 10) and remaining low at higher injection levels [67]. From the scaling relations above, lowering α from 3 to 0.5 should result in a factor of 8 reduction in linewidth and a factor of 162 increase in the critical feedback level. The increased feedback tolerance has been clearly demonstrated in comparisons of our QD material with QW lasers [37] and demonstration of stable operation under feedback levels as high as 90% [68] as reviewed below.

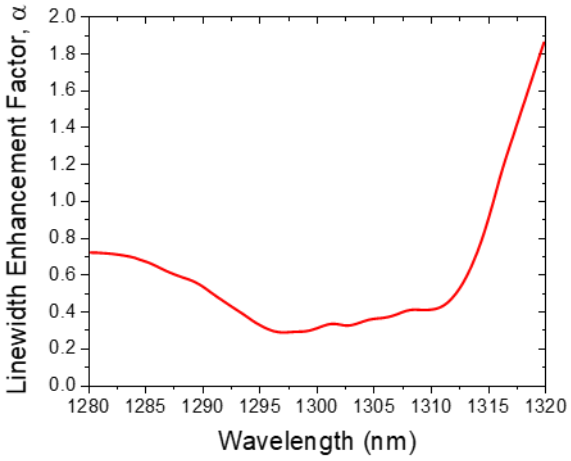

Figure 10. The linewidth enhancement factor, α, extracted from sub-threshold amplified spontaneous emission is plotted as a function of wavelength for a QD laser on (001) Si with five p-modulation doped (5×10^{17} cm^{-3}) dot layers, after [40].

Beyond simply showing near zero α, theoretical calculations and experimental results have shown that for sufficiently low inhomogeneous broadening, negative values can be obtained [58, 69]. Negative values are significant for high power applications where α is sometimes referred to as the antiguiding factor as it relates to spatial hole burning and filamentation. For positive values of α, carrier depletion by the optical mode acts to focus light within the laser cavity leading to further depletion and more focusing in a feedback loop that limits the achievable output power in ridge cavities, particularly for single-mode applications. For negative values of α, the light would be defocused eliminating filamentation.

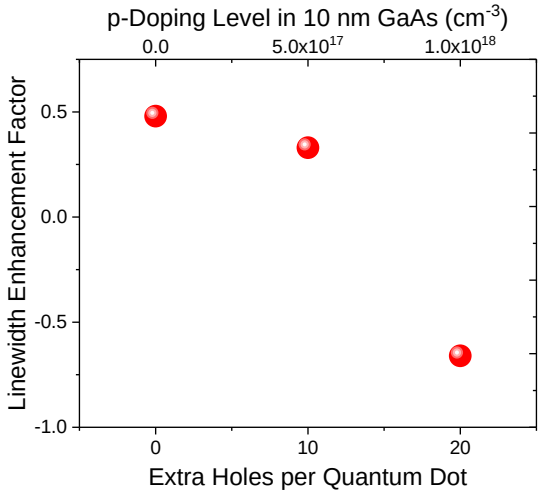

Figure 11. Sub-threshold linewidth enhancement factor as a function of p-doping level for five-layer quantum dot lasers on silicon. The p-doping level is expressed in terms of the ratio of added holes to the number of quantum dots after [70].

Due to its impact on gain and differential gain, modulation p-doping strongly affects the linewidth enhancement factor. By varying the p-doping level from 0 to 1×10^{18} cm^{-3}, we have shown subthreshold linewidth enhancement factors from 0.48 to -0.66 as shown in Figure 11 [70].

Quantum Dots for Epitaxial Integration on Silicon

Existing high-performance PICs utilize either an all III-V material platform or silicon with III-V gain integrated through co-packaging (hybrid integration) or bonding (heterogeneous integration). The primary advantage of using all III-Vs is that it serves as a native platform for integrating optical gain elements; whereas, silicon provides an economic advantage through the lower cost of wafers and scalability of their larger size and well-developed manufacturing infrastructure, but both hybrid and heterogeneous integration have drawbacks.

The problem inherent to hybrid integration is that it increases packaging complexity and has limited scalability for integrating multiple gain elements. Heterogeneous integration where

III-V gain media are bonded onto a processed silicon photonic chip with evanescent coupling of light vertically into silicon waveguides is more promising. Recent advances even show improved performance over monolithic III-V devices [21]. In heterogeneous integration, the challenges arise from the manufacturing complexity of wafer or die bonding and limited scalability due to the reduced size and higher price of III-V substrates relative to Si.

From a manufacturing perspective, the ideal approach is epitaxial integration on silicon [22]. Direct epitaxial growth allows for III-V device production at the Si wafer scale. With a 300 mm or larger III-V/Si platform, the integration method can then take any form [13]. The same techniques used for native substrate III-V devices could be employed with Si serving solely as a low-cost substrate including for full 300 mm wafer-scale bonding. Alternatively, growth could be done on silicon-on-insulator wafers for a silicon photonics approach.

The challenge in epitaxial integration is overcoming the crystalline mismatch that leads to defects in the III-V layers that include dislocations, antiphase domains, and cracks. Antiphase domains can be eliminated through use of miscut Si, or, to maintain CMOS compatibility with on-axis (001) Si, through carefully optimized growth conditions [48, 49, 71, 72] or Si patterning [25, 73]. Cracking can be solved as well through selective area growth if uniform coverage is not required across the full wafer [74] or by allowing the wafer to bow during growth and cooldown. Dislocations can be managed using strained interlayers, thermal cycling, and selective area growth [24, 75, 76], but more work remains to be done to match native substrate device performance, particularly regarding device reliability [13, 77]. In the end, though, even one dislocation can result in the failure of a QW device, and dislocation free III-V/Si is likely not achievable at high yield. Fortunately, QDs offer reduced sensitivity to defects.

Historical Results & Prior State-of-the-Art for Heteroepitaxial Lasers

Given that lasers were the primary missing component in the silicon photonics platform, the bulk of III-V/Si heteroepitaxy research has been focused on generating efficient lasers. The first laser ever reported on Si was an AlGaAs double heterostructure laser that operated in pulsed mode at 77 K with a threshold current density of 10.8 kA/cm^2 and a differential quantum efficiency of 1.2% in 1984 [78]. The best results for a double heterostructure laser were achieved in 1988 for an InGaAsP/InP device with threshold current density of <4 kA/cm^2 and less than 5% increase in current after five hours at constant power aging [79]. After 19 years of further research, room temperature (RT), continuous wave (CW) operation was achieved in a QW laser with threshold current densities of 269 A/cm^2 along with a device lifetime of four hours [80]. To reach these performance levels, Groenert et al. used a heavily optimized Ge/GeSi/Si buffer with TD density of 2×10^6 cm^{-2} grown on miscut Si to avoid antiphase domains [28]. Meanwhile, the first QD laser on Si was grown in 1999 using $In_{.4}Ga_{.6}As$ QDs and lased under pulsed conditions at 80 K with a threshold current density of 3.85 kA/cm^2 [81]. Within six years, quantum dot lasers were also being operated CW on Si at RT and were showing threshold current densities of 1.5 kA/cm^2 despite reported dislocation densities of $2\text{-}5\times10^7$ cm^{-2} [82]. Then, in 2012, the previous QW records were shattered by QD lasers with RT CW threshold current densities of 163 A/cm^2 and CW lasing up to 30°C with reported dislocation densities of 5×10^6 cm^{-2} [83]. In 2014, narrow ridge QD lasers were produced setting records for the absolute threshold current at 16 mA, output power at 176 mW, and continuous wave lasing up to 119°C (exceeding even heterogeneous device performance) despite dislocation densities of 2×10^8 cm^{-2} [84]. These devices were directly compared with simultaneously fabricated QW lasers with identical TD density showing that

QW devices were incapable of lasing at all at these TD densities [36]. Further testing of the same devices showed extrapolated lifetimes of 4600 hours at aging conditions of 30°C and more than twice threshold [85]. These performance results and later results by Chen et al. in 2016 showing 62.5 A/cm^2 current densities and extrapolated lifetimes >100,000 hours at relaxed conditions [27] began to make the case that QD lasers grown on Si can be a commercial technology. Looking forward, one problem inherent to all of the previously mentioned results is that none made use of CMOS compatible on-axis (001) silicon substrates. They have all been grown on miscut Si. The historical trends in threshold current density and device lifetime for these lasers and newer results described below are displayed in Figure 12.

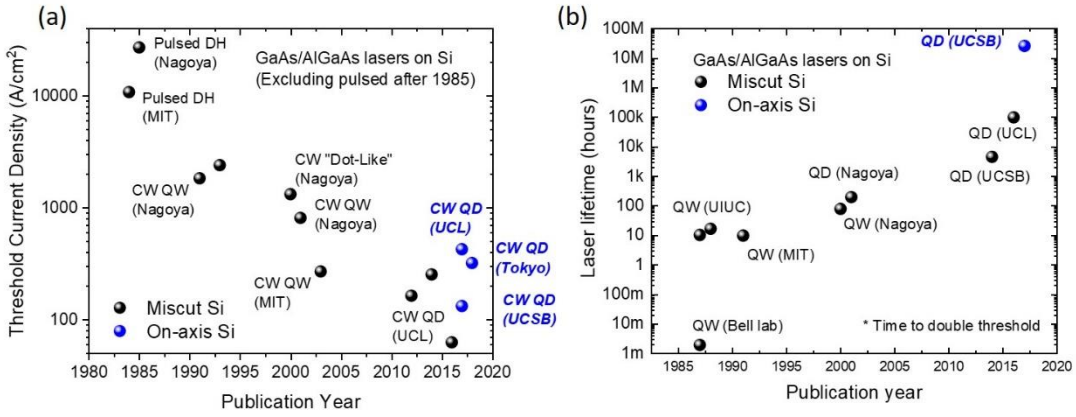

Figure 12. (a) Threshold current density and (b) device lifetime (either extrapolated or measured) for lasers on Si operating in the continuous wave mode. The distinction is noted between historical results on miscut Si substrates and recent results on CMOS compatible on-axis (001) Si. Adapted from [13]

Tolerance to Crystalline Defects

The in-plane carrier confinement provided by QDs inhibits nonradiative recombination at dislocations and other defects. With QD densities as high as 6×10^{10} cm^{-2} and typical dislocation densities in optimized buffers of ~10^6 cm^{-2}, the likelihood of charge carriers finding a dot before a dislocation is extremely high. The relative densities are illustrated in

Figure 13 which shows an AFM image of QDs drawn to scale with a plan-view electron channeling contrast imaging (ECCI) scan showing dislocations in an optimized GaAs/Si buffer at 7×10^{6} cm^{-2} dislocation density.

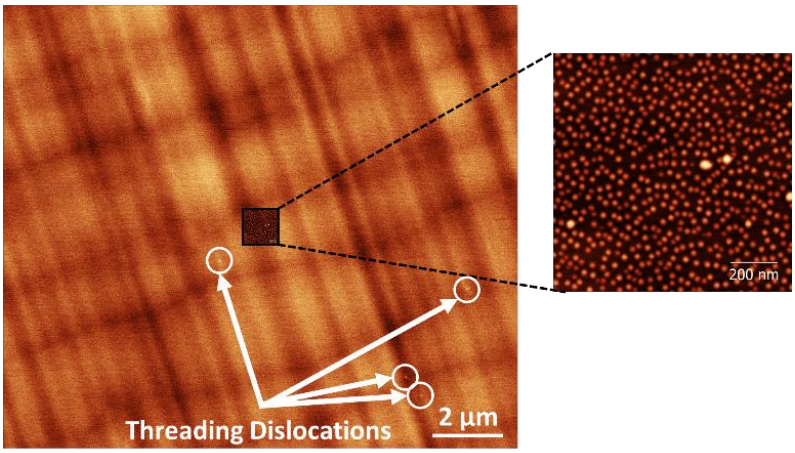

Figure 13. Plan-view electron channeling contrast image showing four threading dislocations in a GaAs/Si template over a 14.5 µm × 14.5 µm field of view. (inset) Atomic force microscopy image of uncapped quantum dots scaled to the size of the ECCI image to illustrate the high dot:dislocation ratio, after [40].

The ability for QDs to tolerate residual dislocations has been confirmed in a direct comparison of QD and QW performance on identical III-V/Si templates [36]. At a dislocation density of 7×10^{6} cm^{-2}, QD material shows nearly identical room temperature photoluminescence, as shown in Figure 14. The dot confinement results in higher injection efficiencies which translate into longer device lifetimes by reducing the in-plane carrier diffusion length.

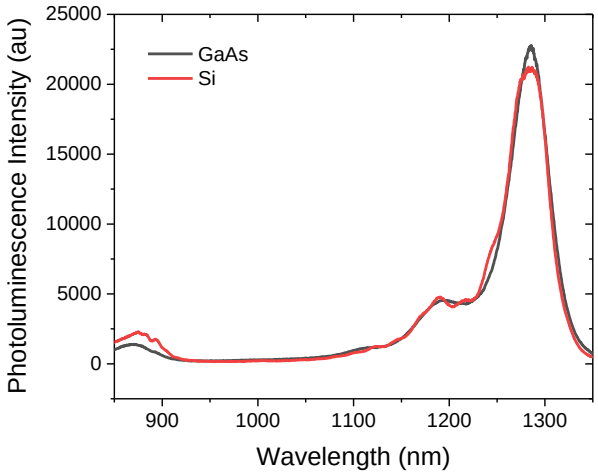

Figure 14. As-grown photoluminescence spectra for quantum dot lasers on GaAs and Si substrates, after [40].

To demonstrate the tolerance of QD gain to dislocations, semiconductor optical amplifier material, with device structure identical to Figure 7, was grown on a Si substrate with a dislocation density of 7×10^{7} cm^{-2}. The active region consisted of seven 5×10^{17} cm^{-3} pMD QD layers. The SOAs were cleaved from 4 µm wide, angled cavities such that the facets had an angle of 8° with a cavity length of 3 mm. No facet coatings were applied. We observed an unsaturated gain factor of 25.4 dB and a saturated input power of 10.9 dBm at a bias of 290 mA. The 3 dB bandwidth of the SOA was 30-40 nm, depending on the bias. The results are shown in Figure 15 and compare favorably with the native substrate amplifiers in [86].

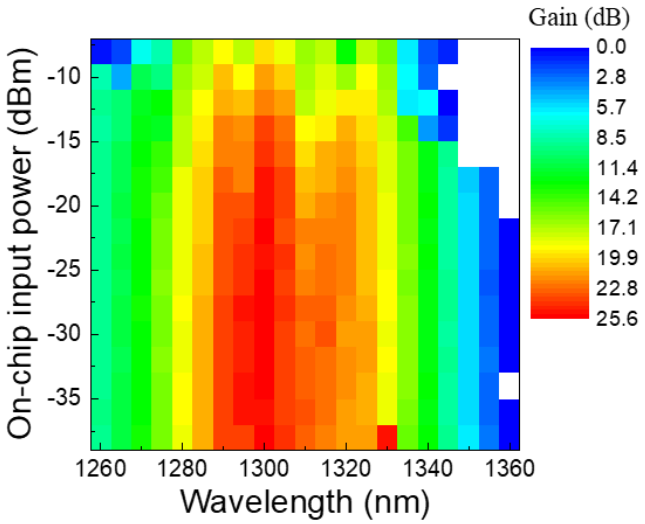

Figure 15. Gain spectra as a function of on-chip input power for a 4 μm x 3 mm semiconductor optical amplifier on silicon with seven layers of 5×10^{17} cm^{-3} p-modulation doped quantum dots, after [40].

Dislocation Climb Inhibition

By reducing the amount of nonradiative recombination at dislocations, the QDs limit the extent of recombination enhanced dislocation climb (REDC) in the material. Figure 16 shows QD and QW devices containing dislocations aged for a similar amount of time and clear evidence of reduced dislocation climb in the QD material is visible. Only under high magnification can the helical components attributed to dislocation climb be seen while the QW device shows an extensive network of climb segments.

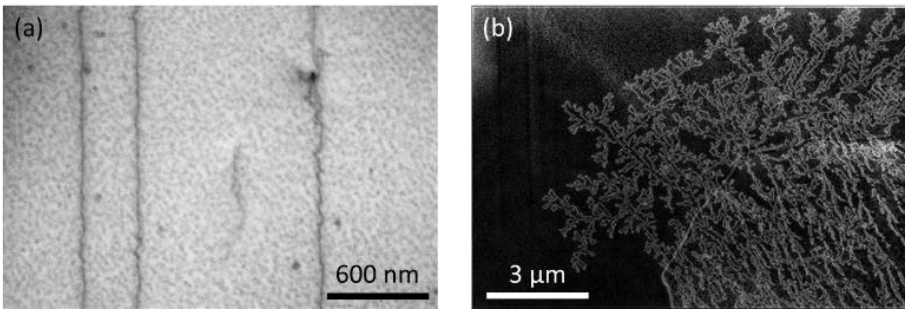

Figure 16. Plan-view transmission electron microscope image of dislocations in the plane of (a) a quantum dot and (b) a quantum well laser after aging showing the dramatic difference in dislocation climb in the well-based device [40].

Through climb inhibition and improved carrier capture, long device lifetimes for QD lasers on Si have been demonstrated. For aging at 35°C, nearly degradation free operation has been observed with extrapolated lifetimes of >10,000,000 h reported [77]. At 60°C, further improvements are still needed to achieve commercial viability, but recent results utilizing pMD active regions have shown promising extrapolated lifetimes of ~100,000 h in some devices [87].

Device Miniaturization

For integrated applications, device miniaturization is desirable to increase integration density, but as devices shrink, the effects of surfaces, which act as extended planar defects, begin to limit performance. In QD devices, the same properties that reduce sensitivity to dislocations, also reduce their sensitivity to recombination at device sidewalls and other surfaces. In QW lasers the minimum device size is limited by their effective in-plane diffusion length of several microns which causes increasing threshold currents as the laser cavity shrinks in width, but in QD layers, the in-plane diffusion length is ~1 µm. Due to limited in-plane diffusion, QD lasers show linearly decreasing thresholds for ridge widths down to 2 µm as depicted in Figure 17.

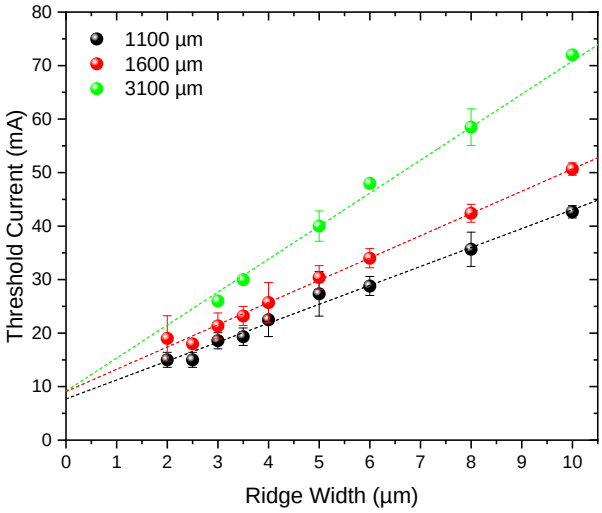

Figure 17. Threshold current versus ridge width for as-cleaved p-modulation doped Fabry-Perot quantum dot lasers at various lengths operating continuous wave at room temperature showing that even for ridges as narrow as 2 µm, threshold currents still decrease linearly [40].

Further emphasis of the scalability of QD devices can be seen in the high performance of micron-scale ring resonator cavities. In devices with uid active regions, ultralow thresholds under 1 mA have been demonstrated on Si substrates by scaling to rings with radii of 4 µm [88]. Devices with pMD in the active region analogous to the Fabry-Perot results in Figure 17 are shown in Figure 18. The smallest devices, with a radius of 15 µm, show threshold currents approaching 2 mA.

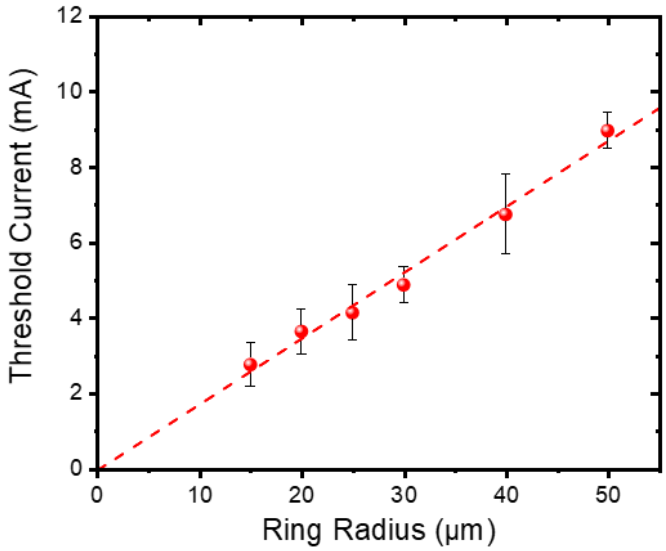

Figure 18. Threshold current versus ring radius for p-modulation doped microring quantum dot lasers on silicon adapted from [89].

High Laser Stability

Stability Against Optical Feedback

As mentioned above, the ultralow values of the linewidth enhancement factor lead to highly stable operation under optical feedback. In a direct comparison of QD lasers on Si with 2×10^{8} cm^{-2} dislocation density and >35 meV PL FWHM showed similar relative intensity noise (RIN) at 10 dB higher feedback levels relative to heterogeneous QW devices [37]. After improving the material quality of the QD lasers to 7×10^{6} cm^{-2} dislocation density and PL FWHM to ~30 meV, the stability against feedback became much more pronounced with stable operation being observed even with 90% of the light reflected back to the cavity [90]. Figure 19 shows the direct comparison of this improved material with a commercial QW laser under the same feedback conditions.

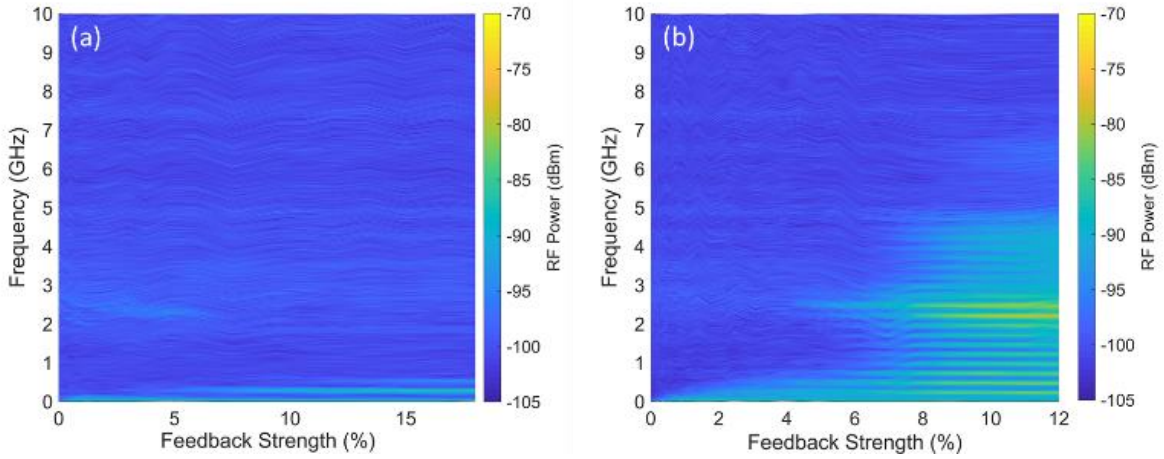

Figure 19. RF spectra of (a) quantum dot and (b) quantum well devices subjected to varying levels of optical feedback showing highly stable operation from the quantum dot laser up to feedback levels of 18% (adapted from [54]).

Stable Mode-Locking

The independence of each QD results in low noise mode-locked lasers. Since each inhomogeneously broadened QD acts as an independent emitter, the multiple modes lasing simultaneously with locked phase in a MLL will not compete for gain as they correspond to different subsets of the overall dot distribution. On silicon, heterogeneous devices have been demonstrated with simultaneous error free transmission from 15 channels [91], and epitaxial devices on silicon have shown 4.1 Tb/s transmission using a single MLL grown on Si with a 3dB bandwidth including 58 comb lines (Figure 20(a)) that were independently modulated [92]. The latter device showed a record low timing jitter of 286 fs from 100 kHz to 100 MHz (Figure 20(b)) and low average RIN of -133 dB/Hz for individual comb lines from 10 MHz to 10 GHz (Figure 20(c). These performance levels provide further evidence that epitaxial QD lasers on silicon can rival the performance of native substrate devices.

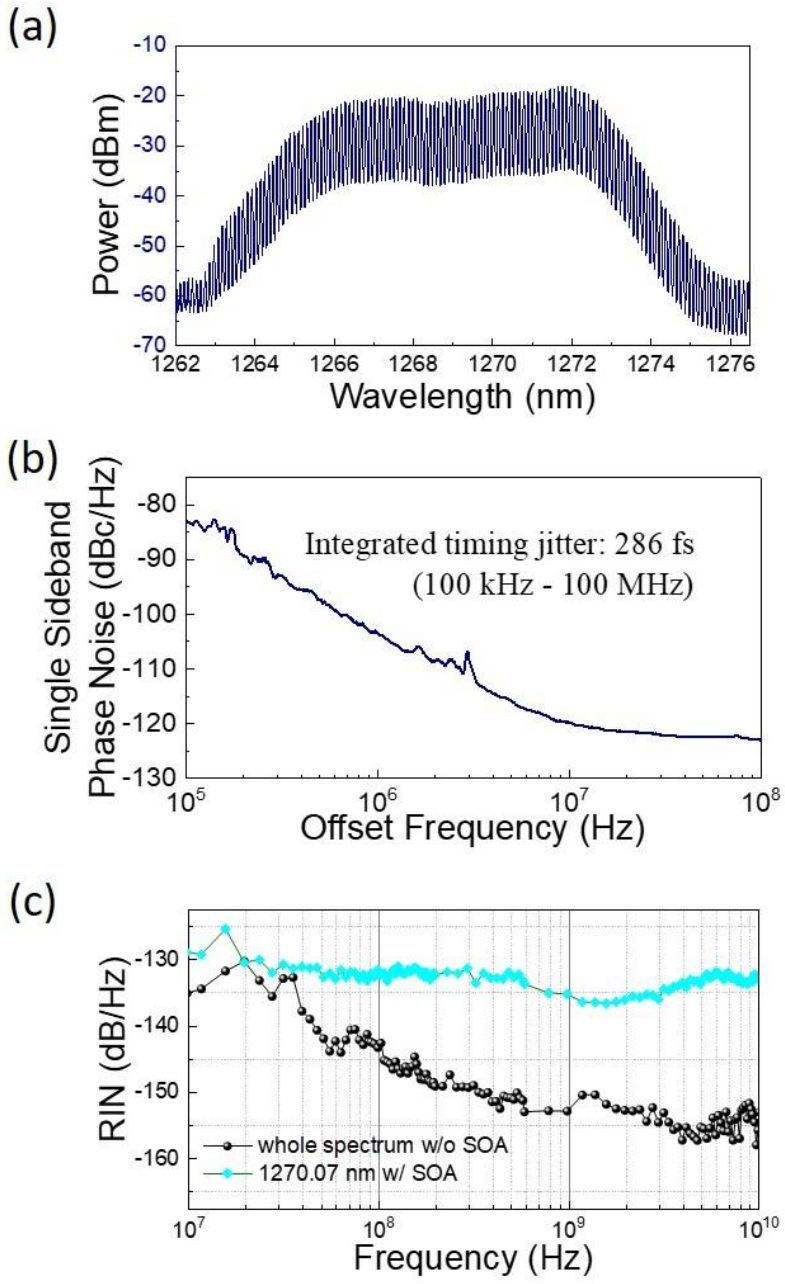

Figure 20. (a) Optical spectrum from a five-layer, p-modulation doped quantum dot mode-locked laser grown on GaP/Si. (b) Single sideband phase noise plot showing record low timing jitter. (c) Relative intensity noise (RIN) spectrum for the entire mode-locked laser spectrum and for an individual comb line after amplification. The bias condition for these results was at a gain current of 110 mA and saturable absorber reverse bias of 5 V [92].

Summary

In summary, quantum dot lasers enable substantial performance improvements over quantum well devices due to their unique atom-like energy level structure properties that can be finely tuned by changing growth conditions. Their discrete density of states and inhomogeneously broadened gain lead to lasers with low threshold, high continuous wave operating temperature, ultrahigh stability against optical feedback, and ultrafast gain recovery. Each of these concepts has been experimentally demonstrated, and due to the reduced sensitivity of quantum dots to crystalline defects, their advantageous properties are also starting to be shown for epitaxially integrated lasers on silicon, enabling significant improvements in manufacturing scalability.

Chapter 3

III-V Heteroepitaxy on Silicon

Overview of the Challenges

To realize the economic benefits of an all-epitaxial integration scheme, the performance discrepancy between grown and bonded devices must be resolved. Epitaxial III-V on Si devices have historically shown diminished performance relative to their counterparts grown on native substrates due to high densities of crystalline defects. With the notable exception of GaP, relative to Si, all III-V materials have a substantial mismatch in their crystalline lattice constant, and all III-Vs show substantial mismatch in their coefficients of thermal expansion (CTE). Additionally, there is a third mismatch in that III-V materials are polar compounds and Group IV materials are nonpolar. This can lead to antiphase boundaries between two regions where Group III and Group V material sublattices are misaligned such as across single atomic steps. Each of these mismatches must be overcome to achieve reasonable device performance. Figure 21 shows representative images of dislocations and antiphase domains taken using transmission electron microscopy.

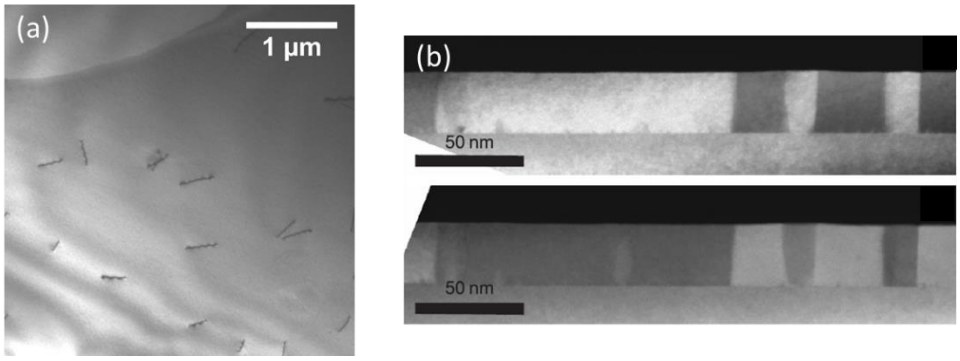

Figure 21. (a) Plan-view transmission electron microscope image of GaAs on Si showing threading dislocations intersecting the surface. (b) Cross-sectional transmission electron microscope image of antiphase domains in GaP on Si, adapted from Ref. [72].

The lattice constant mismatch leads to substantial stress accumulation in the first few pseudomorphic layers of material that are grown, which leads to relaxation above a critical thickness. This relaxation comes about through the generation of misfit dislocations which are essentially lines of aberrant, reconstructed dangling bonds running along the mismatched interface. Since no dislocation can terminate within a crystal for energetic reasons, the misfit dislocations must either reach the edge of the wafer or turn up toward the growth interface to form threading dislocations (TD), eventually reaching the surface. If growth is being done in a region where the distance to a sample edge is much larger than the distance to the epi surface (for example, in planar growth across an entire substrate), then the misfits will preferentially form TDs. TDs would also be expected to form where islands coalesce due to a lack of registry between the cross-hatched misfit networks of neighboring islands. Typically, in growth of III-Vs on Si, the TD density near the growth interface is 10^9-10^{10} cm^{-2} as shown in the cross-sectional transmission electron microscopy (TEM) image of Figure 22. A fairly comprehensive review of material relaxation in heteroepitaxy can be found in [93].

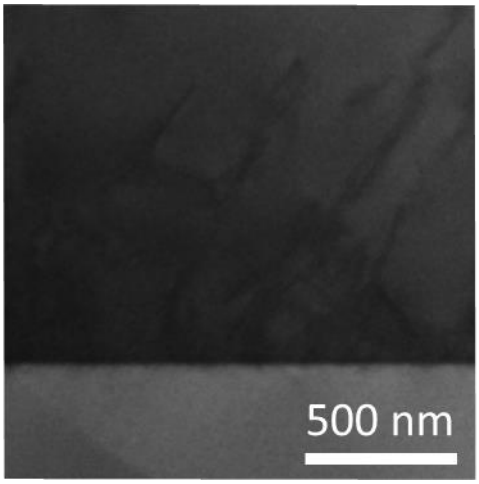

Figure 22. Cross-sectional transmission electron microscope image of GaAs on Si with threading dislocations.

Dislocations have associated trap states that act as nonradiative recombination centers [94] and tend to getter an atmosphere of point defects in their vicinity that promote further recombination and gradual device degradation through recombination enhanced dislocation climb (REDC) [95] whereby the total dislocation length within a region of high recombination (high minority carrier population) grows steadily. As a result, III-V photonic devices grown on Si tend to have lower internal efficiencies and shorter device lifetimes. The bulk of effort that has been put into III-V/Si growth has been in dealing with TDs. The most promising techniques are presented in the last section of this chapter.

The CTE mismatch becomes a problem during the cool down from growth temperature. This problem is well known to the bonding community and led to the development of low temperature bonding techniques to prevent bonded films from cracking or delaminating [96]. In epitaxial growth, the highest temperature steps likely to be reached for III-V materials are ~600°C. Upon cooling to room temperature, following growth of a film that is a few microns thick, a residual strain of ~2% can be expected. This strain has three primary effects: cracking, dislocation generation, and residual tension. If nucleation centers are present on the wafer,

such as surface contaminants, growth defects, or the clips from poorly designed sample holders, then a cross-hatched pattern of cracks will form in the III-V film that will limit device yield. In GaAs grown on Si, the theoretical thickness threshold for cracking is ~5 μm, but with a lack of nucleation centers, experimental values put the cracking threshold at 6-7 μm [97]. Fortunately, the cracking problem is one that can potentially be solved through relatively simple procedures in the engineering of sample holders and sample cleaning prior to growth. Alternatively, III-V growth can be done selectively through masking portions of the substrate to allow some thermal stress to relax [74]. If the cooling rate is slow enough and stress concentrators are not present, then dislocation half-loops can form on the surface to relax the stress and glide into the device. This mechanism is currently hypothesized to be a source of the misfit dislocations that have been observed in our QD laser active regions. Any residual thermal stress not relaxed through cracks or dislocations increases the rate of degradation of III-V devices by creating an additional driving force for dislocation growth [95].

The final challenge associated with III-V/Si heteroepitaxy, that of antiphase boundaries (APB), was largely solved decades ago by utilizing miscut (2-6° toward [110]) Si substrates that preferentially form double atomic steps on the surface. In III-V/Si epitaxy, the Group V species always nucleates preferentially on the Si surface and terminates at one monolayer. As a result, APBs only form at single atomic (half-monolayer in the III-V lattice) steps on the Si surface, and if single-steps are absent, then so are the APBs. However, the problem with using miscut Si is that the Holy Grail for photonic integration is CMOS compatibility, and miscut Si is not CMOS compatible. The need for an APB-free CMOS compatible Si substrate is what has driven recent work in III-V/Si epitaxy.

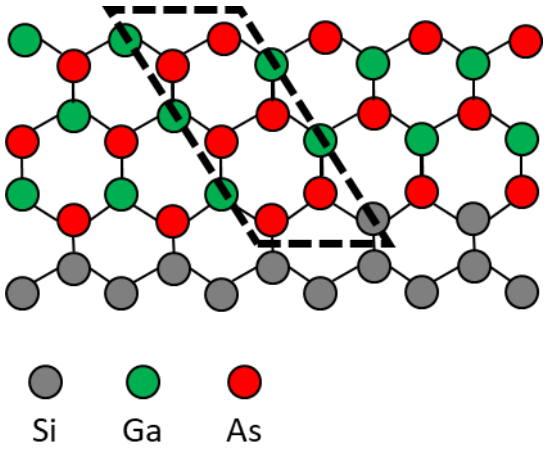

Figure 23. Ball-and-stick illustration of GaAs on (001) Si with a single atomic step on the surface illustrating the presence of an antiphase boundary (dashed box).

Antiphase Domain Free On-Axis III-V/Si

When growing III-V materials on Group IV materials, antiphase domains form at locations of odd-numbered atomic steps. This is schematically illustrated in Figure 23. One approach to minimizing APBs is to perform a series of surface treatment steps to the Si before III-V growth to promote double step formation even on on-axis (001) substrates [72]. While such treatments do not completely restructure the surface into double atomic steps, and, therefore, do not completely eliminate APBs, if appropriate growth conditions are chosen in the subsequent epi layers, the APBs will grow at an inclined angle and annihilate each other within the crystal. APB annihilation has been observed in GaP/Si[72] grown by MOCVD and AlGaAs/Si[48] grown entirely with MBE. Another approach to eliminating APDs is to pattern the silicon substrate with {111} faceted v-grooves. Such facets can be easily formed using selective crystallographic etches such as KOH or TMAH. Due to the atomic structure of such surfaces, APDs cannot form with vertical inclination leading to annihilation within the v-groove trench. The v-groove approach has been demonstrated for InP by MOCVD [50] [98]

and for GaAs by MOCVD [25] and MBE. In the end, no approach to APD elimination has shown an advantage over the others in terms of simplicity or performance in dealing with other defects. As such, the previous techniques are interchangeable.

Threading Dislocations

With APDs solved, dislocations become the focus for further material improvement, and approaches using MOCVD or MBE involving GaP/Si or v-groove Si yield similar dislocation density $>10^9$ cm^{-2} in overgrown films prior to the introduction of additional filtering techniques. These results match growth on miscut silicon as well.

Dislocations can be divided into two general classes based on their orientation relative to the growth direction: misfit dislocations and threading dislocations. Threading dislocations have a component of their dislocation line in the growth direction while misfits lie entirely in the growth plane. Since threading dislocations propagate upward, they are the subject of defect filtering efforts. However, that is not to say that misfits are not harmful; to the contrary, misfit dislocations present in the active region of a laser would be far more detrimental than threads because the overall length of the defect seen by the device would be much larger. Given that nonradiative recombination is minority carrier limited, dislocations away from the laser active region could be relatively innocuous.

While the simple, qualitative description of thread versus misfit is useful in many situations, more rigorous classification can be done in terms of a dislocation's Burgers vector and line direction. Together these geometrical descriptors describe the orientation of a dislocation's dipolar strain field and whether or not two given dislocations would attract each other and annihilate or repel each other. More complicated dislocation interactions--or more specifically, reactions--can also take place resulting in different classifications of dislocation

after their interaction, some of which may be sessile, essentially rendering them unfilterable. For this reason, gradual dislocation filtering through slowly graded buffers is more favorable than rapid changes in composition. Possible grading schemes are limited though due to limitations in film thickness due to cracking and due to the limited availability of lattice constants in III-V materials relative to Si. Graded buffers to GaAs and InP lattice constants can be achieved starting with GaP/Si, but it requires a growth chamber with both As and P sources, which was not available for the work in this thesis.

Since dislocations cannot be eliminated from a film except through interactions with other dislocations, filtering approaches should be designed to bend threading dislocations into the plane—forming misfit segments—and promote enhanced dislocation glide, whereby a threading dislocation moves through the material extending the misfit segment beneath it, ultimately culminating in annihilation of the thread as it meets another thread of complementary Burgers vector with their misfits (and underlying thread segments) forming a closed loop. As a threading dislocation glides through material, it must be extending a misfit segment somewhere underneath, generally at a strained interface to maximize the amount of relaxed strain energy.

The model of Matthews-Blakeslee[99] describes the mechanism of misfit dislocation formation and growth in terms of a force balance between the line tension of a misfit dislocation and the glide force provided by the resolved shear stress at the mismatched interface. All materials have an intrinsic energy barrier to dislocation glide, termed the Peierls barrier, that must be overcome for a threading dislocation to move. As a result, depending on temperature, dislocation glide can be enhanced or suppressed. This would indicate that higher temperatures are superior for dislocation filtering, but high temperatures also reduce the

barrier to nucleation of new dislocations. Since the driving force for dislocation nucleation is also obviously dependent on strain in the material, there should exist some optimum temperature for growing a relaxed buffer of given nominal strain. Given the kinetic nature of dislocation formation, the growth rate should also play a role.

A Note on Characterization

In literature, dislocation densities are reported in a wide variety of ways. Among the frequently used techniques are x-ray diffraction (XRD), cross-sectional transmission electron microscopy (TEM), plan-view TEM, electron channeling contrast imaging (ECCI), cathodoluminescence (CL), electron beam induced current (EBIC), and etch pit density (EPD). Each of these techniques has their own advantages and disadvantages and caution should always be taken when interpreting any reported claims of dislocation density as not all methods are accurate and the majority of methods are not statistically significant.

In XRD, typically the FWHM of an ω rocking curve is analyzed as a proxy for dislocation density. While dislocations do broaden the rocking curve FWHM, so do many other effects including film thickness, wafer curvature, defect filter layers such as strained superlattices, and other types of defects that may be present in addition to dislocations depending on the material system in question. Additionally, dislocations with different Burgers vector/line direction can broaden a given rocking curve differently, so quantitative analysis is difficult. Always view reports of material improvement purely presenting XRD with extreme skepticism. Even qualitative trends can be questionable if defect filter layers are included as their own strain and misfits may more than compensate the reduced broadening due to threading dislocation reduction.

When using TEM, unambiguous counts of dislocations can be readily obtained as well as details of the Burgers vector and line direction of the dislocation by imaging multiple diffraction conditions. The challenge with TEM, however, is that a thin foil must be made such that electrons can transmit through the material, meaning thicknesses < 1 μm. The challenges associated with such sample preparation mean that the amount of the sample that ends up imaged is quite limited in area, especially in the case of cross-sectional measurement. It is not uncommon to find reports of dislocation density < 10^7 cm^{-2} with the only data presented being a cross-sectional image that probes a material volume of < 1 um^2. At 10^7 cm^{-2}, one would expect 1 in 10 TEM images of similar scale to show a dislocation. Accurate data simply cannot be extracted from one image, and given the effort it takes to prepare TEM samples, it's a given that the dozens of images necessary for statistical validation were not taken. Plan-view TEM offers a substantial improvement over cross-sectional but is still limited in area to a micron or two per image.

EBIC, CL, and ECCI are all scanning electron microscope (SEM) based techniques. Being SEM based techniques, each of these methods can utilize the field of view and stage mobility provided by an SEM to look at multiple areas on a large sample. Each technique can also be performed on time scales identical to traditional SEM imaging. CL is an optical technique where emitted light is measured from recombination by electron-hole pairs generated by the electron beam. Since carriers diffuse freely upon generation, the resolution of CL is directly tied to the minority carrier diffusion length in the material. For this reason, crystal-clear (pun intended) images of nitrides can be obtained at dislocation densities of 10^9 cm^{-2}, but in arsenides, anything over ~10^7 cm^{-2} could look washed out. ECCI is a diffraction technique where the sample is imaged in the backscatter mode. When zoomed out to a large field of

view, diffraction patterns can be clearly observed for single crystal material, and then the sample can be tilted and rotated into a channeling condition associated with the expected slip systems in the imaged material system (e.g. an intersection of the (004) and (220) in zinc-blende). Then, when zooming in on a particular location, the strain field of the dislocations will cause local deviation of the channeling condition resulting in light/dark contrast across the dislocation core. Using ECCI, large areas can be rapidly surveyed and accurately counted, but surface roughness can be restricting if it masks contrast in the backscattered electron image (typically >4 nm rms is problematic). Also, if the dislocation density is too high (e.g. $>10^8$ cm^{-2}), dislocation strain fields may overlap and mask each other. EBIC involves measuring electrical current from a sample as the electron beam rasters across the field of view and provides injection. Since current extraction requires an electrode, EBIC requires some sample preparation making it useful for failure analysis in already fabricated devices, but less than ideal for characterizing films intended for further growth with lasers or other devices. As with CL, resolution is limited by carrier diffusion.

The last prominent technique is etch pit density. EPD works by using an etchant that selectively etches material at dislocations faster. The result is that after some time dipped in etchant, a sample will develop many small pits that can be counted to get the dislocation density. The problem with this technique is that it fails to distinguish closely spaced dislocations, and often at low dislocation densities, the dislocations that remain are clusters of sessile dislocations. In general, the following table lists reasonable dislocation densities for applying each technique.

Table 3. Various dislocation density characterization techniques and their range of applicability.

Technique	Acceptable Dislocation Density for Use
X-ray Diffraction Rocking Curve	Weakly quantitative
Cross-section TEM	$>5\times10^{8}$ cm^{-2}
Plan-view TEM	$>1\times10^{8}$ cm^{-2}
ECCI	10^{8} $cm^{-2} > x > 10^{6}$ cm^{-2}
CL/EBIC	$< 5\times10^{6}$ cm^{-2}
EPD	$< 1\times10^{6}$ cm^{-2}

As a final note, remember that all imaging techniques can induce new dislocation or the movement of existing dislocations whether they be mechanical grinding or ion milling for TEM or the electron beam for any SEM based technique. The act of imaging will alter the sample, so always make sure to never image the same area more than once and minimize exposure to any high intensity process.

Dislocation Filtering Techniques

In bulk, planar films, there are two primary methods of dislocation filtering: strained layers and thermal cyclic annealing. Individual dislocations possess a dipolar strain field that can be influenced by material stresses to glide or climb to lower their overall energy. Such stresses include lattice mismatch from layers with different lattice constant, thermal stress due to temperature change in materials with dissimilar coefficients of thermal expansion (CTE), or through the stress gradients associated with proximity to a free surface where bonds can freely relax. All these sources of stress provide a driving force to dislocation motion with direction

dependent on the dislocation's slip system and the nature of the applied stress (tensile or compressive).

In the case of strained filter layers, differences in lattice constant drive threading dislocations to form misfit segments and glide along the strained interface. Depending on the material system being utilized, strained filter layers could be tensile, compressive, or could alternate between the two to efficiently relax through heterogeneous nucleation of misfits rather than exceeding the critical thickness for nucleation of new dislocations. The appropriate choice of composition and thickness for strained filter layers is dependent on the material and prior dislocation density. Filter layers could be relatively thick or formed from thin superlattices of a few nanometers. Ideally, filter layers should be grown slowly at high temperature on a smooth surface to minimize pinning and promote long misfit segments. In reality, practical constraints imposed by material growth windows and the typically enhanced growth rate around dislocations limit the extent to which ideality can be achieved.

Materials with different CTE (e.g. all III-V materials relative to Si) can utilize thermal cyclic annealing (TCA) to filter dislocations. TCA involves cycling the substrate temperature during growth to values above and below the growth temperature resulting in alternating tensile and compressive strain. The cycling stresses promote dislocation glide, increasing the likelihood of interaction with neighboring dislocations and annihilation. In choosing the temperatures for TCA, two factors must be considered. As the temperature increases, so does the glide velocity, further enhancing the technique's filtering capability and suggesting that hotter anneals are always better. In practice, there is an upper limit because in all MBE growth of III-Vs there is a temperature above which the surface will begin to decompose, generally determined by the maximum achievable Group V overpressure. Meanwhile, on the low end,

there comes a point where the Peierls barrier effectively freezes out dislocation motion, inhibiting dislocation interactions.

The driving force associated with free surfaces suggests that selective area growth of devices could be favorable for improving material quality. As the area of the growing film decreases, the effect of surfaces will increase. Additionally, with a smaller area film, coherent misfit arrays without threading dislocations could be more likely to form because the total misfit segment length to reach the edge is reduced. Improved material quality through growth in small regions has been observed experimentally and described theoretically [76, 100]. Furthermore, by growing in smaller regions the effects of thermal mismatch can be relaxed eliminating the prospect of cracking in the mismatched films [74].

Summary

To summarize, the crystalline lattices of silicon and III-V materials are highly incompatible due to differences in lattice constant, polarity, and thermal expansion coefficient. These differences lead to high densities of defects including dislocations, cracks, and antiphase domains that act as nonradiative recombination centers that reduce device performance and limit device lifetime. Antiphase domains have been solved through multiple techniques with single-domain GaP/Si commercially available from $NAsP_{III/V}$ [72] and demonstrated in the laboratory using several approaches including v-groove Si [25] and AlGaAs buffers [48]. The remaining issue to be solved is that of dislocations. Several techniques are well established for dislocation filtering including thermal annealing, and strained filter layers, which are applied in the results of Ch. 6 to demonstrate record laser performance on a silicon substrate.

Chapter 4

Quantum Dot Growth Optimization

Molecular Beam Epitaxy

The materials presented in this thesis were all grown using molecular beam epitaxy. Molecular beam epitaxy (MBE) is a technique for growing crystalline materials with unrivaled precision and purity. To the layman, the notion of "growth" seems to often invoke thoughts of biological processes. In analogy to the formation of an organism through the organized assembly of supplied molecular structures into the larger structures of organelles, cells, and tissues, MBE utilizes atomic or molecular species that assemble into crystalline structures with morphology dependent on the underlying substrate, thermodynamics, and kinetic constraints of the chosen growth conditions. By tuning the growth conditions and supplied molecular or atomic species, the "grower" can create layers of material with atomic precision with tailorable physical properties that when engineered in sequence can form devices with unique structural, electronic, and photonic characteristics.

Molecular beam epitaxy works through the use of an ultrahigh vacuum chamber with ultrahigh purity source materials. A MBE system, while initially intimidating in appearance,

can be reduced to simply a large stainless-steel vessel supported by numerous pumps to provide the low pressures required. Typical MBE chambers, when not growing material, will idle at pressures of 10^{-10} to 10^{-11} Torr. This level of vacuum is lower than that found anywhere in our solar system and only exceeded by that of deep space, and allows for a truly uninteracting molecular beam. Since the pressure is so low, the mean free path of depositing species is on the scale of several meters with the growth substrate typically < 1 m away from the sources. As such, the impinging species have not interacted with any other atoms or molecules leading to what is essentially a "molecular beam". The ultralow pressures result in extremely low levels of background contamination with typical atomic concentrations of unintentional elements of $< 10^{16}$ cm^{-3} or approximately one part per million. At these pressures, the source materials can often be the limiting factor in the purity of the epitaxial layers. MBE source materials are generally described according to their "nine number" which represents the number of nines in the purity percentage (e.g. 7 nines means 99.99999% purity). Typical growth rates using MBE are on the order of one micron per hour, but some materials can require far slower rates while others can achieve higher with proper engineering of the source cells. In all cases, MBE affords atomic layer thickness precision and arbitrarily precise composition control, barring the occurrence of thermodynamically unstable compositions that could limit adatom incorporation.

The Growth Chamber

A schematic of an MBE chamber with typical components is shown in Figure 24. Nearly all MBE chambers contain several common components. In the center of the chamber is the substrate manipulator which has a mounting mechanism for the growth substrate, a heater to control the substrate temperature, and an external motor to rotate the sample during growth.

Since MBE utilizes a molecular beam from the source material, geometric effects will influence the deposition rate, and, thus, rotation is critical to uniformity. The heater is critical to high material quality as the substrate temperature strongly controls how much impinging adatoms can move around the surface before incorporating into the underlying crystal. At growth temperatures that are too low, atoms can incorporate in incorrect lattice sites resulting in point defects or not be able to reach existing step edges leading to increasing roughness, and at temperatures that are too high, the adatoms may even desorb from the sample leading to reduced growth rates, undesired stoichiometry, or surface decomposition. Typical growth temperatures for (Al,Ga)As are above 580C while In containing compounds grow best at lower temperatures around 500C.

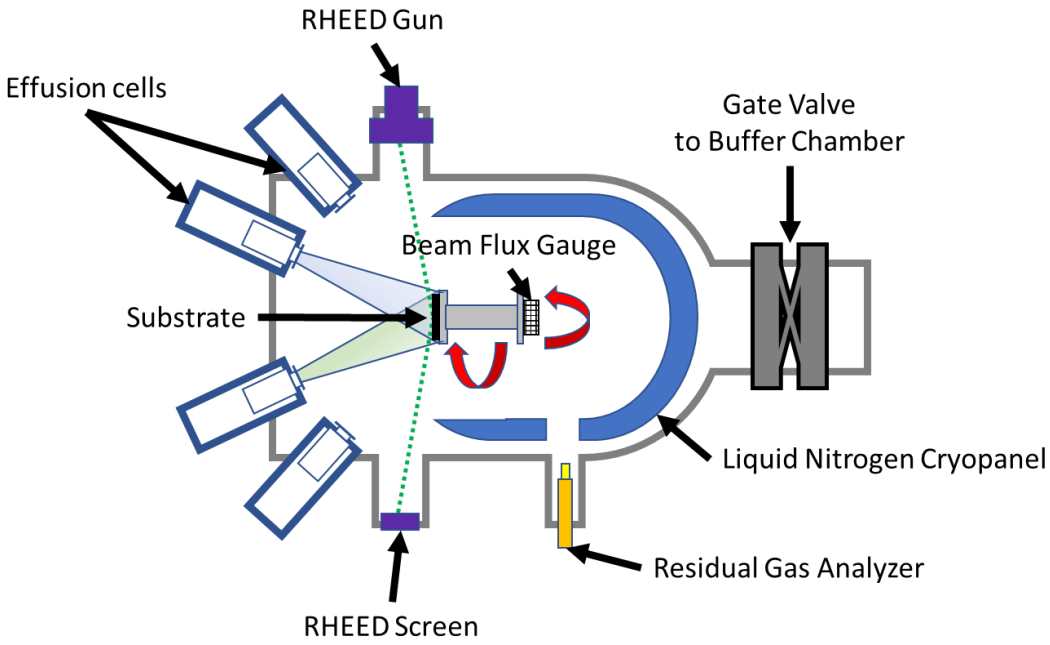

Figure 24. Schematic diagram of a molecular beam epitaxy chamber including critical components.

Diametrically opposite the substrate is an ion gauge. This ion gauge is used to determine a “beam equivalent pressure” (BEP) when facing a material source at growth temperature

which is correlated to the deposition rate of a given source at a particular temperature. The exact pressure to atomic flux relationship is determined through growth rate calibrations that should be done periodically between maintenance cycles with a periodicity of at least every few months. RHEED intensity oscillations, x-ray diffraction, and various optical techniques are all routinely used for growth rate calibration.

Facing the substrate manipulator, typically arranged in a circle such that they are all equidistant from the growth substrate, are the sources that house the material for deposition. Depending on the material in question, the source could be a delivery system for metalorganics, or an ionized gas, or it could house elemental materials in crucibles with material supplied via evaporation or sublimation. For the III-arsenide materials described in this thesis, all sources are elemental precursors with group III materials and dopants (Be and Si) supplied as single atoms and arsenic supplied as a cracked molecule of As_2 or As_4. For cases when the diffusion of dopants is undesirable (e.g. when doping distributed Bragg reflectors for vertical-cavity surface-emitting lasers or the cavity quantum electrodynamics structures of Appendix A), Be may be exchanged for C which is typically supplied using the CBr_4 precursor.

To maintain low background pressures and high material purity, a means of in-situ vacuum characterization is necessary. For this purpose, MBE chambers typically include a residual gas analyzer (RGA), which is a mass spectrometer that allows for monitoring the composition of the background pressure of the MBE chamber. Background monitoring reveals the elements present in the chamber and is critical for leak detection and identification of the source of any observed contamination. Regular RGA scans of the chamber allow for early detection of leaks even before a noticeable background pressure increase can be observed.

The final component common to nearly all MBE systems is the reflection high energy electron diffraction (RHEED) system. The RHEED system consists of an electron gun angled at shallow incidence relative to the substrate growth surface with an opposite phosphor screen for revealing the diffraction pattern of the growing surface. RHEED is used for in-situ monitoring of crystal growth. Depending on the material being grown and growth conditions utilized, the atomic surface structure of the growing material will take on specific patterns, termed reconstructions. These reconstructions result from the unbonded electrons of atoms at the free surface of the growth interface bonding to each other, lowering the overall energy of the surface. The patterns observed in the diffracted electrons from the phosphor screen indicate the reconstruction present which yields information on how the crystal is growing, the accuracy of calibrated growth conditions, and the surface morphology. For III-V materials, the phase space of surface reconstructions as a function of growth conditions is well known and can be utilized to determine ideal conditions for crystal growth and diagnose poor material quality in cases where unexpected surface roughness or defects are present.

Quantum Dot Growth via MBE

There are three thermodynamic growth modes that comprise all of epitaxial growth named for their discoverers: Frank-van der Merwe, Volmer-Weber, and Stranski-Krastanov. The growth mode taken by a given material on a particular substrate is determined by their relative surface energies, which dictate whether or not a given material will wet another material. The energy balance can be simply stated as an inequality relating the combined energy of the epitaxial film surface, γ_f, and the energy associated with the film/substrate interface, γ_i, to the energy of the substrate surface, γ_s. In many cases the interfacial energy has a thickness dependence, h, if the materials are strained. These concepts are illustrated in Figure 25.

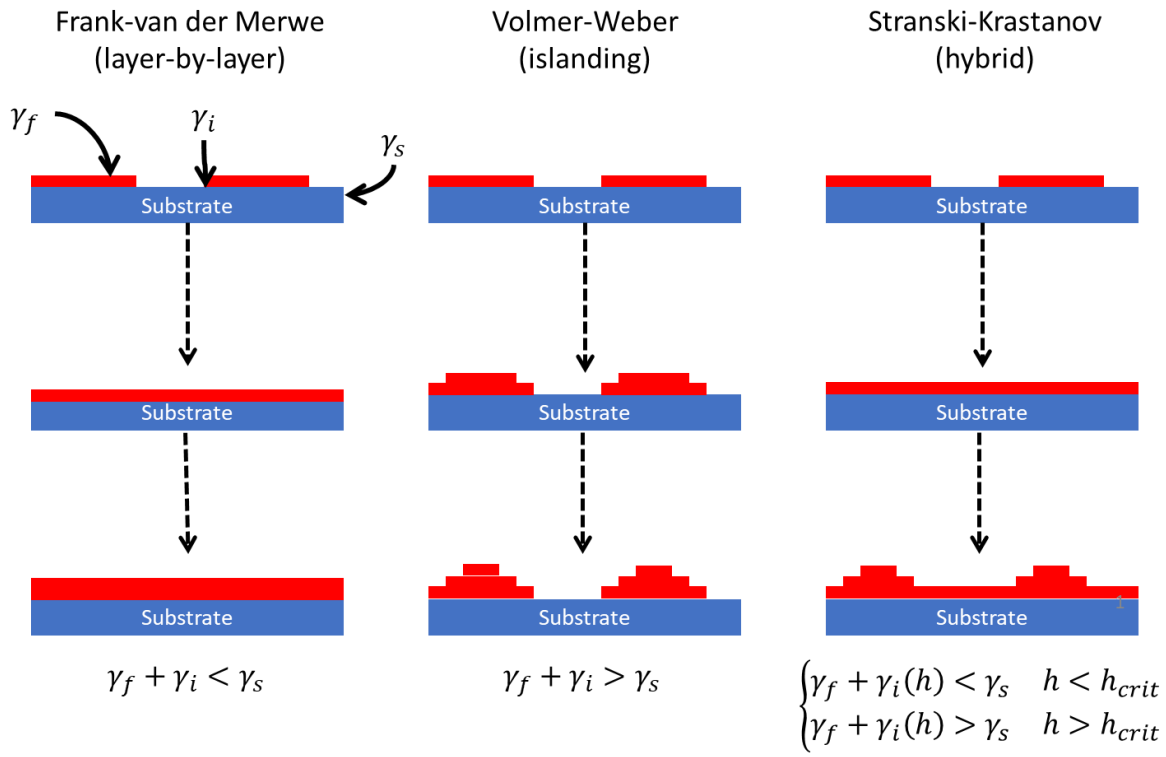

Figure 25. Schematic illustration of the three regimes of epitaxial growth and their dependence on surface and interfacial energies.

The Frank-van der Merwe growth mode is also referred to as layer-by-layer growth and describes conditions where wetting of the substrate by the growing epi layer is favorable. This growth mode produces smooth films and is generally not suitable for growth of quantum dots. The opposite regime, where wetting is energetically unfavorable is described by the Volmer-Weber or islanding growth mode. Quantum dots can be grown using the VW mode, but they tend to produce nonuniform size distributions. In contrast, the intermediate, SK growth regime yields uniform size distributions. The SK growth mode starts with wetting of the substrate but rapidly transitions to three-dimensional, self-assembled growth after exceeding a critical thickness dictated by strain. The strain-based driving force combined with facet energetics promotes a thermodynamically ideal island size and shape which leads to relatively uniform dot size distributions. The SK growth mode has been observed for many materials systems

with wildly varying characteristics of the atomistic mechanisms of the growth mode [101], but the most well-studied is that of InAs on GaAs for the production of QDs emitting at 900-1400 nm. The fundamental physical mechanisms of SK growth, particularly emphasizing their use for QDs is presented in [43].

The precise tunability of growth conditions afforded by MBE makes it ideal for controlling the highly kinetically constrained growth of SK QDs. Since the SK growth mode is a self-assembly process, it is strongly affected by any changes to adatom mobility on the growth surface. Through tuning of the growth temperature, V/III ratio, growth rate, and the use of growth interruptions, the resulting dot size distribution can be narrowed or broadened as desired for a particular application. Furthermore, the mean dot size can be adjusted to shift the emission wavelength, and the density can be tailored for cases where high dot density is desirable (e.g. for lasers and amplifiers) or for cases where low dot density is desirable (e.g. single photon devices).

Beyond the ability to grow highly tunable QD layers, MBE also provides a substantial improvement over MOCVD through its lower growth temperatures for AlGaAs. In most optical devices, some sort of top optical and/or electrical confinement structure is desirable, and AlGaAs provides the most favorable materials systems due to its near lattice matched crystal structure to GaAs and high band gap. The problem with AlGaAs in MOCVD is that it must be grown at high temperatures, often >600C, while QDs start to intermix at temperatures above 550C. This means that during the top half of the growth of a given device structure, that the QDs will steadily interdiffuse, shifting their emission energy and broadening the emission spectrum. In MBE, AlGaAs can be grown at 550C with reasonable quality thus preserving the QDs.

The ability to use RHEED in the growth of QDs via MBE is also highly beneficial. In the SK growth mode, the first layers of deposited material will wet the underlying surface giving 2D growth. At some critical thickness, the strain energy will begin to dominate, and the growth will go 3D. This is the QD nucleation point and is easily visualized using RHEED by observing the transition from streaky diffraction patterns to a spotty, chevron pattern indicative of faceted islands. The precise thickness where nucleation occurs is highly dependent on growth conditions, so being able to see the transition is useful for identifying any drift in calibration or deviation from the targeted growth conditions.

Optimization Methods & Reasoning

Each of the previously mentioned MBE growth conditions is coupled and can have synergistic or anti-synergistic effects on the optical and morphological properties of the resulting dot layer. As a result, each parameter must be optimized and, ideally, iterated upon to obtain an optimal result. Such studies have been undertaken in literature to various extents[47, 102-123] with the most comprehensive analysis presented in [43] and succinct experimental studies presented in [107] and [119]. That said, due to the size of the parameter space and highly coupled nature of all variables, there is no perfectly comprehensive study of QD growth, and the sum of the literature available is difficult to analyze because while one study may examine the effects of growth temperature and another may report on the growth rate, they will likely not have perfectly unified settings for the remaining variables, and it is virtually guaranteed that there is moderate variability in the calibration of their MBE systems in terms of growth rate, temperature, and flux readings. For this reason, I have attempted to reproduce the results in literature and conduct a thorough analysis on a single MBE machine with consistently calibrated measurements to optimize QD growth conditions. The results are

a cumulative effort with a previous student, Alan Liu, consisting of more than 400 individual growths. The key results are presented below.

The optimization samples were designed for photoluminescence (PL) and atomic force microscopy (AFM) characterization. Each sample was grown on a semi-insulating GaAs substrate and contained a single buried QD layer 95 nm below the sample surface and a second dot layer uncapped on the sample surface. A 150 nm buffer was grown to bury any surface contaminants on the epi-ready substrate. The GaAs buffer and cap were grown at standard conditions of 580°C, a V/III ratio of ~25, and growth rate of 1.8 Å/s.

Each QD layer involves four growth steps including: InGaAs prelayer growth, QD growth, QD capping with InGaAs and GaAs, and the In-flush anneal[124]. The InGaAs layers help to gradually transition the strain from the QDs relative to directly growing GaAs which improves the luminescence properties and shifts the luminescence closer to 1300 nm as well as resulting in a dot-in-a-well (DWELL) structure that facilitates carrier capture[118, 125]. The In-flush anneal is a high temperature step where partially capped dots are heated from their growth temperature of ~500°C to the GaAs growth temperature of ~580°C and annealed for five minutes to truncate the size distribution to a uniform value set by the partial capping through In evaporation and In-Ga intermixing. Each of these steps has a significant impact on the luminescence properties of the QDs and would ideally be iteratively optimized, but given that the parameter space includes, temperature, V/III, growth rate, thickness, In composition, and potentially various sequences of growth interruption, a proper factorial design of experiments is not feasible on the time-scales available to a graduate student on a non-automated MBE system. A schematic of the PL structure used in these studies is shown below.

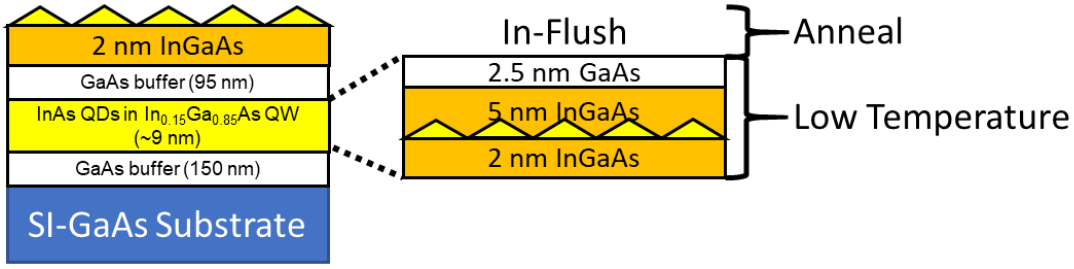

Figure 26. Schematic of the epi design used for quantum dot growth optimization.

During optimization, a high PL intensity along with a narrow FWHM were targeted for high performance lasers, but the general trends could guide designs for broader gain spectra as may be desired for amplifiers or mode-locked lasers. PL measurements were conducted using a previously measured reference sample to account for variability in the pump laser power from day to day. Measurements were conducted at "low" and "high" pumping levels with a 785 nm laser. The relative pumping intensities varied over the course of the study but were on the order of 0.3 mW and 2.5 mW for low and high pumping, respectively. Measurements were taken with a 0.75NA/50x objective giving a minimum laser spot diameter of ~1.28 µm. The optimum focus of the PL system is highly wavelength dependent over spans smaller than the full range that would include the QD ground and excited states, so a consistent methodology was established to optimize the focus (stage z-position) to maximize the PL intensity for the ground state emission at low pumping for each sample and then not change the focus when increasing the pumping for the high intensity measurement. The shift in PL peak wavelength between low and high pumping was < 10 nm, so this method should be suitable for achieving direct comparisons of different samples. However, due to the pump intensity's sensitivity to measurement setup and variability of the pump laser output/coupling on different days, the best method for comparing samples is to measure them back-to-back on the same day, or at the very least, use a consistent reference sample to confirm the PL intensity

is the same as has been measured on previous days. Parameters other than the PL intensity can generally be directly compared because they don't vary significantly with pump power.

The primary figures of merit for QD growth optimization are the low and high pump power PL intensities, the ground state FWHM, the ground state wavelength, and the energy separation between the ground state and first excited state. These parameters are illustrated using representative PL spectra in Figure 27.

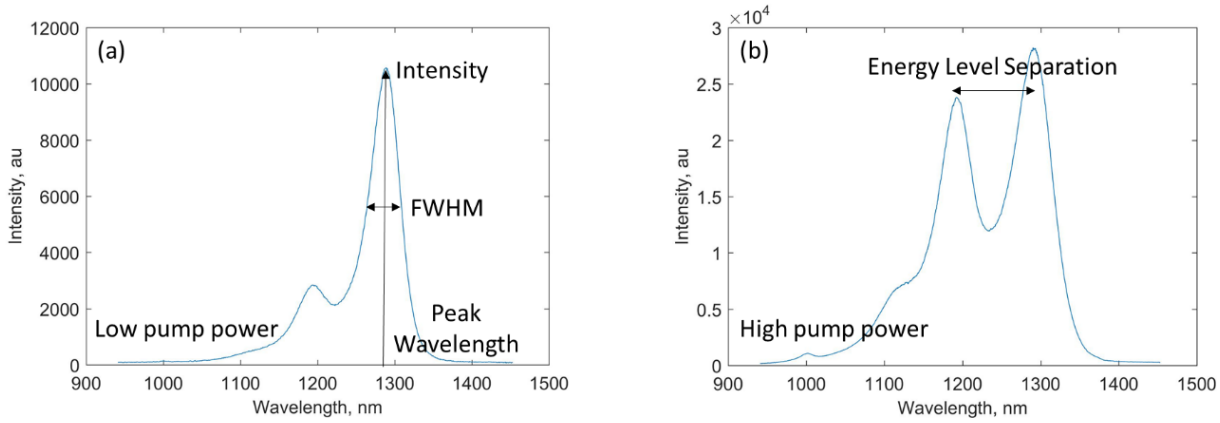

Figure 27. Photoluminescence spectra at (a) low pumping and (b) high pumping level illustrating the figures of merit for growth optimization.

A detailed description of the importance of each of these parameters and their interpretation is given in [126]. In short, the PL intensity correlates with the material gain with high pumping levels giving insight into the maximum gain and low pumping levels indicating material quality as defects in the material would be expected to saturate at high pumping. The FWHM of the ground state PL gives a measure of the inhomogeneous broadening of the material[57] which should be made narrow to improve the laser threshold, differential gain, linewidth enhancement factor, and slope efficiency[58, 127]. Basically, the narrower the PL, the fewer dots that are taking charge carriers and not contributing photons to the lasing mode. The energy level separation is important for achieving all of the predicted attributes of QD devices

to the extent that excited states of some dots do not overlap with the ground states of others which would result in a quasi-continuum and not the atom-like density of states desired, but even once the energy levels are distinct, the separation determines how easily carriers can escape from the QDs which has implications for high temperature performance, device lifetime, and dark current in QD photodetectors.

In addition to PL, the dot morphology and density should be considered. Using atomic force microscopy (AFM), the size, shape, and density of uncapped QDs can be measured. The dot density (typically in the mid 10^{10} cm^{-2}) is of interest because it should relate directly to the laser gain and eliminates any potential ambiguity regarding whether brighter PL is due to a reduction of nonradiative recombination or an increase in dot density. The size and shape of the dots is generally of less use because it changes dramatically during capping due to In-Ga exchange and the use of the "In-flush" technique where dots are partially capped and annealed to evaporate the tops and truncate the size distribution for greater uniformity[124]. Of note is that AFM can show the density of oversized, coalesced QDs which may contain defects; however, transmission electron microscopy imaging has not shown a correlation between these dots and dislocations or other visible defects.

Qualitative Growth-Structure-Property Relationships

The growth conditions to be discussed below affect the optical properties of the QDs through changing the way atoms move and assemble on the epi surface leading to different structural properties of the dots such as the size, composition, strain, and band offsets relative to the surrounding matrix. From the qualitative particle-in-a-box picture the structure-property relationships can be described relatively intuitively. Since a typical uncapped Stranski-Kastanov QD has a diameter of ~20 nm and height of ~8 nm, the quantum confinement will

be primarily set by the height of the dot. The surrounding material will then dictate the band offset and strain in the QD which will also shift the energy levels. In general, the effects of strain are complicated and poorly understood due to the irregular shape of the QDs and the dependence of that shape on growth conditions. The composition of the dot can also be tuned by adding Ga to reach shorter wavelengths, but this is beyond the scope of this thesis.

The relationship between the structural or morphological properties of the QDs and the growth conditions is also largely intuitive. The knobs that can be tuned during MBE growth include temperature, V/III, growth rate, use of growth interruptions, and annealing. The effect of each parameter can be described in terms of how it affects adatom behavior on the surface. Layer thicknesses and compositions can also be varied to change the dot morphology in addition to the changes in quantum confinement and strain described previously.

Parametric Study of Quantum Dot Growth Conditions

The following sections describe in detail the results of various growth series performed to optimize the PL properties of the QDs. In each experiment, one parameter is varied while all remaining parameters are held constant. Only illustrative examples for each condition are included for brevity.

Substrate Temperature & V/III Ratio

Temperature controls the adatom diffusion length and desorption rate. At long diffusion lengths, impinging In adatoms can more easily find an existing QD to incorporate rather than nucleating a new dot on the underlying film. Since the unconstrained 3D nature of a QD allows strain relaxation at its free surfaces, dot incorporation is more thermodynamically favorable than incorporating in the film elsewhere—up to some critical dot size where strain can no longer be efficiently relaxed. This thermodynamic driving force helps promote uniform dot size distributions. Long diffusion lengths and preferential incorporation at QDs means that higher temperatures tend to result in lower dot densities with larger dot sizes. In the extreme limit of increasing temperature, the In sticking coefficient will drop below unity and desorption rates will increase such that dot size will decrease with further increase in temperature. At low temperatures, higher densities of smaller dots would be expected with the kinetic constraints leading to a broader size distribution. At sufficiently low temperatures, nucleation can be completely suppressed leading to relaxed films instead of QD growth.

In Figure 28, the trends in PL properties are shown as a function of growth temperature. Clear optimum temperatures exist for obtaining bright, narrow PL in accordance with the tradeoff between overly kinetically constrained growth conditions and In desorption. Given that dot size is the largest factor that dictates the emission wavelength, the data in Figure 28(a) shows how smaller dots are obtained for higher and lower temperatures than the optimum. The energy level separation Figure 28(c), being largely dictated by the surrounding material, is roughly constant across the range of growth temperatures indicating that the InGaAs well surrounding the dots is not being affected until a temperature of 520°C where it is likely also suffering the effects of In desorption leading to changes in shape and strain field in the dots.

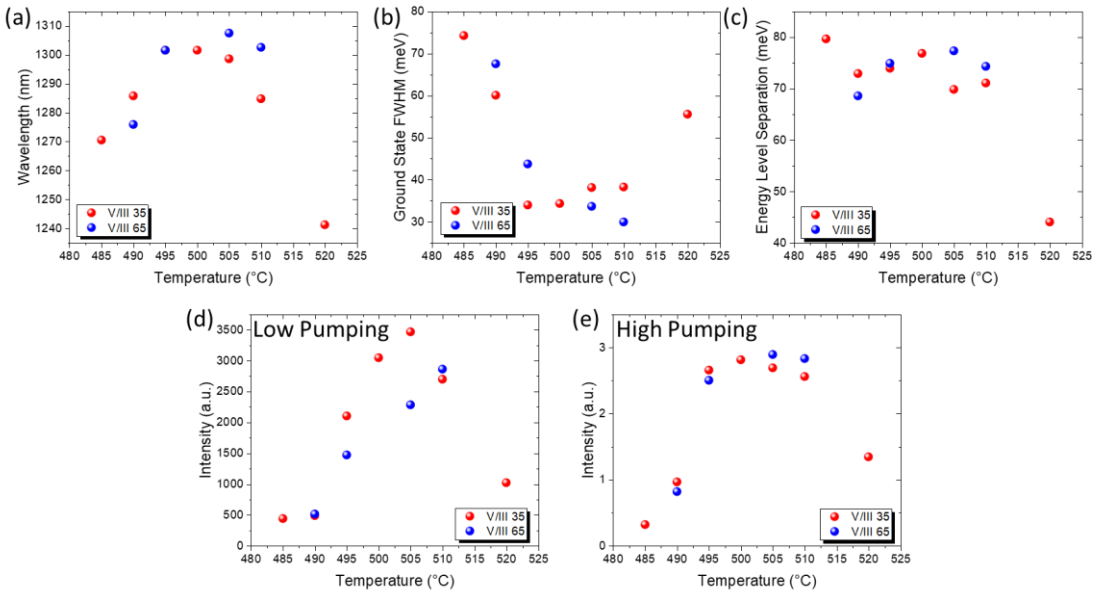

Figure 28. The variation of photoluminescence properties with substrate growth temperature is shown for quantum dot V/III ratios of 35 and 65 including (a) ground state peak wavelength, (b) ground state full-width at half-maximum (FWHM), (c) energy level separation between the ground state and first excited state, (d) the ground state peak intensity at low optical pumping, and (e) the ground state peak intensity at high optical pumping. All samples use an As_2 overpressure.

The effects of changing V/III ratio are a bit more complicated than changing temperature. In MBE growth of III-Vs, the Group V element (in this case, As) is always present in excess due to its low sticking coefficient, and Group III incorporation into the crystal is dictated by the presence of As dimers on the surface. From this picture, one would intuitively predict that high As overpressure (high V/III) would reduce adatom diffusion lengths by increasing the number of favorable incorporation sites on the epi surface; however, in reality this is not always the case. One observation reported in literature is that with increasing V/III ratio, the QDs get taller and density gets lower which has been attributed to roughening and strain in the initial wetting layer[128]. Contradictory results have been obtained by Konishi *et al.* who use scanning tunneling microscopy *in-situ* to correlate dot nucleation to the evolving $(n \times 3)$ reconstruction domains during InAs deposition[129] with higher As overpressure stabilizing

the (8×3) reconstruction domains that preceded dot nucleation on an InGaAs surface. While no study of (8×3) coverage and subsequent dot density has been reported, one could hypothesize that if an (8×3) reconstruction precedes nucleation, that a greater coverage of the reconstruction would lead to a higher dot density. Therefore, higher V/III ratios could lead to a greater dot density, which I have observed when using an overpressure of As_4 (see Figure 29(a)). Potential sources of the discrepancy in literature could be the use of As_4 versus As_2 [122] or may have to do with growing on a GaAs surface as opposed to InGaAs which have different reconstruction dynamics. Due to the likely dependence on surface reconstruction and that the As sticking coefficient is temperature dependent, one would expect the growth conditions of temperature and V/III ratio to be coupled.

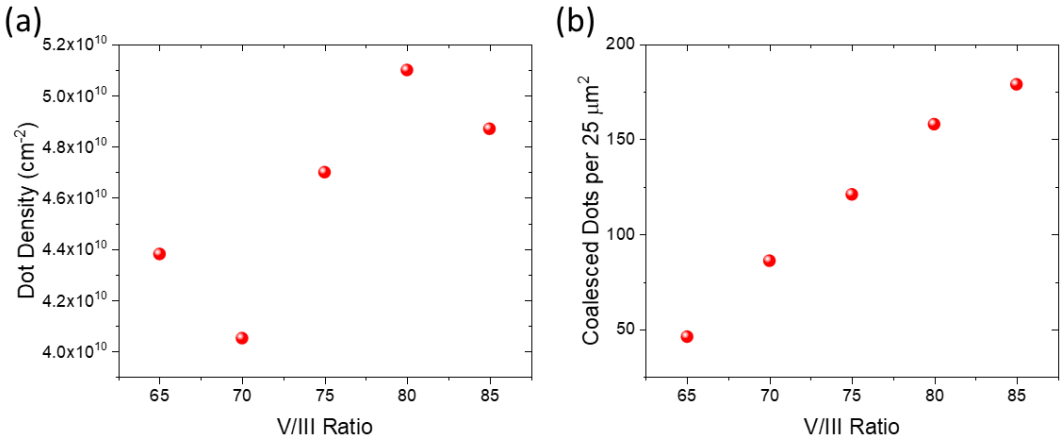

Figure 29. (a) Dot density and (b) total number of coalesced dots in a 25 µm^2 area as a function of V/III ratio for an As_4 overpressure with dots grown at 500°C.

Returning to Figure 28, the coupling between V/III and growth temperature can be clearly seen. In going from a V/III ratio of 35 to 65, the optimum growth temperature shifts to higher values. An increase in the dot size with higher V/III is also suggested by the relative redshift in the wavelength at the optimum temperature in Figure 28(a). The different relative PL intensities between the samples with different V/III at low pumping and similar intensities at

high PL pumping suggest there is a difference in nonradiative recombination with higher V/III ratios leading to lower material quality. This could be attributed to defects associated with the increased density of coalesced dots at higher V/III ratios (see Figure 29(b)), but due to differences in the As species, a clear conclusion cannot be drawn. The samples in Figure 28 were grown at an early stage in the optimization process with an As cracker temperature of 850°C which supplies mostly As_2 while the data in Figure 29 was grown with As_4. Reproduction and further iteration could be valuable.

Dimeric vs Tetrameric Arsenic

The choice of arsenic species affects the reactivity of As on the epi surface with As_2 incorporating via a first-order process and As_4 incorporating via a second-order process[130]. The higher reactivity of As_2 increases its incorporation leading to more available sites for Group III incorporation thus suppressing re-evaporation and reducing adatom diffusion lengths[131]. In terms of QD growth, switching from As_2 to As_4 would be expected to be akin to raising the growth temperature or lowering the V/III ratio. These trends are largely born out in the experimental data of Figure 30. The longer wavelength associated with As_4 in Figure 30(a) at the same V/III ratio suggests that the dots are larger while the data converges at higher V/III ratios where the difference in reactivity may be offset by the sheer amount of excess As. Longer diffusion lengths also seem to benefit the ground state FWHM as shown in Figure 30(b) as would be expected if the dot sizes could move closer to a thermodynamic equilibrium. Trends in the energy level separation are consistent with larger dots, and improvements in intensity at low and high pumping suggest higher dot quality with As_4; however, the data at V/III ratios of 45 and 50 is inconsistent with previous trends in intensity suggesting that further

growths should be done to reproduce the results. Additionally, the continuously improving PL intensity at higher V/III ratios merits further investigation since all other parameters remain similar. At the time such studies were not pursued because of the increase in density of coalesced dots (as shown in Figure 29(b)) which were suspected to result in defects that could limit laser lifetime. More recently, lifetime studies and material characterization using ECCI and TEM have shown this not to be the case.

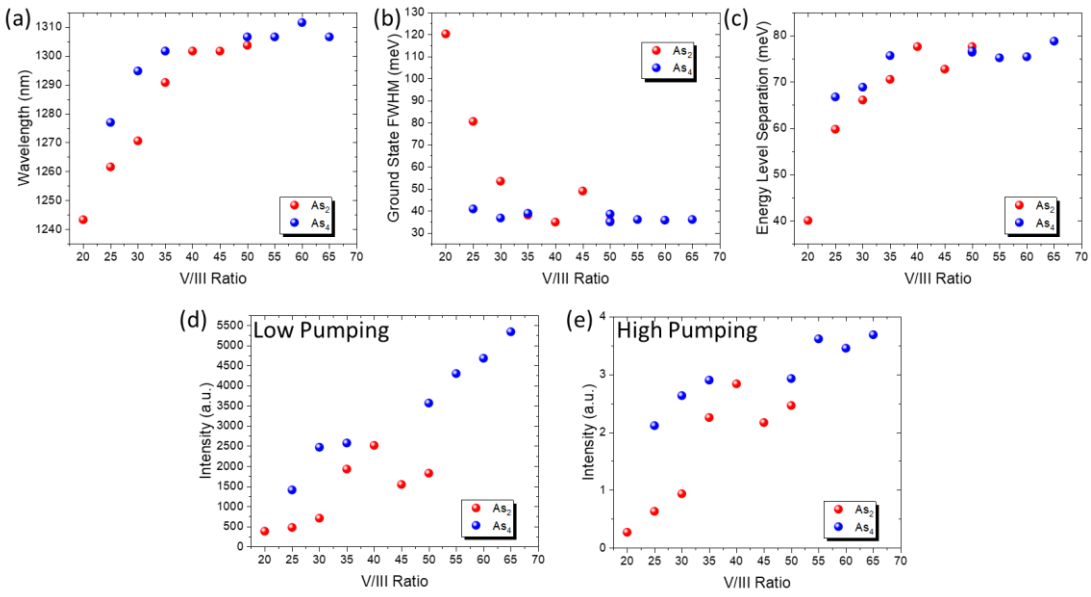

Figure 30. The variation of photoluminescence properties with V/III ratio is shown for dimeric and tetrameric As species including (a) ground state peak wavelength, (b) ground state full-width at half-maximum (FWHM), (c) energy level separation between the ground state and first excited state, (d) the ground state peak intensity at low optical pumping, and (e) the ground state peak intensity at high optical pumping. All samples are grown at 500°C.

Total Nominal InAs Thickness

The effect of the total amount of InAs deposited is fairly straightforward. Since MBE growth rates are determined in terms of thickness per unit time, nominal deposition thicknesses are used as a proxy for the amount of In deposited despite the fact that it organizes

into 3D structures with heights much taller than the thickness deposited. Since these QDs form via the Stranski-Krastanov growth mode, the range of nominal thicknesses has a lower bound set by the critical thickness for the 2D to 3D transition. While the exact transition is dependent on growth conditions, it always falls in the 1-2 ML range, with optimized conditions yielding a critical thickness of 1.4 ML. The maximum amount of In that can be deposited is set by the thickness where dots start to relax forming defects, which seems to be >3 ML. Experimental variations of the total InAs deposited show an increase in the emission wavelength with increasing deposition of ~4 nm per 0.1 ML up to ~2.6 ML and then saturating. All other relevant PL quantities do not vary significantly with InAs deposition up to 2.9 ML. A nominal thickness of 2.55 ML was adopted for laser growths to get the benefits of longer wavelengths that push closer to 1310 nm while minimizing the chance of relaxation from strain buildup due to multiple dot layers.

InGaAs DWELL Composition

As previously discussed, the InGaAs QW helps to facilitate carrier capture by the QDs. The well has the added bonus of reducing the quantum confinement of the dots which shifts the wavelength favorably into the O-band for optical communications and, for the portion of the well above the QDs, provides more gradual strain relaxation relative to going directly from InAs QDs to GaAs which improves optical performance. The thickness and growth conditions of the InGaAs well will be discussed below in terms of the prelayer and and capping layers since they can be easily tuned and optimized independently. For the case of composition, such independent tuning has not been conducted because, at the time of optimization, we only had one In cell. Due to the time and necessary growth interruptions it would take to ramp the In

cell temperature for different growth rates for the prelayer, dots, and capping layer, only constant InGaAs compositions were considered. Through multiple In or Ga cells that could be set to different growth rates, asymmetric DWELL structures could be grown which would be an interesting avenue for future experiments. The results for constant composition optimization of the InGaAs DWELL for a prelayer thickness of 2 nm and capping thickness of 5 nm are shown below.

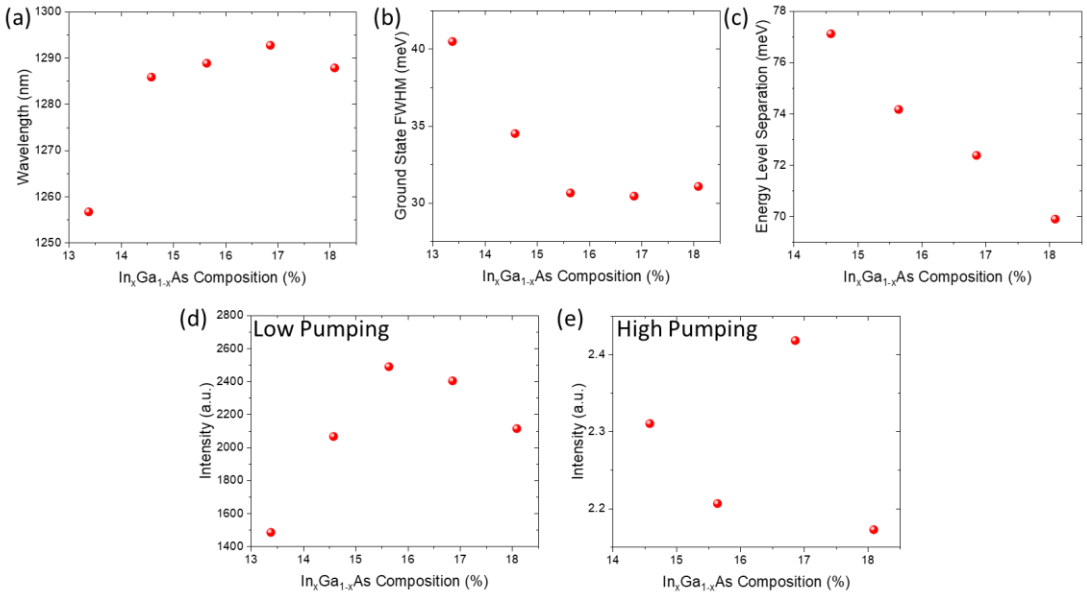

Figure 31. The variation of photoluminescence properties with the composition, x, of the $In_xGa_{1-x}As$ DWELL is shown including (a) ground state peak wavelength, (b) ground state full-width at half-maximum (FWHM), (c) energy level separation between the ground state and first excited state, (d) the ground state peak intensity at low optical pumping, and (e) the ground state peak intensity at high optical pumping. All samples utilized a 2 nm prelayer and 5 nm InGaAs cap.

Several interesting trends can be observed as the InGaAs DWELL composition changes. From Figure 31(a), there is a large redshift in wavelength between compositions of 13.5% and 14.5% In content followed by relatively little change as the composition increases. Since there is very little bowing in the InGaAs bandgap with composition change, such an abrupt shift

must be due to a change in the dot morphology rather than confinement. The dot ground state FWHM decreases continuously up to a composition of 15.5% In and then largely stabilizes. The significant changes at lower compositions suggest changing adatom mobility, possibly due to changing surface structure/reconstruction or the effects of strain. The energy level separation decreases continuously with increasing In content. Given that the emission wavelength does not change significantly above 14.5%, the decreasing quantum confinement must be driving the trends in energy level separation. Despite implied changes in the adatom mobility by the FWHM Figure 31(b), the high pumping level PL intensity in Figure 31(e) shows very similar values for each sample suggesting similar dot density. At low pumping level, the PL shows an optimum intensity between 15% and 17% In suggesting that nonradiative recombination is minimized for a particular capping composition. This could be due to a balance between improvement due to the gradual strain transition from having InGaAs around the dots rather than GaAs and the penalty paid in total strain accumulation due to an overall increase in In content in the sample, but the results presented below for changing InGaAs thickness do not support this conclusion. The exact cause of the variation in PL intensity is not known.

InGaAs Prelayer

The InGaAs prelayer refers to the portion of the QW used to make the DWELL structure that is below the QD layer. The composition and thickness of this layer set the strain that will be seen by adatoms on the surface during growth as well as the band offsets on the substrate side of the QD layer. The use of an InGaAs prelayer is not universal as pioneering groups at QD Laser, Inc. and the University of Tokyo produce high performance QD lasers with dots

directly grown on GaAs[132]; nevertheless, in my experiments, an InGaAs prelayer has always yielded improved PL performance in terms of ground state intensity and FWHM. Three parameters can be easily varied to optimize the InGaAs prelayer: composition, thickness, and V/III ratio. The growth temperature would be another parameter, but due to the finite times necessary to ramp the growth temperature and allow it to stabilize, changes in temperature also necessitate a growth interruption, which was found to substantially decrease PL intensity.

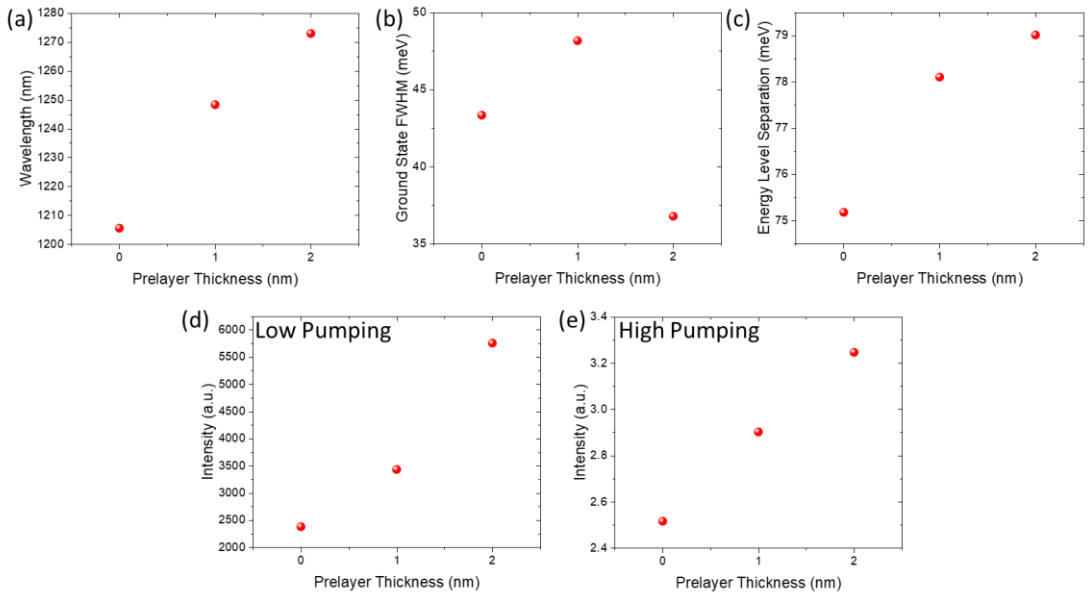

Figure 32. The variation of photoluminescence properties with the thickness of the InGaAs prelayer is shown including (a) ground state peak wavelength, (b) ground state full-width at half-maximum (FWHM), (c) energy level separation between the ground state and first excited state, (d) the ground state peak intensity at low optical pumping, and (e) the ground state peak intensity at high optical pumping. All samples utilized a 5 nm InGaAs cap and 15% In composition.

The results from varying the prelayer thickness, holding the composition constant at 15% and including a 5 nm $In_{.15}Ga_{.85}As$ cap, are presented in Figure 32. The results in Figure 32(a) and (b) are consistent with a reduction in the quantum confinement for the dots as the prelayer thickness increases. Given that energy levels decrease with increasing well width and since

InGaAs has a narrower bandgap than GaAs, the PL is behaving as expected. The lack of trend in the ground state FWHM is unusual and suggests that other factors are dominating the adatom mobility rather than any surface evolution with thickness. The increasing PL intensity at low and high pumping with prelayer thickness could be due to better carrier injection due to the DWELL structure or due to an increase in dot density. Unfortunately, a surface layer of dots for AFM was not included in these samples to determine the relative influence of improved carrier injection versus dot density. Since dot density would depend on adatom mobility, the lack of trend in the ground state FWHM could suggest that the dot density did not change significantly for the three samples. The continuous improvement in the low pumping intensity indicates that the increasing thickness has not resulted in defect formation.

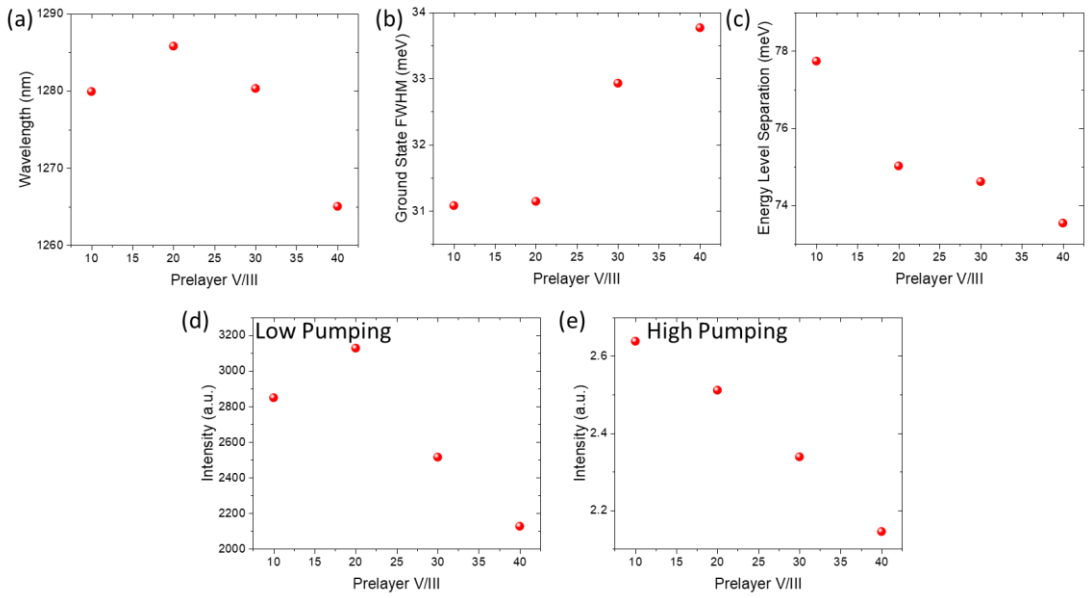

Figure 33. The variation of photoluminescence properties with the V/III ratio of the InGaAs prelayer is shown including (a) ground state peak wavelength, (b) ground state full-width at half-maximum (FWHM), (c) energy level separation between the ground state and first excited state, (d) the ground state peak intensity at low optical pumping, and (e) the ground state peak intensity at high optical pumping. All samples utilized a V/III ratio of 65 for the quantum dots and during capping, a 5 nm InGaAs cap, and 15% In composition for the cap and prelayer.

Given that QD formation is likely influenced by surface reconstructions and that such reconstructions depend on temperature and V/III ratio, the V/III ratio was also varied for the prelayer. While varying the V/III ratio from 10 to 40, the V/III ratio during QD growth and the capping layer were held at 65. As_4 was used in these experiments. The results are given in Figure 33. Understanding these results would likely require a scanning tunneling microscopy study of the surface at incremental growth steps in the prelayer through the QD nucleation point. In terms of performance, all metrics clearly indicate that a lower V/III ratio is better. Lower values lead to brighter PL, a more uniform dot size distribution, and a wider energy level separation. At the growth temperature of 510°C, it is unlikely that the V/III ratio is significantly altering the In sticking coefficient or desorption rate. The trends in wavelength and energy level separation could indicate a decrease in dot size while the increase in PL intensity suggests an improvement in material quality or increased dot density. AFM studies (Figure 34) show that the dot density does indeed increase at lower V/III ratios. Interestingly, the PL intensity at low pumping shows a maximum at a V/III of 20 with a decrease at 10 while the high pumping PL intensity increases monotonically. From the AFM scans, the density of coalesced dots is found to increase significantly going from a V/III of 20 to 10 which could further indicate their influence as nonradiative recombination centers.

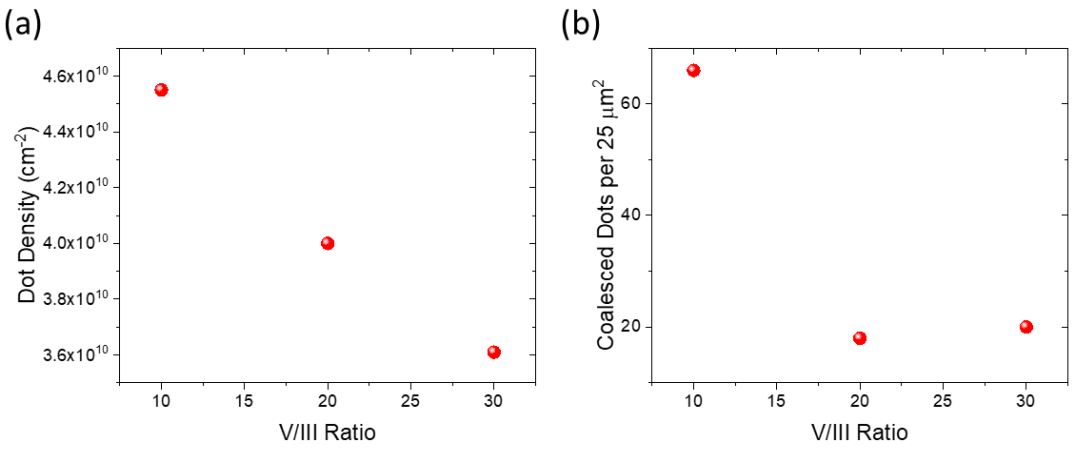

Figure 34. (a) Dot density and (b) total number of coalesced dots in a 25 μm^2 area as a function of V/III ratio used in the InGaAs prelayer. All samples had a V/III ratio of 65 during dot growth and capping.

InGaAs Capping

The dot capping procedure including layer compositions, thicknesses, growth interruptions, and annealing are all critical to achieving bright, narrow PL spectra. For all studies presented, the QDs are capped with $In_{.15}Ga_{.85}As$ and 2.5 nm of GaAs at the QD growth temperature and then heated up to 580°C to anneal for 5 min before continuing growth of any remaining material. As discussed previously the combination of capping and annealing is termed the "In-flush" technique and serves to improve QD size homogeneity through dot truncation[124]. The $In_{.15}Ga_{.85}As$ composition was found to be optimal as described previously and was held constant for further optimizations while the capping thickness, V/III ratio, and growth interruptions were varied. The 2.5 nm GaAs growth at low temperature was also held constant because any increase in thickness was found to yield extremely high oval defect densities, and decreases in thickness led to substantially dimmer PL. Furthermore, the series of growths to optimize the capping V/III ratio yielded no meaningful trends, so a V/III of 35 was used to match the As flux desired for subsequent GaAs growth.

Since the In-flush technique is intended to homogenize the dot heights through truncation, selecting the appropriate capping thickness relative to the uncapped QD height is critical. If the cap is too thick, not all dots will be truncated to the same height. If the cap is too thin, dots may be truncated too short leading to undesired blue shift in the emission, or if excessively thin, the dots can partially decompose due to In desorption leading to dim, broad PL. It should be noted that during overgrowth of InAs QDs with (In,Ga)As that the deposited material does not cover the dots uniformly but rather, preferentially fills the space between the dots leading to a smoothening of the surface and enables a partial capping for height truncation in the first place.

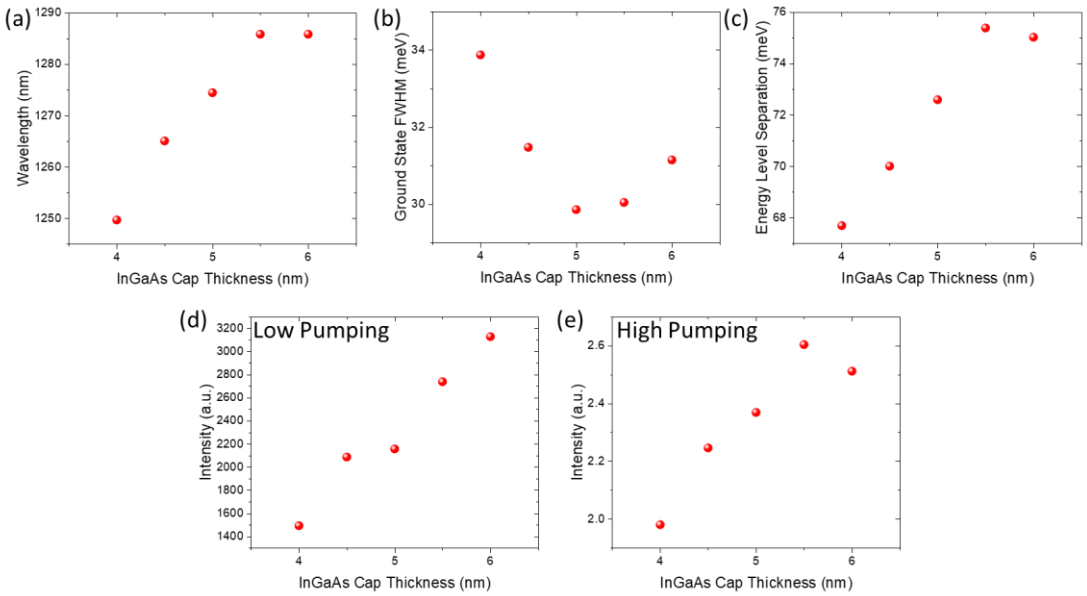

Figure 35. The variation of photoluminescence properties with the thickness of the $In_{.15}Ga_{.85}As$ capping layer is shown including (a) ground state peak wavelength, (b) ground state full-width at half-maximum (FWHM), (c) energy level separation between the ground state and first excited state, (d) the ground state peak intensity at low optical pumping, and (e) the ground state peak intensity at high optical pumping. All samples utilized a GaAs cap of 2.5 nm on top of the $In_{.15}Ga_{.85}As$.

The results of varying the InGaAs cap layer thickness from 4-6 nm are shown in Figure 35. The total thickness of InGaAs effectively sets the dot height meaning that thicker caps will

yield taller dots. In Figure 35(a) the wavelength is shown to increase steadily as the capping thickness increases from 4 nm to 5.5 nm and then remains unchanged at 6 nm suggesting that the capping thickness exceeded the QD height rendering the In-flush less effective. This agrees roughly with the histogram of uncapped dot heights in Figure 36(b), but based on the remaining PL characteristics, other effects may also be in play. The ground state FWHM, shown in Figure 35(b), suggests that there is a very narrow boundary between the deleterious effects of insufficient capping thickness and burying the shorter dots leading to truncation of only a portion of the dot population. The minimum point agrees well with the histogram of dot sizes as measured by AFM which peak at 5 nm as shown in Figure 36. The sharp distribution is a testament to the highly self-limited growth mode of Stranski-Krastanov quantum dots. The trends in pump intensity and energy level separation are more surprising. Larger dots should lead to smaller energy level separation as should a lower bandgap QW. This suggests that strain effects are to blame. Being closer in lattice constant, the InGaAs cladding is likely resulting in reduced compressive strain in the QDs. Literature results where QD lasers have been tuned from transverse electric (TE) to transverse magnetic (TM) emission[45] support this hypothesis. The strong correlation between the wavelength, energy level separation, and PL intensity indicate that the strain effects are actually the dominant mechanism in the effects of InGaAs capping on QD PL.

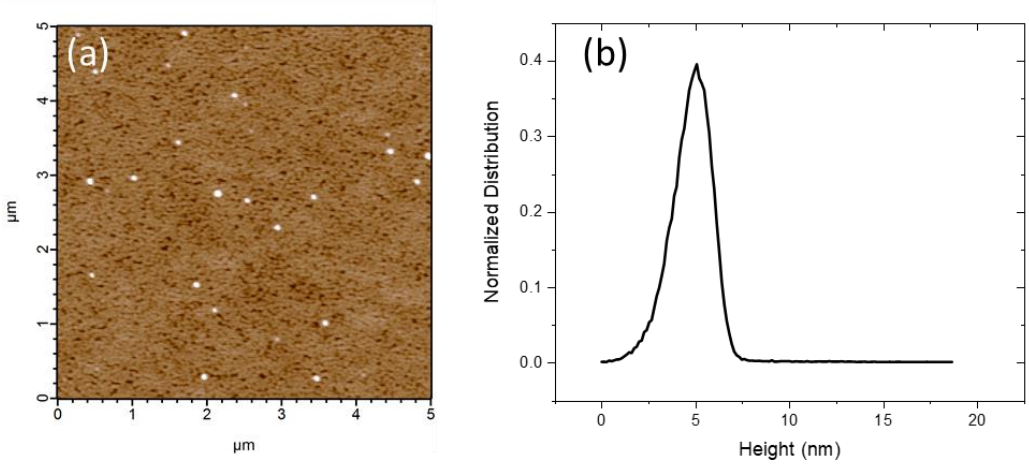

Figure 36. (a) Atomic force micrograph of a 5×5 µm^2 area of uncapped quantum dots. The large white spots represent defective, coalesced dots. (b) Histogram of the height distribution from (a) showing that the majority of uncapped dots are ~5 nm in height.

Growth Interruptions

Due to the self-assembled nature of InAs QDs, growth interruptions can be a useful tool for helping the dots evolve to a more uniform size distribution. The adatom diffusion length on the growing surface is strongly influenced by the flux of additional impinging adatoms. Any break in this flux leads to longer diffusion lengths which promotes the QD ensemble's evolution to a more thermodynamically ideal, uniform size distribution[116]. To confirm the hypothesis in our samples, experiments were conducted with growth interruptions during QD growth and after completing InAs deposition before capping to explore potential coarsening processes known to exist in Stranski-Krastanov QDs[43]. In some experiments, the As flux was interrupted in addition to In, but this was found to universally degrade the optical properties of the film likely due to surface decomposition and point defects.

The initial interruption scheme consisted of continuous deposition of InAs up to the nucleation thickness of 1.4 ML. After nucleation, the In shutter was opened and closed repeatedly to deposit the remaining 1.15 ML of material. An additional experiment was done with growth interruptions over the full 2.55 ML of QD growth, but it was found to give identical results to only using interruptions after nucleation. The first growth interruption parameter that was optimized was the length of the pause between bursts of material. The results are shown in Figure 37. As the length of time for each growth interruption increases, the wavelength is found to decrease. If a coarsening or Ostwald ripening process were taking place, the average dot size should be increasing leading to a red shift as dots below a critical radius disperse their atoms to their larger neighbors. In addition to the wavelength blue shift, the PL intensity is also decreasing with interruption time. This suggests that In is desorbing from the surface. The energy level separations in Figure 37(c) show very little change until an interruption time of 10s, which suggests that most of the In is being lost from the QDs and that the InGaAs well is largely unaffected. As hoped, the uniformity was found to improve with growth interruptions, but the change was relatively small at ~1 meV (Figure 37(b)). While 1 meV is nearly the experimental error, reproductions were found to offer a similar relative change.

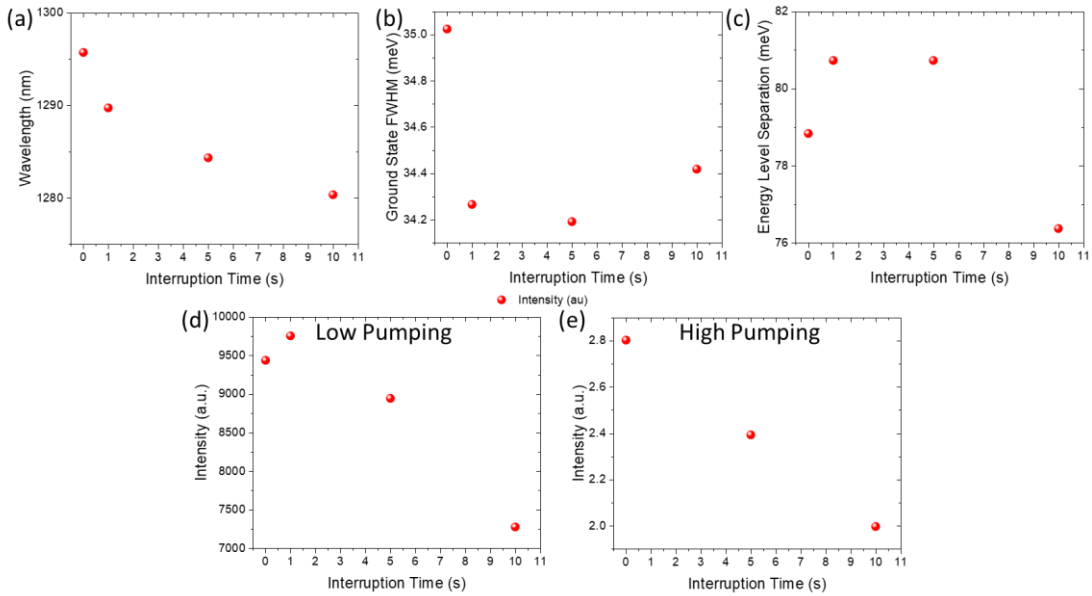

Figure 37. The variation of photoluminescence properties with the interruption time for quantum dots deposited in ten steps of 0.115 ML after nucleation is shown including (a) ground state peak wavelength, (b) ground state full-width at half-maximum (FWHM), (c) energy level separation between the ground state and first excited state, (d) the ground state peak intensity at low optical pumping, and (e) the ground state peak intensity at high optical pumping.

Having determined that growth interruptions do offer some minor benefit to uniformity, but that they should be kept short to minimize desorption, a series of growths was conducted varying the amount of In deposited in each cycle and limiting the pause to 1s. The variation was conducted by keeping the total deposition fixed at 2.55 ML (with growth interruptions after 1.4 ML) and varying the number of cycles from one to fifteen. With the exception of the wavelength at 15 cycles, the wavelength, ground state FWHM, and energy level separation all remained essentially constant (variations are at the instrument resolution) with the number of cycles. However, the intensity showed significant changes (excluding the outlier at 10 cycles) with the PL intensity increasing up to 5 cycles and remaining unchanged at higher values for low pumping levels and dropping back off at 15 cycles for high pump intensity. The drop off in intensity at a high number of cycles corresponds to a small redshift in the peak

wavelength. Perhaps at the lower adatom density corresponding to 15 cycles, coarsening effects can play a role leading to fewer, larger QDs.

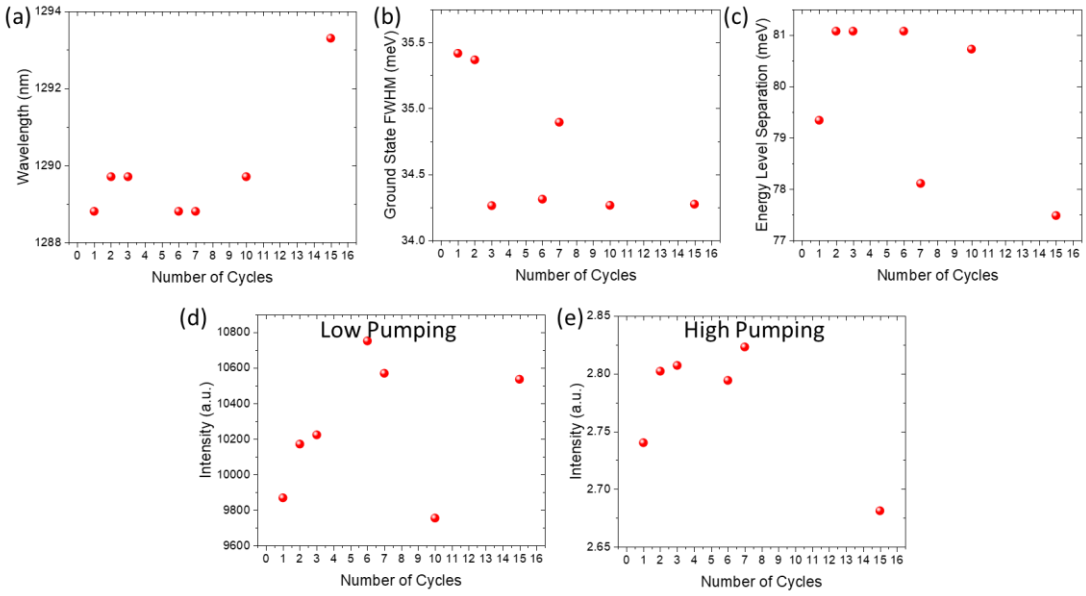

Figure 38. The variation of photoluminescence properties with the number of cycles of growth interruption during quantum dot deposition after nucleation is shown including (a) ground state peak wavelength, (b) ground state full-width at half-maximum (FWHM), (c) energy level separation between the ground state and first excited state, (d) the ground state peak intensity at low optical pumping, and (e) the ground state peak intensity at high optical pumping.

Overall, while the inclusion of growth interruptions provided some benefit to the PL FWHM and intensity, the results were much more modest than expected and less pronounced than what has been reported in literature[116]. The literature discrepancy could be due to differences of other growth conditions, most notably the growth rate, here held constant at 0.11 ML/s while 0.22 ML/s was used in Ref. [116].

Another point for growth interruption that may be considered is after deposition of the QDs is completed before capping begins[108]. Convertino *et al.* showed very strong dependence of the PL wavelength and FWHM on the interruption time for pauses up to 600s with narrow PL at 100-300s, but they grew in the regime of high temperature (530-545°C)

and high As overpressure (4-7×10^{-6} Torr, likely V/III >100) with a total deposition of 3.5 ML which may result in relaxed, defective dots. One series was grown to investigate this "ripening time", and the interruption time was varied from 40s to 80s. Unfortunately, the 50s and 80s growths had unstable temperature readings during the dot deposition, leaving only three data points; nevertheless, the results (Figure 39) show very little improvement in the FWHM with longer ripening time (Figure 39(b)), but the PL intensity at low and high pumping did improve (Figure 39(d-e)). Considering the previous results involving growth interruptions—done chronologically after this series on ripening time—the results of Figure 39 are not surprising. Given the temperature of 495°C, V/III ratio of 35, and growth rate of 0.11 ML/s, there doesn't appear to be enough of a kinetic restriction to uniform dot formation to significantly benefit dramatically from growth interruptions.

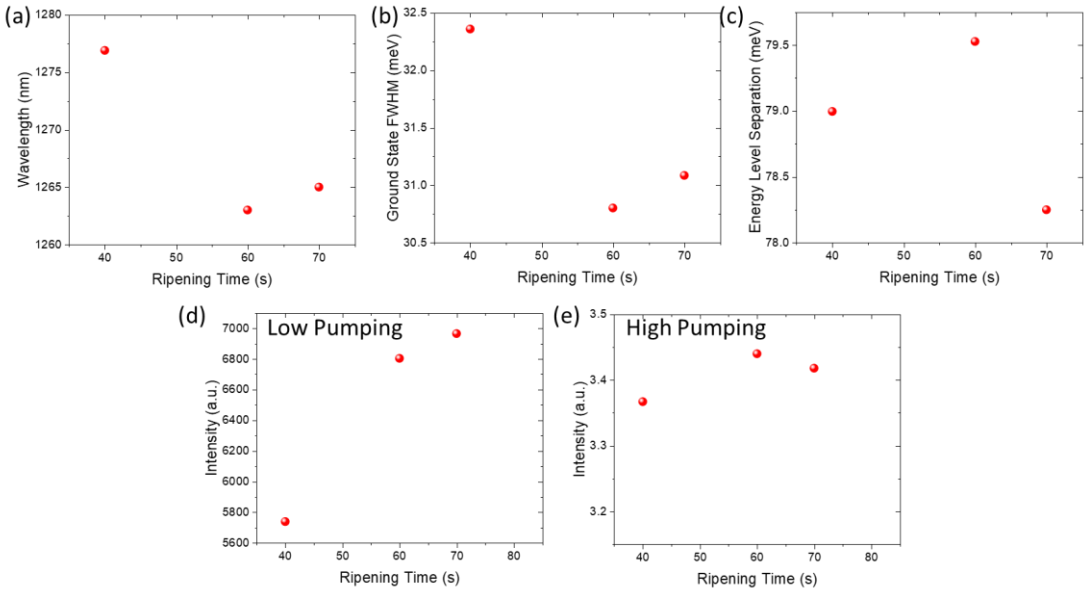

Figure 39. The variation of photoluminescence properties with ripening time after dot deposition is shown including (a) ground state peak wavelength, (b) ground state full-width at half-maximum (FWHM), (c) energy level separation between the ground state and first excited state, (d) the ground state peak intensity at low optical pumping, and (e) the ground state peak intensity at high optical pumping.

Further Considerations for Full Device Structures

The detailed growth conditions of the QDs themselves is not the only important growth parameter in making a QD based device. Two specific parameters that are critical to device performance are the spacer thicknesses between dot layers and the growth temperature of the top half of the device structure. If the spacers are not adequately thick, the strain fields of the buried QDs will influence the dots grown above leading to vertical alignment of QDs with increasing size in each subsequent layer. Such variations utilized for deliberately broad-band applications such as mode-locked lasers with excellent performance[52] but are undesirable for traditional laser structures where broadening increases threshold, increases the linewidth enhancement factor, and decreases gain and differential gain. The minimum spacer thickness depends on the dot density[133] but is generally 30-40 nm. The growth temperature of the top cladding is important because it determines the extent of In-Ga interdiffusion in the QDs. For adequate optical confinement and to minimize absorption loss from the highly doped top contact (generally p-type), the thickness of the top cladding is generally kept to ~1.5 μm of AlGaAs with 30-70% Al content. Typically, AlGaAs is grown at temperatures above 580°C and growth rates < 1 μm/h which means the QD layers experience a significant amount of time at high temperatures. Using MOCVD growth the temperatures are generally much higher, potentially as high as 700°C, due to the cracking temperatures of Al precursors. At these temperatures the QDs rapidly intermix with their surroundings leading to significant blue shifts of the peak emission, a dramatic reduction in PL intensity, and a broadening of the emission spectrum. The effect of the top cladding growth was simulated for a single layer QD PL sample by holding it at 580°C for one hour. The results shown in Figure 40 display an

extreme level of degradation in the luminescent properties. To avoid interdiffusion, the top cladding can be grown at a temperature <560°C leading to no observable PL degradation.

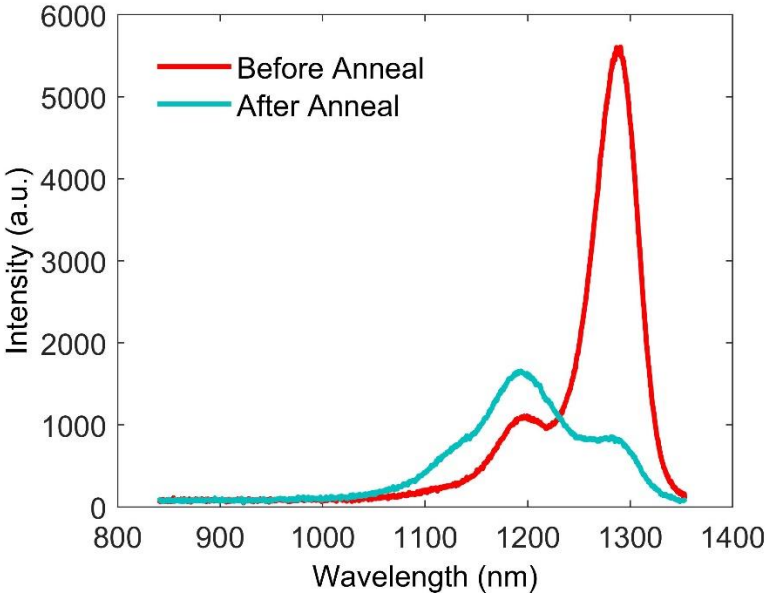

Figure 40. Photoluminescence spectra for a single buried quantum dot layer before and after annealing in the molecular beam epitaxy chamber for 1 h at 580°C to simulate the growth of the top laser cladding.

Final Results

Following the growth series presented above, an optimized set of QD growth conditions were established. Optimization prioritized a narrow size distribution above all else, but the PL intensity, energy level separation, and emission wavelength were all found to change favorably as the PL was narrowed. Starting growth conditions and the conditions after optimization are presented in Table 4. These conditions were used for the growth of all of the lasers presented in the remainder of this thesis. As described in previous chapters the improvement in dot homogeneity was found to significantly improve the dynamic performance of the lasers.

Table 4. Comparison of quantum dot growth conditions before and after optimization

Parameter	*Unoptimized Value*	*Optimized Value*
Substrate Temperature	510°C	495°C
Quantum Dot V/III	35	35
As Cracker Temperature	850°C	825°C
Total InAs Deposition	2.75 ML	2.55 ML
Ripening Time	10s	60s
InGaAs Composition	$In_{15}Ga_{85}As$	$In_{15}Ga_{85}As$
InGaAs Prelayer V/III	20	10
InGaAs Cap V/III	20	35
InGaAs Prelayer Thickness	2 nm	2 nm
InGaAs Cap Thickness	6 nm	5 nm
Punctuated Growth?	No	Yes (6 burst, 1 s pause)
Spacer Thickness	37.5 nm	37.5 nm
Top Cladding Growth Temperature	580°C	560°C
Characterization Results		
FWHM	34 meV	28 meV
Normalized PL Intensity	1.0	2.31 au
ΔE	78 meV	80 meV
Dot Density	4.5e10 cm^{-2}	6.2e10 cm^{-2}

While these results compare favorably with state-of-the-art measurements in literature[132], several parameters have not been explored and further iteration could be beneficial. Were time not a limiting factor, a proper factorial design of experiments could be conducted to fully map the dot growth parameter space, but given the coupled nature of temperature, V/III ratio, growth rate, the use of growth interruptions, and the choice of dimeric or tetrameric As, such a growth series would be impractical without an automated MBE system to perform continuous growths. One could suppose that such studies would be easily possible for commercial manufacturers of QD lasers, and given the fact that the PL results of Table 4 compare favorably with those of QD Laser, Inc., there may not be a large increase in performance to discover. In any case, the results presented above suggest that further iteration on the space of growth temperature and V/III ratio could be useful. I have also made no

attempts to vary the growth rate, which is a known parameter to strongly affect QD growth[111]. Another avenue for future investigation is to use more than one In or Ga cell to use different InGaAs compositions for the QD prelayer and capping layers, or to incorporate Al to increase the band offsets.

Chapter 5

Quantum Dot Laser Gain Characterization

Gain Characterization Methods

To understand the effect of material quality on laser performance, the gain characteristics, loss mechanisms, and injection efficiency must be investigated. The gain parameters and, to a significant extent, the internal loss and injection efficiency are intrinsic material parameters that can isolate the influence of device design and processing from growth and material quality. Processing can still have an influence through potential current leakage pathways, Schottky barriers, sidewall optical scattering, but nevertheless, the gain and loss characteristics are much more direct metrics of material quality than device properties such as laser threshold and output power.

The most common method for gain characterization is the cutback method [30] where lasers from the same epi material are cleaved to different cavity lengths, L, of known mirror reflectivity, $R = 0.3$, and the differential quantum efficiency, η_d, is measured and fit to extract the internal loss, $\langle \alpha_i \rangle$, and injection efficiency, η_i according to

$$\frac{1}{\eta_d} = \frac{\langle \alpha_i \rangle}{\eta_i \ln\left(\frac{1}{R}\right)} L + \frac{1}{\eta_i}. \quad (1)$$

Once the losses are known, the threshold modal gain can be plotted as a function of threshold current density to generate the gain curve. A logarithmic fit to the gain curve can then be used to obtain the transparency current density and gain coefficient, g_{0J}. This method is commonly utilized in literature, but has several sources of error. The necessary use of multiple laser cavities from different spatial regions of the epi material or progressive cleaving of a single cavity to shorter lengths leads to sensitivity to spatial nonuniformities that may be present (e.g. oval defects or locally bad metal contacts). Furthermore, cleaved facets are often imperfect leading to uncertainty in the mirror reflectivity, and the internal loss could easily depend on carrier density and wavelength which would violate the necessary assumption that internal loss is constant as cavity length decreases.

A more rigorous technique for gain characterization is Andrekson's method [29]. This method combines a direct measurement of the transparency current with gain extraction from the amplified spontaneous emission spectra to yield accurate measurements of the gain, internal loss, transparency, and injection efficiency as a function of wavelength and current up to threshold for a single device. By repeating the study on multiple devices statistical data on yield and performance could be obtained that cannot be easily extracted from the cutback method. Additionally, having the data as a function of wavelength aids in the design of single mode and/or tunable lasers and broadband amplifiers. In sections below the cutback method and Andrekson's method will be compared using the same batch of p-modulation doped quantum dot lasers to show the discrepancies between methods and highlight new physical insights provided by Andrekson's method.

Gain from Amplified Spontaneous Emission

Andrekson's method extracts gain from the Fabry-Perot ripples of the amplified spontaneous emission spectrum using the mode-sum method [59]. Inside a Fabry-Perot laser cavity, the below-threshold amplified spontaneous emission (ASE) spectrum can be described by[134]:

$$A(\lambda) = \frac{B(1+r_1 r_2 e^{(\Gamma G-\alpha_{\text{int}})L})(1-r_1 r_2)}{(1+r_1 r_2 e^{(\Gamma G-\alpha_{\text{int}})L})^2 - 4 r_1 r_2 e^{(\Gamma G-\alpha_{\text{int}})L} \cdot \sin^2(\frac{2\pi n L}{\lambda})}, \qquad (1)$$

where B is the proportion of the total amount of ASE coupled into the cavity mode; r_1 and r_2 are the reflectivity of the mirror; Γ is the confinement factor of the active region; G is the material gain of the active medium; α_{int} is the internal loss; L is the cavity length; n is the effective index of the waveguide; and λ is the wavelength of spontaneous emission. Based on Eq. (1), the net modal gain (g_{net}) can be calculated based on[59]:

$$g_{\text{net}} = \Gamma G - (\alpha_{\text{int}} + \alpha_{\text{m}}) = \frac{1}{L} \ln \frac{y(\lambda)-1}{y(\lambda)+1}, \quad (2)$$

where $\alpha_{\text{m}} = \frac{1}{L} \ln \frac{1}{r_1 r_2}$ is the mirror loss of the laser cavity, $y(\lambda)$ is the ratio of the integral across one free spectral range (FSR) of the ASE spectrum over the cavity mode minimum[134]:

$$y(\lambda) = \frac{\int_{\lambda_1}^{\lambda_2} A(\lambda')\mathrm{d}\lambda'}{A_{min}(\lambda) \cdot (\lambda_2 - \lambda_1)}. \quad (3)$$

In practice, gain measurements are conducted by coupling light out of the laser cavity through a single mode lensed fiber to an optical spectrum analyzer (OSA) with a resolution of 20 pm. The use of single mode lensed fiber and narrow wavelength resolution are critical to obtaining reliable data. Angled, straight, and multi-mode fibers were also tested, but reflections from the fiber facet were found to destabilize the ASE ripples leading to inaccurate

data and excitation of higher order modes in the cavity. Minimizing the presence of higher order orthogonal modes in this technique is critical as modes that do not interfere will superimpose in the ASE ripples to give an erroneously high baseline on the stronger mode (see Figure 41) leading to underestimated gain due to the increased denominator in Eq. (3).

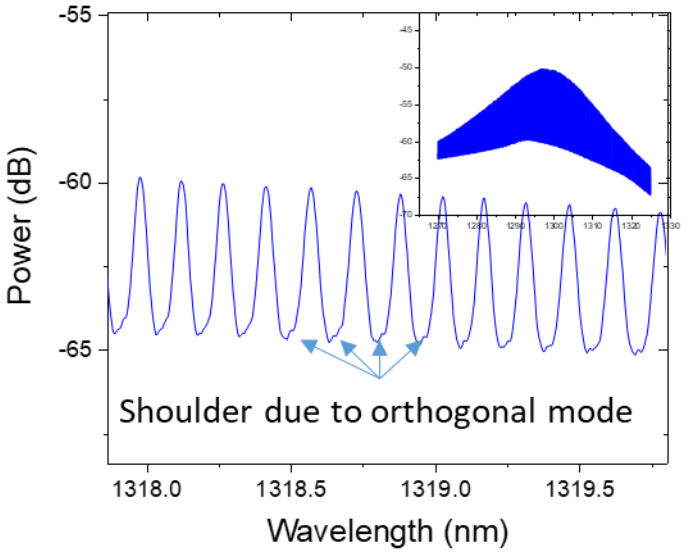

Figure 41. Example amplified spontaneous emission spectrum showing emission in two orthogonal modes. The mode with less intensity has resulted in shoulder like features at the bottom of the ripples preventing the full amplitude of the emission from being measured resulting in an underestimate of the gain. The inset shows the full amplified spontaneous emission spectrum.

Example ASE measurement results for a 3.5 × 1341 μm^2 laser with a uid active region at 10.5 mA are displayed in Figure 42(a). The same measurement was repeated by varying the bias current from 3.5 mA to 14 mA. Next, the gain spectrum was calculated using Eq. (2) and (3). The results are shown in the Figure 42(c) inset. At threshold, the device lased near the gain maximum of 1298.6 nm. The gain versus current relationship for this wavelength is plotted in Figure 42(c). The extracted data points show a gradual decrease in the differential gain as the bias increases, and closely matches the typical logarithmic gain-current relationship of semiconductor quantum well lasers.

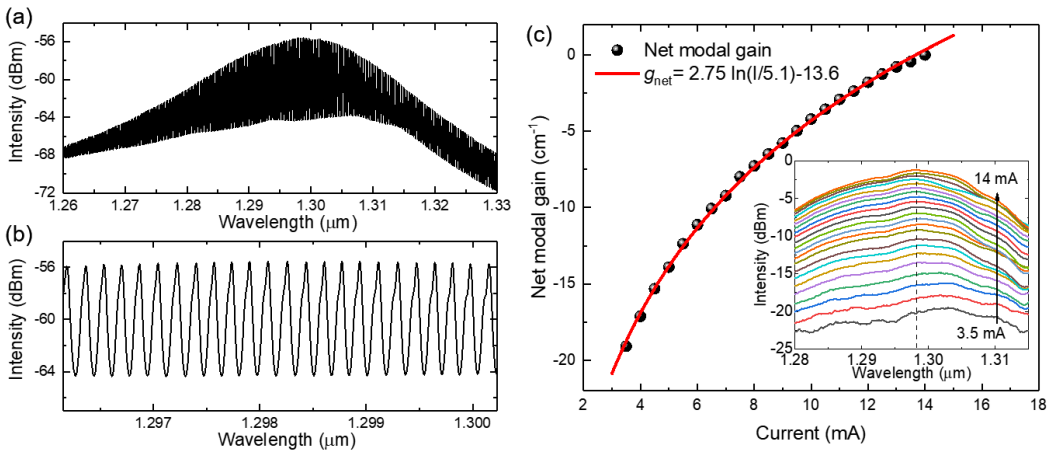

Figure 42. Net modal gain measurement and calculation. (a) ASE spectrum of a 3.5 × 1341 μm^2 laser. (b) a close-up view of the longitudinal modes in the ASE spectrum. (c) Calculated net modal gain at 1298.6 nm of the device. The inset shows the net modal gain spectrum of the device, where the dotted line marks the wavelength of the gain spectrum peak at the threshold. From [135]

Since the gain-current relationship has been determined to be logarithmic, the net modal gain can be phenomenologically described as:

$$g_{\text{net}} = g_0 \ln \frac{I}{I_{\text{tr}}} - g_{\text{th}} \qquad (4)$$

where g_0 is the gain parameter, I_{tr} is the device transparency current, and $g_{\text{th}} = \alpha_{\text{int}} + \alpha_{\text{m}}$ is the threshold modal gain. It is clear from Eq. (4) that when the current reaches I_{tr}, the absolute value of the net modal gain equals the threshold modal gain (i.e. total optical loss) of the laser. Therefore, by combining a transparency measurement with the mode-sum method, the gain and loss characteristics of the laser can be separated, and accurate optical loss can be reliably extracted.

Transparency Measurement

When a gain medium reaches transparency, the active material changes from an absorber to an amplifier, which implies that the quasi-Fermi level shift in the device due to injected photons will change polarity and reach a minimum in amplitude at the transparency point [29].

From these principles a measurement scheme can be developed based on measuring photon induced changes in voltage for a bias source on the gain medium in constant current mode. Such a measurement setup is shown in Figure 43(a). When measuring the transparency, a narrow linewidth, externally modulated tunable laser source (TLS) was used to optically probe the device under test (DUT). The alternating current (AC) signal from the electrode of the laser was detected by a lock-in amplifier. It is worth mentioning that the transparency current was uniquely defined by the wavelength of the probing light[29, 136]. Therefore, by tuning the TLS, the transparency current can be obtained across the full gain spectrum. The transparency measurement results for the same laser used for ASE measurement in Figure 42 are shown in Figure 43(b). Based on the previous analysis, the laser unambiguously reaches transparency at 5.1 mA.

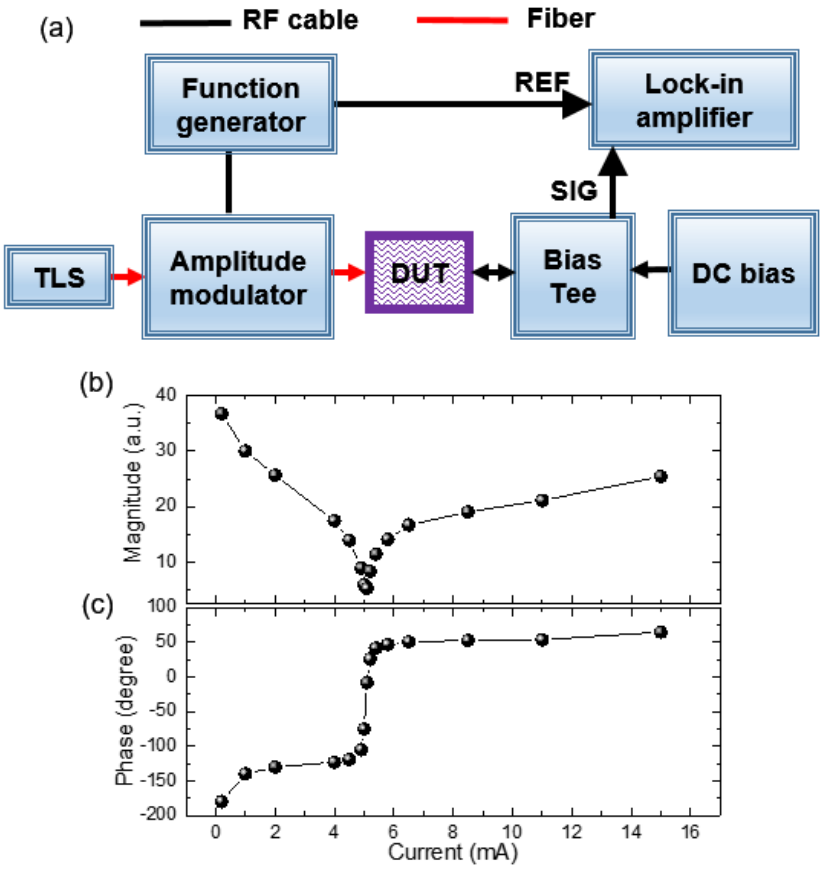

Figure 43. (a) Schematic representation of the transparency current measurement setup. (b) The magnitude and phase of the AC signal detected by the lock-in amplifier for the 3.5 × 1341 μm^2 laser when probed at 1298.6 nm. From [135]

Knowing the transparency current, the threshold gain of this laser is determined from Figure 42(c) to be 13.6 cm^{-1}. The gain parameter g_0 is extracted to be 13.8 cm^{-1} (2.75 cm^{-1} per QD layer) by Eq. (4). The coefficient of determination (R^2) is 99.9 %, reaffirming the accuracy of the model. Assuming a commonly accepted value of 0.32 for the power reflectivity of the semiconductor-air interface after cleaving, the mirror loss for this laser (length 1341 μm) is 8.5 cm^{-1}. Thus, the internal loss is calculated to be 5.1 cm^{-1}. Finally, the injection efficiency (η_i) can be determined from the slope efficiency (SE), which is expressed as:

$$SE = \eta_i \frac{h\nu}{q} \frac{\alpha_m}{g_{th}} \qquad (5)$$

where h is the Planck's constant, v is the lasing frequency, q is the electron charge and η_i is the injection efficiency. For the same laser used in the gain and transparency measurement, η_i is calculated to be 74% for a slope efficiency of 0.442 W/A.

Cutback vs. Andrekson's Method

To illustrate the points made earlier in this chapter, a direct comparison was made between the cutback method and Andrekson's method for a set of p-modulation doped quantum dot lasers on silicon. The methods employed were not the true cutback method in the sense that one device was not progressively cleaved to shorter lengths during measurement, but, instead, lasers from the same epi with identical width and different length were measured. The same devices were used for Andrekson's method; although, only one subset was measured consisting of 3.5×1500 μm^2 cavities.

The individual fitting curves for the inverse differential quantum efficiency, $1/\eta_d$, and the coefficient of determination for their linear fits are presented in Figure 44 for each of the ridge widths analyzed. Most of the fitted data was reasonably linear as expected for the cutback method. The device measurements were chosen to match the best performance available at each cavity length and ridge width combination.

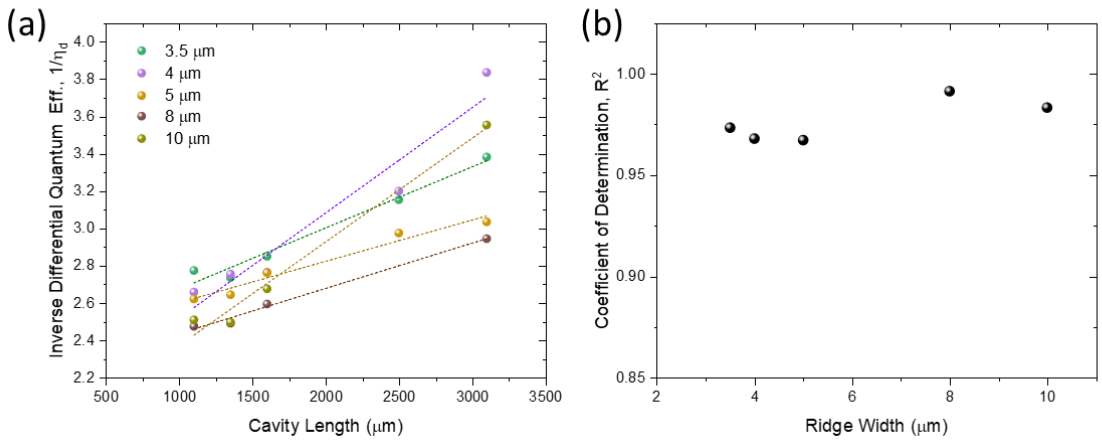

Figure 44. (a) Inverse differential quantum efficiency vs. cavity length with linear fits. (b) The coefficient of determination for each of the linear fits in (a).

The slopes and intercepts of the data in Figure 44(a) are highly varied which results in different values of the internal optical loss, $\langle \alpha_i \rangle$, and injection efficiency, η_i. Both parameters vary with no apparent trends with regard to ridge width. The injection efficiencies range from 43-55%, which could be naively considered reasonable for a laser on silicon, but other devices using Andrekson's method have shown similar laser structures having no p-doping in the active region can exhibit injection efficiencies as high as 87% [135]. These low injection efficiencies also seem improbable given the device lifetime achievements to be presented in Chapter 6, which show minimal nonradiative recombination enhanced dislocation climb. Meanwhile the internal optical loss shows a range of relatively low values from 1.1-3.7 cm^{-1}. Such numbers would be considered to be very good and imply that the optical loss has not increased with the addition of p-doping to the quantum dots in these lasers relative to our previous results [135]. Overall the numbers are similar to previous reports of p-doped QD lasers on GaAs that were extracted via the cutback method [137].

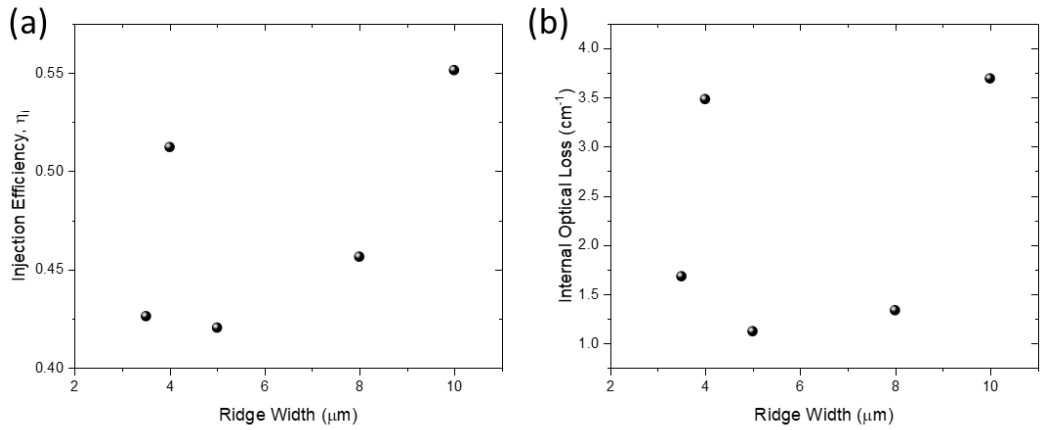

Figure 45. (a) Injection efficiency and (b) internal optical loss extracted via the cutback method for lasers of various ridge widths.

From the extracted internal loss, the threshold modal gain of each device can be obtained, and plotted as a function of the threshold current to generate gain curves. The gain curve can then be fit with the assumed logarithmic function, and the modal gain coefficient and transparency current density can be extracted. The transparency current comes from the y-intercept of the fit, and the gain coefficient is calculated according to

$$\Gamma g_{0J} = \Gamma g_{th} \exp\left(\frac{J_{th}}{J_{tr}}\right) \tag{2}$$

where Γg_{th} is the threshold modal gain. The results are plotted in Figure 46. The gain coefficients were found to vary from 12.2-14.2 cm^{-1}. The transparency current density varies significantly from 136-179 A/cm^2 with a clearly decreasing trend with wider ridge widths. Considering that the transparency is only affected by the injection efficiency—due to these currents being as-generated from the power supply and not the internal current into the quantum dots—the results seem to contradict Figure 45(a) and suggest significant sidewall recombination even in ridges several microns wide. Since quantum dots inhibit in-plane carrier diffusion, they are known to be particularly insensitive to sidewall recombination.

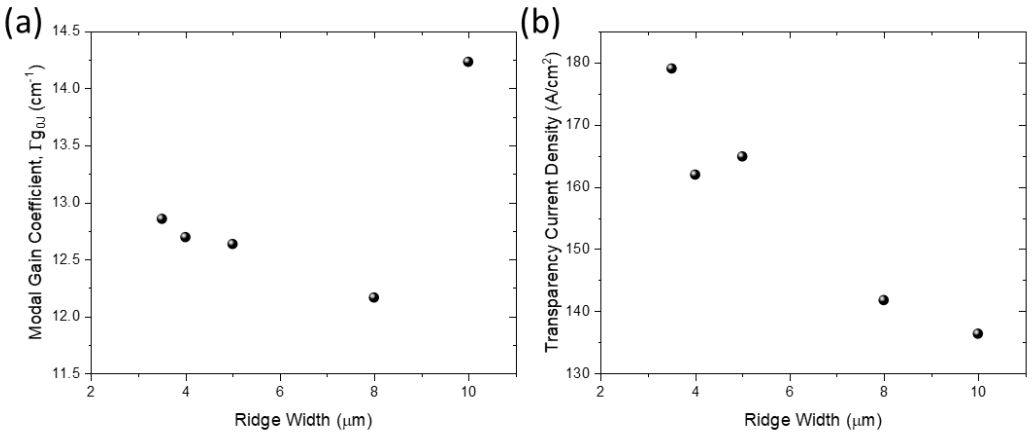

Figure 46. (a) Modal gain coefficient with respect to current density and (b) the transparency current density are plotted vs. ridge width for laser cavities analyzed using the cutback method.

From the results above, the 3.5×1500 μm^2 ridge width was selected for analysis with Andrekson's method. For clear comparison, only the parameters at the lasing wavelength are presented, but the full spectral data was obtained and is presented in detail in Chapter 6 to describe the effects of p-modulation doping in the quantum dot active region. The extracted parameters are given in Table 5. The injection efficiency has been omitted because the physics associated with p-doped QD lasers complicates its extraction as is detailed in Chapter 6.

Table 5. Summary of gain parameters extracted via cutback and Andrekson's method for 3.5×1500 μm^2 laser analyzed above via the cutback method.

Method of Extraction	Internal Optical Loss	Modal Gain Coefficient	Transparency Current Density
Cutback	1.68 cm^{-1}	12.9 cm^{-1}	179 A/cm^2
Andrekson's Method	38.7 cm^{-1}	25.2 cm^{-1}	68.3 A/cm^2

Results extracted from the two methods show stark differences. Andrekson's method reveals an optical loss that is more than an order of magnitude larger than what cutback gives, the modal gain is a factor of two larger, and the transparency current density is a factor three

lower. These differences have substantial implications for device design and should be kept in mind when comparing to results in literature. The measurements from Andrekson's method have been found to accurately predict device thresholds for varied cavity lengths and reflectivity coatings.

Summary

Two methods of gain characterization were presented and used to analyze quantum dot lasers on silicon: the cutback method and Andrekson's method. The cutback method is the most prevalent throughout literature but does not provide as much detail as Andrekson's method, and the cutback method is found to yield dramatically different results when compared to Andrekson's method on the same set of devices. The results from Andrekson's method yield gain and loss parameters that better predict laser performance. This distinction is important to note when comparing the gain and transparency analyses in Ch. 6 with those in literature and suggests that the cutback method may not be appropriate for quantum dot lasers.

Chapter 6

Epitaxial III-V Lasers on Silicon

Results on On-Axis Silicon

The first demonstration of room temperature, continuous wave operation of an electrically injected laser on on-axis (001) silicon was simultaneously achieved using GaP/Si [138] and GaAs-on-v-groove-silicon (GoVS) templates [139]. At the time, the GoVS template provided slightly lower dislocation density, and the laser was grown at improved QD growth conditions leading to slightly better performance in the static laser characteristics. Both templates are MOCVD grown and discussed in more detail in previous chapters. Since my laser efforts began with the GoVS template, I will emphasize its results as the first generation devices, but later lifetime results will reference back to the results reported by Liu et al. as the first generation tested to be consistent with the following results that were developed on GaP/Si templates. Shortly thereafter, results were also achieved on planar on-axis Si templates by Chen et al. [71] but the performance lagged that achieved with GaP/Si and GoVS. Over time, the performance of lasers on GaP/Si and GoVS rapidly improved demonstrating the best

performance among all lasers on silicon in many parameters. The progression of these devices as the material improved is presented in the following sections.

First Generation: GaAs on v-groove Si

An n-type on-axis (001) silicon substrates was used for the lasers. The silicon substrates were prepared according to the methods presented in [27]. The silicon was initially patterned with 90 nm wide stripes of SiO_2 with 40 nm spacing using standard dry etching techniques. After patterning, the substrates were subjected to an RCA-1 clean and a brief 1% HF dip to remove the native oxide before immediately etching the v-grooves. The v-grooves were etched using a 45% KOH solution at 70°C for 15 s. The KOH solution etches anisotropically with a high selectivity for the {111} crystal planes.

Growth of the GaAs-on-v-groove Si template was performed in a low-pressure (100 mbar) metal-organic chemical deposition (MOCVD) system with a horizontal reactor (AIXTRON 200/4). Triethylgallium (TEGa), Trimethylgallium (TMGa), and Trimethylaluminum (TMAl) were used as group III precursors, while Tertiarybutylarsine (TBA) was used as the Group V precursor. The patterned Si substrate was thermally cleaned in the MOCVD chamber at 800 °C for 15 min in an H_2 ambient. Selective area heteroepitaxy of GaAs nanowires was conducted with parameters detailed in [25]. After removing the SiO_2 stripes using buffered oxide etch (BOE), the GaAs nanowires were coalesced into a 1 µm continuous thin film at 600 °C with stepped growth rates from 8 nm/min to 32 nm/min. This is followed by ten periods of an $Al_{0.3}Ga_{0.7}As$/GaAs (10 nm/ 8 nm) superlattice and finally 800 nm of GaAs grown at 700 °C. The GaAs growth was performed at V/III ratios ranging from 5 to 20. The insertion of the superlattice greatly smoothened the surface of the GoVS template. An AFM scan across an area of 10 × 10 μm^2 revealed a root-mean-square roughness of 0.9 nm. Analysis from XRD

x-rocking curves yielded a full-width-at-half-maximum value of 140 arcsec, indicating the good crystalline quality.

Molecular beam epitaxy (MBE) was used to grow the laser structure. Prior to regrowth, the samples were cleaned with solvents and a dilute HF dip. The samples were grown using a Veeco Gen II MBE system. Growth was initiated with the n-contact layer and no additional buffer layers. The epi structure consisted of five InAs quantum dot layers in $In_{0.15}Ga_{0.85}As$ quantum wells clad in a GaAs/AlGaAs graded-index separate-confinement heterostructure for optical and electrical confinement. The active dot-in-a-well layers were grown at 495°C under As_4 overpressure with V/III ratios of 10, 35, and 35 for the 2 nm InGaAs prelayer, InAs quantum dots, and 5 nm InGaAs cap, respectively. The nominal InAs thickness was 2.75 ML. Following the deposition of each active layer, a 2.5 nm GaAs layer was deposited at 495°C, and the substrate temperature was increased to 580°C for a five minute anneal to evaporate oversized defective dots and truncate the overall size distribution for increased uniformity. Cladding and contact layers were grown at 580°C. A full schematic of the epitaxial structure is shown in Figure 47.

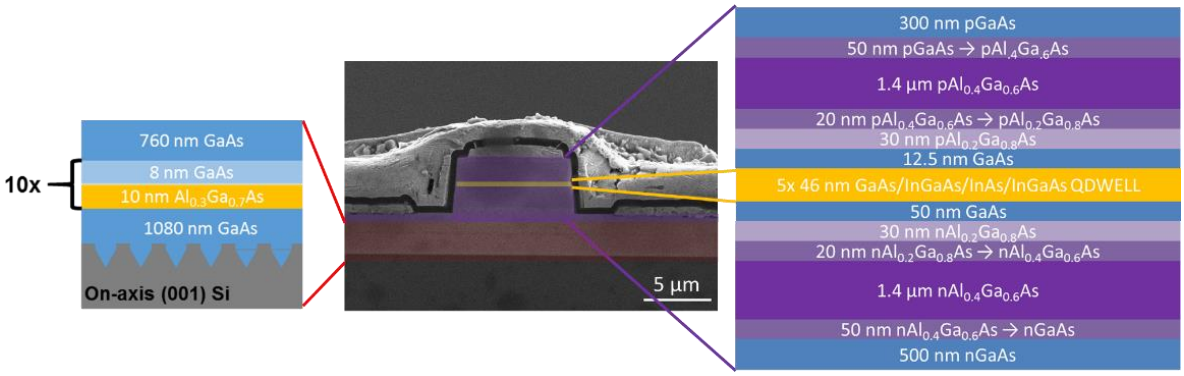

Figure 47. Scanning electron microscope image of a polished facet with false color indicating the various sections of the device. From [139].

The laser material was processed into deeply-etched ridge lasers with ridges running perpendicular to the v-grooves, using standard dry etching and deposition techniques. Devices were fabricated with cavity lengths of 800, 1000, and 1200 µm and ridge widths ranging from 4 to 12 µm. Pd/Ti/Pd/Au and Pd/Ge/Au metallizations were used for the p- and n-contacts respectively. The n-contact was probed from laterally displaced pads while the p-contact was injected from the top of the ridge as depicted in Figure 48. Laser facets were formed by dicing and polishing. A subset of the devices later had a 95% high reflectivity coating applied to one facet for high temperature measurement. A scanning electron microscope image of the cleaved cross-section and a top-down optical micrograph of the finished devices are shown in Figure 47 and Figure 48, respectively.

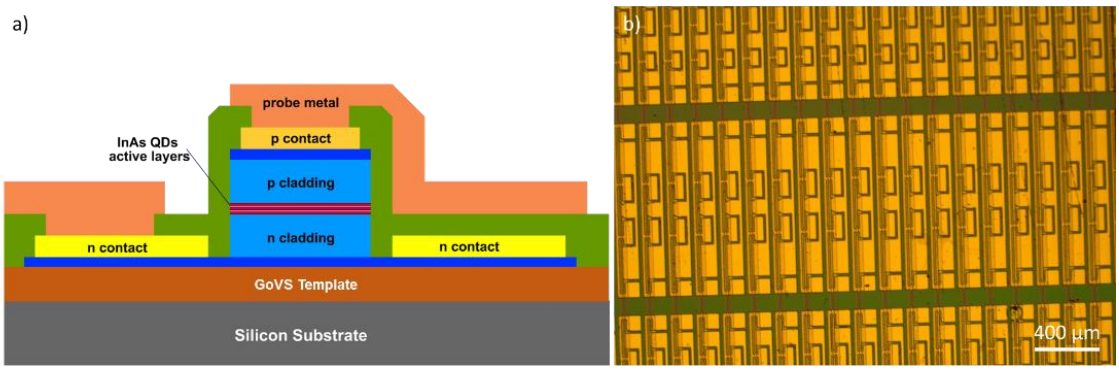

Figure 48. (a) A schematic cross-section of the fabricated devices. (b) Top-down optical micrograph of the fabricated ridge lasers before dicing. From [139].

The as-grown GoVS template material quality was assessed through electron channeling contrast imaging (ECCI). This technique uses a scanning electron microscope in backscatter mode at a given diffraction condition to image deviations from the Bragg condition caused by strain fields such as those around dislocations and local phase shifts of the electron wave caused by the non-integer lattice translations across stacking faults. ECCI allows for rapid

acquisition of large area scans without any material preparation making it advantageous over transmission electron microscopy for obtaining accurate defect densities in low defect density materials. Figure 49 displays a scan of a GoVS template comparable to the design used for laser regrowth. In the image, the lines and pinpoints of bright contrast respectively indicate stacking faults and threading dislocations intersecting the surface. By counting the defects, densities of $7x10^7$ cm^{-2} and $2x10^7$ cm^{-2} were calculated for threading dislocations and stacking faults respectively. The threading dislocation density compares favorably with our previous work on miscut GaAs/Ge/Si in [2]. It is reasonable to expect this defect density to be comparable to if slightly larger than what would be measured in the laser's active layers as there are no additional strained layers between the as-grown GoVS template and the quantum dot layers.

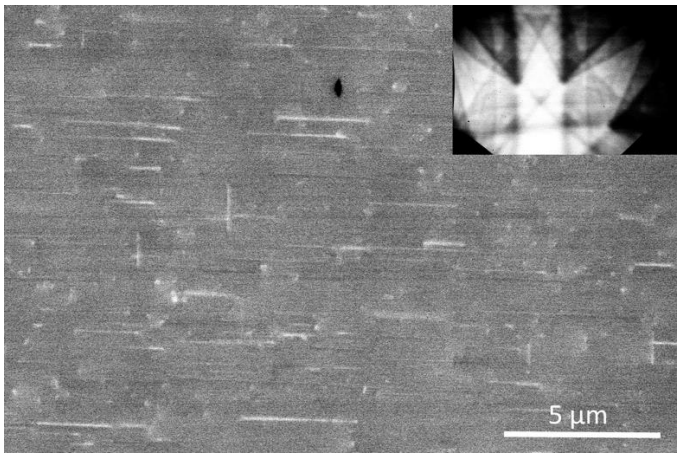

Figure 49. Plan-view electron channeling contrast image (ECCI) of a GaAs-on-v-groove-Si template. The bright dashes are attributed to stacking faults while the pinpoints represent threading dislocations intersecting the sample surface. Counting reveals a threading dislocation density of $7x10^7$ cm^{-2} and a stacking fault density of $2x10^7$ cm^{-2}. (Inset) The electron channeling pattern corresponding to the $(\bar{2}20)$ and $(0\bar{2}0)$ imaging condition used. From [139].

The optical quality of the quantum dots was assessed through the growth of photoluminescence (PL) structures on native GaAs substrates containing one embedded layer of quantum dots and one surface layer for atomic force microscopy (AFM) measurement of

the dot density. The dots in the PL structures were grown with identical conditions to those used in the laser. The AFM and photoluminescence results are shown in Figure 50. From the AFM scan a dot density of $6x10^{10}$ cm^{-2} can be estimated while the PL shows strong luminescence at 1277 nm with a full-width at half-maximum of 36 meV.

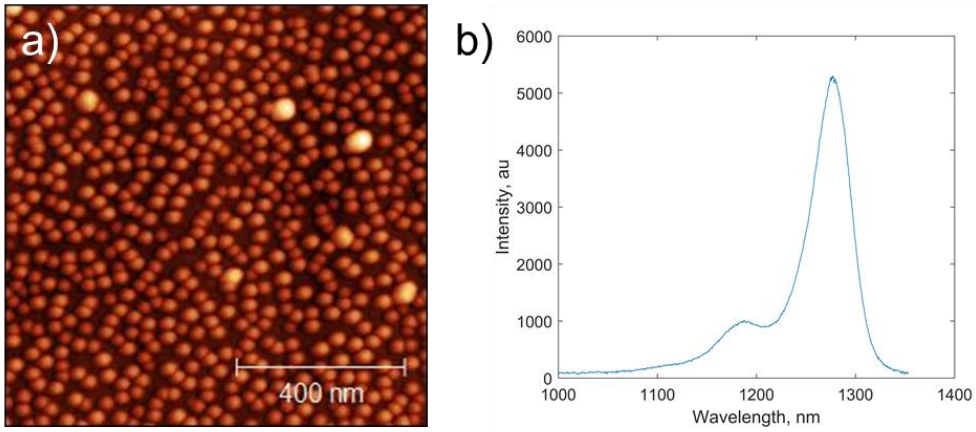

Figure 50. (a) Atomic force microscope image of a 1x1 μm^2 region of quantum dots showing a total dot density of 6x10^{10} cm^{-2}. (b) A photoluminescence spectrum for the quantum dots grown on a native GaAs substrate with conditions identical to those used for the laser showing a peak wavelength of 1277 nm and full-width at half-maximum of 36 meV. From [139].

Approximately 200 ridge lasers were fabricated and tested at room temperature in CW operation. Figure 51(a) displays representative single-side light output and voltage versus injection current curves for a 9x1200 μm^2 device showing a clear threshold at 81 mA and single-side output power over 50 mW. The I-V curve indicates a relatively low series resistance of 2-3 Ω. Figure 51(b) shows the lasing spectrum of the same device indicating ground state lasing initially at 1250 nm and shifting to 1257 and 1270 nm as it picks up supermodulation that is attributed to lasing from higher order transverse modes and is consistent with previous observations. Higher resolution scans show side lobes on the Fabry-Perot ripples further adding support to simultaneous lasing from orthogonal transverse modes. Excited state lasing is not observed prior to the thermal rollover point at 700 mA.

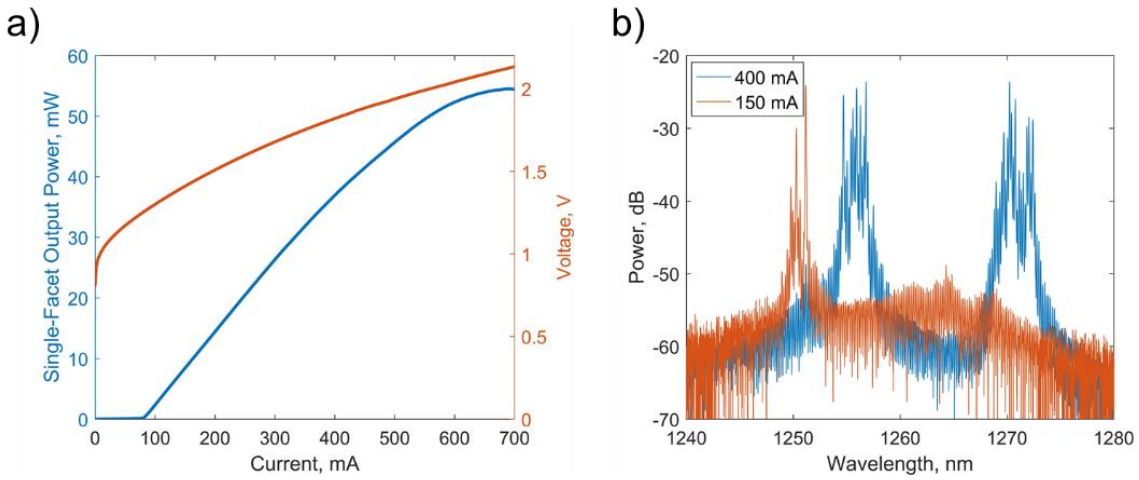

Figure 51(a) Continuous wave light output and voltage as a function of the injection current of a 9x1200 µm2 device showing a threshold of 81 mA and maximum single-side output power of 55 mW. (b) The above threshold optical spectrum showing ground state lasing near 1250 nm which transitions to dual lasing attributed to multimode lasing from higher order transverse modes. Excited state lasing was not observed for the given injection levels. From [139].

A full depiction of the measurement data is presented in Figure 52. Figure 52(a) shows the absolute thresholds of 183 lasers with polished facets broken down by the ridge width and cavity length. There is a clear trend of higher thresholds with wider ridges as would be expected, but there is an unexpected dip for the wider ridges at 10 and 11 µm. This discrepancy is attributed to facet damage during polishing which is potentially less severe for the lower aspect ratio ridges. Figure 52(b) shows a histogram of the threshold current density broken down by cavity length showing a minimum value of 498 A/cm^2. Similar devices on miscut Ge/Si substrates showed thresholds current densities down to 200 A/cm^2 [84] indicating room for improvement through further optimization of the GoVS template design and growth conditions. The high threshold tail of the distributions is attributed to the yield of mechanical facet polishing. Figure 52(c) and 7(d) show the light output characteristics of the lasers through the maximum ground state output power and the differential quantum efficiency (DQE)—

calculated using the central wavelength of 1260 nm from Figure 50(b) and assuming equal output from both facets. The assumption of equal output could be violated if facet damage during polishing is not similar for both facets. In this case device output power and DQE could be larger as-measured due to only collecting light output from one facet. Devices of all sizes routinely put out a few tens of milliwatts of output power with the maximum single-side output power of 84 mW being achieved by a 10x1200 μm^2 ridge. The threshold current of this device was 73 mA (607 A/cm^2) which is comparable to other ridges of the same size indicating that the high output power is likely not erroneous due to facet damage. Most of the measured values for the DQE fall within the range of 0.15-0.30 which is similar to values obtained in our previous devices on miscut Ge/Si [84] and is roughly half of the value of 0.50 that we have obtained on cleaved broad area lasers on native GaAs substrates.

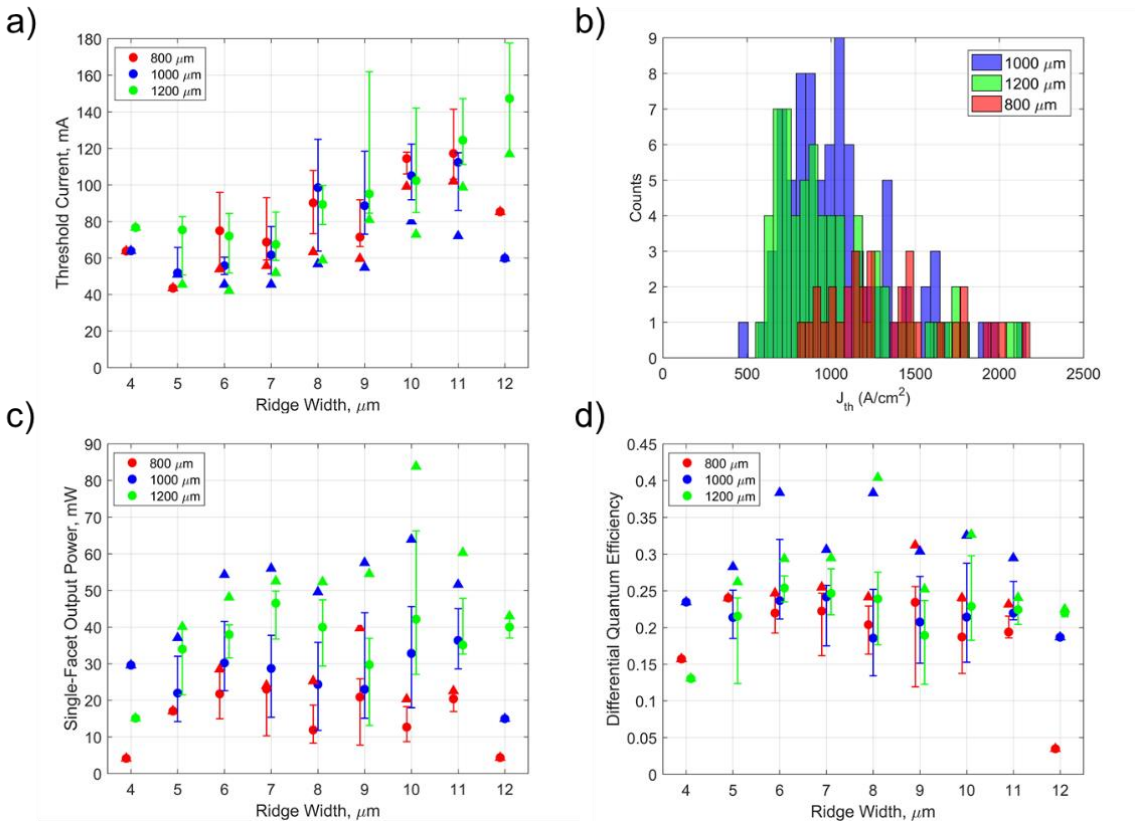

Figure 52. The aggregation of laser performance figures of merit is presented. For clarity data from different cavity lengths has been shifted in the scatter plots to the left or right about a given ridge width. Error bars indicate the interquartile range of device performance, circular data points indicate the median performance, and triangles designate the best measurement for each cavity size. (a) Threshold current for all lasers of varying ridge width and length is plotted. (b) Threshold current density is plotted for all devices as a histogram showing peaked distribution around 700-1000 A/cm^2 and a minimum value of 498 A/cm^2. (c) The single-side peak output power (ground state lasing only) is plotted for according to geometry for all devices with a peak value of 84 mW. (d) The differential quantum efficiency is plotted for all devices calculated using the central wavelength of 1260 nm from Figure 50(b) with a maximum value of 40%. From [139].

A subset of the previous devices was coated on one facet with a 95% reflectivity coating using Ta_2O_5/SiO_2 quarter wavelength distributed Bragg reflectors. Unfortunately, most of the devices were damaged during preparation for the coating deposition. From the devices that survived, a minimum threshold current of 36 mA was achieved with a 6x1200 μm^2 ridge.

Realistic datacenter environments operate at elevated temperatures, so prospective laser technologies must be able to function in these environments under CW operation with

minimal cooling. To test the high temperature performance of our devices, we placed an 8x1200 μm^2 ridge with one HR coated facet on a heated stage and measured the LI curves at elevated temperatures. The room temperature threshold current and maximum output power for this device were 40 mA and 93 mW respectively. The results are plotted in Figure 53. A clear threshold is observed in each measurement over the temperature range from 20-80°C. This result matches that of our first generation lasers on GaP/Si templates [138] for ground state lasing (note that the 90°C result was from the excited state) despite the reduced number of active layers (five versus seven) and lack of modulation p-doping in the current structure.

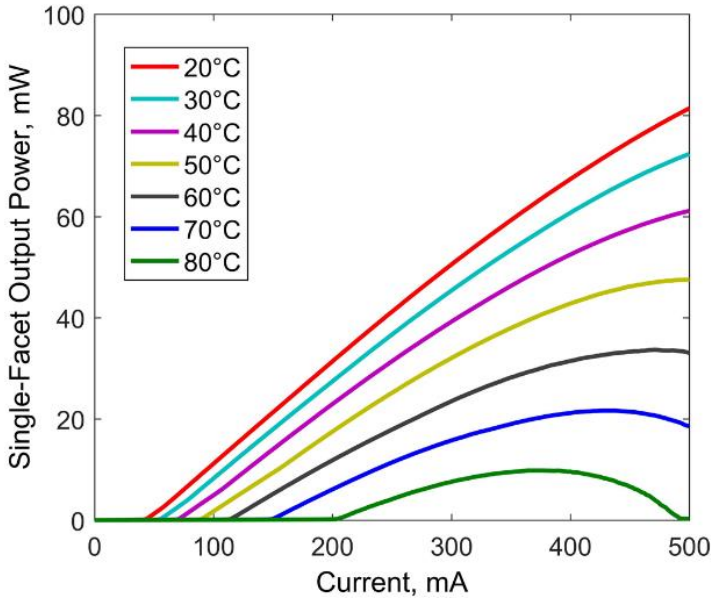

Figure 53. Continuous wave light output power as a function of injection current for a 8x1200 μm^2 device with one polished facet and one 95% high reflection coated facet at temperatures from 20-80°C. From [139].

Second Generation: Lasers on GaP/Si with Reduced Defect Density & Improved Quantum Dots

Following the laser results on GoVS substrates which had a dislocation density of 7×10^7 cm^{-2} and stacking fault density of 2×10^7 cm^{-2}, the epitaxial buffer on GaP/Si was improved to have an identical dislocation density with no stacking faults. Stacking faults were only ever observed in the GoVS templates due to the unique relaxation mechanism of the growth mode[25]. In later iterations such problems were solved making the two templates, GoVS and GaP/Si, essentially interchangeable depending on dislocation density. These lasers also had more optimized QD active regions than previous results on GaP/Si with a narrowing of the FWHM from 54 meV to 30 meV on Si (41 meV to 30 meV on GaAs), an increase in the energy level separation from 70 meV to 80 meV, and brighter PL intensity. The net result of improved QD PL and lower defect density led to several, albeit short-lived, world records in laser performance.

The epitaxial laser structure was grown on a commercially available GaP/Si (001) template purchased from $NAsP_{III/V}$ GmbH. The as-received template consisted of a 775 μm thick (001) on-axis p-doped Si substrate, with 200 nm thick n-doped Si homo-epitaxial buffer and a subsequent 45 nm thick n-doped GaP layer, all grown by metalorganic chemical vapor deposition (MOCVD). On this template a GaAs buffer and graded-index separate-confinement heterostructure were grown by molecular beam epitaxy. The layer stack is shown in Figure 54(a). The active region consisted of seven layers of p-modulation doped InAs quantum dots (grown at 495°C and 0.11 ML/s) in $In_{.15}Ga_{.85}As$ quantum wells. Identical epitaxial structures were grown on GaAs substrates for a direct comparison of laser performance.

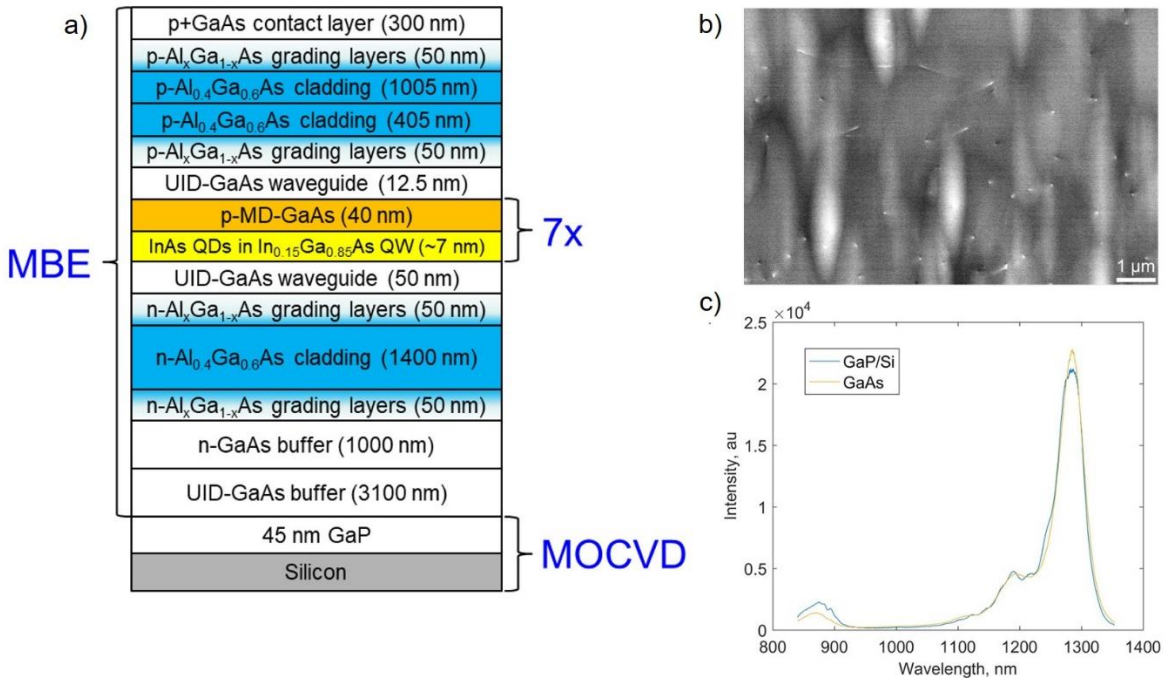

Figure 54. (a) Schematic of the laser structure. (b) Electron channeling contrast image of the uid-GaAs buffer surface. Pinpoints indicate threading dislocations. (c) Photoluminescence of as-grown laser material on GaAs and Si substrates. From [140].

Electron channeling contrast imaging (ECCI) was used to image the dislocation density of the material stack after the MBE buffer but before laser growth (Figure 54(b)) revealing a dislocation density of ~7 × 10^7 cm^{-2}. Photoluminescence measurements taken on the as-grown laser epi on Si and GaAs are shown in Figure 54(c) revealing a relative intensity of 93% for the laser on Si relative to GaAs and nearly identical peak wavelength (1286 nm) and full-width at half-maximum (34 meV) of the ground state emission.

The material was processed into deeply etched lasers with varying stripe widths using standard dry etching and metallization techniques. The lasers utilized a Pd/Ti/Pd/Au p-contact on top of the etched mesa and Pd/Ge/Au n-contact metal deposited on the exposed n-GaAs layers adjacent to the ridge. Laser cavities were formed by thinning the substrate through mechanical polishing to 150 μm and then cleaving. Broad area lasers with lengths up to 3.1

mm and widths of 20 and 50 µm and ridge lasers with lengths from 400 to 1600 µm and widths from 2 to 10 µm were fabricated.

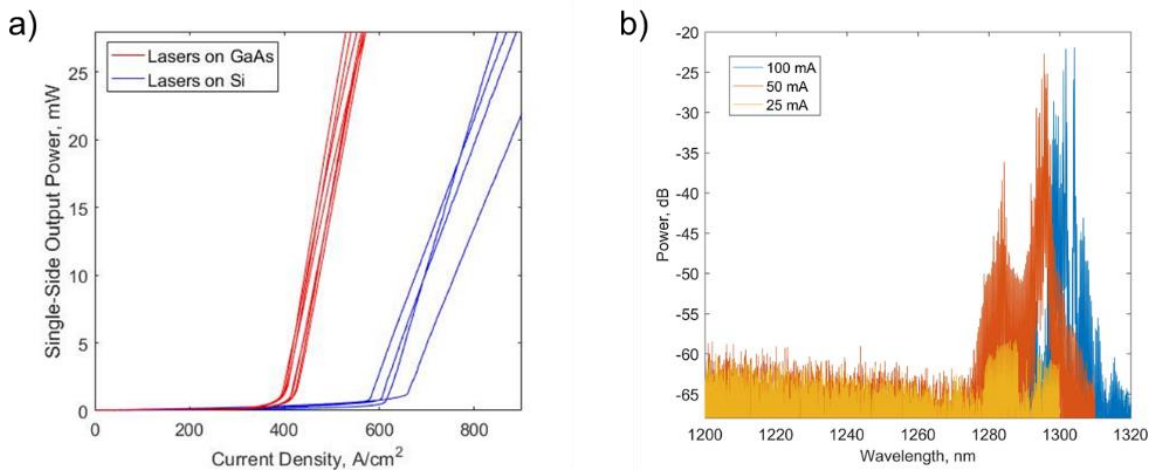

Figure 55. (a) Light output versus bias current density for 50×3100 µm^2 broad area devices on GaAs and Si showing a 1.5× increase in threshold. (b) Lasing spectra of a 2.5×750 µm^2 ridge above threshold. From [140].

As cleaved laser results are shown in Figure 55 and Figure 56. Figure 55(a) shows a direct comparison of 3100×50 µm^2 broad area lasers on GaAs and Si. The lowest threshold current densities are 396 A/cm^2 (57 A/cm^2 per layer) and 577 A/cm^2 (82 A/cm^2 per layer) for lasers on GaAs and Si, respectively. Ridge lasers showed a minimum threshold of 27 mA for a 5×850 µm^2 device and maximum single facet output power of 88 mW for a 10×1350 µm^2 device. These thresholds outperform the previous record[6] set with 95%/55% high reflectivity coatings despite utilizing as-cleaved facets. The full breakdown of device results on Si is shown in Figure 56(a-b). Ground state lasing at 1300 nm was confirmed for a 2.5×750 µm^2 as shown in Figure 55(b). One 5×850 µm^2 device was measured at elevated temperatures (Figure 56(c)). CW lasing is clearly visible up to 60°C from the ground state at lower currents with a T_0 of 103K from 20°C to 40°C, 54K from 40-50°C, and drops dramatically to 8K from 50-60°C. This is the highest reported temperature for CW operation on on-axis Si without facet coatings. The

kink and second rise in the LI curves is due to excited state lasing. All data shown is of as-cleaved devices with no facet coatings.

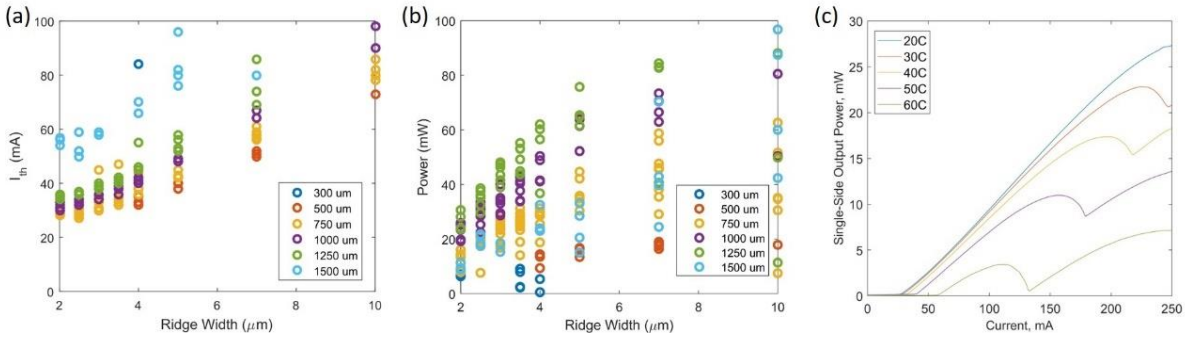

Figure 56. Scatterplots of (a) threshold current and (b) single facet output power for laser ridges of varying width and length grown on Si. (c) Power output versus bias current at elevated temperature for a 5×850 μm^2 device. From [140].

Third Generation: Further Dislocation Density Reduction

Following the first generation results on GaP/Si, a heroic effort was undertaken and led by Daehwan Jung to reduce the dislocation density in our GaAs/GaP/Si templates. The results were briefly summarized in Chapter 3 of this thesis and are presented in Ref. [24]. By incorporating a two-step (low and high temperature) growth procedure with $In_{.1}Ga_{.9}As$ filter layers and thermal cyclic annealing, the dislocation density was decreased from 3×10^8 cm^{-2} to 7×10^6 cm^{-2}. The result was a quantum leap in performance leading to world records in nearly every laser figure of merit [77, 135, 141] and allowed many of the promised unique benefits of quantum dots described in Chapter 2 to be clearly observed for the first time on silicon substrates.

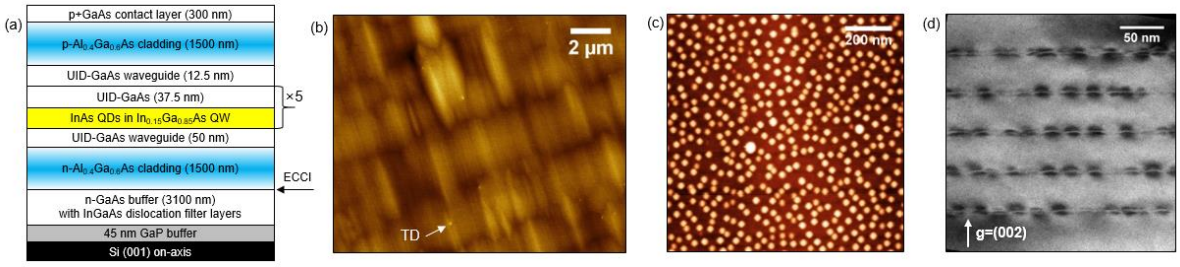

Figure 57. (a) Schematic of GaAs/AlGaAs separate confinement heterostructure laser diode grown on GaAs buffer layer on Si. (b) Electron channeling contrast image to show threading dislocations on the GaAs buffer layer. One of the threading dislocations is indicated by an arrow. (c) Atomic force microscopy image of quantum dots with a density of 4.9 × 10^{10} cm^{-2}. (d) Cross-sectional bright-field transmission electron microscopy image of coherently grown five layers of quantum dot active region in the laser epi material. The two-beam condition used in the image is g= (002). From [135].

The samples were grown by solid-source MBE. Figure 57(a) illustrates the epitaxial layer structure grown on a GaP/Si substrate. A 100 nm thick low-temperature GaAs layer was first grown at 500 °C at a growth rate of 0.1 µm/hr after oxide desorption. The substrate temperature was raised to 600 °C to grow a 1.5 µm GaAs layer at 1 µm/hr growth rate. Then, the growth was interrupted and thermal cyclic annealing was performed four times between 320 °C and 700 °C under As_2 overpressure. A superlattice of 10 pairs of 20 nm $In_{0.1}Ga_{0.9}As$/10 nm GaAs was grown at 500 °C as a dislocation filter after the annealing, and a 700 nm n-type GaAs cap layer was grown to complete the buffer growth.

The sample was removed from the chamber to analyze the threading dislocation density and surface roughness. Figure 57(b) shows an electron channeling contrast image (ECCI) of the GaAs buffer layer on the Si substrate. The channeling condition used in the imaging is a cross-point of {220} and {400} patterns to capture all possible Burgers vectors in the zinc-blende system. Threading dislocations are clearly seen as bright or dark spots in the image. The threading dislocation density was found to be 8.4 × 10^6 cm^{-2} by surveying a ~4500 μm^2 scan area. The smooth surface morphology of the GaAs buffer layer was confirmed by atomic force microscopy measurement with root-mean-square (rms) roughness of 2.6 nm. The primary

concern regarding surface roughness is that the adatom mobility could be restricted during QD growth leading to increased nonuniformity in the size distribution. Fortunately, the previous generation's PL shown in Figure 54(c) which had a higher rms roughness confirmed that adatom mobility was not being limited.

The atomic force microscopy results of Figure 57(c) also show that highly uniform InAs QDs can be grown on the GaAs/GaP/Si template. These lasers were the first grown with the fully optimized growth conditions presented in Chapter 4. The density of the uncapped QDs is ~5×10^{10} cm^{-2}. The average QD height is 11.5 nm with a standard deviation of 2.1 nm, confirming the highly homogeneous height distribution of the QDs grown on Si substrates. The bright-field cross-sectional transmission electron microscope (X-TEM) image of Figure 57(d) shows five stacks of QD layers in the laser structure. The X-TEM image reveals coherently grown QD layers with no strain coupling between them due to the relatively thick GaAs spacer layer (37.5 nm).

The as-grown material was processed into ridge-waveguide lasers with various device widths using standard dry-etching techniques. The cavity length was determined by cleaving after thinning the backside of the Si substrate to ~150 μm. All light-current-voltage (LIV) measurements were measured in the CW mode at 20 °C, and threshold currents from 55 devices are displayed in Figure 58(a). The threshold current is linearly decreased with device width down to 2.5 μm. The inset reveals a threshold current of 8.7 mA from a 2.5×1341 μm^2 device. The lowest threshold current density is 198 A/cm^2 at 20 °C and the highest wall-plug efficiency is 31%. Applying high-reflectivity (8 pairs of SiO_2 and Ta_2O_5) coatings on one facet further reduced the threshold current, and Figure 58(b) shows a CW threshold current of 6.2 mA, demonstrating the lowest threshold current among any Fabry-Perot lasers epitaxially

grown on Si at the time and was less than a quarter of the lowest threshold current in the previous generation. The QD lasers grown on Si also produced high output powers up to 185 mW single facet with one side HR coated. The highest uncoated single-facet output power was 117 mW.

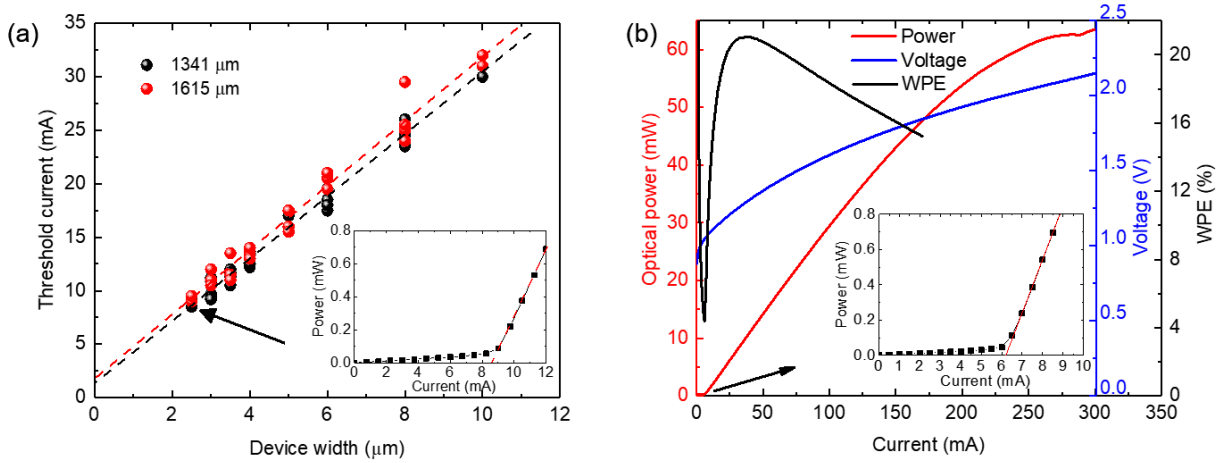

Figure 58. (a) Continuous-wave (CW) threshold current versus device width plot at 20 °C for two cavity lengths (As-cleaved facets). The dashed lines are linear fittings and the inset shows threshold current of 8.7 mA from a 2.5 × 1341 μm^2 device. (b) CW LIV and wall-plug-efficiency plots from a 2.5 × 1079 μm^2 device at 20 °C show a 6.2 mA threshold current and 21% single-side peak efficiency. From [135].

To further understand the effect of material improvement on the laser performance, a comprehensive study on the gain characteristics was conducted using Andrekson's method [29]. These results were presented for illustrative purposes in the previous chapter and have been omitted here in favor of a more detailed analysis of the effects of dislocations on gain characteristics to be presented below.

In addition to these devices, additional lasers were fabricated on the same growth template containing four quantum dot layers. The idea was that the laser threshold was limited mainly by the transparency current density rather than loss mechanisms, so reducing the number of dot layers could lower the threshold current. To test this hypothesis, lasers were grown with cladding identical to Figure 57(a) but with one fewer dot layers.

The results are shown below. Figure 59(a) shows the threshold current results with the lowest result of 9 mA occurring at a ridge with of 2.5 μm and cavity length of 1350 μm. Having the optimum at such a long cavity length suggests that the optical loss of the material is relatively low. The largest cavities showed very high output powers, setting a record for an uncoated laser grown on Si at 175 mW from a single facet. The data is highly scattered relative to the five layer samples suggesting nonuniformity in the cleaved facets considering the four and five layer samples were grown at identical conditions and processed simultaneously.

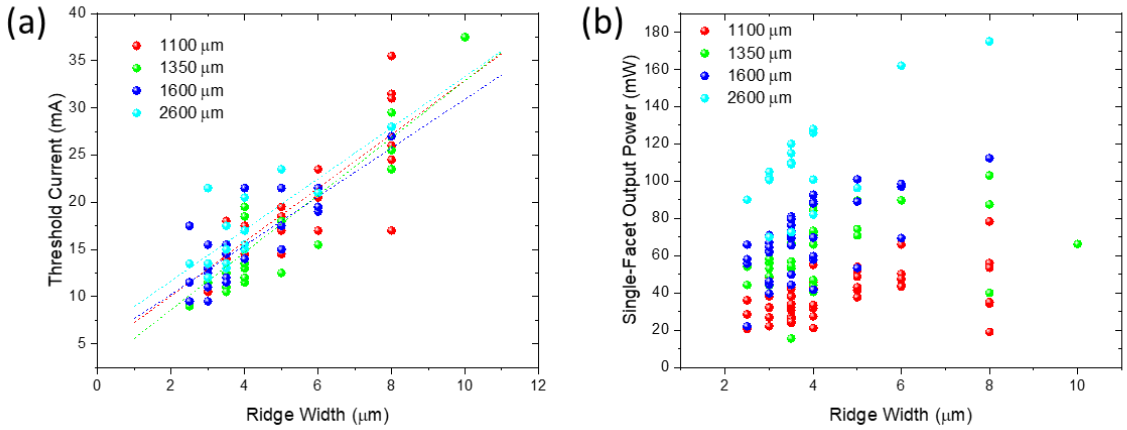

Figure 59. (a) Threshold current vs. ridge width for different cavity length lasers with four quantum dot layers and 7×10^{6} cm^{-2} dislocation density.

Overall, the performance was similar between four and five dot layers, but the best thresholds at four layers were slightly higher and the maximum output power was significantly higher. Taken together, these results could suggest that the mirror loss is higher in the four layer samples as supported by the irregularity of the data being attributed to imperfect cleaving. In general, cleaving yields significantly higher uniformity than polished facets with exactly identical performance across many devices being achievable. The problems with this

sample could be due to imperfect alignment of the laser ridges to the cleavage plane of the material.

For both four and five dot layer samples, the devices lased continuous wave up to a temperature of 80°C from the ground state setting a new record for devices on on-axis silicon, but falling short of results on miscut Si[84], which reached 120ºC despite a higher dislocation density. The primary differences in the material on miscut silicon and the material on on-axis GaP/Si were the use of p-modulation doping (pMD) in the dot active region and using a total of seven dot layers in the lasers on miscut Si. The addition of pMD led to the fourth generation of quantum dot material on silicon.

It is worth noting that the third generation devices deviated from those before and after by using a mask layout containing both shallow and deeply etched ridges. While shallow ridges are generally expected to give improved performance due to reduced sidewall recombination at narrow ridge widths, no difference in the performance of the devices was found in terms of threshold, output power, slope efficiency, characteristic temperature, or maximum CW operating temperature. The lack of improvement with shallow etching was attributed to the unique insensitivity of QD lasers to surface recombination due to inhibited in-plane carrier diffusion to sidewalls.

Fourth Generation: p-Modulation Doping the Quantum Dots

Static Characteristics

The fourth generation of quantum dot lasers utilized five dot layers with varied pMD densities including 5×10^{17} cm^{-3}, 1×10^{18} cm^{-3}, and 1.5×10^{18} cm^{-3}. The p-doping was done with Be in a 10 nm layer of GaAs in the middle of the 37.5 nm spacer between each dot layer. A schematic of one period of the active region is shown in Figure 60. The target doping levels

were designed to give 10, 20, and 30 extra holes per QD based on a dot density of 5×10^{10} cm^{-2}. The benefits of pMD were already well known as described previously in Chapter 2 having first been demonstrated by Deppe and Shchekin *et al.* [54, 55, 137].

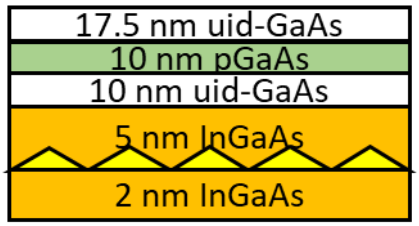

Figure 60. Single period of the doped active region of a p-modulation doped quantum dot laser.

The lasers contained five dot-in-a-well layers identical to those in the previous generation, and the laser cladding and buffer remained identical giving the same dislocation density. This batch of lasers was thoroughly characterized in terms of its static and dynamic performance and was found to contain the first demonstration of a single-section mode-locked laser on a silicon substrate. All of the previously claimed benefits of pMD were observed and are described below and in the following chapter. The most impactful benefits were improved device lifetime at elevated temperatures and reduced linewidth enhancement factor that showed the possibility of reaching zero depending on the bias and pMD level.

Threshold, output power, and slope efficiency data are shown below comparing devices with different doping levels. As expected, the pMD samples show higher thresholds and lower slope efficiencies indicative of their higher optical absorption. Auger recombination is also typically blamed for the difference in performance but later results will show that injection and temperature dependent absorption mechanisms could be the true culprit. Interestingly, despite higher threshold and lower slope efficiency, the samples with different pMD levels show similar output powers providing evidence of the increased gain provided by p-doping.

The overall similarity between the highest p-doping samples is surprising. If the increasing threshold currents and decreasing slope efficiencies were the result of absorption by the increased density of free holes in the active region, then it should scale directly with the p-doping level, but instead it seems to saturate for the 1×10^{18} cm^{-3} and 1.5×10^{18} cm^{-3} samples. While the highest doping sample has not been reproduced to confirm the results, lower doping samples have continued to be grown showing similar results to those below.

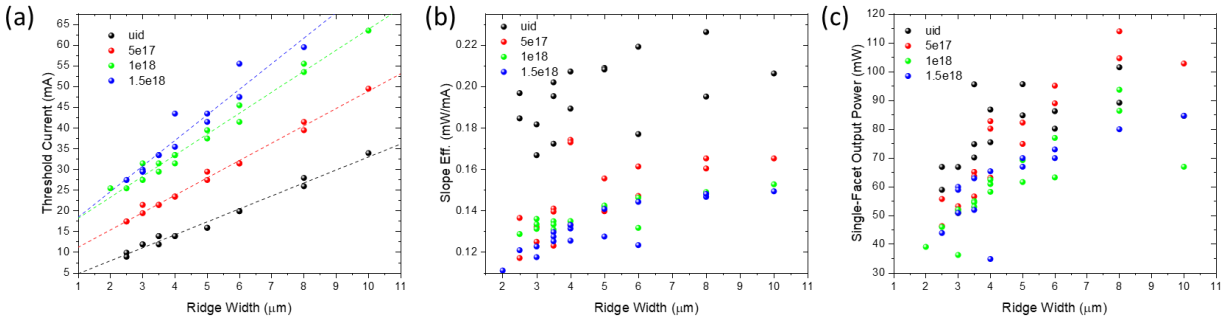

Figure 61. (a) Threshold current, (b) slope efficiency, and (c) maximum single-facet output power for 1.5 mm long laser cavities with varied p-modulation doping level and ridge width.

High Temperature Performance & Gain Characteristics

In terms of high temperature performance, the devices performed as expected with extra holes increasing the maximum operating temperature as well as the characteristic temperatures, T_0 and T_1, which relate to the scaling of the threshold current density, J_{th}, and differential quantum efficiency (DQE), η_d, respectively. The quantities are defined below.

$$\frac{1}{T_0} = \frac{\partial \ln(J_{th})}{\partial T} \tag{1}$$

$$\frac{1}{T_1} = -\frac{\partial \ln(\eta_d)}{\partial T} \tag{2}$$

These definitions arise from an assumed exponential dependence on temperature of carrier leakage and Auger recombination along with linear and inverse dependencies of the modal gain coefficient, Γg_{0J}, and internal loss, $\langle \alpha_i \rangle$, which appear in the exponential term of the equation for threshold current (shown below) [30]. The mirror loss, α_m, should not change significantly with temperature. For the DQE, from Eq. 4, the injection efficiency, η_i, is expected to decrease exponentially due to leakage, which dwarfs the expected linearity dependence of internal optical loss on temperature. These assumptions tend to hold well for quantum well lasers [142, 143].

$$J_{th} = J_{tr} \exp\left(\frac{\langle \alpha_i \rangle + \alpha_m}{\Gamma g_{0J}}\right) \tag{3}$$

$$\eta_d = \eta_i \frac{\alpha_m}{\alpha_m + \langle \alpha_i \rangle} \tag{4}$$

The threshold current density and differential quantum efficiency as a function of temperature for lasers with varied pMD are shown in Figure 62(a) and Figure 62(c). The lasers in this comparison have a cavity length of 1.5 mm and ridge width of 8 μm. The pMD lasers have a 95% HR coating on one facet while the uid sample is left as-cleaved, which is accounted for in the DQE measurements presented. While an HR coating would shift the threshold vs. temperature curve for the uid sample downward and the DQE curve upward, there should not be an effect on the characteristic temperature because the mirror loss does not change with temperature, and, as will be shown below, the internal loss and gain coefficient are also unchanging with temperature in the uid sample.

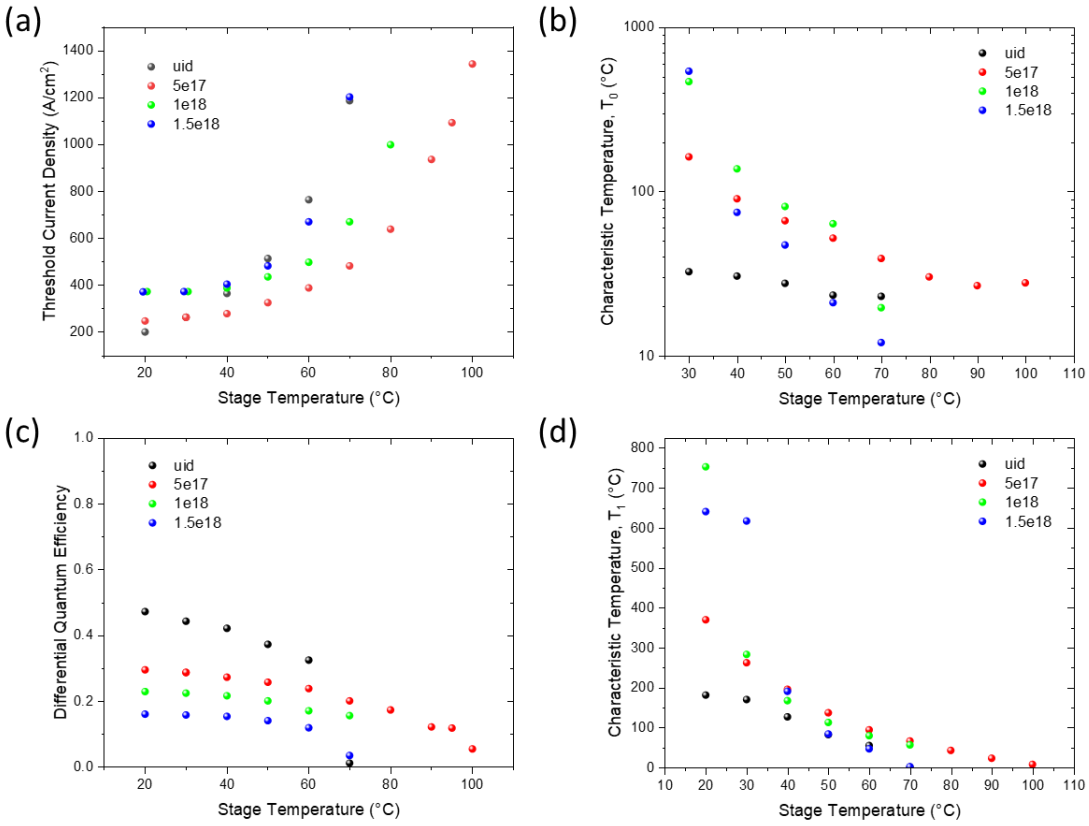

Figure 62. (a) Threshold current density, (b) threshold characteristic temperature, T_0, (c) differential quantum efficiency, and (d) differential quantum efficiency characteristic temperature, T_1, are plotted as a function of stage temperature for lasers with different levels of p-modulation doping in the active region. All devices have a cavity length of 1.5 mm and ridge width of 8 µm.

Near room temperature the trends in laser performance with doping level align with expectations of increased characteristic temperature, higher threshold current density, and lowered DQE. At elevated temperatures the benefits of pMD doping become obvious as the high temperature threshold (DQE) falls below (above) that of the uid sample. Surprisingly, however, the trends with doping level in the characteristic temperature do not hold at higher temperatures. As the stage temperature increases, the higher doped samples with 1×10^{18} cm^{-3} and 1.5×10^{18} cm^{-3} doping level show a dramatic reduction in their characteristic temperatures for both threshold and DQE. The trend worsens at higher temperature with the characteristic

temperature dropping below the uid laser at a stage temperature of 70°C. While the sample with 5×10^{17} cm^{-3} doping managed to perform better with a maximum CW lasing temperature of 105°C, its characteristic temperatures also dropped to approximately match those of the uid device at lower temperatures. To gain insight into the physics of these trends, gain and transparency measurements were performed, as described previously, at elevated temperatures to decompose the various contributions to the characteristic temperature.

From Eqs. 1 through 4, the characteristic temperature can be trivially broken down into contributions from the transparency current, gain coefficient, internal loss, and injection efficiency [142, 144]. The resulting equations are shown below.

$$\frac{1}{T_0} = \frac{\partial}{\partial T}\ln(J_{tr}) + \frac{\partial}{\partial T}\left(\frac{\langle\alpha_i\rangle}{\Gamma g_{0J}}\right) + \alpha_m \frac{\partial}{\partial T}\left(\frac{1}{\Gamma g_{0J}}\right) = \frac{1}{T_{J_{tr}}} + \frac{1}{T_{\alpha_i}} + \frac{1}{T_{\Gamma g_{0J}}} \tag{5}$$

$$\frac{1}{T_1} = \frac{\partial}{\partial T}\ln(\eta_i) + \alpha_m \frac{\partial}{\partial T}\ln\left(\frac{1}{\alpha_m + \langle\alpha_i\rangle}\right) = \frac{1}{T_{\eta_i}} + \frac{1}{T_{\eta_m}} \tag{6}$$

Using Andrekson's method at varied temperatures, each of the above terms can be independently measured. Unfortunately, the devices presented in Figure 62 could not be used for such a study because they exhibit higher order lateral modes that interfere with the mode-sum gain calculation. Instead, narrower devices with cavity lengths of 1.5 mm and ridge widths of 3.5 μm were chosen with the same doping levels as used above. The range of temperatures investigated was from 20°C to 56°C. At each temperature step, the transparency current was measured across the full gain spectrum and amplified spontaneous emission spectra were taken at currents up to the threshold. Since transparency was obtained across the full gain spectrum, the optical loss could be obtained as a function of wavelength.

The transparency current density for each of the samples as a function of wavelength at elevated temperatures is plotted in Figure 63. At 20°C, pMD is found to reduce the transparency current density as would be expected considering that electron confinement in the QDs is much greater than the hole confinement such that the extra doping helps to pull the Fermi level down such that the quasi-Fermi levels separate more symmetrically leading to an earlier population inversion. Interestingly, at higher temperatures, the trend does not hold with the uid sample having slightly lower transparency current densities at 60°C. Another trend is that the shorter wavelength side of the gain spectrum has a much more rapidly increasing transparency in the p-doped samples than in the uid sample. The shorter wavelength side of the spectrum corresponds to QDs with lower quantum confinement suggesting that pMD has enhanced scattering out of the QDs. This would align with reported observations of increased Auger recombination in pMD QD lasers [145-147], but the extent of the variation over such a small region in energy-space is unexpected. In particular, the sudden, large changes in the 1.5×10^{18} cm^{-3} transparency current density between 33°C and 45°C at wavelengths shorter than 1310 nm seem abnormal and may suggest a different mechanism that "turns-on" at some injection or temperature threshold. To truly arrive at any detailed understanding of these results would likely require detailed pump-probe experiments to investigate carrier capture and escape from QDs.

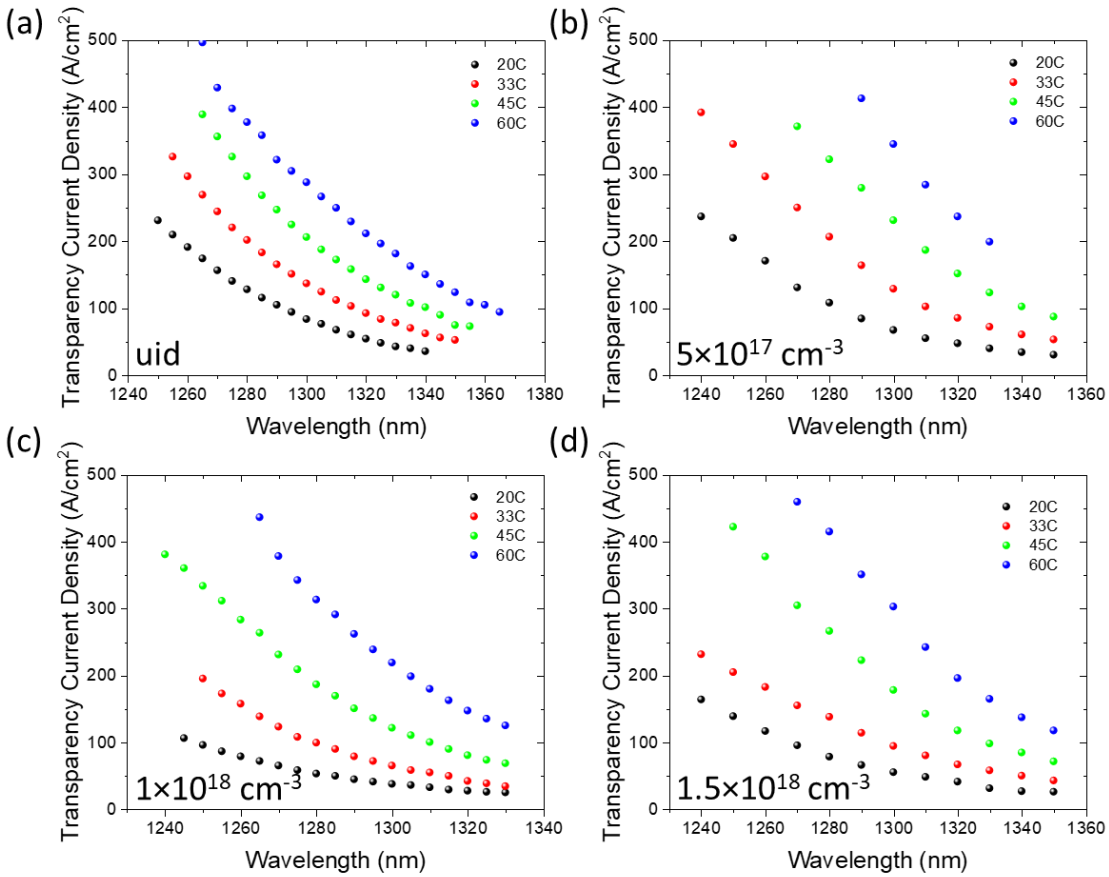

Figure 63. The transparency current density as a function of wavelength is plotted for temperatures from 20°C to 60°C for (a) uid, (b) 5×10^{17} cm^{-3}(c) 1×10^{18} cm^{-3}, and (d) 1.5×10^{18} cm^{-3} doping levels in the laser active region. The laser cavities were 1.5 mm long with a ridge width of 3.5 µm.

From the data in Figure 63, the characteristic temperature of the transparency current density was obtained from each sample by plotting the transparency of the lasing wavelength at threshold. For reference, the lasing wavelength at threshold for each of the samples at each temperature is presented in Figure 64. Each sample shifts similarly to the others and roughly matches the expected shift for bulk InAs indicating that the InAs bandgap determines the transition energy.

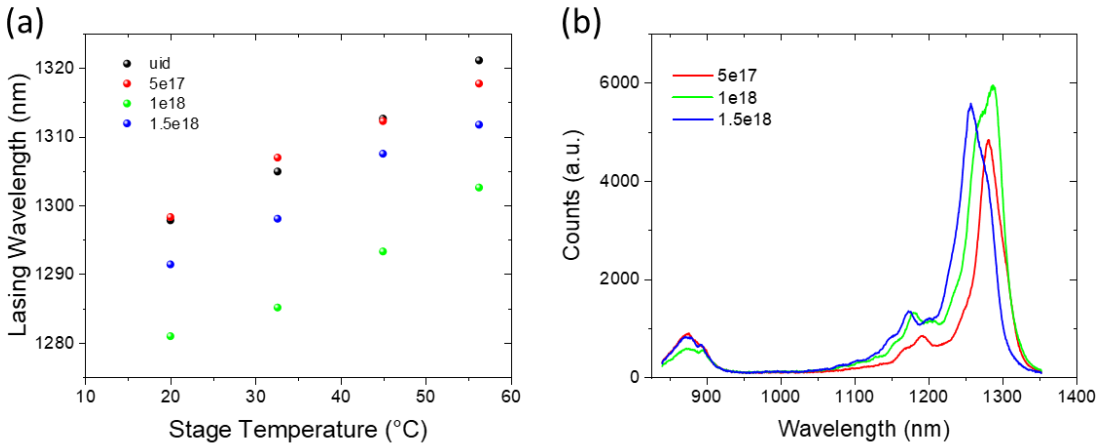

Figure 64. (a) The lasing wavelength as a function of stage temperature for 1.5 mm × 3.5 µm ridge lasers with varied active region p-modulation doping used for gain analysis. (b) Photoluminescence spectra for the three doped samples from (a). Samples with uid active region do not emit detectable photoluminescence signals.

Using the wavelengths from Figure 64(a), the relevant transparency currents were extracted by interpolating the data of Figure 63. Fitting the transparency current density was done with an exponential that provided near perfect agreement over the full temperature range indicating that $T_{J_{tr}}$ could be represented by a constant value. The uid sample showed the highest characteristic temperature for the transparency current density at ~41°C while the p-doped samples showed a nearly constant value of ~29°C. That the transparency is more sensitive to temperature in the pMD samples is surprising because the primary hypothesis behind adding extra holes was to compensate for how easily they can thermalize out of the QDs and likely points to more complex behavior in the carrier capture/escape dynamics.

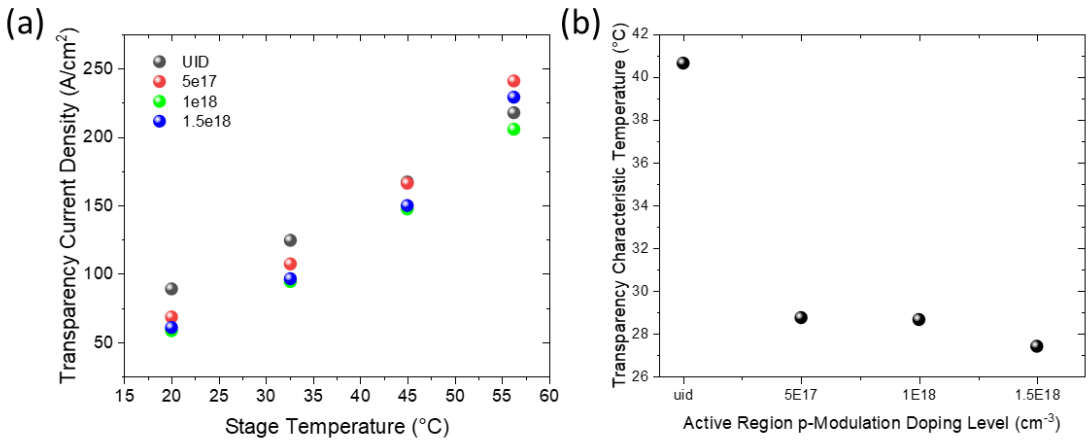

Figure 65. (a) Transparency current density as a function of temperature for lasers with varied p-modulation doping level. (b) Extracted characteristic temperature for the transparency current for each doping level from an exponential fit.

Returning to Eqs. (5) and (6), it is clear that the transparency alone cannot explain the variability of the characteristic temperature. To further investigate, the net gain was extracted from amplified spontaneous emission spectra below threshold using the mode-sum method as described in the previous chapter. By taking the net gain at transparency and knowing the mirror loss of the devices, the internal optical loss was extracted as a function of wavelength at each temperature. Meanwhile, the gain coefficient was found by a logarithmic fitting of the gain curves at each wavelength near threshold.

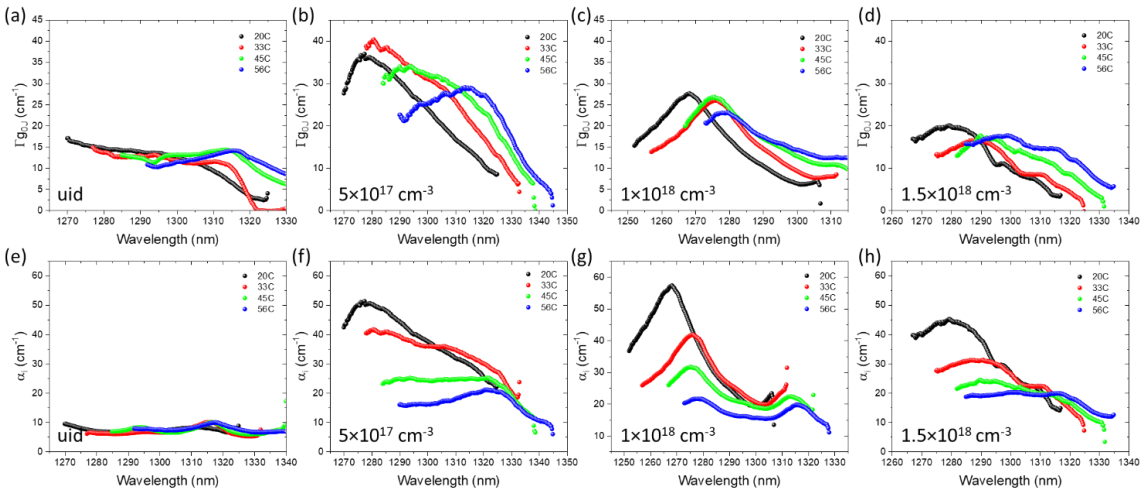

Figure 66. (a)-(e) Modal gain coefficient with respect to current density and (e)-(h) internal optical loss plotted as a function of wavelength spanning the gain spectrum for various temperatures for lasers with varying p-modulation doping level.

The results in Figure 66 show stark differences between the pMD samples and the uid sample in both the gain coefficient and internal loss. The gain coefficient is much higher in the pMD samples peaking at over 40 cm^{-1} (8 cm^{-1} per layer) in the 5×10^{17} cm^{-3} sample as compared to ~15 cm^{-1} (3 cm^{-1} per layer) in the uid sample. The gain coefficient then decreases at higher doping levels. Higher differential gain, which is directly proportional to the gain coefficient, was theorized and demonstrated to be a result of pMD [57, 65], and a decrease with temperature could be expected due to thermalization of the holes leading to some offset to the amount of extra holes available to the QDs relative to room temperature, so these results are not particularly surprising.

The internal loss results, on the other hand, were extremely surprising. While the uid sample shows relatively flat, low loss across the full spectrum and does not vary with temperature, the pMD samples all show very high absorption levels over a relatively narrow resonance on the blue side of the gain spectrum that decreases and red shifts with increasing temperature. The fact that the feature is narrow and exists only at the blue side of the gain

spectrum (note that each sample has slight variations in the peak as illustrated in the PL of Figure 64(b)) indicates that the absorption is somehow tied to states within the QDs, seemingly those dots with lower quantum confinement. The loss is also only observed in the pMD samples and depends only weakly on the doping level and reaching a similar value by 60°C of slightly less than 20 cm^{-1}. Since the loss only appears with pMD, it must be an intervalence band transition. Between the decreasing internal loss with increasing temperature and the wavelength dependence showing much higher loss at shorter wavelengths, the physical origins seem like they must be related to carrier distribution amongst the dot population with higher occupancies reducing the absorption. Furthermore, the optical loss appears to decrease with the electrical injection level. If the gain parameters and transparency data of Figure 63-Figure 66 are plugged back into Eqs. (3) and (4), the threshold current density can be predicted with near perfect precision in all of the samples, including uid and p-doped. The differential quantum efficiency, on the other hand, cannot be reproduced because the internal loss values in Figure 66 are so high that the injection efficiency would have to be >100% to match the experimentally measured DQE of the pMD lasers. If reasonable injection efficiencies are assumed, and rough estimates of loss extracted from the slope efficiency, they would lead to dramatically underestimated laser threshold currents. An understanding of what is actually happening in these devices is critically important because this absorption is clearly the limiting factor in the laser threshold and, as shown below, reveals the source of the QD lasers' increased characteristic temperatures with pMD. Elucidating the physics behind this anomalous optical loss is the subject of ongoing work.

Returning to the topic of temperature sensitivity, it can be seen that the relatively weak changes in the modal gain coefficient with respect to temperature are not the driving factor in

the T_0 of the pMD lasers. Clearly the absorption is the primary player, and from the data in Figure 66(e-h), and looking at the wavelengths in Figure 64(a), the exact contribution of the absorption can be calculated through Eq. (5). The modal gain coefficient and internal loss are plotted as a function of doping density for the uid and pMD samples in Figure 67. From Figure 67(a), the gain coefficient is seen to not change significantly with temperature for any of the samples giving a near infinite value for its characteristic temperature in Eq. (5). Meanwhile, the internal optical loss changes significantly with temperature in the pMD samples while remaining nearly constant for the uid laser. The loss decreases such that the characteristic temperature associated with it, T_{α_i}, would be negative and thus compensate for the positive characteristic temperature of the transparency current density, $T_{J_{tr}}$, leading to the high threshold characteristic temperature, T_0. Due to the lack of physical understanding behind the loss mechanism, the correct functional form to fit the data is unknown, and the number of data points is insufficient for reasonable spline fitting. As a result, the exact value of T_{α_i} was not extracted. The changing loss also makes accurate extraction of the injection efficiency difficult, so the trends in T_1 were not quantitatively examined. Nevertheless, the qualitative trends in high temperature performance of pMD QD lasers has been qualitatively described. The presented result contradicts earlier studies claiming Auger recombination as the compensating mechanism in the laser threshold at higher temperatures [60]. The apparent source of the error is that Fathpour *et al*. and all other literature reports have failed to examine wavelength dependent loss mechanisms and have not conducted independent measurements of the transparency current density. Generally, the transparency is extracted from a logarithmic fit to the gain curve generated from the cutback method.

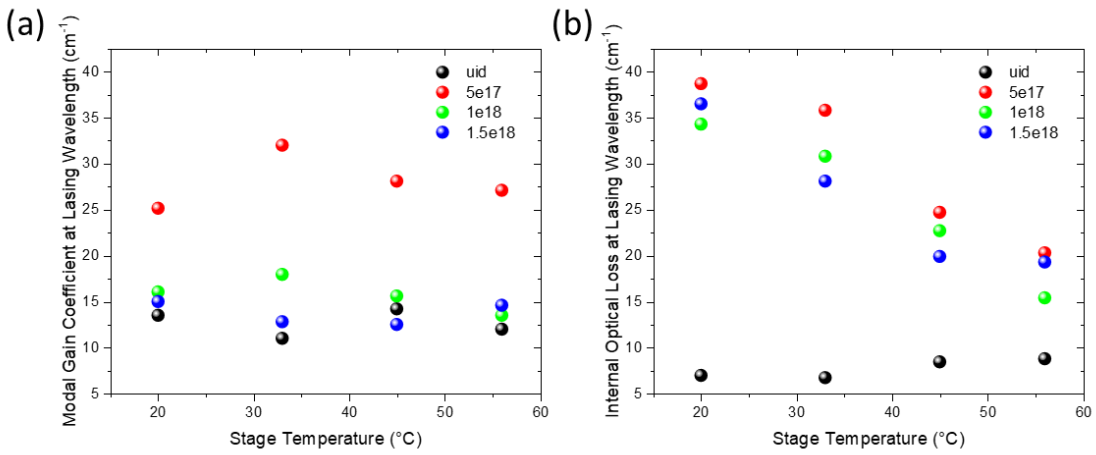

Figure 67. (a) The modal gain coefficient with respect to current density, g_{0J}, and (b) internal optical loss, $\langle \alpha_i \rangle$, are plotted as a function of temperature for samples with varied p-modulation doping density in the laser active region.

Beyond improving high temperature performance, the increased maximum gain and differential gain associated with pMD lead to improved laser reliability and dynamic performance. Reliability will be discussed in the next section. The improved dynamic performance manifests itself in increased direct modulation bandwidth and lower, potentially negative, values of the linewidth enhancement factor. Each of these results is presented below with reliability being covered in detail in the next section.

Small-Signal Direct Modulation

A laser's relaxation oscillation frequency scales as $f_r \propto g_{0J}^{1/2}$. Given the gain coefficients measured in Figure 66, one would expect a factor of ~1.63 increase in the resonance frequency at the 5×10^{17} cm^{-3} doping level. To test the dynamic performance of the lasers, two devices with 3×580 μm^2 ridges and a single-facet 95% high reflectivity coating were selected, and their small-signal direct modulation characteristics were measured [148].

The small-signal response, S_{21}, was measured by directly probing the device using a signal/ground (SG) RF probe. A 20 GHz lightwave component analyzer (LCA, HP8703A) was used for the measurement. A QD laser chip was placed on a heat sink without any temperature control. Bias current to the QD laser was injected via the internal bias-tee of the LCA. The light output of the QD laser was collected by a spherical-lensed single-mode fiber and modulated light output was detected by an internal detector of the LCA. To extract the damping rate γ and relaxation oscillation frequency f_r, the following three-pole fitting function H(f) [149] was used to draw fitting curves,

$$\mathrm{H}(f) = \frac{1}{\left(1 + \left(2\pi f \tau_p\right)^2\right)} \frac{f_r^4}{(f_r^2 - f)^2 + \left(\frac{\gamma f}{2\pi}\right)^2}, \tag{7}$$

where τ_p stands for the RC or carrier transport delay.

Figure 68 shows small-signal responses for the devices with UID barriers (Figure 68(a)) and pMD barriers (Figure 68(b)). Both devices have a ridge stripe width of 3.0 μm, cavity length of 580 μm and HR coating at one side of the facets. Thus, these devices are expected to have the same *RC* cutoff frequency. The UID device has a lower threshold current of 5.5 mA than that of *p*-doped device of 10 mA. The frequency response of the UID device saturated at the low bias current condition of 69.5 mA. In addition, a dip in the frequency response was observed at around 3 GHz. The maximum f_{3dB} was 4 GHz at the bias current of 69.5 mA. In contrast, the *p*-doped device showed flat response up to 3 dB bandwidth. The bandwidth increased up to a bias current of 110 mA. The relative magnitude of the 3 dB bandwidth between the uid, 4.0 GHz, and pMD sample, 6.5 GHz, matches perfectly with the measured ratios of the gain coefficient from Figure 66.

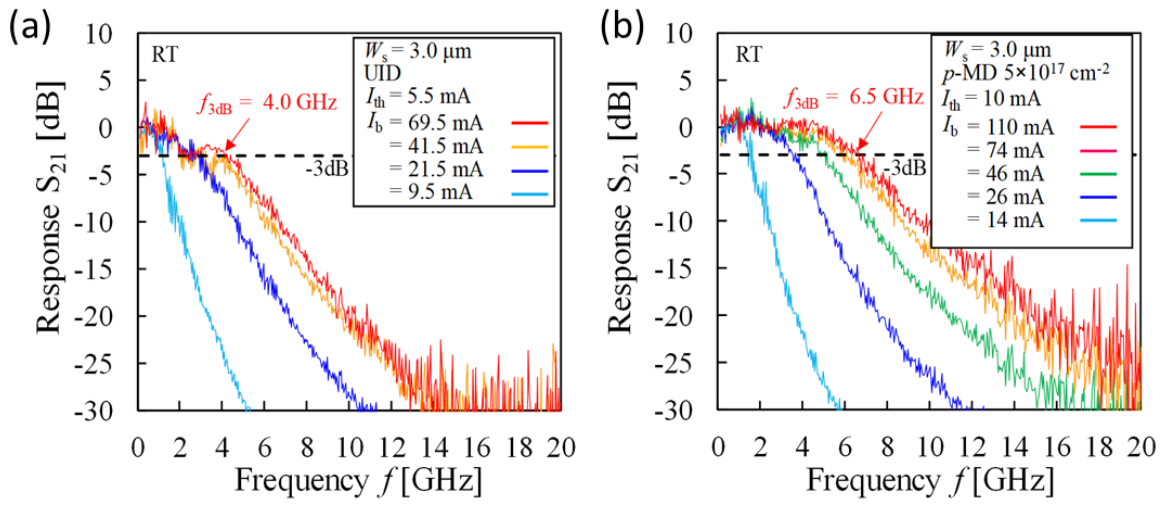

Figure 68. Comparison of small signal modulation response between (a) UID device and (b)p-MD device. These devices have identical device geometry except for p-modulation doping in the active layers. From [148].

Figure 69 shows the plots of f_{3dB} and f_r of the *p*-doped QD laser shown in Figure 68(b) as a function of the square root of bias current above threshold obtained from fitting curves. The modulation efficiencies for f_{3dB} and f_r are 0.74 GHz/mA$^{1/2}$ and 0.68 GHz/mA$^{1/2}$. These slopes are calculated using plots below $(I_b - I_{th})^{1/2} < 7$ mA$^{1/2}$. These values are small compared with state-of-the-art QW lasers for direct modulation that have modulation efficiency for f_r of 3–4 GHz GHz/mA$^{1/2}$ [150]. This is due to the lower confinement factor and high gain compression caused by slow carrier capture in the QD active layer.

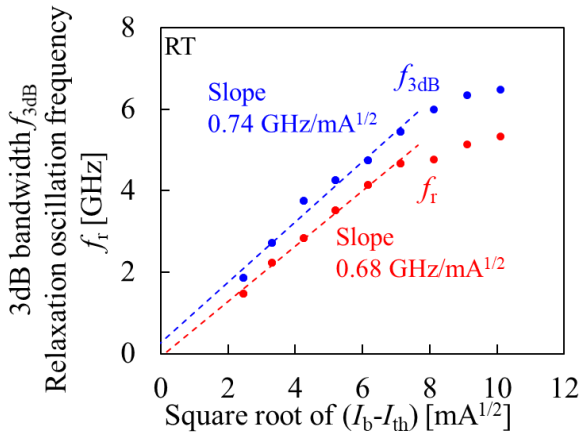

Figure 69. 3dB bandwidth f_{3dB} and relaxation oscillation frequency f_r versus square-root of the bias current above threshold for the p-doped QD laser on Si (5.0 × 580 μm^2). From [148].

The *K*-factor is derived by plotting the damping rate γ versus squared f_r. In Figure 70, the linear fitting is drawn using the following equation,

$$\gamma = K \cdot f_r^2 + \gamma_0 \tag{8}$$

where γ_0 represents damping offset. The *K*-factor is estimated to be 0.92 ns from the slope of the fitting curve. The maximum 3 dB bandwidth limited by *K*-factor ($f_{3dB,\ max}$) can be calculated by the following equation,

$$f_{3dB,max} = \frac{2\sqrt{2}\pi}{K} \tag{9}$$

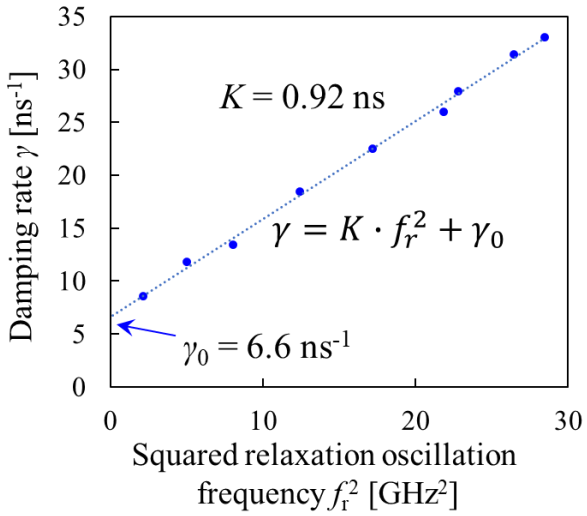

Figure 70. Damping rate γ versus squared relaxation oscillation frequency f_r^2. The maximum 3 dB bandwidth limited by K-factor $f_{3dB,\,max}$ is 9.5 GHz. From [148].

The maximum $f_{3dB,\,max}$ is calculated to be 9.5 GHz. Hence, the measured f_{3dB} of 6.5 GHz from our small signal modulation is close to this *K*-factor limited bandwidth, but is lower due to a large pad capacitance of the electrodes, which are not optimized for high-frequency operation. The maximum 3 dB bandwidth compares favorably to the current record on native substrates of 13.1 GHz [133], and is nearly identical to more typical native substrate results in literature [151] indicating the high optical quality of this generation of lasers on Si.

Linewidth Enhancement Factor & Optical Feedback Susceptibility

The linewidth enhancement factor, α, is a critical parameter for laser integration. It scales inversely with the gain coefficient suggesting that pMD should yield lower values. Since the laser linewidth scales as $\Delta\nu \propto (1+\alpha^2)$ and the critical feedback level for coherence collapse scales as $f_{crit} \propto (1+\alpha^2)/\alpha^4$, a small reduction in α can yield dramatic improvements in performance. The unique capability of QD lasers to achieve ultralow values of α, as described

in Chapter 2, is one of the primary motivating factors for their deployment in photonic integrated circuits.

The linewidth enhancement factor has been measured below threshold from the shift of the Fabry-Perot modes with increased electrical injection and above threshold through injection locking experiments [67] with record low results observed. To achieve the promise of low linewidth enhancement factors in QD lasers, the dot inhomogeneous broadening has to be made extremely narrow. Through the optimizations of Chapter 4, the inhomogeneous broadening was reduced from >20 meV [127] to ~10 meV (corresponding to a PL FWHM of ~28 meV) [57] which enabled the ultralow values of α.

Measured values of α from subthreshold measurements near the laser threshold are shown in Figure 71. Figure 71(a) shows the wavelength dependence of α showing uniformly low values across the gain bandwidth. Results presented in Ref. [67] show that α remains low up to a bias of twice threshold. One factor that improves α at high injection levels is the amount of ground state emission relative to excited state emission. Once the excited state turns on, the linewidth enhancement factor increases dramatically until the ground state is fully suppressed [68]. By increasing the ground state gain, reducing the defect density, or lowering the optical loss, the ground state saturation can be pushed to higher currents leading to higher output powers while maintaining lower α which is beneficial for virtually all applications.

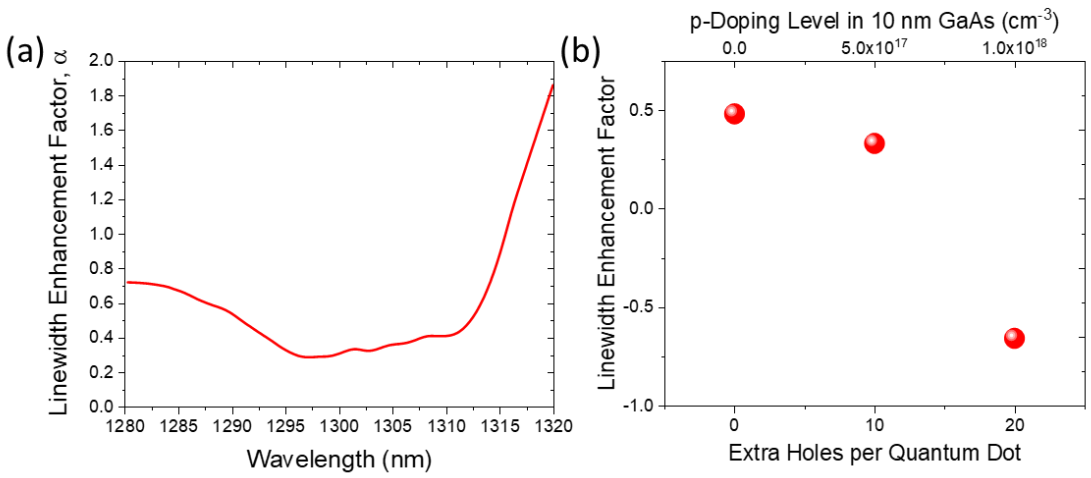

Figure 71. (a) Subthreshold linewidth enhancement factor across the gain spectrum for a laser with 5×10^{17} cm^{-3} p-modulation doping in the active region. (b) Subthreshold linewidth enhancement factor at the gain peak vs. doping level. Adapted from [70].

The influence of pMD on α is shown in Figure 71(b). As the doping level increases, the linewidth shifts continuously to lower values passing zero and becoming negative [70]. These measurements were taken in pulsed mode to eliminate the effects of self-heating on the shift of the Fabry-Perot modes. The results indicate that by tuning the pMD level, α can be tuned giving the possibility of designing a laser to have zero α at a particular bias point. Beyond reaching ultralow α for feedback stability and narrow linewidth, using pMD to engineer negative alpha could be beneficial for high power lasers by reducing filamentation. The linewidth enhancement factor is also sometimes referred to as the guiding or antiguiding factor because it can lead to a focusing effect at high photon densities due to spatial hole burning. Basically, the optical mode depletes carriers at regions of high intensity which leads to an increase in the refractive index (due to positive α) which further focuses the mode and further increases carrier depletion in a feedback loop. If α goes negative, then an antiguiding effect would be expected as the refractive index effect changes sign leading to reduced focusing. Investigations of the optical mode profile in these devices is the subject of future work.

While single mode devices have not yet been fabricated to test the benefits of low α on laser linewidth, the performance of lasers under optical feedback has been thoroughly investigated. Devices from the first generation of material that were grown on GaP/Si—prior to optimization of the QD size homogeneity—were tested under optical feedback and compared with heterogeneous QW lasers [37]. Even in these devices a 20 dB improvement in feedback stability was observed for the QD devices relative to QWs. Using this fourth generation of highly optimized, pMD material, experiments were conducted by collaborators in Frédéric Grillot's group at the Université Paris-Saclay where 90% of the QD laser's output power was reflected back into the laser cavity (18% after accounting for coupling loss in the plots below), and the lasers show perfect stability. In Figure 72(a) and (c) the stability of the QD lasers as a function of feedback level is displayed. The first generation of material showed coherence collapse at feedback levels of 1% to 10% depending on the device. The shift in the Fabry-Perot modes is actually due to device heating from the extreme amount of optical power being fed back into the cavity. In Figure 72(b) and (d), the feedback performance of a commercial QW laser is presented showing complete coherence collapse at a feedback level of only 0.4%.

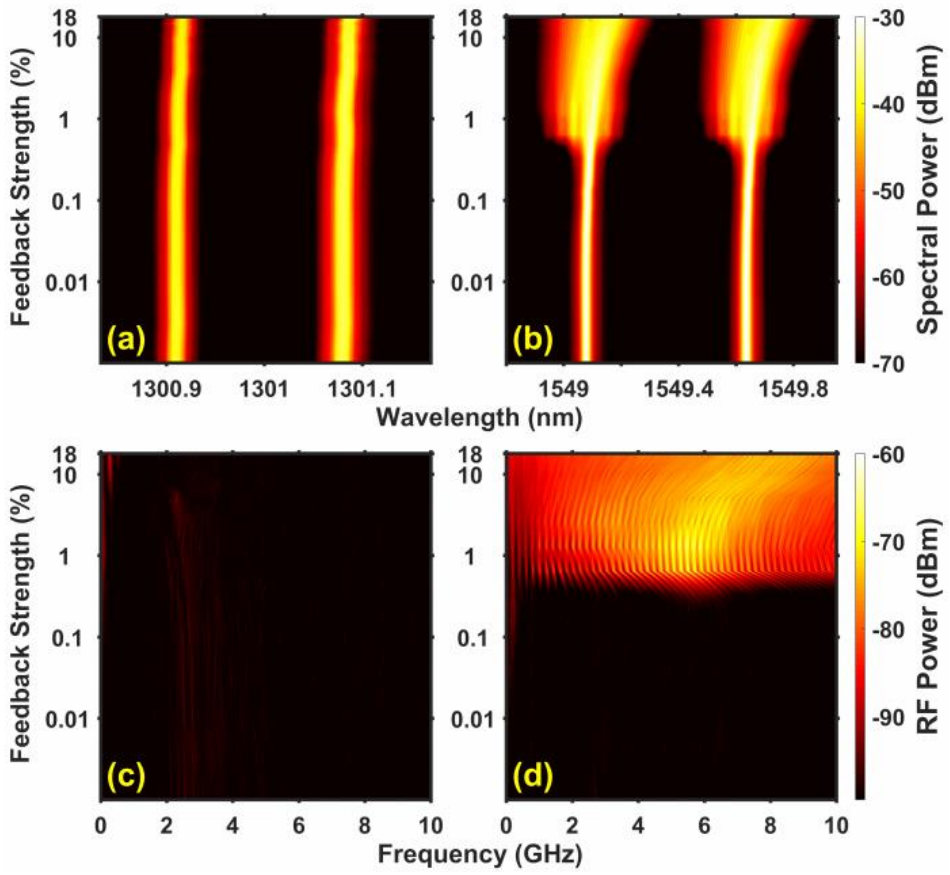

Figure 72. (a) Optical and (b) radio frequency spectral mappings of the quantum dot laser and (b)(d) a commercial quantum well laser as a function of feedback level on a log scale. From [90].

To further illustrate the stability of the QD laser, transmission experiments were conducted with external 10 GHz modulation at the same 90% feedback level above. In back-to-back testing and transmission over 2 km of fiber, no power penalty was observed between no feedback and 90% feedback. In contrast, the QW device suffered a power penalty of 2 dB at only 0.004% optical feedback. These results clearly demonstrate the potential for isolator-free photonic integrated circuits by using QD lasers.

Laser Performance & Reliability vs. Dislocation Density

Since the challenges associated with making high performance lasers on Si are entirely related to dealing with dislocations, detailed analysis of the effects of dislocation density on device performance and reliability deserve focused discussion separate from what has been presented above. Device reliability has historically been the limiting factor to adoption of epitaxial III-V lasers on silicon, and, through use of QDs as the laser active medium, results have rapidly progressed to the point of possible near-term commercial viability. In the section below, performance will be compared through the previous generations of laser material grown on Si for a detailed analysis of how dislocations affect QD lasers.

Recently, replacing the QW active region with InAs quantum dots (QDs) in GaAs-based lasers grown on Si has demonstrated considerable advances in laser performance as well as reliability. Liu *et al.* reported an extrapolated laser lifetime (time to doubling of the initial threshold current) up to ~4600 hours from QD lasers grown on Ge/Si templates after a 2700-hour aging test at 30°C [85]. Also, Chen *et al.* demonstrated one broad-area QD laser with an extrapolated lifetime of ~100,000 hours by aging it at 26 °C under a constant current injection of 1.75× initial threshold [27]. Both studies showed gradual degradation, in stark contrast to previous reliability studies of QW and bulk lasers[152, 153]. The sections above show the improvements in device characteristics with different generations of material that have progressively lower dislocation densities, but in parallel to dislocation density reduction, changes were also being made to optimize the QD active region in terms of inhomogeneous broadening and p-modulation doping (pMD).

Static Performance vs. Dislocation Density

To provide a direct look at the impact of dislocations on the static performance of QD lasers, devices were grown with identical growth conditions of the QD active region including pMD doping level. These lasers utilized the epitaxial structure shown in Figure 73. The structure is the same as that of the fourth generation results above with a pMD level of 5×10^{17} cm^{-3} and seven layers of QDs instead of five used above. The threading dislocation densities (TDD) compared were 7×10^{7} cm^{-2}, 1×10^{7} cm^{-2}, and native substrate devices which are effectively zero dislocation density since the density is low enough that the expected number of dislocations in a given device is zero.

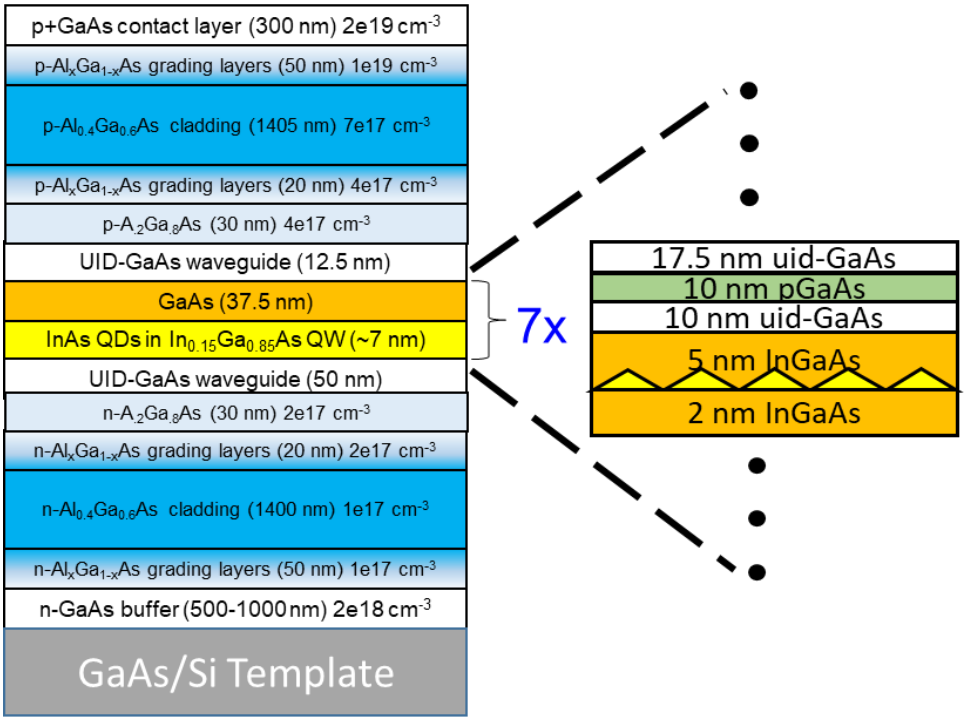

Figure 73. Epitaxial laser structure for the study on the effect of dislocation density on device performance in un-aged quantum dot lasers.

The performance of lasers with varied ridge width and as-cleaved 1350 µm cavity lengths are plotted in Figure 74. The data shows clear improvements in performance in terms of lower

threshold current density (Figure 74(a)), higher differential quantum efficiency (Figure 74(b)), and higher output power (Figure 74(c)) as the dislocation density decreases. Three laser characteristics could be hypothesized to change as a result of dislocations: the gain coefficient, the injection efficiency, and the internal loss. There is a noticeable discontinuity between the results at 1×10^{7} cm^{-2} and the results on a native GaAs substrate.

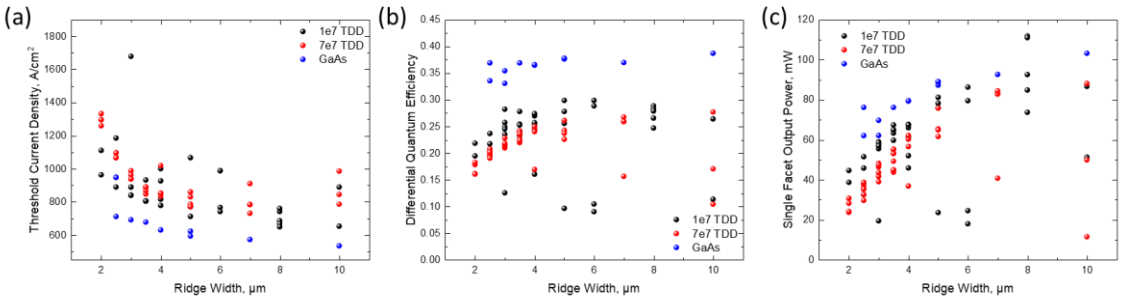

Figure 74. (a) Threshold current density, (b) differential quantum efficiency, and (c) single facet output power vs. ridge width for p-modulation doped quantum dot lasers with 1350 μm cavity length and varied ridge width at two different dislocation densities on silicon and one sample on a native GaAs substrate.

The gain characteristics were measured for each of the devices to independently characterize the effects of dislocations on the gain coefficient, optical loss, and injection efficiency. Unfortunately, there is no trend in the gain characteristics suggesting that something went wrong in one of the growths or perhaps processing since all samples had normal PL characteristics as-grown; nevertheless, some interpretations can still be made on the data. The abnormal result is that the transparency current density is higher in the 1×10^{7} cm^{-2} TDD sample than in the 7×10^{7} cm^{-2} TDD sample as shown in Figure 75(a). Transparency, being the current required to invert the gain medium, depends solely on dot density and injection efficiency. While the dot density could vary with growth conditions, the likelihood that it would vary enough to increase the transparency current density by ~33% seems low. Furthermore, an increase in dot density would increase the gain coefficient, which is not

observed in Figure 75(c) where all three samples are nearly identical. Since the injection efficiency cannot be made artificially high by problems in growth or fabrication, this suggests that the 1×10^{7} cm^{-2} TDD sample could have lower injection efficiency than it should, perhaps through leakage pathways due to fabrication issues; however, no noticeable irregularities were visible from in the current-voltage curves. Also, the transparency results in an internal loss measurement that is lower in the 1×10^{7} cm^{-2} TDD sample than in the sample on GaAs. It is extremely unlikely that dislocations would decrease the optical loss in the sample. They should either have negligible impact, or increase loss. These results suggest that dislocations have minimal impact on optical loss and the gain coefficient and, thus, have their impact entirely in the injection efficiency, but such speculation needs further investigation.

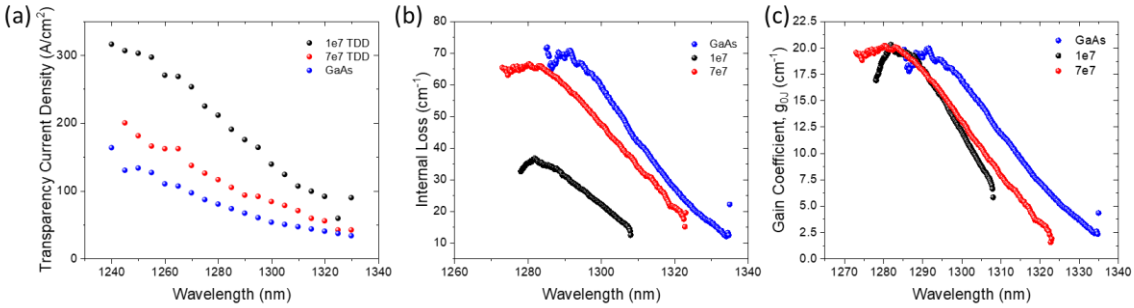

Figure 75. (a) Transparency current density, (b) internal optical loss, and (c) the gain coefficient with respect to current density are plotted for lasers with three different threading dislocation densities as a function of wavelength.

Laser Reliability vs. Dislocation Density

Carrier localization in QDs considerably improves laser reliability over QW lasers on Si by suppressing growth of dark-line defects through inhibited recombination enhanced dislocation climb (REDC). REDC is still the dominant degradation mechanism in QD lasers on Si [85, 154], but the reduced nonradiative recombination prevented the characteristic dislocation networks that constitute dark line defects from forming. A relative comparison of

similarly aged QD and QW lasers in the presence of dislocations is shown in Figure 76. Notice that the misfit dislocations in the QD laser of Figure 76(a) have barely developed the helical components associated with dislocation climb, while the QW laser in Figure 76(b) shows an extensive climb network that would appear as a dark-line defect.

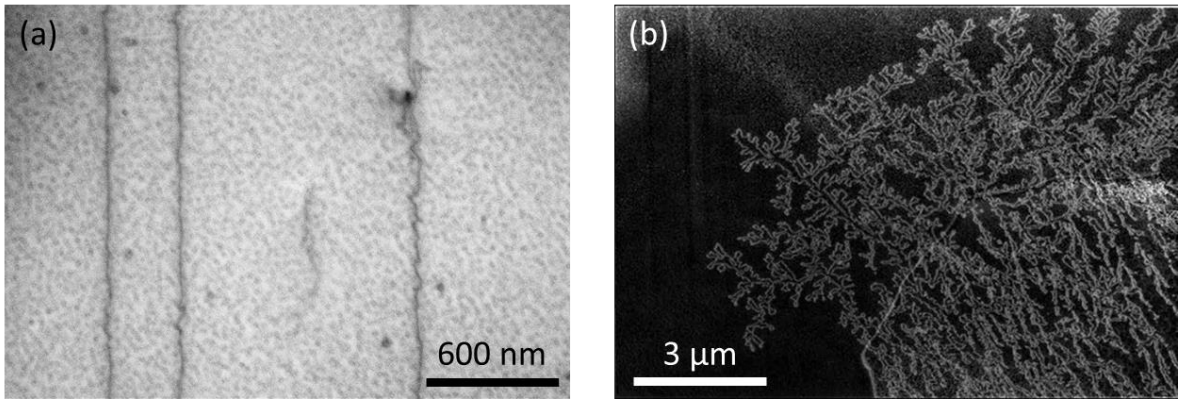

Figure 76. Plan-view transmission electron microscope images of aged (a) quantum dot and (b) quantum well lasers containing dislocations [40].

The lasers from the first three generations of device material presented above—with GaP/Si for the first generation, not GoVS—were aged to determine the influence of TDD on device lifetime. The device lifetime in this study was defined as the time to double the initial threshold current. The extrapolated lifetimes from the QD lasers grown on the 7.3×10^6 cm^{-2} template are more than 10 million hours while those on the high TDD template are limited to ~500 hours of lifetime. A similar trend in the laser slope efficiencies was observed during the aging test. Moreover, QD lasers with a low TDD were aged at an elevated temperature (60 °C) to investigate the temperature effects, and p-modulation doped QD lasers demonstrated an extrapolated lifetime of ~65,000 hours.

As described above, the three generations of material were grown at different stages of buffer growth optimization. For Generation-I lasers (Gen-I), only a two-step growth temperature technique was applied for the GaAs buffer layer, while four repeats of thermal

cyclic annealing were added for the Gen-II template. For the Gen-III buffer, InGaAs/GaAs strained layer superlattices were inserted as dislocation filter layers to further reduce the TDD in addition to the two-step growth and thermal cycle annealing.[24] The samples were characterized using the electron channeling contrast imaging (ECCI) technique to determine the TDD.[24] Figure 77(a-c) shows representative ECCI images from each GaAs/Si template. An area of 181 μm^2, ~580 μm^2, and ~3000 μm^2 for the Gen-I, II, and III buffers, respectively, has been surveyed. The TDD for each buffer is 2.8 × 10^8 cm^{-2}, 7.1 × 10^7 cm^{-2}, and 7.3 × 10^6 cm^{-2}.

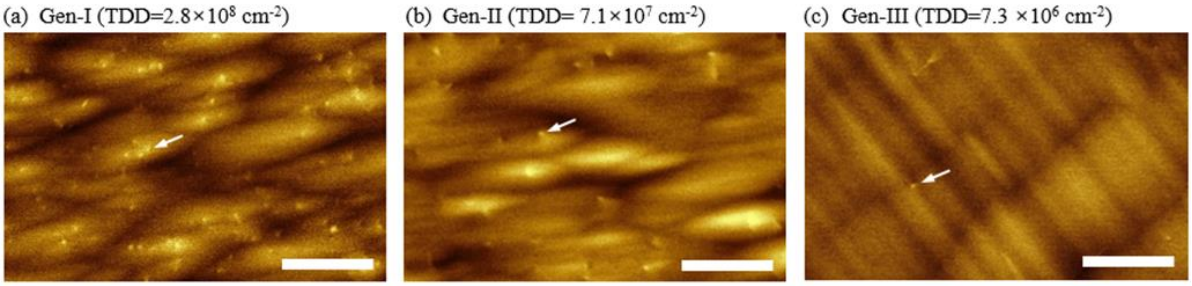

Figure 77. Electron channeling contrast images on GaAs buffers grown on Si. (a) Gen-I template, (b) Gen-II template, and (c) Gen-III template. Arrows indicate a single threading dislocation observed on the surface. The scale bar is 2 μm. From [77].

The Gen-I and Gen-II lasers have seven layers of p-modulation doped (p=5 × 10^{17} cm^{-3}) QD layers while Gen-III have five repeats of unintentionally doped (UID) QD layers. The lasers presented here have ridge widths from 3 to 5 μm and cavity lengths from 1000 to 1641 μm. One facet of the lasers was coated with a 95% high-reflectivity film.

For the reliability test, the laser chips were wirebonded onto AlN aging carriers and aged at Intel Corp. The QD lasers were stressed at 35 °C or 60 °C under continuous-wave (CW) operation and the driving current was set at about 2× the initial threshold current of each laser. Light-current-voltage (LIV) sweeps were periodically performed to monitor the laser performance.

Threshold currents were extracted from the LI curves, and they are displayed in Figure 78. The Gen-I lasers revealed rapid sub-linear increases in the threshold currents. One Gen-I laser (red circle) has a lifetime of 355 hours while the other (black circle) is expected to double the initial threshold in 1097 hours using a non-linear model.[36] The Gen-II and Gen-III lasers, which were grown on the 7×10^{7} cm^{-2} and 7×10^{6} cm^{-2} TDD templates, revealed improved reliability with slower increases in the threshold current over the aging periods shown in Figure 78(b-c). It should be noted that the Gen-III lasers operated with almost no degradation after the initial ~200 hours of aging at 35 °C, leading to extrapolated lifetimes $>10^{6}$ h.

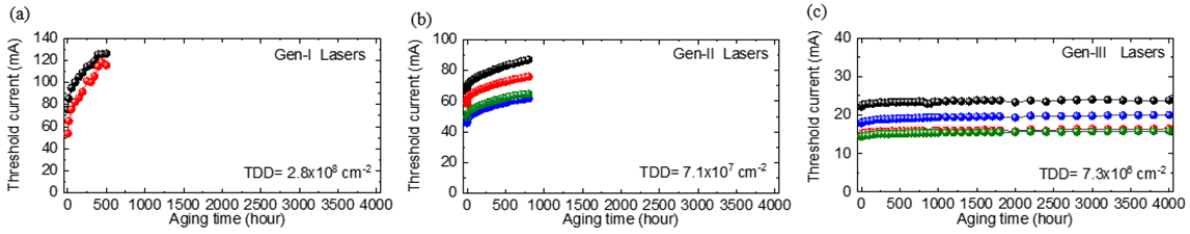

Figure 78. Continuous-wave threshold current versus aging time from (a) two Gen-I lasers, (b) four Gen-II lasers, and (c) four Gen-III lasers at 35 °C. From [77].

Figure 79 summarizes the extrapolated lifetimes of various QD lasers grown on the three different GaAs/Si templates and the lasers grown on Ge/Si template from Ref. [36]. The strong linear relationship between extrapolated lifetime and TDD indicates that dislocations dominate the device reliability despite a 20% increase in the dot density between Gen-I and Gen-II and significant increases in gain due to improved QD size homogeneity.

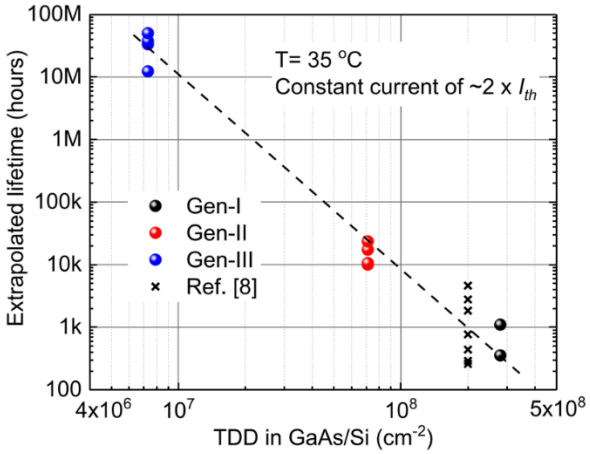

Figure 79. Extrapolated quantum dot laser lifetime versus the threading dislocation density. Lasers from Ref. [85] were aged at 30°C. The dashed line is a linear fit. From [77].

Note that the typical carrier migration length in the InAs/InGaAs QD system is around ~1 μm near room temperature in our material as confirmed by cathodoluminescence. In the case of the Gen-I lasers where the TDD is 2.8×10^8 cm^{-2}, there are roughly ~3 TDs in 1 μm^2. Therefore, injected carriers are highly likely to be captured by TDs and nonradiatively recombine before being captured by nearby QDs. However, the carriers in the Gen-III lasers, for instance, will have to migrate much farther to find TDs since they are ~3.7 μm from each other. This effectively increases the laser injection efficiency (η_i) and reduces the amount of REDC, enabling the superior reliability of the Gen-III lasers.[135]

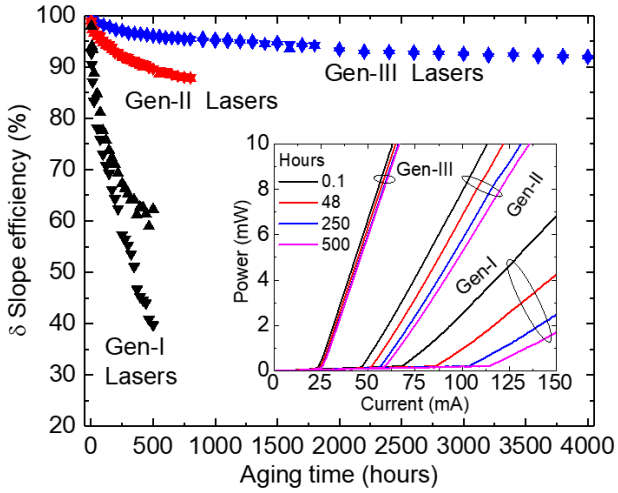

Figure 80. Changes in slope efficiency over aging time at 35 °C. Two representative lasers are shown from each template. Inset shows LI curves taken from a representative laser from each sample during the initial 500-hour aging period. From [77].

Another important parameter to study is the slope efficiency change above threshold since some applications may require some minimum output power. Figure 80 shows that the slope efficiencies of the Gen-I lasers dropped to almost half of the initial values during the 500-hour aging. However, the slope efficiencies of the Gen-III lasers decreased by only ~8% during the entire 4000-hour aging period. Figure 81 shows the average bias current increases to produce certain output powers during the aging tests: 2 mW for Gen-I and 10 mW for Gen-II and Gen-III. Using a power law fit ($y=a\times t^b$), lifetimes have been extrapolated based on a doubling of the bias needed for the prescribed output power and have achieved ~500 hours, ~27,000 hours, and ~5 million hours for Gen-I, Gen-II, and Gen-III, respectively. These results demonstrate that the Gen-III lasers grown on the low TDD template are able to maintain a low threshold current as well as a high slope efficiency.

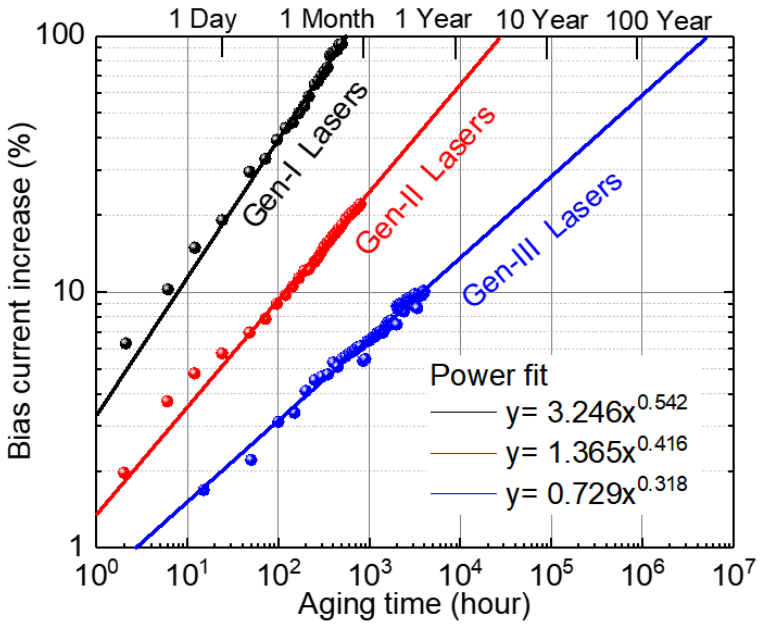

Figure 81. Bias current increase versus aging time. Solid lines are a power fit. R-squared values are 0.995, 0.996, and 0.978 for Gen-I, Gen-II and Gen-III, respectively. From [77].

Practical applications of QD lasers on Si such as data centers or on-chip optical interconnects may require long-term stable operation at an elevated temperature. To study reliability above room temperature, two undoped Gen-III lasers have been aged at 60°C and periodic LIV sweeps were taken at 35°C to investigate their accelerating degradation. The aging current (100 mA) was set at 2 × initial threshold current (44 mA and 49 mA) at 60°C. Unlike the 35°C aging result, we have observed faster degradation rates in both lasers, as shown in Figure 82(a). The lifetimes of the two lasers are ~2,500 hours at the 60°C aging condition. The higher temperature as well as the required higher bias current should both be contributing to the accelerated degradation rate. From the results above in the Gen-IV samples, one would expect pMD samples to have better lifetime at higher temperatures since they have lower thresholds, higher differential gain, and higher ground state maximum gain to provide for more margin for degradation before the failure point is reached. Figure 82(b) shows 35°C LI curves from one of the p-doped QD lasers (p=1 × 18 cm^{-2}, TDD ~7 × 10^6 cm^{-}

^{2}) that has been aged at 60°C and 80 mA driving current. The laser initial threshold current was 37.5 mA at 60°C. The extrapolated lifetimes (doubling the initial threshold) of the pMD lasers are ~65,000 hours.

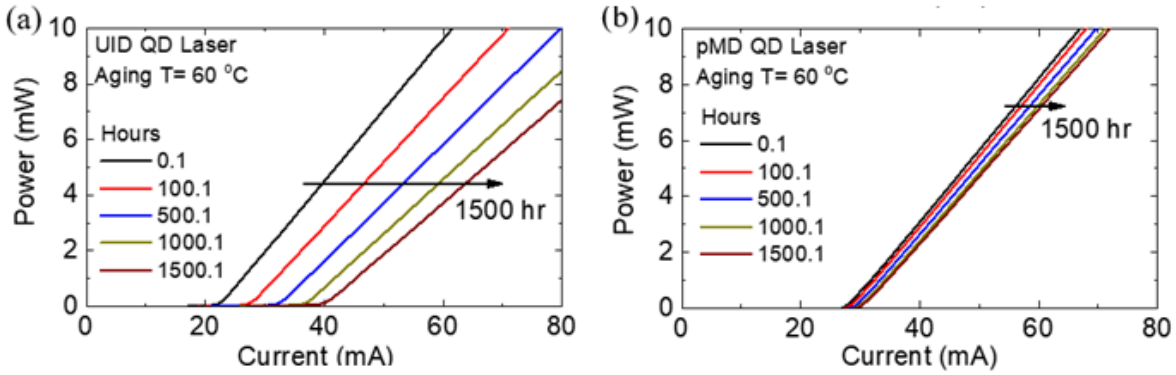

Figure 82. LI curves from 60 °C aging test of (a) 3.5 × 1633 µm UID QD laser and (b) 3.5×1364 µm p-doped QD laser. LIV sweeps taken at 35 °C after cooling from aging temperature. From [77].

The results above show extraordinary improvements in the device lifetime as the threading dislocation density has been reduced, but the results still lag behind what is needed for commercial applications and fall far short of commercialized heterogeneously integrated lasers. While an obvious path forward is to reduce the dislocation density, the methods to filter dislocations become far less effective as the dislocation density decreases, and state-of-the-art GaAs/Si dislocation densities have been stuck at ~1×10^{6} cm^{-2} for decades suggesting that there is not a lot of room for improvement. However, threading dislocations, while a good surrogate, are not the true problem.

Returning to Figure 76(a), there are clearly misfit dislocations in the active region of the laser. These misfits seem to be present at a density of ~1 μm^{-1} in the [110] direction and much lower density in the $[1\bar{1}0]$ direction, as expected in GaAs. Given that a single misfit affects dots all along its length, misfits should be far more detrimental than the threading dislocations that intersect the dot layer at a single point. The correlation between threading dislocation

density and lifetime suggests that existing threads are a nucleation source for misfits in the active region. It should be noted that no such misfits are observed in identical QD lasers grown on GaAs substrates, so the existence of threading dislocations has either lowered the critical thickness by reducing energy barriers to misfit formation, or the driving force for misfit formation is the thermal stress during device cooldown that only exists on Si due to the thermal expansion mismatch.

If the dot layers are passing critical thickness on Si and relaxing during growth, then the only hope for improvement is to reduce the number of dot layers. Cross-sectional and plan-view transmission electron microscopy (TEM) images of four QD layer samples showed that all visible misfits were in the top dot layer. In response, lasers were grown with three layers of quantum dots, but their reliability was similar to the lasers with four or five dot layers. TEM studies are in progress to determine if there are misfits in the top dot layer.

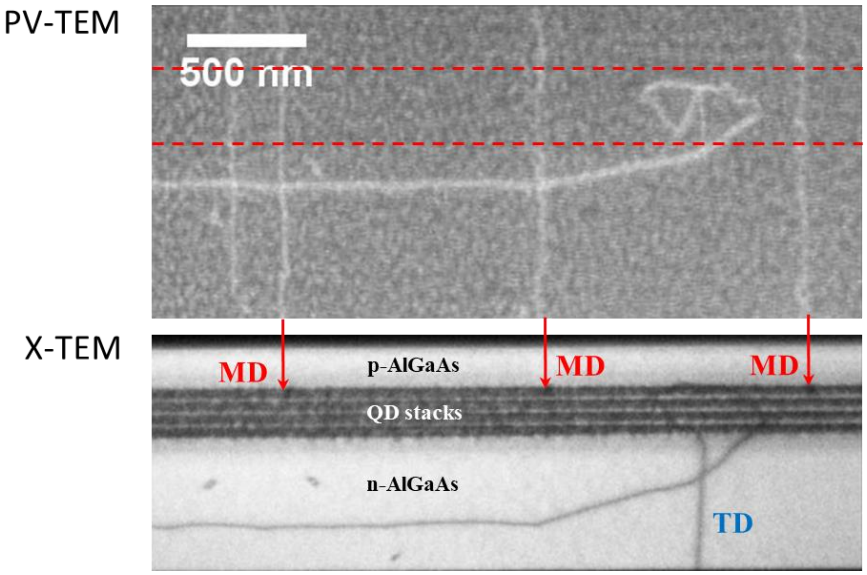

Figure 83. (Top) Plan-view and (Bottom) cross-sectional transmission electron microscope images of the active region of a quantum dot laser with four layers of dots showing misfit dislocations (MD) all appearing in the top layer of dots.

In parallel to growing lasers with fewer dot layers, two samples were grown for cathodoluminescence (CL) studies that used the usual GaAs/GaP/Si buffer structure but replaced the laser that would be grown on top with either a single QD layer or five QD layers. ECCI and CL were performed, and, unfortunately, similar misfit dislocation densities were observed in both samples. This result was highly surprising, and the samples should be reproduced to confirm the result, but it suggests that the misfits are not coming from the cumulative lattice mismatch associated with multiple dot layers.

If the misfits result from the thermal expansion mismatch, then they are likely forming from the epi surface during cooldown post-growth and are gliding downward into the material and becoming pinned at the top dot interface. To minimize thermal stresses the III-V material could be grown selectively, or the stress could, in theory, be compensated mechanically in the sample mount for growth or through backside coatings on the Si. Alternatively, strained dislocation pinning layers could be added near the top of the epi stack to possibly prevent the dislocations from gliding to the dot layers. Solving this problem is likely necessary to realizing true commercial viability and should remain an ongoing focus of the project.

Summary

Device performance and reliability were presented through multiple generations of material optimization. Each generation of material improved either the quantum dot growth conditions for narrower, brighter luminescence, the III-V/Si buffer layers for lower dislocation densities, or both. All results presented were obtained on industry-standard, on-axis silicon substrates. Through optimized growth conditions, the quantum dot photoluminescence full-width at half-maximum was reduced from >50 meV on silicon to 30 meV, and the dislocation density of the GaAs/Si templates was reduced from 3×10^{8} cm^{-2} to 7×10^{6} cm^{-2}. The material

improvement translated into dramatic enhancements in laser performance with threshold currents being reduced from initial values of ~30 mA to < 5 mA in similar devices, more than doubling of the laser output power, increased maximum continuous wave operating temperatures from 80°C to 107°C, and, most significantly, improved device lifetimes from a few thousand hours at 35°C to >10,000,000 hours and even led to >100,000 hour lifetimes at 60°C. These results are very near what is necessary for commercial applications, and through further material improvements to eliminate misfit dislocations from the quantum dot active region, commercially viable lifetimes should be attainable with performance rivaling native substrate devices.

Chapter 7

Summary & Future Work

Summary of Results

Over the course of this thesis, efforts have doubled down globally on developing CMOS compatible, epitaxial materials platforms on Si leading to impressive results in material quality and record setting device performance. Many strategies are being pursued by various groups. The first ever lasing results on on-axis Si were achieved simultaneously at the University of California, Santa Barbara by Liu et al.[138] and Norman et al.[139] using III-V/Si buffer templates developed by Huang et al. at Yale University [155] and Li et al. at the Hong Kong University of Science and Technology [25]. The approach by Huang et al. utilized a 45 nm pseudomorphic GaP layer grown directly on Si by metal-organic chemical vapor deposition (MOCVD) that was pioneered by $NAsP_{III/V}$, GmbH. $NAsP_{III/V}$ utilizes a series of carefully optimized surface treatments including Si homoepitaxy to grow antiphase domain free GaP directly on on-axis Si with no additional defect formation due to the small mismatch between GaP and Si [156]. Using such a template for subsequent mismatched growth of GaAs is simpler than direct Si growth because only the TDs must be contended with and GaAs

nucleates more favorably on GaP. The first results on this template yielded TD densities of 2×10^{8} cm^{-2}. Further refinement of the GaAs/GaP growth conditions by Jung et al. and the inclusion of thermal cycle annealing and dislocation filter layers pushed the TD density down to 7×10^{6} cm^{-2} [24]. The procedure developed by Li et al. at HKUST is equally promising and utilizes a CMOS compatible crystallographic etch to pattern v-shaped trenches in an on-axis Si substrate, aspect ratio trapping to limit defect propagation, and coalescence of an overgrown GaAs layer to provide bulk templates [157]. The {111} v-groove surface suppresses the formation of antiphase domains and limits TD propagation as demonstrated in the pioneering work at IMEC by Paladugu et al. [73]. Coalesced films of GaAs-on-v-groove-Si (GoVS) yielded TD densities of 4×10^{6} cm^{-2} when grown with identical filtering layers to that used on GaP/Si. Efforts are also underway to grow GaAs directly on planar Si by way of an AlAs nucleation layer by Chen et al. at University College London resulting in electrically injected lasing, but defect densities have not been reported [71]. Additional work is ongoing to produce as-grown laser cavities using III-V from a single trench [158, 159], which has yielded optically pumped devices operating at room temperature [159].

Of the previous approaches to CMOS compatible Si integration, the GaP/Si and GoVS templates are most mature and have yielded the most promising device results with performance exceeding that obtained on miscut Si and rivaling or exceeding even what has been achieved through heterogeneous integration. We have achieved CW RT threshold currents as low as 4.8 mA, single-facet output powers of 175 mW, ground state lasing up to 107°C, and wall-plug-efficiencies as high as 38.4%, and extrapolated lifetimes in excess of 10,000,000 hours for aging at 35°C and twice the threshold current density [135, 141]. Highlights are shown in Figure 84.

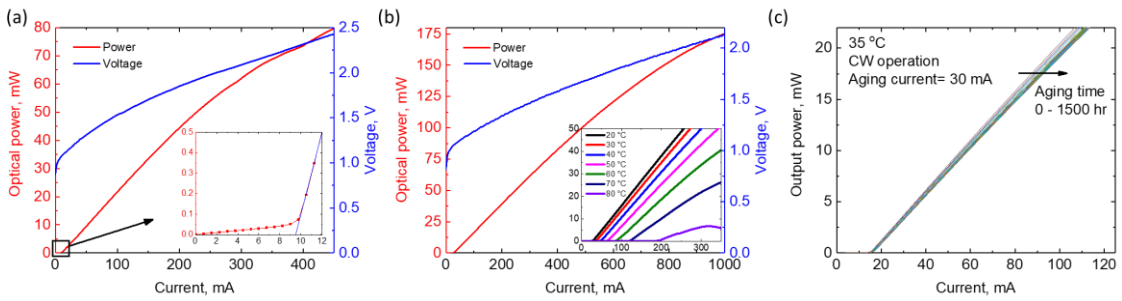

Figure 84. Highlighted results for as-cleaved Fabry-Perot lasers on on-axis (001) Si substrates showcasing (a) record low threshold currents of <10 mA (from [141]), (b) record single-facet output powers of 175 mW and continuous wave lasing up to 80°C (from [141]), and (c) LI curves as a function of continuous aging time at twice threshold and 35°C from zero to 1,500 hours aging (from [135]).

Beyond reducing the dislocation density, dramatic improvements in performance were obtained by adding p-type modulation doping to the laser active region and narrowing the inhomogeneous broadening of the material through optimized QD growth conditions. By introducing just 5×10^{17} cm^{-3} doping to a 10 nm GaAs layer in the spacer between QD layers, the gain coefficient, ground state saturated gain, and high temperature performance can all be improved. Improving these parameters led to demonstration of designing lasers with zero linewidth enhancement factor [70], perfectly stable laser operation at 90% optical feedback levels [90], 9.5 GHz K-factor limited direct modulation bandwidth [148], and record long extrapolated device lifetimes of >1,000,000 h at 60°C. Results are highlighted in Figure 85.

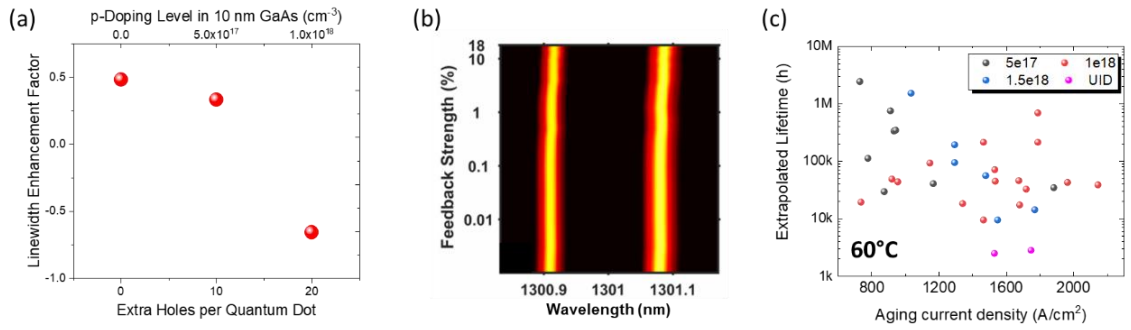

Figure 85. (a) Variation in the linewidth enhancement factor with different levels of p-modulation doping in the laser active region showing the possibility of achieving zero or negative values after [70]. (b) Optical spectra of a laser with varied levels of optical feedback up to 90% reflected (18% after coupling losses) of the laser output power after [90]. (c) Extrapolated device lifetime for lasers with varied p-doping level aged at 60°C and varied current density with a failure criterion of doubling the threshold current.

While excellent performance has now been demonstrated in epitaxial quantum dot lasers on silicon, more work remains to be done in a few key areas: high temperature reliability, quantum dot devices other than lasers, and in device integration with waveguides and other components. Long lifetimes have been achieved at 60°C but only in a few hero devices. The overall performance needs to be brought up to a similar level and likely needs to show similar results at >80°C for commercial viability. To achieve that goal more work needs to be done to understand the failure mechanisms of quantum dot lasers and to reduce the number of misfit dislocations in the laser active region. Other than lasers, quantum dot devices have not been widely explored. Some work has been done on detectors and modulators, but it is very preliminary and should be explored further, particularly for the possibility of device integration without multiple regrowth steps, which brings up the final point: integration. For all of the benefits of quantum dots described in this thesis to be realized, they must be incorporated in photonic integrated circuits. The methods for doing so could be many. Platforms could include growth in trenches on silicon-on-insulator (SOI) wafers to align the quantum dots to the Si device layer, other designs could use dielectric waveguides deposited

to couple between components, or other embodiments could utilize an all III-V platform where silicon only serves as a cheap, scalable substrate.

Eliminating Misfit Dislocations

While the previous chapter showed strong correlations between threading dislocation density and device lifetime, it is likely that misfit dislocations are the real culprit in degradation since they lie in the quantum dot plane affecting much larger fractions of the active region. To remove the misfits, their source must first be understood. Single quantum dot layers grown on silicon show misfits at similar density to five quantum dot layers suggesting that the lattice mismatch of the dots is not the culprit, but instead that the thermal expansion mismatch is forming misfits that glide to the active layers on cooldown. Potential solutions to such a problem include sacrificial dislocation pinning layers near the device surface or growth in narrow trenches where thermal stress can relax through the sidewalls. That being said, the conclusion that thermal expansion mismatch is the culprit is not absolutely certain. The quantum dot layers could be relaxing during growth starting from the first layer, and if that is the case, then growing at a lattice constant incorporating more In could be the answer. Since the substrate is already Si, there is not a significant disadvantage to shifting the laser lattice constant longer by adding perhaps 5% In to the buffer layers and laser cladding. In any case, detailed failure analysis and defect formation studies need to be conducted to understand the problem before it can be solved.

Other Quantum Dot Devices

The unique characteristics of quantum dots apply to optoelectronic devices other than just lasers and amplifiers [13]. Their unique density of states leads to ultralow dark currents for

photodetectors, and their excitonic nature and high electro-optic coefficients could be useful in optical modulators. Quantum dots exhibit ultrafast gain recovery that has enabled record low pulsewidths in mode-locked lasers, and their high four-wave mixing has led to single-section mode-locked lasers with no absorber. Quantum dots also have tunable bandwidth in the growth conditions for making broad, flat frequency combs and broadband amplifiers. These areas are all the subject of ongoing work with very promising recent results in our material on silicon.

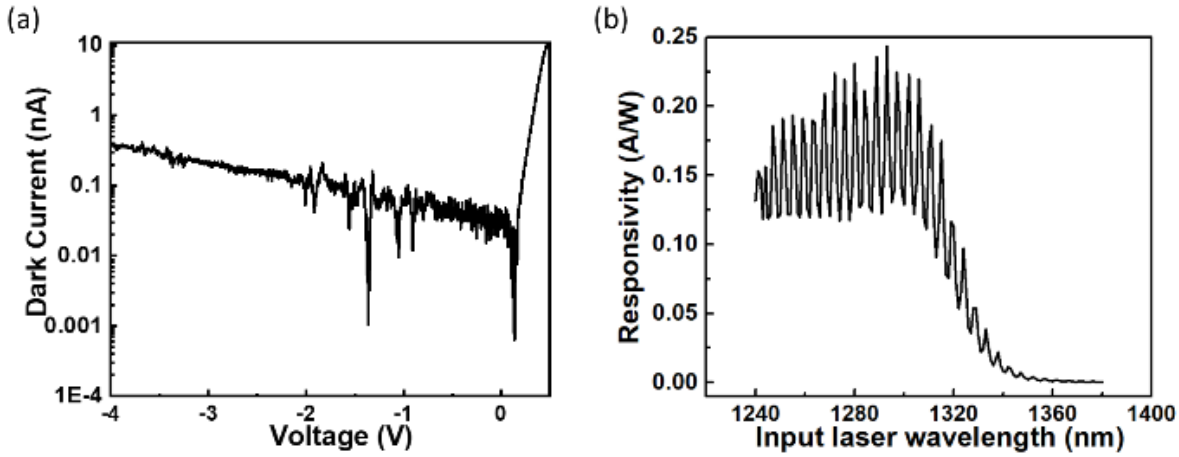

Figure 86. **(a) Photodetector dark current as a function of reverse bias voltage. (b) Responsivity versus wavelength of received light after [160].**

Using the Gen-III optimized GaAs/Si buffers and multiple layers of InAs quantum dots in $In_{.15}Ga_{.85}As$ quantum wells, we have demonstrated high performance mode-locked lasers, modulators, and photodetectors on silicon and have begun developing an epitaxial platform for integration of these components. Waveguide photodetectors have been produced with record low ~0.1 nA dark current and responsivity of >0.2 A/W (Figure 86), and 10 mm Mach-Zehnder modulators with a single-arm $V\pi$ of 3.69 V and extinction ratio of 80% (Figure 87) have also been fabricated. Each component individually represents a breakthrough in epitaxial

III-V material on Si, but they are only first-generation devices and could be further optimized. For example, the photodetector uses an identical epi structure to the five quantum dot layer lasers presented previously, and the responsivity could likely be increased with more layers. Meanwhile, the modulator of Figure 87 did not utilize traveling-wave electrodes for high speed operation and was not optimized for light coupling such that significant fractions of the light was guided in mesa modes that did not see the quantum dot layers.

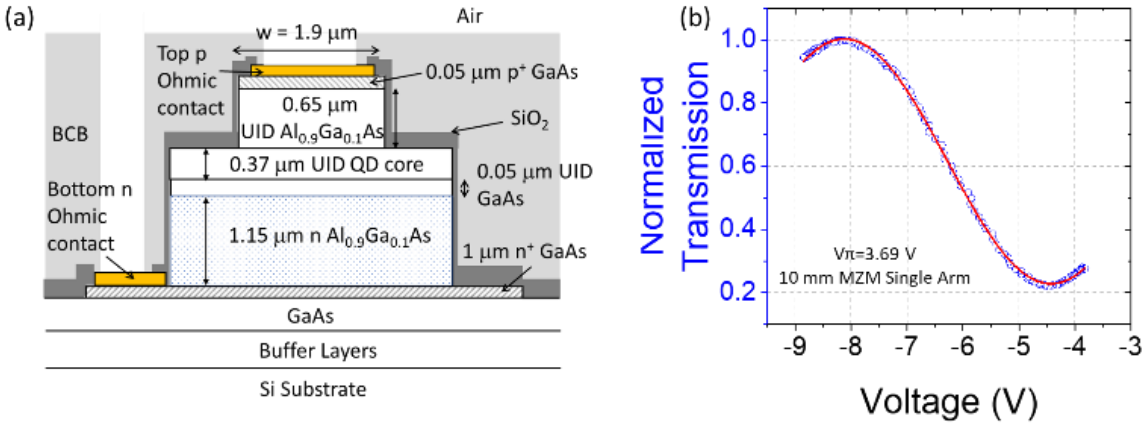

Figure 87. (a) Mach-Zehnder modulator cross-sectional schematic. (b) Normalized transmission versus bias voltage in single-arm configuration [161].

First generation mode-locked lasers have also been fabricated demonstrating in various devices: high repetition rates of 96 GHz, narrow pulse widths of 490 fs [162], and broad frequency combs containing 58 comb lines within the 3 dB bandwidth at 20 GHz spacing[92]. The 96 GHz result was achieved using quantum dots designed for narrow inhomogeneous broadening and only exhibited four locked modes within 3 dB. The pulsewidth was also chirped with a width of 1.5 ps. With design of a broader gain bandwidth through chirped quantum dot layers, more modes could be locked together, and with dispersion engineering, the chirp could be reduced leading to significant narrowing on the pulse. The 490 fs pulsewidth result is a world record for a laser on silicon and was the first

observation of self-mode-locking on silicon. Ongoing collaborations with Weng Chow at Sandia National Laboratories promises to reveal the underlying theoretical mechanisms of self-mode-locking in quantum dot lasers which could lead to improved designs. The first attempt made at using chirped quantum dot layers on silicon yielded 58 comb lines locked together at a 20 GHz spacing that showed record low timing jitter and yielded 4.1 Tb/s PAM-4 transmission with each comb line modulated at 25 Gbaud below the soft-decision forward error correction limit. The 70 nm FWHM chirped gain bandwidth of the laser is likely significantly below what is achievable, and with an integrated amplifier, error rates could be reduced dramatically.

Epitaxial Integration Schemes

Epitaxial integration could take one of several embodiments. One approach pursued by IMEC uses aspect ratio trapping in nanoscale trenches to eliminate crystalline defects within a couple hundred nanometers of growth [159]. Such an approach could be integrated with SOI (Figure 88(a)) and is promising in that the active layers can be grown within reasonable coupling distances of the underlying Si, and the optical cavity is formed as-grown rather than being etched, which may lead to improved passivation and reduced optical scattering. The problem with such an approach is that electrical injection of such structures is challenging and will likely have to be done through the highly defective III-V/Si interface which could generate a large resistance. Alternatively, standard III-V laser epi structures with thick buffers and contact layers could be grown on SOI with electrical injection all in the III-V layers and tapers or grating couplers could be used to inject the light into the underlying Si waveguides. Tapers are commonly used for heterogeneous integration to force the optical mode into the Si, and recently, a slotted waveguide was used to incline emitted light from a laser at 54.6°

with a low divergence angle of 1.7° which could be directed on a vertical coupler in the Si substrate for waveguide integration [163]. Another approach is to follow the established methods of heterogeneous integration and bond III-V epi grown on Si to patterned SOI substrates. Such an approach gains the economic benefits of eliminating the III-V substrate cost but retains the manufacturing complexity associated with wafer or die bonding, which is much simpler when bonding two 300 mm wafers than multiple smaller wafers on a single Si wafer. A simpler but analogous method would be to deposit amorphous Si [164] or simply bond a Si wafer to the top of the III-V epi and process it into waveguides (Figure 88(c)). This approach would use evanescent coupling in the upward direction analogous to the coupling scheme in current bonded lasers. The bonding in this case would be a bit simpler than bonding dies of III-V epi since it could easily be done at the wafer scale requiring minimal alignment. A fourth approach could involve the direct growth of III-V material from the handle wafer of an SOI substrate with the device active layers aligned to the device layer silicon (Figure 88(b)). The device layer would then be processed into standard silicon photonic components optimized around the SOI platform, and the III-V material would be butt-coupled to a waveguide. The principle challenge with this approach is that the III-V must completely fill the space up to the waveguide as the coupling efficiency drops rapidly with gaps even as small as 500 nm [165]. We discuss this embodiment in more detail in [36]. A final proposed approach would be to simply perform all functions in the III-V epi layers either through evanescent coupling to a waveguide layer (Figure 88(e)), regrowth, or intermixing. This embodiment would purely adopt Si as a cheap scalable substrate and leverage the suite of techniques and processes already commercialized in InP PICs for active and passive functions [166]. Such an approach achieves all the advantages of III-V PICs over heterogeneous

integration, eliminates the III-V substrate cost, and improves the thermal impedance of devices due to silicon's higher thermal conductivity than III-Vs [167].

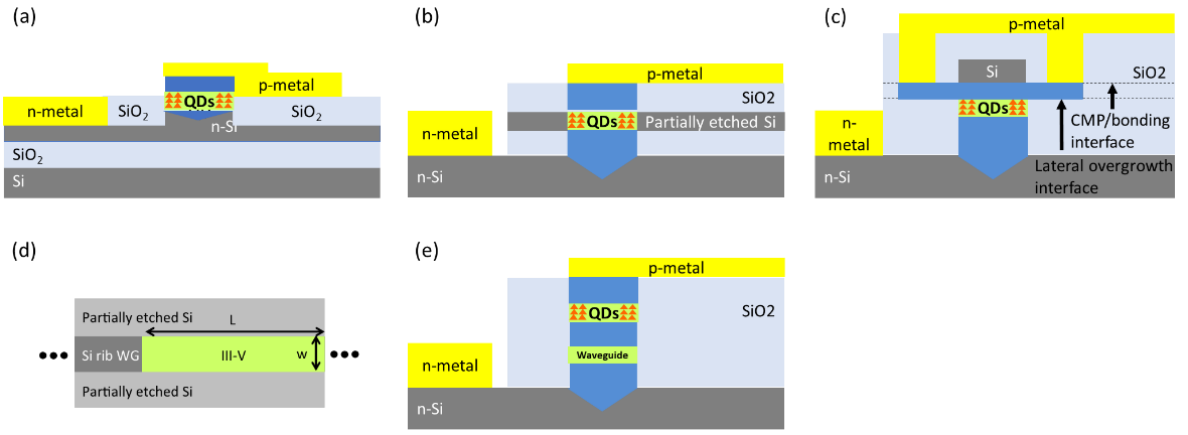

Figure 88. Schematic illustrations of potential III-V/Si integration schemes including embodiments using a silicon waveguide: (a) direct growth on SOI, (b) growth on patterned SOI from the handle wafer with butt-coupling to a Si device layer waveguide, and (c) growth on Si with a bonded Si waveguide on top of the III-V epi. (d) Top-down schematic of structures (a-c) showing III-V and Si waveguides. (e) An all III-V integration scheme where a separate waveguide layer is grown in the III-V layers for evanescent coupling. From [13].

Preliminary designs and growth of an all III-V platform have been conducted. Starting from our optimized buffer and laser epi, we have designed, simulated, and grown a material stack on Si (Figure 89(a)) that includes an evanescently coupled GaAs waveguide layer while maintaining a total buffer+laser epi thickness of ~7 μm to avoid cracking. Despite cutting the dislocation filtering region in half relative to our optimized structure, we have maintained a low dislocation density of $2\text{-}3\times10^{7}$ cm^{-2} prior to the $Al_{.7}Ga_{.3}As$ cladding as shown in Figure 89(e). These structures are currently undergoing process development.

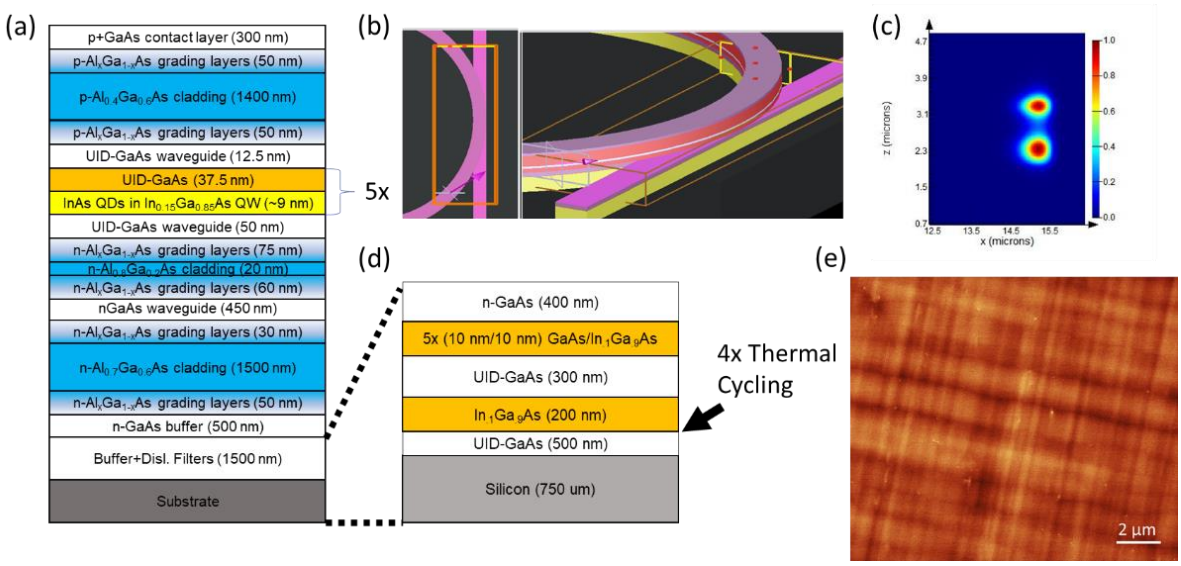

Figure 89. (a) Full epitaxial layer structure of waveguide coupled laser. (b) Schematic illustration of epitaxial ring laser with straight waveguide. (c) Simulated mode profile within ring. (d) Dislocation filtering layers for epitaxial buffer on Si. (e) Electron channeling contrast image at the top of the buffer showing dislocations and surface morphology.

Conclusion

Through the work presented in this thesis significant advancements in the performance of lasers on silicon have been made. Records have been set in every laser figure of merit for an epitaxial device on silicon. For the first time, device reliability has reached a point where commercial viability appears to be a very real possibility, potentially even in just a few years' time. More work remains to be done to lower the density of threading dislocations and eliminate or reduce the density of misfit dislocations, but based on the reliability scaling presented in Chapter 6 of this thesis, it appears likely that only modest improvements are necessary (perhaps to 1×10^{6} cm^{-2} threading dislocation density) for commercial viability rather than orders of magnitude improvement being necessary. Such results are almost certainly achievable through straightforward growth iteration and optimization for the epitaxial buffer. Equally important to the laser performance is its integrability into a photonic

integrated circuit. To this end, waveguide coupling is a necessity, and this has not been demonstrated in an epitaxial device. While many embodiments are possible as described above, some will require material quality sacrifices or redesigning (and, therefore, re-optimizing) of the epitaxial III-V/Si buffer. That said, irrespective of the future of lasers grown on Si, quantum dots will have uses for their unique high temperature performance, stable and high-performance mode-locking, and low susceptibility to optical feedback. Except in cases where high speed direct modulation is needed, there is no benefit to choosing a quantum well device over a quantum dot device if a quantum dot device can be supplied with sufficiently low inhomogeneous broadening (similar to the levels demonstrated here and commercially available from QD Laser, Inc.).

References

[1] R. Courtland, "Intel Now Packs 100 Million Transistors in Each Square Millimeter," 2017.

[2] Z. I. Alferov, V. Andreev, D. Garbuzov, Y. V. Zhilyaev, E. Morozov, E. Portnoi, and V. Trofim, "Investigation of the influence of the AlAs-GaAs heterostructure parameters on the laser threshold current and the realization of continuous emission at room temperature," *Sov. Phys. Semicond,* vol. 4, no. 9, pp. 1573-1575, 1971.

[3] H. Kroemer, "A proposed class of hetero-junction injection lasers," *Proceedings of the IEEE,* vol. 51, no. 12, pp. 1782-1783, 1963.

[4] Z. I. Alferov and R. Kazarinov, "Double heterostructure laser," *Authors Certificate,* no. 27448, 1963.

[5] G. Li, J. Yao, H. Thacker, A. Mekis, X. Zheng, I. Shubin, Y. Luo, J.-H. Lee, K. Raj, and J. E. Cunningham, "Ultralow-loss, high-density SOI optical waveguide routing for macrochip interconnects," *Optics express,* vol. 20, no. 11, pp. 12035-12039, 2012.

[6] J. F. Bauters, M. J. Heck, D. D. John, J. S. Barton, C. M. Bruinink, A. Leinse, R. G. Heideman, D. J. Blumenthal, and J. E. Bowers, "Planar waveguides with less than 0.1 dB/m propagation loss fabricated with wafer bonding," *Optics express,* vol. 19, no. 24, pp. 24090-24101, 2011.

[7] E. J. Stanton, M. J. Heck, J. Bovington, A. Spott, and J. E. Bowers, "Multi-octave spectral beam combiner on ultra-broadband photonic integrated circuit platform," *Optics express,* vol. 23, no. 9, pp. 11272-11283, 2015.

[8] R. A. Soref, S. J. Emelett, and W. R. Buchwald, "Silicon waveguided components for the long-wave infrared region," *Journal of Optics A: Pure and Applied Optics,* vol. 8, no. 10, p. 840, 2006.

[9] L. Shen, N. Healy, C. J. Mitchell, J. S. Penades, M. Nedeljkovic, G. Z. Mashanovich, and A. C. Peacock, "Mid-infrared all-optical modulation in low-loss germanium-on-silicon waveguides," *Optics letters,* vol. 40, no. 2, pp. 268-271, 2015.

[10] C. Doerr, L. Chen, T. Nielsen, R. Aroca, L. Chen, M. Banaee, S. Azemati, G. McBrien, S. Y. Park, and J. Geyer, "O, E, S, C, and L band silicon photonics coherent modulator/receiver," in *Optical Fiber Communications Conference and Exhibition (OFC), 2016,* 2016, pp. 1-3: IEEE.

[11] R. E. Camacho-Aguilera, Y. Cai, N. Patel, J. T. Bessette, M. Romagnoli, L. C. Kimerling, and J. Michel, "An electrically pumped germanium laser," *Optics express,* vol. 20, no. 10, pp. 11316-11320, 2012.

[12] N. Kobayashi, K. Sato, M. Namiwaka, K. Yamamoto, S. Watanabe, T. Kita, H. Yamada, and H. Yamazaki, "Silicon photonic hybrid ring-filter external cavity wavelength tunable lasers," *Journal of Lightwave Technology,* vol. 33, no. 6, pp. 1241-1246, 2015.

[13] J. C. Norman, D. Jung, Y. Wan, and J. E. Bowers, "Perspective: The future of quantum dot photonic integrated circuits," *APL Photonics,* vol. 3, no. 3, p. 030901, 2018.

[14] A. W. Fang, H. Park, O. Cohen, R. Jones, M. J. Paniccia, and J. E. Bowers, "Electrically pumped hybrid AlGaInAs-silicon evanescent laser," *Optics express,* vol. 14, no. 20, pp. 9203-9210, 2006.
[15] T. Komljenovic, D. Huang, P. Pintus, M. A. Tran, M. L. Davenport, and J. E. Bowers, "Heterogeneous III-V silicon photonic integrated circuits," *Proceedings of the IEEE,* 2018.
[16] C. Zhang and J. E. Bowers, "Silicon photonic terabit/s network-on-chip for datacenter interconnection," *Optical Fiber Technology,* 2017.
[17] B. R. Koch, E. J. Norberg, B. Kim, J. Hutchinson, J.-H. Shin, G. Fish, and A. Fang, "Integrated silicon photonic laser sources for telecom and datacom," in *National Fiber Optic Engineers Conference*, 2013, p. PDP5C. 8: Optical Society of America.
[18] D. Liang, X. Huang, G. Kurczveil, M. Fiorentino, and R. Beausoleil, "Integrated finely tunable microring laser on silicon," *Nature Photonics,* vol. 10, no. 11, p. 719, 2016.
[19] R. Intel, "Intel® silicon photonics 100G PSM4 optical transceiver brief," ed, 2017.
[20] R. Jones, P. Doussiere, J. B. Driscoll, W. Lin, H. Yu, Y. Akulova, T. Komljenovic, and J. E. Bowers, "Heterogeneously Integrated Photonics," *Nanotechnology Magazine,* 2018.
[21] T. Komljenovic, D. Huang, P. Pintus, M. A. Tran, M. L. Davenport, and J. E. Bowers, "Photonic Integrated Circuits Using Heterogeneous Integration on Silicon," *Proceedings of the IEEE,* no. 99, pp. 1-12, 2018.
[22] A. Y. Liu and J. Bowers, "Photonic Integration with Epitaxial III-V on Silicon," *IEEE Journal of Selected Topics in Quantum Electronics*, 09 July 2018 2018.
[23] I. George, F. Becagli, H. Liu, J. Wu, M. Tang, and R. Beanland, "Dislocation filters in GaAs on Si," *Semiconductor Science and Technology,* vol. 30, no. 11, p. 114004, 2015.
[24] D. Jung, P. G. Callahan, B. Shin, K. Mukherjee, A. C. Gossard, and J. E. Bowers, "Low threading dislocation density GaAs growth on on-axis GaP/Si (001)," *Journal of Applied Physics,* vol. 122, no. 22, p. 225703, 2017.
[25] Q. Li, K. W. Ng, and K. M. Lau, "Growing antiphase-domain-free GaAs thin films out of highly ordered planar nanowire arrays on exact (001) silicon," *Applied Physics Letters,* vol. 106, no. 7, p. 072105, 2015.
[26] S. Adachi, *Handbook on physical properties of semiconductors*. Springer Science & Business Media, 2004.
[27] S. Chen, W. Li, J. Wu, Q. Jiang, M. Tang, S. Shutts, S. N. Elliott, A. Sobiesierski, A. J. Seeds, and I. Ross, "Electrically pumped continuous-wave III–V quantum dot lasers on silicon," *Nature Photonics,* vol. 10, no. 5, p. 307, 2016.
[28] S. Ting, M. T. Bulsara, V. Yang, M. Groenert, S. Samavedam, M. Currie, T. Langdo, E. A. Fitzgerald, A. M. Joshi, and R. Brown, "Monolithic integration of III-V materials and devices on silicon," in *Silicon-based Optoelectronics*, 1999, vol. 3630, pp. 19-29: International Society for Optics and Photonics.
[29] P. A. Andrekson, N. A. Olsson, T. Tanbun-Ek, R. A. Logan, D. Coblentz, and H. Temkin, "Novel technique for determining internal loss of individual semiconductor lasers," *Electronics Letters,* vol. 28, no. 2, pp. 171-172, 1992.
[30] L. A. Coldren, S. W. Corzine, and M. L. Mashanovitch, *Diode lasers and photonic integrated circuits*. John Wiley & Sons, 2012.

[31] Y. Arakawa and H. Sakaki, "Multidimensional quantum well laser and temperature dependence of its threshold current," *Applied Physics Letters,* vol. 40, no. 11, pp. 939-941, 1982.
[32] N. Kirstaedter, N. Ledentsov, M. Grundmann, D. Bimberg, V. Ustinov, S. Ruvimov, M. Maximov, P. S. Kop'ev, Z. I. Alferov, and U. Richter, "Low threshold, large T/sub o/injection laser emission from (InGa) As quantum dots," *Electronics Letters,* vol. 30, no. 17, pp. 1416-1417, 1994.
[33] R. Mirin, A. Gossard, and J. Bowers, "Room temperature lasing from InGaAs quantum dots," *Electronics Letters,* vol. 32, no. 18, p. 1732, 1996.
[34] D. Bimberg and U. W. Pohl, "Quantum dots: promises and accomplishments," *Materials Today,* vol. 14, no. 9, pp. 388-397, 2011.
[35] T. Kageyama, K. Nishi, M. Yamaguchi, R. Mochida, Y. Maeda, K. Takemasa, Y. Tanaka, T. Yamamoto, M. Sugawara, and Y. Arakawa, "Extremely high temperature (220° C) continuous-wave operation of 1300-nm-range quantum-dot lasers," in *The European Conference on Lasers and Electro-Optics*, 2011, p. PDA_1: Optical Society of America.
[36] A. Y. Liu, S. Srinivasan, J. Norman, A. C. Gossard, and J. E. Bowers, "Quantum dot lasers for silicon photonics," *Photonics Research,* vol. 3, no. 5, pp. B1-B9, 2015.
[37] A. Y. Liu, T. Komljenovic, M. L. Davenport, A. C. Gossard, and J. E. Bowers, "Reflection sensitivity of 1.3 μm quantum dot lasers epitaxially grown on silicon," *Optics Express,* vol. 25, no. 9, pp. 9535-9543, 2017.
[38] H. Schmeckebier and D. Bimberg, "Quantum-dot semiconductor optical amplifiers for energy-efficient optical communication," in *Green Photonics and Electronics*: Springer, 2017, pp. 37-74.
[39] D. Arsenijević and D. Bimberg, "Quantum-dot mode-locked lasers: Sources for tunable optical and electrical pulse combs," in *Green Photonics and Electronics*: Springer, 2017, pp. 75-106.
[40] J. C. Norman, D. Jung, Z. Zhang, Y. Wan, S. Liu, C. Shang, R. W. Herrick, W. W. Chow, A. C. Gossard, and J. E. Bowers, "High Performance Quantum Dot Lasers on Silicon," *IEEE Journal of Quantum Electronics,* Submitted.
[41] R. Mirin, J. Ibbetson, K. Nishi, A. Gossard, and J. Bowers, "1.3 μm photoluminescence from InGaAs quantum dots on GaAs," *Applied physics letters,* vol. 67, no. 25, pp. 3795-3797, 1995.
[42] A. J. Zilkie, J. Meier, M. Mojahedi, P. J. Poole, P. Barrios, D. Poitras, T. J. Rotter, C. Yang, A. Stintz, and K. J. Malloy, "Carrier Dynamics of Quantum-Dot, Quantum-Dash, and Quantum-Well Semiconductor Optical Amplifiers Operating at 1.55$\mu {\hbox {m}} $," *IEEE Journal of Quantum Electronics,* vol. 43, no. 11, pp. 982-991, 2007.
[43] V. Shchukin, N. N. Ledentsov, and D. Bimberg, *Epitaxy of nanostructures*. Springer Science & Business Media, 2013.
[44] O. Stier, M. Grundmann, and D. Bimberg, "Electronic and optical properties of strained quantum dots modeled by 8-band k· p theory," *Physical Review B,* vol. 59, no. 8, p. 5688, 1999.
[45] P. Jayavel, H. Tanaka, T. Kita, O. Wada, H. Ebe, M. Sugawara, J. Tatebayashi, Y. Arakawa, Y. Nakata, and T. Akiyama, "Control of optical polarization anisotropy in

edge emitting luminescence of InAs/GaAs self-assembled quantum dots," *Applied Physics Letters,* vol. 84, no. 11, pp. 1820-1822, 2004.
[46] K. Nishi, K. Takemasa, M. Sugawara, and Y. Arakawa, "Development of quantum dot lasers for data-com and silicon photonics applications," *IEEE Journal of Selected Topics in Quantum Electronics,* vol. 23, no. 6, pp. 1-7, 2017.
[47] A. O. Kosogov, P. Werner, U. Gösele, N. N. Ledentsov, D. Bimberg, V. M. Ustinov, A. Y. Egorov, A. E. Zhukov, P. S. Kop'ev, N. A. Bert, and Z. I. Alferov, "Structural and optical properties of InAs–GaAs quantum dots subjected to high temperature annealing," *Applied Physics Letters,* vol. 69, no. 20, pp. 3072-3074, 1996.
[48] J. Kwoen, B. Jang, J. Lee, T. Kageyama, K. Watanabe, and Y. Arakawa, "All MBE grown InAs/GaAs quantum dot lasers on on-axis Si (001)," *Optics express,* vol. 26, no. 9, pp. 11568-11576, 2018.
[49] R. Alcotte, M. Martin, J. Moeyaert, R. Cipro, S. David, F. Bassani, F. Ducroquet, Y. Bogumilowicz, E. Sanchez, and Z. Ye, "Epitaxial growth of antiphase boundary free GaAs layer on 300 mm Si (001) substrate by metalorganic chemical vapour deposition with high mobility," *Apl Materials,* vol. 4, no. 4, p. 046101, 2016.
[50] L. Megalini, B. C. Cabinian, H. Zhao, D. C. Oakley, J. E. Bowers, and J. Klamkin, "Large-area direct hetero-epitaxial growth of 1550-nm ingaasp multi-quantum-well structures on patterned exact-oriented (001) silicon substrates by metal organic chemical vapor deposition," *Journal of Electronic Materials,* vol. 47, no. 2, pp. 982-987, 2018.
[51] Y. Urino, N. Hatori, K. Mizutani, T. Usuki, J. Fujikata, K. Yamada, T. Horikawa, T. Nakamura, and Y. Arakawa, "First demonstration of athermal silicon optical interposers with quantum dot lasers operating up to 125° C," *Journal of Lightwave Technology,* vol. 33, no. 6, pp. 1223-1229, 2015.
[52] Z. Lu, J. Liu, S. Raymond, P. Poole, P. Barrios, and D. Poitras, "312-fs pulse generation from a passive C-band InAs/InP quantum dot mode-locked laser," *Optics Express,* vol. 16, no. 14, pp. 10835-10840, 2008.
[53] A. Zeghuzi, H. Schmeckebier, M. Stubenrauch, C. Meuer, C. Schubert, C.-A. Bunge, and D. Bimberg, "25 Gbit/s differential phase-shift-keying signal generation using directly modulated quantum-dot semiconductor optical amplifiers," *Applied Physics Letters,* vol. 106, no. 21, p. 213501, 2015.
[54] O. Shchekin and D. Deppe, "Low-threshold high-t/sub 0/1.3-/spl mu/m inas quantum-dot lasers due to p-type modulation doping of the active region," *IEEE Photonics Technology Letters,* vol. 14, no. 9, pp. 1231-1233, 2002.
[55] O. Shchekin, J. Ahn, and D. Deppe, "High temperature performance of self-organised quantum dot laser with stacked p-doped active region," *Electronics Letters,* vol. 38, no. 14, pp. 712-713, 2002.
[56] P. M. Smowton, I. C. Sandall, H. Liu, and M. Hopkinson, "Gain in p-doped quantum dot lasers," *Journal of applied physics,* vol. 101, no. 1, p. 013107, 2007.
[57] Z. Zhang, D. Jung, J. C. Norman, P. Patel, W. W. Chow, and J. E. Bowers, "Effects of modulation p doping in InAs quantum dot lasers on silicon," *Applied Physics Letters,* vol. 113, no. 6, p. 061105, 2018.
[58] W. W. Chow and F. Jahnke, "On the physics of semiconductor quantum dots for applications in lasers and quantum optics," *Progress in Quantum Electronics,* vol. 37, no. 3, pp. 109-184, 2013.

[59] D. T. Cassidy, "Technique for measurement of the gain spectra of semiconductor diode lasers," *Journal of applied physics,* vol. 56, no. 11, pp. 3096-3099, 1984.
[60] S. Fathpour, Z. Mi, P. Bhattacharya, A. Kovsh, S. Mikhrin, I. Krestnikov, A. Kozhukhov, and N. Ledentsov, "The role of Auger recombination in the temperature-dependent output characteristics (T 0=∞) of p-doped 1.3 μm quantum dot lasers," *Applied Physics Letters,* vol. 85, no. 22, pp. 5164-5166, 2004.
[61] M. Sugawara, K. Mukai, and H. Shoji, "Effect of phonon bottleneck on quantum-dot laser performance," *Applied Physics Letters,* vol. 71, no. 19, pp. 2791-2793, 1997.
[62] T. W. Berg, S. Bischoff, I. Magnusdottir, and J. Mork, "Ultrafast gain recovery and modulation limitations in self-assembled quantum-dot devices," *IEEE Photonics Technology Letters,* vol. 13, no. 6, pp. 541-543, 2001.
[63] K. Kim, J. Urayama, T. Norris, J. Singh, J. Phillips, and P. Bhattacharya, "Gain dynamics and ultrafast spectral hole burning in In (Ga) As self-organized quantum dots," *Applied physics letters,* vol. 81, no. 4, pp. 670-672, 2002.
[64] P. Bhattacharya, S. Ghosh, S. Pradhan, J. Singh, Z.-K. Wu, J. Urayama, K. Kim, and T. B. Norris, "Carrier dynamics and high-speed modulation properties of tunnel injection InGaAs-GaAs quantum-dot lasers," *IEEE Journal of Quantum Electronics,* vol. 39, no. 8, pp. 952-962, 2003.
[65] Z. Mi and P. Bhattacharya, "DC and Dynamic Characteristics of P-Doped and Tunnel Injection 1.65-$\mu {\hbox {m}} $ InAs Quantum-Dash Lasers Grown on InP (001)," *IEEE journal of quantum electronics,* vol. 42, no. 12, pp. 1224-1232, 2006.
[66] Z. Mi, P. Bhattacharya, and S. Fathpour, "High-speed 1.3 μ m tunnel injection quantum-dot lasers," *Applied Physics Letters,* vol. 86, no. 15, p. 153109, 2005.
[67] J. Duan, H. Huang, D. Jung, Z. Zhang, J. Norman, J. Bowers, and F. Grillot, "Semiconductor quantum dot lasers epitaxially grown on silicon with low linewidth enhancement factor," *Applied Physics Letters,* vol. 112, no. 25, p. 251111, 2018.
[68] H. Huang, J. Duan, D. Jung, A. Y. Liu, Z. Zhang, J. Norman, J. E. Bowers, and F. Grillot, "Analysis of the optical feedback dynamics in InAs/GaAs quantum dot lasers directly grown on silicon," *JOSA B,* vol. 35, no. 11, pp. 2780-2787, 2018.
[69] P. M. Smowton, E. J. Pearce, H. Schneider, W. Chow, and M. Hopkinson, "Filamentation and linewidth enhancement factor in InGaAs quantum dot lasers," *Applied physics letters,* vol. 81, no. 17, pp. 3251-3253, 2002.
[70] Z. Zhang, D. Jung, J. C. Norman, P. Patel, W. W. Chow, and J. E. Bowers, "Across Zero Continuously Tunable Linewidth Enhancement Factor in 1.3 μm InAs Quantum Dot Lasers on Silicon," presented at the 26th International Semiconductor Laser Conference, Santa Fe, New Mexico, USA, 2018.
[71] S. Chen, M. Liao, M. Tang, J. Wu, M. Martin, T. Baron, A. Seeds, and H. Liu, "Electrically pumped continuous-wave 1.3 μm InAs/GaAs quantum dot lasers monolithically grown on on-axis Si (001) substrates," *Optics express,* vol. 25, no. 5, pp. 4632-4639, 2017.
[72] B. Kunert, I. Nemeth, S. Reinhard, K. Volz, and W. Stolz, "Si (001) surface preparation for the antiphase domain free heteroepitaxial growth of GaP on Si substrate," *Thin Solid Films,* vol. 517, no. 1, pp. 140-143, 2008.
[73] M. Paladugu, C. Merckling, R. Loo, O. Richard, H. Bender, J. Dekoster, W. Vandervorst, M. Caymax, and M. Heyns, "Site selective integration of III–V

materials on Si for nanoscale logic and photonic devices," *Crystal Growth & Design,* vol. 12, no. 10, pp. 4696-4702, 2012.
[74] H. Huang, X. Ren, J. Lv, Q. Wang, H. Song, S. Cai, Y. Huang, and B. Qu, "Crack-free GaAs epitaxy on Si by using midpatterned growth: Application to Si-based wavelength-selective photodetector," *Journal of Applied Physics,* vol. 104, no. 11, p. 113114, 2008.
[75] M. Tang, S. Chen, J. Wu, Q. Jiang, K. Kennedy, P. Jurczak, M. Liao, R. Beanland, A. Seeds, and H. Liu, "Optimizations of defect filter layers for 1.3-μm InAs/GaAs quantum-dot lasers monolithically grown on Si substrates," *IEEE Journal of Selected Topics in Quantum Electronics,* vol. 22, no. 6, 2016.
[76] E. Fitzgerald and N. Chand, "Epitaxial necking in GaAs grown on pre-pattemed Si substrates," *Journal of electronic materials,* vol. 20, no. 7, pp. 839-853, 1991.
[77] D. Jung, R. Herrick, J. Norman, K. Turnlund, C. Jan, K. Feng, A. C. Gossard, and J. E. Bowers, "Impact of threading dislocation density on the lifetime of InAs quantum dot lasers on Si," *Applied Physics Letters,* vol. 112, no. 15, p. 153507, 2018.
[78] T. Windhorn, G. Metze, B. Y. Tsaur, and J. C. Fan, "AlGaAs double-heterostructure diode lasers fabricated on a monolithic GaAs/Si substrate," *Applied Physics Letters,* vol. 45, no. 4, pp. 309-311, 1984.
[79] M. Razeghi, M. Defour, R. Blondeau, F. Omnes, P. Maurel, O. Acher, F. Brillouet, J. C-Fan, and J. Salerno, "First cw operation of a Ga0. 25In0. 75As0. 5P0. 5-InP laser on a silicon substrate," *Applied physics letters,* vol. 53, no. 24, pp. 2389-2390, 1988.
[80] M. E. Groenert, A. J. Pitera, R. J. Ram, and E. A. Fitzgerald, "Improved room-temperature continuous wave GaAs/AlGaAs and InGaAs/GaAs/AlGaAs lasers fabricated on Si substrates via relaxed graded Ge x Si 1− x buffer layers," *Journal of Vacuum Science & Technology B: Microelectronics and Nanometer Structures Processing, Measurement, and Phenomena,* vol. 21, no. 3, pp. 1064-1069, 2003.
[81] K. Linder, J. Phillips, O. Qasaimeh, X. Liu, S. Krishna, P. Bhattacharya, and J. Jiang, "Self-organized In 0.4 Ga 0.6 As quantum-dot lasers grown on Si substrates," *Applied physics letters,* vol. 74, no. 10, pp. 1355-1357, 1999.
[82] Z. Mi, P. Bhattacharya, J. Yang, P. Chan, and K. Pipe, "Room-temperature self-organized in0. 5Ga0. 5As quantum dot lasers on silicon," in *Device Research Conference-Conference Digest, DRC,* 2005: United States.
[83] A. Lee, Q. Jiang, M. Tang, A. Seeds, and H. Liu, "Continuous-wave InAs/GaAs quantum-dot laser diodes monolithically grown on Si substrate with low threshold current densities," *Optics express,* vol. 20, no. 20, pp. 22181-22187, 2012.
[84] A. Y. Liu, C. Zhang, J. Norman, A. Snyder, D. Lubyshev, J. M. Fastenau, A. W. Liu, A. C. Gossard, and J. E. Bowers, "High performance continuous wave 1.3 μ m quantum dot lasers on silicon," *Applied Physics Letters,* vol. 104, no. 4, p. 041104, 2014.
[85] A. Y. Liu, R. W. Herrick, O. Ueda, P. M. Petroff, A. C. Gossard, and J. E. Bowers, "Reliability of InAs/GaAs Quantum Dot Lasers Epitaxially Grown on Silicon," *IEEE Journal of Selected Topics in Quantum Electronics,* vol. 21, no. 6, pp. 690-697, 2015.
[86] M. Kuntz, G. Fiol, M. Laemmlin, C. Meuer, and D. Bimberg, "High-Speed Mode-Locked Quantum-Dot Lasers and Optical Amplifiers," *Proceedings of the IEEE,* vol. 95, no. 9, 2007.

[87] J. C. Norman, Z. Zhang, D. Jung, Y. Wan, M. Kennedy, A. Torres, R. W. Herrick, A. C. Gossard, and J. E. Bowers, "High performance quantum dot lasers epitaxially integrated on Si," in *Quantum Communications and Quantum Imaging XVI*, 2018, vol. 10771, p. 107710D: International Society for Optics and Photonics.
[88] Y. Wan, J. Norman, Q. Li, M. Kennedy, D. Liang, C. Zhang, D. Huang, Z. Zhang, A. Y. Liu, and A. Torres, "1.3 μm submilliamp threshold quantum dot micro-lasers on Si," *Optica*, vol. 4, no. 8, pp. 940-944, 2017.
[89] Y. Wan, D. Jung, J. Norman, C. Shang, I. MacFarlane, Q. Li, M. Kennedy, A. C. Gossard, K. M. Lau, and J. E. Bowers, "O-band electrically injected quantum dot micro-ring lasers on on-axis (001) GaP/Si and V-groove Si," *Optics express*, vol. 25, no. 22, pp. 26853-26860, 2017.
[90] J. Duan, H. Huang, D. Jung, J. Norman, J. E. Bowers, and F. Grillot, "Low Linewidth Enhancement Factor and High Optical Feedback Resistance of p-Doped Silicon Based Quantum Dot Lasers," presented at the 31st Annual Conference of the IEEE Photonics Society, Reston, Virginia, USA, 2018.
[91] G. Kurczveil, C. Zhang, A. Descos, D. Liang, M. Fiorentino, and R. G. Beausoleil, "On-chip Hybrid Silicon Quantum Dot Comb Laser With 14 Error-Free Channels," presented at the 26th International Semiconductor Laser Conference, Santa Fe, New Mexico, 2018.
[92] S. Liu, X. Wu, D. Jung, J. C. Norman, M. Kennedy, H. K. Tsang, A. C. Gossard, and J. E. Bowers, "High-channel-count low-noise 20 GHz passively mode locked quantum dot laser directly grown on Si with 4.1 Tbit/s transmission capacity," 2018.
[93] J. E. Ayers, T. Kujofsa, P. Rago, and J. Raphael, *Heteroepitaxy of semiconductors: theory, growth, and characterization*. CRC press, 2016.
[94] A. Ourmazd, "The electrical properties of dislocations in semiconductors," *Contemporary Physics*, vol. 25, no. 3, pp. 251-268, 1984.
[95] O. Ueda and S. J. Pearton, *Materials and reliability handbook for semiconductor optical and electron devices*. Springer Science & Business Media, 2012.
[96] D. Pasquariello and K. Hjort, "Plasma-assisted InP-to-Si low temperature wafer bonding," *IEEE Journal of Selected Topics in Quantum Electronics*, vol. 8, no. 1, pp. 118-131, 2002.
[97] V. Yang, M. Groenert, C. Leitz, A. Pitera, M. Currie, and E. A. Fitzgerald, "Crack formation in GaAs heteroepitaxial films on Si and SiGe virtual substrates," *Journal of applied physics*, vol. 93, no. 7, pp. 3859-3865, 2003.
[98] C. Merckling, N. Waldron, S. Jiang, W. Guo, N. Collaert, M. Caymax, E. Vancoille, K. Barla, A. Thean, M. Heyns, and W. Vandervorst, "Heteroepitaxy of InP on Si(001) by selective-area metal organic vapor-phase epitaxy in sub-50 nm width trenches: The role of the nucleation layer and the recess engineering," *Journal of Applied Physics*, vol. 115, no. 2, 2014.
[99] J. Matthews and A. Blakeslee, "Defects in epitaxial multilayers: I. Misfit dislocations," *Journal of Crystal growth*, vol. 27, pp. 118-125, 1974.
[100] X. Zhang, P. Li, G. Zhao, D. Parent, F. Jain, and J. Ayers, "Removal of threading dislocations from patterned heteroepitaxial semiconductors by glide to sidewalls," *Journal of electronic materials*, vol. 27, no. 11, pp. 1248-1253, 1998.
[101] J. Wu and P. Jin, "Self-assembly of InAs quantum dots on GaAs (001) by molecular beam epitaxy," *Frontiers of Physics*, vol. 10, no. 1, pp. 7-58, 2015.

[102] T. Amano, T. Sugaya, and K. Komori, "Highest density 1.3 μm InAs quantum dots covered with gradient composition InGaAs strain reduced layer grown with an As2 source using molecular beam epitaxy," *Japanese journal of applied physics*, vol. 44, no. 3L, p. L432, 2005.
[103] A. Balzarotti, "The evolution of self-assembled InAs/GaAs (001) quantum dots grown by growth-interrupted molecular beam epitaxy," *Nanotechnology*, vol. 19, no. 50, p. 505701, 2008.
[104] F. Chang, C. Wu, and H. Lin, "Effect of InGaAs capping layer on the properties of InAs/InGaAs quantum dots and lasers," *Applied physics letters*, vol. 82, no. 25, pp. 4477-4479, 2003.
[105] C. K. Chia, Y. W. Zhang, S. S. Wong, A. M. Yong, S. Y. Chow, S. J. Chua, and J. Guo, "Saturated dot density of InAs/GaAs self-assembled quantum dots grown at high growth rate," *Applied Physics Letters*, vol. 90, no. 16, 2007.
[106] N. Cho, S. Ryu, J. Song, W. Choi, J. Lee, and H. Jeon, "Comparison of structural and optical properties of InAs quantum dots grown by migration-enhanced molecular-beam epitaxy and conventional molecular-beam epitaxy," *Applied physics letters*, vol. 88, no. 13, p. 133104, 2006.
[107] L. Chu, M. Arzberger, G. Böhm, and G. Abstreiter, "Influence of growth conditions on the photoluminescence of self-assembled InAs/GaAs quantum dots," *Journal of Applied Physics*, vol. 85, no. 4, pp. 2355-2362, 1999.
[108] A. Convertino, L. Cerri, G. Leo, and S. Viticoli, "Growth interruption to tune the emission of InAs quantum dots embedded in InGaAs matrix in the long wavelength region," *Journal of crystal growth*, vol. 261, no. 4, pp. 458-465, 2004.
[109] J. Dubowski, C. N. Allen, and S. Fafard, "Laser-induced InAs/GaAs quantum dot intermixing," *Applied Physics Letters*, vol. 77, no. 22, pp. 3583-3585, 2000.
[110] F. Ferdos, S. Wang, Y. Wei, M. Sadeghi, Q. Zhao, and A. Larsson, "Influence of initial GaAs and AlAs cap layers on InAs quantum dots grown by molecular beam epitaxy," *Journal of crystal growth*, vol. 251, no. 1-4, pp. 145-149, 2003.
[111] P. Joyce, T. Krzyzewski, G. Bell, T. Jones, S. Malik, D. Childs, and R. Murray, "Effect of growth rate on the size, composition, and optical properties of InAs/GaAs quantum dots grown by molecular-beam epitaxy," *Physical Review B*, vol. 62, no. 16, p. 10891, 2000.
[112] P. Joyce, T. Krzyzewski, G. Bell, B. Joyce, and T. Jones, "Composition of InAs quantum dots on GaAs (001): Direct evidence for (In, Ga) As alloying," *Physical Review B*, vol. 58, no. 24, p. R15981, 1998.
[113] A. Kovsh, N. Maleev, A. Zhukov, S. Mikhrin, A. Vasil'ev, E. Semenova, Y. M. Shernyakov, M. Maximov, D. Livshits, and V. Ustinov, "InAs/InGaAs/GaAs quantum dot lasers of 1.3 μm range with enhanced optical gain," *Journal of Crystal Growth*, vol. 251, no. 1-4, pp. 729-736, 2003.
[114] H. Y. Liu, M. Hopkinson, C. N. Harrison, M. J. Steer, R. Frith, I. R. Sellers, D. J. Mowbray, and M. S. Skolnick, "Optimizing the growth of 1.3 μm InAs/InGaAs dots-in-a-well structure," *Journal of Applied Physics*, vol. 93, no. 5, pp. 2931-2936, 2003.
[115] A. Madhukar, Q. Xie, P. Chen, and A. Konkar, "Nature of strained InAs three-dimensional island formation and distribution on GaAs(100)," *Applied Physics Letters*, vol. 64, no. 20, pp. 2727-2729, 1994.

[116] I. Mukhametzhanov, Z. Wei, R. Heitz, and A. Madhukar, "Punctuated island growth: An approach to examination and control of quantum dot density, size, and shape evolution," *Applied Physics Letters,* vol. 75, no. 1, pp. 85-87, 1999.
[117] Y. Nakata, K. Mukai, M. Sugawara, K. Ohtsubo, H. Ishikawa, and N. Yokoyama, "Molecular beam epitaxial growth of InAs self-assembled quantum dots with light-emission at 1.3 μm," *Journal of Crystal Growth,* vol. 208, no. 1-4, pp. 93-99, 2000.
[118] K. Nishi, H. Saito, S. Sugou, and J.-S. Lee, "A narrow photoluminescence linewidth of 21 meV at 1.35 μm from strain-reduced InAs quantum dots covered by In 0.2 Ga 0.8 As grown on GaAs substrates," *Applied Physics Letters,* vol. 74, no. 8, pp. 1111-1113, 1999.
[119] S. Ozdemir, Y. E. Suyolcu, S. Turan, and B. Aslan, "Influence of the growth conditions on the optical and structural properties of self-assembled InAs/GaAs quantum dots for low As/In ratio," *Applied Surface Science,* vol. 392, pp. 817-825, 2017.
[120] P. Petroff and S. DenBaars, "MBE and MOCVD growth and properties of self-assembling quantum dot arrays in III-V semiconductor structures," *Superlattices and Microstructures,* vol. 15, no. 1, p. 15, 1994.
[121] A. Stintz, G. Liu, A. Gray, R. Spillers, S. Delgado, and K. Malloy, "Characterization of InAs quantum dots in strained In x Ga 1− x As quantum wells," *Journal of Vacuum Science & Technology B: Microelectronics and Nanometer Structures Processing, Measurement, and Phenomena,* vol. 18, no. 3, pp. 1496-1501, 2000.
[122] T. Sugaya, K. Komori, S. Yamauchi, and T. Amano, "1.3 μ m InAs quantum dots grown with an As 2 source using molecular-beam epitaxy," *Journal of Vacuum Science & Technology B: Microelectronics and Nanometer Structures Processing, Measurement, and Phenomena,* vol. 23, no. 3, pp. 1243-1246, 2005.
[123] J. Sun, P. Jin, and Z.-G. Wang, "Extremely low density InAs quantum dots realized in situ on (100) GaAs," *Nanotechnology,* vol. 15, no. 12, p. 1763, 2004.
[124] Z. Wasilewski, S. Fafard, and J. McCaffrey, "Size and shape engineering of vertically stacked self-assembled quantum dots," *Journal of crystal growth,* vol. 201, pp. 1131-1135, 1999.
[125] V. Ustinov, N. Maleev, A. Zhukov, A. Kovsh, A. Y. Egorov, A. Lunev, B. Volovik, I. Krestnikov, Y. G. Musikhin, and N. Bert, "InAs/InGaAs quantum dot structures on GaAs substrates emitting at 1.3 μm," *Applied physics letters,* vol. 74, no. 19, pp. 2815-2817, 1999.
[126] A. Y. Liu, "Quantum Dot Lasers Epitaxially Grown on Silicon," University of California, Santa Barbara, 2016.
[127] W. W. Chow, A. Y. Liu, A. C. Gossard, and J. E. Bowers, "Extraction of inhomogeneous broadening and nonradiative losses in InAs quantum-dot lasers," *Applied Physics Letters,* vol. 107, no. 17, p. 171106, 2015.
[128] G. Solomon, J. Trezza, and J. Harris Jr, "Effects of monolayer coverage, flux ratio, and growth rate on the island density of InAs islands on GaAs," *Applied physics letters,* vol. 66, no. 23, pp. 3161-3163, 1995.
[129] T. Konishi, S. Tsukamoto, T. Ito, T. Akiyama, and R. Kaida, "Atomistic behaviour of (n× 3)-reconstructed areas of InAs–GaAs (001) surface at the growth condition," *Journal of Crystal Growth,* vol. 477, pp. 104-109, 2017.

[130] C. Foxon and B. Joyce, "Interaction kinetics of As2 and Ga on {100} GaAs surfaces," *Surface Science,* vol. 64, no. 1, pp. 293-304, 1977.
[131] T. Sugaya, T. Nakagawa, Y. Sugiyama, Y. Tanuma, and K. Yonei, "Difference in Diffusion Length of Ga Atoms under As2 and As4 Flux in Molecular Beam Epitaxy," *Japanese journal of applied physics,* vol. 36, no. 9R, p. 5670, 1997.
[132] K. Nishi, T. Kageyama, M. Yamaguchi, Y. Maeda, K. Takemasa, T. Yamamoto, M. Sugawara, and Y. Arakawa, "Molecular beam epitaxial growths of high-optical-gain InAs quantum dots on GaAs for long-wavelength emission," *Journal of Crystal Growth,* vol. 378, pp. 459-462, 2013.
[133] T. Kageyama, Q. Vo, K. Watanabe, K. Takemasa, M. Sugawara, S. Iwamoto, and Y. Arakawa, "Large modulation bandwidth (13.1 GHz) of 1.3 μm-range quantum dot lasers with high dot density and thin barrier layer," in *Compound Semiconductor Week (CSW)[Includes 28th International Conference on Indium Phosphide & Related Materials (IPRM) & 43rd International Symposium on Compound Semiconductors (ISCS), 2016,* 2016, pp. 1-2: IEEE.
[134] G. Shtengel, R. Kazarinov, G. Belenky, M. Hybertsen, and D. Ackerman, "Advances in measurements of physical parameters of semiconductor lasers," *International journal of high speed electronics and systems,* vol. 9, no. 04, pp. 901-940, 1998.
[135] D. Jung, Z. Zhang, J. Norman, R. Herrick, M. Kennedy, P. Patel, K. Turnlund, C. Jan, Y. Wan, and A. C. Gossard, "Highly reliable low-threshold InAs quantum dot lasers on on-axis (001) Si with 87% injection efficiency," *ACS Photonics,* vol. 5, no. 3, pp. 1094-1100, 2017.
[136] G. Shtengel and D. Ackerman, "Internal optical loss measurements in 1.3 mu m InGaAsP lasers," *Electronics Letters,* vol. 31, no. 14, pp. 1157-1159, 1995.
[137] D. G. Deppe, H. Huang, and O. B. Shchekin, "Modulation characteristics of quantum-dot lasers: The influence of p-type doping and the electronic density of states on obtaining high speed," *IEEE Journal of Quantum Electronics,* vol. 38, no. 12, pp. 1587-1593, 2002.
[138] A. Y. Liu, J. Peters, X. Huang, D. Jung, J. Norman, M. L. Lee, A. C. Gossard, and J. E. Bowers, "Electrically pumped continuous-wave 1.3 μm quantum-dot lasers epitaxially grown on on-axis (001) GaP/Si," *Optics letters,* vol. 42, no. 2, pp. 338-341, 2017.
[139] J. Norman, M. J. Kennedy, J. Selvidge, Q. Li, Y. Wan, A. Y. Liu, P. G. Callahan, M. P. Echlin, T. M. Pollock, K. M. Lau, A. C. Gossard, and J. E. Bowers, "Electrically pumped continuous wave quantum dot lasers epitaxially grown on patterned, on-axis (001) Si," *Opt Express,* vol. 25, no. 4, pp. 3927-3934, Feb 20 2017.
[140] J. Norman, D. Jung, M. Kennedy, C. Shang, A. C. Gossard, and J. E. Bowers, "Low threshold epitaxial InAs quantum dot lasers on on-axis GaP/Si (001)," in *Photonics Conference (IPC), 2017 IEEE,* 2017, pp. 403-404: IEEE.
[141] D. Jung, J. Norman, M. Kennedy, C. Shang, B. Shin, Y. Wan, A. C. Gossard, and J. E. Bowers, "High efficiency low threshold current 1.3 μ m InAs quantum dot lasers on on-axis (001) GaP/Si," *Applied Physics Letters,* vol. 111, no. 12, p. 122107, 2017.
[142] H. Park, P. Srinivasan, M. L. Davenport, M. N. Sysak, and R. Jones, "Experimental Investigations of Characteristic Temperatures of Hybrid Silicon Lasers," *IEEE Journal of Quantum Electronics,* vol. 48, no. 12, pp. 1512-1518, 2012.

[143] T. Higashi, T. Yamamoto, S. Ogita, and M. Kobayashi, "Experimental analysis of characteristic temperature in quantum-well semiconductor lasers," *IEEE Journal of Selected Topics in Quantum Electronics,* vol. 3, no. 2, pp. 513-521, 1997.
[144] T. Higashi, T. Yamamoto, S. Kubota, and S. Ogita, "Experimental analysis of characteristic temperature in quantum-well semiconductor lasers," in *Semiconductor Laser Conference, 1996., 15th IEEE International*, 1996, pp. 49-50: IEEE.
[145] S. Fathpour, Z. Mi, P. Bhattacharya, A. R. Kovsh, S. S. Mikhrin, I. L. Krestnikov, A. V. Kozhukhov, and N. N. Ledentsov, "The role of Auger recombination in the temperature-dependent output characteristics (T0=∞) of p-doped 1.3 μm quantum dot lasers," *Applied Physics Letters,* vol. 85, no. 22, pp. 5164-5166, 2004.
[146] Y. Jang, T. Badcock, D. Mowbray, M. Skolnick, J. Park, D. Lee, H. Liu, M. Hopkinson, R. Hogg, and A. Andreev, "Enhanced nonradiative Auger recombination in p-type modulation doped InAs/GaAs quantum dots," *Applied Physics Letters,* vol. 93, no. 10, p. 101903, 2008.
[147] I. P. Marko, A. D. Andreev, A. R. Adams, R. Krebs, J. P. Reithmaier, and A. Forchel, "The role of auger recombination in inas 1.3-μm quantum-dot lasers investigated using high hydrostatic pressure," *IEEE Journal of Selected Topics in Quantum Electronics,* vol. 9, no. 5, pp. 1300-1307, 2003.
[148] D. Inoue, D. Jung, J. Norman, Y. Wan, N. Nishiyama, S. Arai, A. C. Gossard, and J. E. Bowers, "Directly modulated 1.3 μm quantum dot lasers epitaxially grown on silicon," *Optics express,* vol. 26, no. 6, pp. 7022-7033, 2018.
[149] R. Nagarajan, M. Ishikawa, T. Fukushima, R. S. Geels, and J. E. Bowers, "High speed quantum-well lasers and carrier transport effects," *IEEE Journal of Quantum Electronics,* vol. 28, no. 10, pp. 1990-2008, 1992.
[150] W. Kobayashi, T. Ito, T. Yamanaka, T. Fujisawa, Y. Shibata, T. Kurosaki, M. Kohtoku, T. Tadokoro, and H. Sanjoh, "50-Gb/s direct modulation of 1.3-μm InGaAlAs-based DFB laser with ridge waveguide structure," *IEEE J. Sel. Top. Quantum Electron.,* vol. 19, no. 4, p. 1500908, 2013.
[151] D. Arsenijević and D. Bimberg, "Quantum-dot lasers for 35 Gbit/s pulse-amplitude modulation and 160 Gbit/s differential quadrature phase-shift keying," in *Semiconductor Lasers and Laser Dynamics VII*, 2016, vol. 9892, p. 98920S: International Society for Optics and Photonics.
[152] S. Yellen, A. Shepard, R. Dalby, J. Baumann, H. Serreze, T. Guido, R. Soltz, K. Bystrom, C. Harding, and R. Waters, "Reliability of GaAs-based semiconductor diode lasers: 0.6-1.1 mu m," *IEEE journal of quantum electronics,* vol. 29, no. 6, pp. 2058-2067, 1993.
[153] Z. I. Kazi, P. Thilakan, T. Egawa, M. Umeno, and T. Jimbo, "Realization of GaAs/AlGaAs lasers on Si substrates using epitaxial lateral overgrowth by metalorganic chemical vapor deposition," *Japanese Journal of Applied Physics,* vol. 40, no. 8R, p. 4903, 2001.
[154] L. Kimerling, "Recombination enhanced defect reactions," *Solid-State Electronics,* vol. 21, no. 11-12, pp. 1391-1401, 1978.
[155] X. Huang, Y. Song, T. Masuda, D. Jung, and M. Lee, "InGaAs/GaAs quantum well lasers grown on exact GaP/Si (001)," *Electronics Letters,* vol. 50, no. 17, pp. 1226-1227, 2014.

[156] K. Volz, A. Beyer, W. Witte, J. Ohlmann, I. Németh, B. Kunert, and W. Stolz, "GaP-nucleation on exact Si (0 0 1) substrates for III/V device integration," *Journal of Crystal Growth,* vol. 315, no. 1, pp. 37-47, 2011.
[157] Q. Li and K. M. Lau, "Epitaxial growth of highly mismatched III-V materials on (001) silicon for electronics and optoelectronics," *Progress in Crystal Growth and Characterization of Materials,* vol. 63, no. 4, pp. 105-120, 2017.
[158] L. Megalini, B. Bonef, B. C. Cabinian, H. Zhao, A. Taylor, J. S. Speck, J. E. Bowers, and J. Klamkin, "1550-nm InGaAsP multi-quantum-well structures selectively grown on v-groove-patterned SOI substrates," *Applied Physics Letters,* vol. 111, no. 3, p. 032105, 2017.
[159] Z. Wang, A. Abbasi, U. Dave, A. De Groote, S. Kumari, B. Kunert, C. Merckling, M. Pantouvaki, Y. Shi, and B. Tian, "Novel light source integration approaches for silicon photonics," *Laser & Photonics Reviews,* vol. 11, no. 4, p. 1700063, 2017.
[160] Y. Wan, Z. Zhang, R. Chao, J. Norman, D. Jung, C. Shang, Q. Li, M. Kennedy, D. Liang, and C. Zhang, "Monolithically integrated InAs/InGaAs quantum dot photodetectors on silicon substrates," *Optics express,* vol. 25, no. 22, pp. 27715-27723, 2017.
[161] P. Bhasker, J. Norman, J. Bowers, and N. Dagli, "Intensity and Phase Modulators at 1.55 μm with InAs/InGaAs Quantum Dots Epitaxially Grown on Silicon," in *Conference on Lasers and Electro-Optics/Pacific Rim*, 2018, p. Th2J. 3: Optical Society of America.
[162] S. Liu, D. Jung, J. Norman, M. Kennedy, A. Gossard, and J. Bowers, "490 fs pulse generation from passively mode-locked single section quantum dot laser directly grown on on-axis GaP/Si," *Electronics Letters,* vol. 54, no. 7, pp. 432-433, 2018.
[163] Y. Zhang, Y. Su, Y. Bi, J. Pan, H. Yu, Y. Zhang, J. Sun, X. Sun, and M. Chong, "Inclined emitting slotted single-mode laser with 1.7° vertical divergence angle for PIC applications," *Optics letters,* vol. 43, no. 1, pp. 86-89, 2018.
[164] Y. Wan, Q. Li, A. Y. Liu, Y. Geng, J. Norman, W. W. Chow, A. C. Gossard, J. E. Bowers, E. L. Hu, and K. M. Lau, "Quantum dot lasers grown on (001) Si substrate for integration with amorphous Si waveguides," in *Optical Fiber Communications Conference and Exhibition (OFC), 2017*, 2017, pp. 1-3: IEEE.
[165] S. Feng, Y. Geng, K. M. Lau, and A. W. Poon, "Epitaxial III-V-on-silicon waveguide butt-coupled photodetectors," *Optics letters,* vol. 37, no. 19, pp. 4035-4037, 2012.
[166] M. Smit, X. Leijtens, H. Ambrosius, E. Bente, J. Van der Tol, B. Smalbrugge, T. De Vries, E.-J. Geluk, J. Bolk, and R. Van Veldhoven, "An introduction to InP-based generic integration technology," *Semiconductor Science and Technology,* vol. 29, no. 8, p. 083001, 2014.
[167] J. E. Bowers and A. Y. Liu, "A comparison of four approaches to photonic integration," in *Optical Fiber Communication Conference*, 2017, p. M2B. 4: Optical Society of America.

Appendix A

Quantum Dot Microcavity Growth Summary

The following sections are intended to document the methods and growth conditions utilized for the quantum dot microcavity structures grown for collaborations with Prof. Dirk Bouwmeester's group. Exact growth recipes and details for each sample are stored on the Gen III computer and in the onenote document. All samples were grown on the Gen III system using Andy Jackson's band edge thermometer and reflection monitoring system. Publications from this work include [1-5].

Growth Conditions

The microcavity samples were grown at a temperature of 600°C for all layers except the quantum dots. The As_2 (cracker temperature 850°C) flux beam-equivalent pressure was 9e-6 mbar for all layers except the quantum dots. The Ga and Al growth rates used were 2.60 Å/s.

Silicon was used as the n-type dopant, and carbon was used for p-type doping. All AlGaAs alloy layers were grown digitally with a period of 20 Å.

The quantum dot layers were grown at an optimized temperature to give a ground state photoluminescence (PL) peak at ~1010 nm at room temperature. This temperature was determined through a series of PL calibration growths at varying temperature for each campaign but should be ~500°C. The InAs growth rate was 0.0625 ML/s, and an As_2 (cracker temperature 850°C) beam-equivalent pressure of 7e-6 mbar was used. Rotation remained at 20-30 rpm throughout deposition. The total InAs deposition thickness was 2.3 ML with the first 1.6 ML deposited continuously and the remaining material deposited in fourteen 0.05 ML increments separated by a 1s pause. The dots should nucleate on RHEED at ~1.8 ML. While remaining at the dot growth temperature, a cap of 5 nm of GaAs was deposited. No "In-flush" step was performed. After heating back to 600°C, growth was immediately continued.

Growth Techniques & Other Notes

Since a very precise cavity resonance was needed, flux variations from the cells had to be minimized and the growth rates had to be adjusted in-situ.

To achieve stable operation of the Ga cell, power was supplied purely from the tip heating zone using PID control. When the base was utilized, the flux was found to drift lower by 0.67% per hour continuously. The Al cell showed stable operation when manual power was supplied to the tip and the base was controlled via PID. When PID control was used on base and tip, the flux became much noisier with >1% fluctuations over <1 h timespans. The In cell was stable with base and tip on PID control. The target for acceptable flux variation was <1 % over the full growth day. Flux variations were measured after system maintenance by running a recipe to measure the flux in 10 min intervals over a five-hour period.

The growth rate was monitored using Andy Jackson's band edge thermometer and reflection measurement system. Prior to growing a sample, the reflection spectrum of the full epitaxial structure was simulated layer-by-layer at the growth temperature using Vertical with the reflectivity dip recorded at one or two points in every single layer until the top p-DBR. During growth the reflection spectrum was monitored as the growth approached the simulated points. A broad-spectrum light source at normal incidence was used to guarantee sufficient signal in the fiber-coupled spectrometer. If the dip in reflectivity reached its simulated wavelength early, the amount of time it was early would be recorded and growth would be paused with that amount of time remaining in the layer, and then the rest of the layer would be skipped. If the dip did not reach the target reflectivity when it should, then the growth would be paused with shutters open until the dip was correct at which point growth would be resumed. If the growth is off less than 3 s, then no modifications described above need be performed. If the growth is off more than 30s, the cavity is likely not recoverable. Based on whether the dip was early or late (by more than 3 s), the growth rate stored in AMBER would be increased or decreased for *both* Ga *and* Al by 0.009 Å/s for Ga and 0.005 Å/s for Al. This rule of thumb has been passed down through generations of growers and works very well. Attempting to calculate the exact errors in each growth rate is not practical due to the alloys and unknown independent variation of the cells with time on a given growth day and would result in more error. Only reflectivity dips between 960 nm and 1070 nm are accurate enough on the spectrometer to be used for adjustments.

Epitaxial Layer Structure

Table 6. Epitaxial layer structure in the order of growth. In the finished sample, the bottom layers of the table would correspond to the top layers of material. For the various published results, variations in the SCH regions were performed to alter thicknesses.

Layer	Material	Thickness (A)	Al Composition	Refractive Index	n/p	Doping
UID DBR	GaAs	673	0	3.47643	UID	
Repeat 13	AlAs	799	1	2.93015	UID	
UID DBR	GaAs	673	0	3.47643	UID	
Repeat 10	AlGaAs	788	0.9	2.97858	UID	
nGaAs Contact	GaAs	4637		3.47643	n	5.00E+17
nDBR	AlGaAs	160	0-.9	3.20593	n	2.50E+18
	AlGaAs	620	0.9	2.97858	n	6.00E+17
	AlGaAs	160	.9-0	3.20593	n	5.00E+17
	GaAs	520		3.47643	n	2.00E+17
	AlGaAs	160	0-.9	3.20593	n	2.50E+18
	AlGaAs	620	0.9	2.97858	n	6.00E+17
	AlGaAs	160	.9-0	3.20593	n	5.00E+17
	GaAs	520		3.47643	n	2.00E+17
	AlGaAs	160	0-.9	3.20593	n	2.50E+18
	AlGaAs	620	0.9	2.97858	n	6.00E+17
	AlGaAs	160	.9-0	3.20593	n	5.00E+17
	GaAs	520		3.47643	n	2.00E+17
	AlGaAs	160	0-.9	3.20593	n	2.50E+18
	AlGaAs	620	0.9	2.97858	n	6.00E+17
	AlGaAs	160	.9-0	3.20593	n	5.00E+17
	GaAs	520		3.47643	n	2.00E+17
n Half Period	AlGaAs	160	0-.9	3.20593	n	2.50E+18
	AlGaAs	620	0.9	2.97858	n	6.00E+17
	AlGaAs	160	.9-0	3.20593	n	5.00E+17
n SCH	GaAs	480	0	3.47643	n	2.00E+18
	GaAs	573	0	3.47643	n	1.00E+18
	GaAs	350	0	3.47643	UID	
Active Region	InAs	2.3 (ML)	0	3.84287	UID	
~500°C	GaAs	50	0	3.47643	UID	
p SCH	GaAs	100	0	3.47643	UID	
	GaAs	922	0	3.47643	UID	
	GaAs	200	0	3.47643	p	1.00E+18
Aperture	AlGaAs	120	0-.75	3.20593	p	1.00E+18
	AlGaAs	656	0.75	3.05341	p	1.00E+18
	AlAs	100		2.93015	p	1.00E+18
	AlGaAs	953	0.83	3.01317	p	1.00E+18
	AlGaAs	432	0.75	3.05341	p	1.00E+18
	AlGaAs	210	.75-0	3.20593	p	1.00E+18
	GaAs	20		3.47643	p	1.00E+18
	GaAs	413.8		3.47643	p	1.00E+18
p DBR	AlGaAs	280	0-.9	3.20593	p	1.00E+18
	AlGaAs	417	0.9	2.97858	p	2.00E+18
	AlGaAs	210	.85-0	3.20593	p	3.00E+18
	GaAs	543.82		3.47643	p	2.00E+18
	AlGaAs	280	0-.9	3.20593	p	1.00E+18
	AlGaAs	417	0.9	2.97858	p	2.00E+18
	AlGaAs	210	.85-0	3.20593	p	3.00E+18
	GaAs	543.82		3.47643	p	2.00E+18
	AlGaAs	280	0-.9	3.20593	p	1.00E+18
	AlGaAs	417	0.9	2.97858	p	2.00E+18
	AlGaAs	210	.85-0	3.20593	p	3.00E+18
	GaAs	130		3.47643	p	1.00E+18
pGaAs Contact	GaAs	3301.52		3.47643	p	1.00E+18
UID DBR	AlGaAs	786	0.9	2.97858	UID	
Repeat 22	GaAs	673	0	3.47643	UID	

[1] H. Snijders *et al.*, "Purification of a single-photon nonlinearity," *Nature communications,* vol. 7, p. 12578, 2016.
[2] H. Snijders *et al.*, "Observation of the Unconventional Photon Blockade," *Physical review letters,* vol. 121, no. 4, p. 043601, 2018.
[3] H. Snijders *et al.*, "Fiber-Coupled Cavity-QED Source of Identical Single Photons," *Physical Review Applied,* vol. 9, no. 3, p. 031002, 2018.
[4] H. Snijders *et al.*, "Polarized quantum dot cavity-QED and single photons," *arXiv preprint arXiv:1811.10571,* 2018.
[5] J. Frey *et al.*, "Electro-optic polarization tuning of microcavities with a single quantum dot," *arXiv preprint arXiv:1805.03387,* 2018.

Appendix B

ErAs THz Device Growth

The following sections are intended to document the methods and growth conditions utilized for the ErAs THz photoconductors grown for Prof. Sascha Preu. Exact growth recipes and details for each sample are stored on the Gen III computer and in the onenote document. All samples were grown on the Gen III system. Publications from this work are [1-3].

Growth Conditions

The samples grown consisted of ternaries and quaternaries in the InAlGaAs system lattice-matched to InP with additional ErAs inclusions. All layers were grown at 490°C. Any quaternaries were grown by digital alloy. The InGaAs and InAlAs layers were grown at 4.05 Å/s with a V/III ratio of 30-40. The ErAs growth rate was 0.02 ML/s and used the same As_2 flux as the other layers. Carbon was the only dopant used. The samples consisted of various superlattice structures of 90 repeats of ~18 nm of superlattices of various composition and doping containing 0.8-1.6 ML of ErAs.

Growth Techniques & Other Notes

The ErAs growth rate was determined using RHEED oscillations on a GaAs substrate. Fewer than ten oscillations were generally attainable per substrate, but the result was reproducible. RHEED oscillations were taken at 350°C with an As_2 overpressure of 1e-5 mbar.

The as-grown samples were generally slightly hazy to the eye with visible roughness under Nomarski microscope. The source of the roughness was not determined but could have been due to the ErAs, high carbon doping levels up to 10^{19} cm^{-3}, or due to phase separation of the InAlAs layers. Nevertheless, the devices exhibited extremely high-performance levels setting records for THz power and bandwidth using 1550 nm laser sources. In any case, the roughness and its source may have been beneficial for the material goal of high electrical resistance (~MOhm) and short carrier lifetime.

[1] M. M. Aller, H. Lu, A. Gossard, U. Nandi, J. Norman, and S. Preu, "ErAs Enhanced Active Photonic THz Components," in *2018 First International Workshop on Mobile Terahertz Systems (IWMTS)*, 2018, pp. 1-4: IEEE.

[2] U. Nandi, J. Norman, A. Gossard, H. Lu, and S. Preu, "1550-nm Driven ErAs: In (Al) GaAs Photoconductor-Based Terahertz Time Domain System with 6.5 THz Bandwidth," *Journal of Infrared, Millimeter, and Terahertz Waves*, vol. 39, no. 4, pp. 340-348, 2018.

[3] A. F. Olvera, U. Nandi, J. Norman, A. Gossard, H. Roskos, and S. Preu, "Dispersive properties of self-complementary log-periodic antennas in pulsed THz systems," in *Infrared, Millimeter, and Terahertz Waves (IRMMW-THz), 2017 42nd International Conference on*, 2017, pp. 1-2: IEEE.

Appendix C

GaAs/AlAs Coupled Quantum Wells

The following sections are intended to document the methods and growth conditions utilized for the coupled quantum well structures grown for Prof. Leonid Butov. Exact growth recipes and details for each sample are stored on the Gen III and System C computer and in the associated onenote documents. Some samples were grown on the Gen III, and others were grown on System C.

Growth Conditions

The samples grown consisted of GaAs quantum wells with AlAs and AlGaAs barriers. All layers were grown at 625°C. This growth temperature is on the edge of the growth window for smooth, specular AlGaAs, which can lead to some difficulty if the pyrometer is not perfectly calibrated. Digital alloys were found to give superior AlGaAs to analog alloys as evidenced by narrower exciton linewidths, brighter luminescence, and superior transport. GaAs and AlAs were grown at a growth rate of 2 Å/s and 1 Å/s, respectively. The V/III ratio used was 25 with As_2 (850°C As cracker temperature).